Instabilités convectives et absolues dans l'écoulement de Taylor-Couette-Poiseuille excentrique

Colin Leclercq

ÉCOLE CENTRALE LYON

LMFA

N° d'ordre : 2013-46

THÈSE DE L'UNIVERSITÉ DE LYON

délivrée par

L'ÉCOLE CENTRALE DE LYON

École doctorale MEGA

Laboratoire de mécanique des fluides et d'acoustique (LMFA)

Spécialité : mécanique des fluides

par

Colin LECLERCQ

Instabilités convectives et absolues dans l'écoulement de Taylor–Couette–Poiseuille excentrique

soutenue le 16 décembre 2013 devant le jury composé de :

Colm-Cille Caulfield	examinateur
Fabien Godeferd	examinateur
Dan Henningson	rapporteur
Patrick Huerre	examinateur
Matthew Juniper	examinateur
Benoît Pier	directeur de thèse
Julian Scott	directeur de thèse
Éric Serre	rapporteur

UNIVERSITÉ DE LYON

Remerciements

Même si ce « chapitre » est le plus court de ma thèse, ces quelques lignes de remerciements ne sont pas à prendre à la légère ! Bien loin du cliché du travailleur solitaire, j'ai effectué mes premiers pas de chercheur débutant avec un encadrement exceptionnel et dans un environnement solidaire : cette thèse est le fruit de tout cela.

Je commence par remercier les membres du jury de m'avoir fait l'honneur d'examiner mon manuscrit, et d'avoir été présents le jour de ma soutenance, malgré la distance et des emplois du temps bien chargés. Je remercie tout particulièrement les deux rapporteurs pour leurs relectures détaillées.

S'il y a deux personnes que je souhaite remercier plus que toute autre ici, ce sont mes directeurs de thèse, Benoît et Julian. Un mélange de rigueur scientifique et de gentillesse, et un investissement considérable. Merci pour ces réunions de 3h (oui 3h !) où l'on discutait de tout dans les moindres détails. Benoît, merci pour ta disponibilité de tous les instants et ta patience à toute épreuve. Julian, merci pour ton intérêt profond pour les questions théoriques : j'admire ta capacité à systématiquement réduire en miettes les problèmes les plus ardus, et cela toujours en un temps record. Benoît, merci de m'avoir patiemment initié à l'usage raisonné d'un ordinateur : Linux, bash, `C++` et même postscript ! Je m'incline devant le virtuose du terminal, et m'efforcerai de cliquer toujours moins ! J'en profite au passage pour remercier Fabien d'avoir également partagé ses grandes compétences en informatique, et de m'avoir si souvent aidé, toujours très spontanément. Julian et Benoît, merci pour vos relectures minutieuses des articles et de la thèse. Julian, tu as mis un point d'honneur à m'apprendre à rédiger en anglais, et pas simplement à corriger mes erreurs ponctuellement. Je ne peux pas omettre de mentionner ici la capacité hors-horme (et reconnue de tous) de Benoît à repérer les erreurs typographiques les plus subtiles : vous m'aurez décidément tout appris, de la mise en équation des problèmes jusqu'au placement des deux-points ! La liste des compliments n'est bien sûr pas exhaustive : merci pour tout ce que vous m'avez transmis, merci de m'avoir accompagné, et merci de m'avoir armé pour la suite. Je reste très humble devant mes deux mentors.

Je salue à présent tous mes « camarades de galère », ceux qui ont déjà soutenu et ceux pour qui la ligne d'arrivée est proche. À mes camarades de bureau, Clément, Alex, Jorge, Shyam et Sébastien (dans le désordre), merci pour tous les bons moments passés au laboratoire de mécanique des fluides, d'acoustique et de babyfoot. Je remercie aussi toute l'équipe des thésards de la cafét pour l'indispensable pause bonne humeur du midi. Je ne peux vous citer tous ici tant vous êtes nombreux, mais je pense à chacun de vous. Un grand merci aussi à mon ami tout-terrain Pedro, « assimilé LMFA », pour les instants mémorables partagés durant les deux dernières années de thèse. Que ce soit

à l'ECL, en planche à voile sur le Rhône, aux Canaries ou ailleurs, les bons souvenirs ne manquent pas. Un hommage aussi à Kevin du LTDS pour avoir réussi à rendre les formations CIES particulièrement attrayantes.

Merci à toute l'équipe d'enseignement et en particulier aux anciens, André et Dominique, pour leur gentillesse avec les novices. Débuter l'enseignement à vos côtés a été un réel plaisir. Je voudrais aussi remercier Michel Lance, directeur du LMFA, de m'avoir encouragé à prendre des risques lors de mes recherches de postdoc. Je le remercie sincèrement pour sa confiance : ses conseils m'ont permis de faire des choix audacieux qui se sont révélés fructueux. Merci à Philippe pour son aide précieuse à débusquer les nombreux papiers introuvables de ma bibliographie. Merci à Wouter pour ses bons conseils et sa bienveillance de « jeune ancien ». Un dernier merci aux absents de cette liste, forcément lacunaire, qui m'ont parfois aidé ou simplement donné le sourire : ils sont nombreux au LMFA.

Merci à mes parents d'avoir vibré avec moi durant ces trois années, et en particulier le jour de la soutenance. Votre présence le jour J m'a particulièrement touché. Merci à mes amis de s'être intéressé à mes travaux obscurs et de ne pas m'avoir pris pour un fou, malgré l'intitulé de cette thèse. Pour finir, un très grand merci à Laura, pour avoir toujours été à mes côtés dans les hauts comme dans les bas. Merci de m'avoir autant soutenu et d'avoir été à ce point à l'écoute. Merci d'avoir été si compréhensive dans les moments difficiles, et merci d'avoir partagé avec moi les instants de joie. Tu as vécu ce travail de l'intérieur, le résultat de cette thèse est donc aussi un peu le tien.

Lyon, le 20 décembre 2013.

Contents

Chapter 1

Introduction

In this brief introductory chapter, we start by presenting industrial applications of eccentric Taylor–Couette–Poiseuille flow, which motivate the need for a better understanding of its stability properties. Then we introduce Taylor–Couette flow, with its incredibly rich dynamics, and explain the physical mechanism of the centrifugal instability. The main existing results concerning the effects of eccentricity and axial advection on this flow are then recalled.

1.1 Industrial motivations

Although the flow studied in this thesis is of fundamental interest, it also has practical applications in a number of industrial configurations.

1.1.1 Oil-well drilling

In oil-well drilling, the fluid of interest is mud, injected through the rotating drillstring (or drill pipe) and flowing back to the surface through the annular domain between it and the wellbore (see figure 1.1a). In figure 1.1(b), we illustrate the bending of the drillstring along the axis of the well due to hydrodynamic and mechanical forces and flexibility of the pipe. The axial length scale of the bending is much larger than the well diameter, so the geometry can be locally modelled by two eccentric cylinders with parallel axes. According to Pearson (1988), no less than $10^6\,\mathrm{m}^3$ of mud was used annually to drill 10^4 or more oil and gas wells back in the late eighties, so the flow is of major industrial interest. Despite recent studies concerning the basic laminar flow (Escudier et al., 2000, 2002), very little is known about the stability properties of this flow, as will be apparent in section 1.3. Predicting transition to complex flow régimes, such as vortical flows or turbulence, is of interest because these may well result in increased pressure losses and viscous torque.

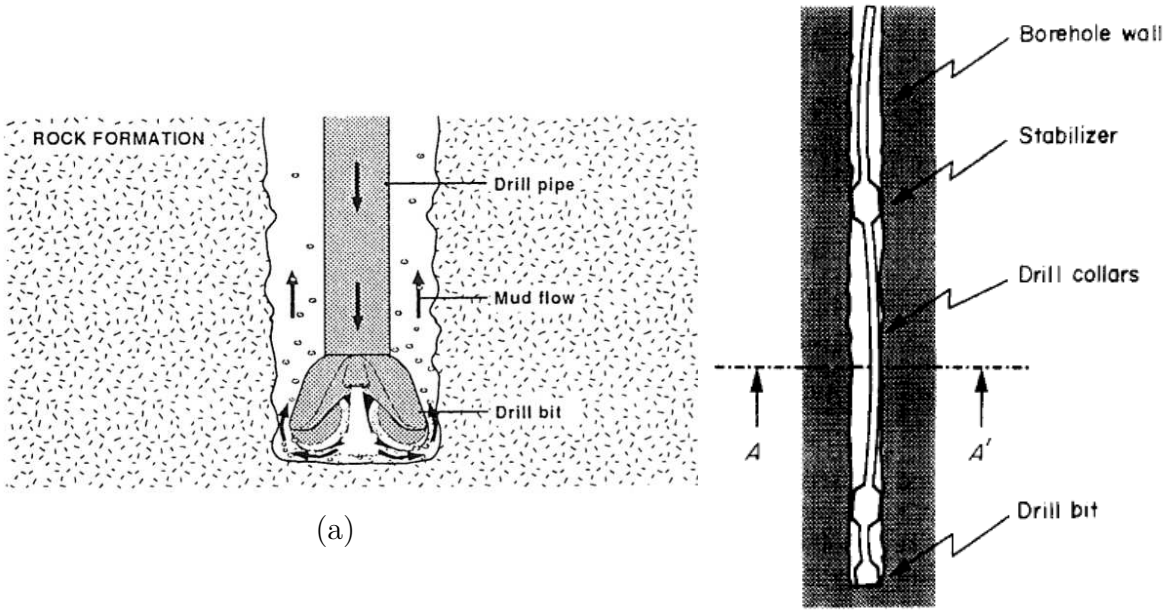

Figure 1.1 – (a) Sketch of the borehole and drill pipe (Ooms and Kampman-Reinhartz, 1996). (b) Deflection of the drillstring in the borehole (Jansen, 1991).

1.1.2 High-speed journal bearings and other applications

This flow can also be used to model journal bearings with axial flow, even though their geometry is usually more complex. According to Dai et al. (1992), 'bearings of turbines, generators, hydraulic prime movers and other power generating equipment operate in the superlaminar regime', which motivates the need for better understanding of the flow's stability properties. In their theoretical analysis, these authors did not consider the effect of axial flow. However, we know in practice that 'the damaging effect of impurities contained in oil can be considerably reduced when they are quickly removed from the friction contact area' (Sep, 2008) and that this can be achieved by axial flow. In this case again, eccentric Taylor–Couette–Poiseuille flow can be used to model the complex fluid motion, thus neglecting finite length effects, grooves, etc.

Escudier et al. (2002), who studied the basic laminar flow in this geometry for a non-Newtonian fluid, provide a list of other potential applications comprising 'oil-well-completion operations [...], industries dealing with industrial waste, with slurries and suspensions such as processed foodstuffs, synthetic fibres and even blood, and with the extrusion of molten plastics and polymer solutions.'

1.2 Taylor–Couette flow

The Taylor–Couette flow, or flow between two concentric cylinders in differential rotation, is an archetype of centrifugally unstable flow, but also one of the best-studied fundamental flows of hydrodynamic stability theory because of its extremely rich dynamics.

1.2.1 The centrifugal instability mechanism

The centrifugal instability mechanism is of inviscid nature, and can be explained by considering the Euler equations and assuming the flow to be purely azimuthal and steady. With these assumptions, the radial component of the momentum equation reduces to

$$\rho \frac{U_\theta^2}{r} = \frac{\partial P}{\partial r},$$

with ρ the density, P the pressure and U_θ the azimuthal velocity. This equation indicates a *cyclostrophic balance*, namely the centrifugal force (left hand side) is counterbalanced by a centripetal pressure gradient (right hand side). For some radial velocity profiles, this equilibrium can become unstable to axisymmetric perturbations, as shown by Rayleigh (1917). We give here Kármán (1934)'s physical interpretation of the instability criterion. Consider a circular material line at radius r_1, displaced to $r_2 = r_1 + \delta r$, with small $\delta r > 0$. According to Kelvin's theorem [1], the circulation $\Gamma = 2\pi r U_\theta(r)$ of the material line is conserved, therefore, the new velocity $U'_\theta(r_2)$ at $r = r_2$ is equal to $U_\theta(r_1) r_1/r_2$. As a result, the new centrifugal force at this position is $\rho U'^2_\theta(r_2)/r_2 = \rho U_\theta^2(r_1) r_1^2/r_2^3$, which should be compared to the equilibrium pressure gradient $\partial P/\partial r(r_2) = \rho U_\theta(r_2)^2/r_2$. If the new centrifugal force is weaker than this pressure gradient, the material line is pushed back towards lower values of r and the flow is stable. If on the other hand the centrifugal force is greater, then the flow is unstable, and this occurs if $r_1^2 U_\theta^2(r_1) > r_2^2 U_\theta^2(r_2)$, or equivalently if $\Gamma^2(r_1) > \Gamma^2(r_2)$. Considering an infinitesimal axisymmetric perturbation $\delta r \to 0$, the *Rayleigh criterion* for centrifugal instability can be written as

$$\frac{\mathrm{d}\Gamma^2}{\mathrm{d}r} < 0.$$

To obtain the radial velocity profile in a circular Couette flow, one needs to keep the viscous terms in the momentum equations. Indeed, the basic axisymmetric, steady and axially invariant Couette flow is the result of diffusion of axial vorticity from the rotating walls. When viscosity is taken into account, one easily finds a velocity profile of the form

$$U_\theta(r) = Ar + \frac{B}{r},$$

with A and B two coefficients depending on the geometry and the boundary conditions. Denoting Ω_i and Ω_o the rotation rates of the inner and outer cylinder respectively, and a and b their respective radii, the coefficients A and B have the following expressions

$$A = \frac{\Omega_o b^2 - \Omega_i a^2}{b^2 - a^2}, \quad B = \frac{(\Omega_i - \Omega_o) a^2 b^2}{b^2 - a^2}.$$

The Rayleigh criterion predicts instability when $\Omega_i \neq 0$ and $\Omega_o/\Omega_i < \eta^2$, where $\eta = a/b$. Taking viscosity into account, the flow has three nondimensional parameters: namely η and the inner and outer Reynolds numbers, $R_\mathrm{i} = a\Omega_i(b-a)/\nu$ and $R_\mathrm{o} = b\Omega_o(b-a)/\nu$. The Rayleigh instability criterion is $R_i \neq 0$ and $R_o/R_i < \eta$. Figure 1.2 shows observed flow régimes in the R_o–R_i plane for a particular value of η. The Rayleigh criterion corresponds to the straight-line asymptote of the stability threshold of Couette flow at large, positive R_o. The stabilising effect of viscosity is apparent, in particular the existence of a critical value of R_i when $R_o = 0$.

1. In an inviscid, barotropic flow with conservative body forces, the circulation around a closed curve moving with the fluid remains constant with time.

1.2.2 A very rich dynamics

More than 20 years ago, Tagg (1992) undertook an inventory of the literature on Taylor–Couette and related flows, listing almost 1500 references [2]. One of the reasons for the 'popularity' of this flow is the vast range of dynamical phenomena that can be found in this deceptively simple geometry. Indeed, considering only the effect of changing inner and outer cylinder rotation, the classical state diagram shown in figure 1.2 illustrates the wide variety of flow patterns that can be be observed experimentally. These states range from simple Couette flow to steady, periodic and quasi-periodic secondary flows, intermittent flows (coexistence of laminar and turbulent regions), patterned and featureless turbulence. As a result, many fundamental aspects of the transition to turbulence can be investigated with a simple laboratory experiment. The simple geometry also makes analytical and numerical analyses relatively easy to implement.

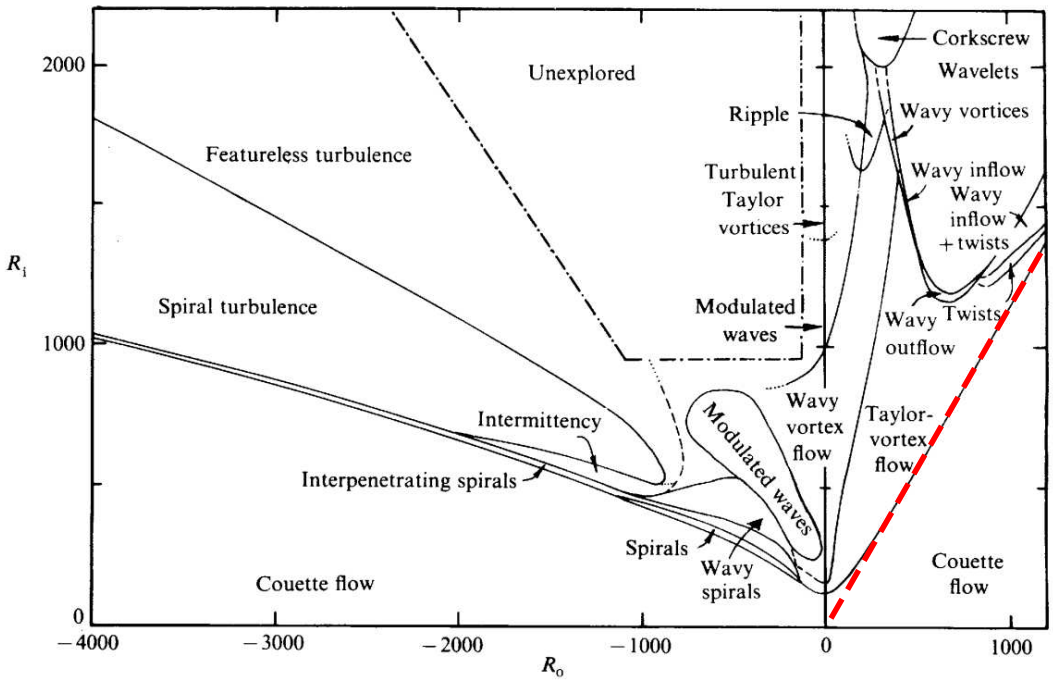

Figure 1.2 – Multiple flow régimes observed in the Taylor–Couette system with independent rotation of inner and outer cylinders (from Andereck et al. (1986), here $\eta = 0.883$). For positive R_o, the primary instability threshold is seen to asymptote to the red dashed line given by the Rayleigh criterion: $R_i = R_o/\eta$.

When eccentricity and axial flow are added, with a fixed outer cylinder, we will see in this thesis that the primary instability can lead to temporal growth of deformed toroidal and helical structures. Examples of such secondary flows for the concentric case in the absence of axial flow (but with rotation of the outer cylinder in case b) are given in figure 1.3. The toroidal vortices are named after Taylor (1923), who successfully carried out the first viscous stability analysis of the flow, without the help of a computer!

2. An updated version online, with references up to 1999, can be found at `http://clasfaculty.ucdenver.edu/rtagg/tc_refs/taylor_couette.html`.

(a) 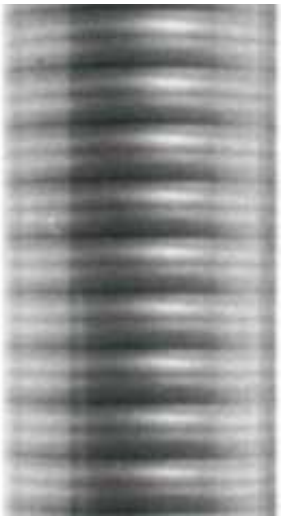 (b) 

Figure 1.3 – (a) Taylor vortex flow (Burkhalter and Koschmieder, 1974), (b) spiral vortex flow for counterrotating cylinders (H. Swinney [3]).

1.3 Effects of eccentricity and axial flow

The Taylor–Couette flow by itself is a rather crude model for oil-well drilling applications, but additional effects can be considered to bridge the gap with this industrial configuration. The first effect that must be taken into account is the axial flow, necessary to carry the rock cuttings out of the well. When axial flow is added, the flow becomes *open*, which has important qualitative and quantitative implications for the spatio-temporal dynamics of instabilities (see chapter 2). Eccentricity can also be taken into account to model the fact that the drillstring does not remain centered inside the well, due to its flexibility (see figure 1.1b). Other potentially significant effects such as the non-Newtonian nature of drilling muds, fluid-structure interaction or axially varying eccentricity and well diameter are however neglected in this study. The reason for this choice is that, as we will see in this section, quite a large number of open questions still remains regarding the dynamics of Taylor–Couette flow under the combined effects of axial advection and eccentricity. For a thorough review of references concerning the effect of axial flow on the one hand and eccentricity on the other, we refer the reader to §4.1.3, §4.1.4, §4.1.5 and §5.1 of the manuscript. In this introductory section, we focus on just a few results that we consider the most important contributions to the state-of-the-art at the time of this work.

Before proceeding to this brief review, the concepts of *temporal*, *convective* and *absolute* instabilities need be introduced. A flow is temporally unstable if an infinitesimal perturbation is amplified in time. Absolute instability occurs when the response to a localized impulsive disturbance leads to temporal growth in both the downstream and upstream directions. If the flow is temporally unstable but not absolutely unstable, it is convectively unstable. Thus, parameter space is divided into stable and unstable regions, of which the latter consists of convectively and absolutely unstable subregions. All these concepts will be discussed in more detail in the next chapter.

3. `http://rsta.royalsocietypublishing.org/content/366/1864.cover-expansion`

Important remark In all the plots given in this section, the vertical axis corresponds to an author-specific parameter measuring the intensity of centrifugal effects against viscosity. In all cases though, it is proportional to the inner cylinder rotation rate Ω_i. For the sake of simplicity, we will not provide the exact definition of this parameter for each curve, but will rather assume the radii and fluid properties to remain fixed and let only Ω_i vary. Under this assumption, the following curves indicate the critical rotation rate above which instability (temporal or absolute) occurs.

1.3.1 Eccentricity

We choose to reproduce in figure 1.4 the results of Oikawa et al. (1989b), who numerically computed the critical threshold of instability for the case $\eta = 0.5$, with and without rotation of the outer cylinder. The results without outer cylinder rotation are highlighted in green. It appears that upon increasing the eccentricity parameter, the inner cylinder needs to be rotated faster to trigger an instability. For the range of moderate eccentricities considered here, the corresponding mode at critical conditions is a deformed Taylor-vortex flow. To the author's knowledge, this paper, together with Oikawa et al. (1989a) for a smaller gap configuration, contain the most up to date theoretical predictions concerning eccentric Taylor–Couette flow.

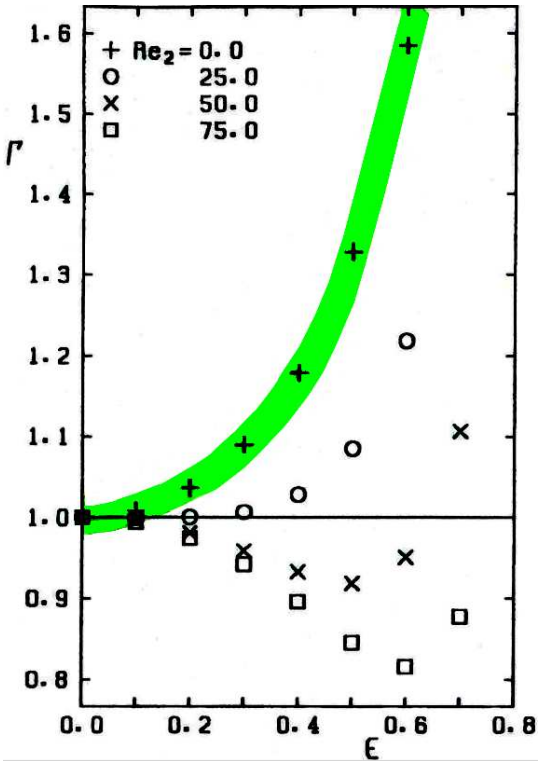

Figure 1.4 – Temporal instability threshold for the Taylor–Couette flow with $\eta = 0.5$ as a function of eccentricity (denoted here ϵ) for various outer Reynolds numbers (denoted here Re_2). From Oikawa et al. (1989b).

1.3.2 Axial flow

When the cylinders are concentric but axial flow is added, the most up to date theoretical results are those of Cotrell and Pearlstein (2004) and Cotrell et al. (2004), in which the authors cover several decades of the axial Reynolds number for different outer cylinder rotation rates. Figure 1.5 shows the temporal instability threshold as a function of axial advection rate, for a fixed outer cylinder and different radius ratios including the wide-gap case $\eta = 0.5$. We note a stabilising effect of axial advection for all radii ratios at low values of Re. For $10^2 \lesssim Re \lesssim 10^4$, there is a plateau in critical Ω_i. For the wide-gap case, the plateau is substantially lower than the maximum value of critical Ω_i, obtained for Re just below 100. At $Re \sim 10^4$, there is an abrupt transition to a Tollmien–Schlichting-like instability of viscous origin, even in the absence of rotation. For all values of η, the mode at criticality is toroidal (propagating Taylor vortices) at small enough Re, then helical with increasing azimuthal angular order as Re is increased.

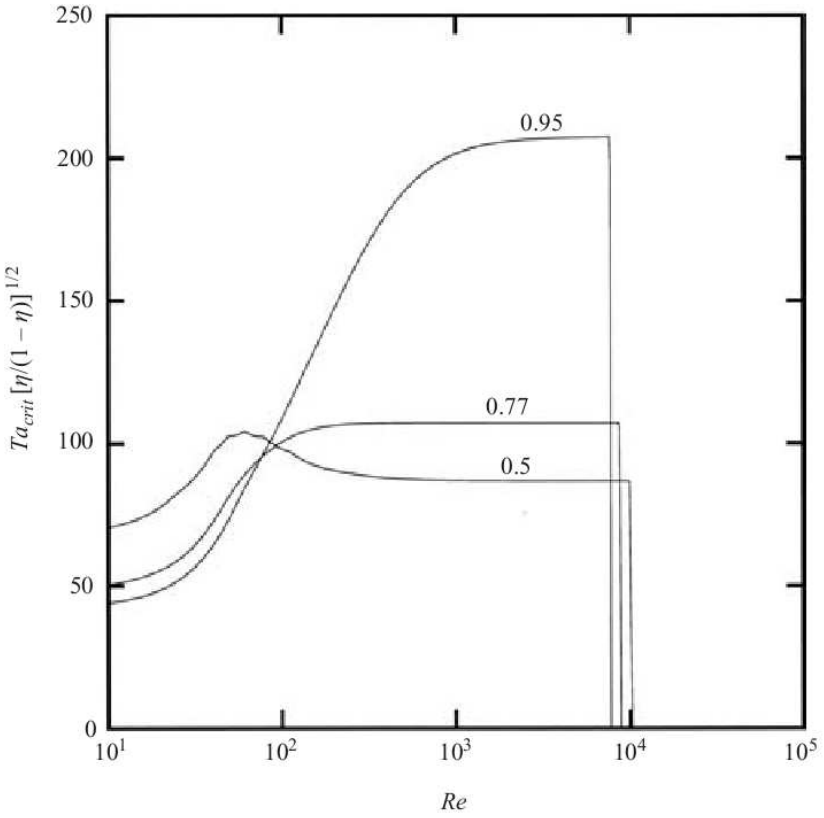

Figure 1.5 – Temporal instability threshold of the Taylor–Couette–Poiseuille flow as a function of the axial Reynolds number (denoted here Re), for three radius ratios $\eta = 0.5, 0.77, 0.95$. From Cotrell et al. (2004).

The effect of axial flow on the convective and absolute instability thresholds is clearly represented in figure 1.6. Note that convective and absolute instability thresholds are identical in the absence of axial advection. When axial advection is added, the absolute instability threshold increases faster than the convective instability. This indicates the need to rotate faster to force amplification of the perturbations *in situ*, despite transport by the basic flow. For the relatively small values, $Re \leq 3$, shown here, both the

convective and absolute instability thresholds are associated with axisymmetric perturbations (propagating Taylor vortices). These results, initially established by Babcock et al. (1991, 1992) for the full set of hydrodynamic equations, were followed by other studies by different authors concerning the helical modes of instability. It was found that none of these other modes compete with axisymmetric Taylor vortices, which are always the most absolutely unstable, at least for the moderate range of Re considered by these authors. As a result, figure 1.6 shows, in my view, the most important conclusions regarding absolute instabilities in Taylor–Couette–Poiseuille flow.

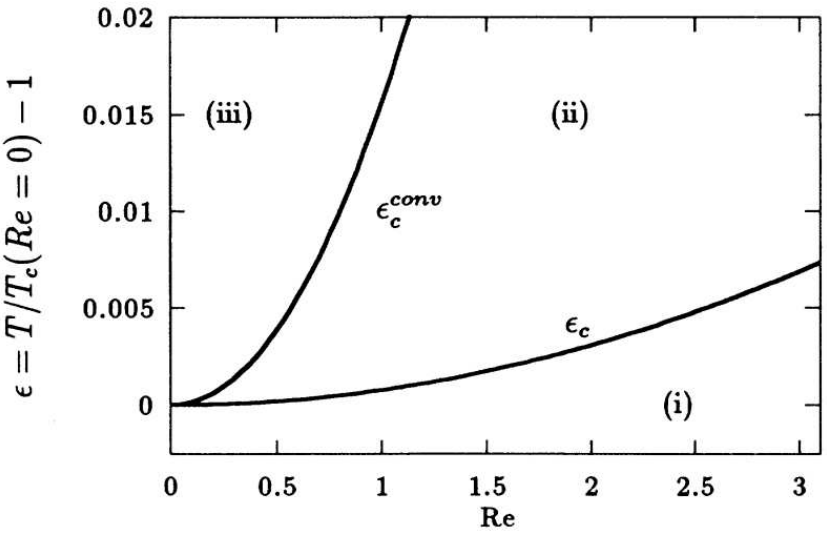

Figure 1.6 – Convective and absolute instability thresholds, respectively denoted ϵ_c and ϵ_c^{conv}, as a function of axial Reynolds number Re in Taylor–Couette–Poiseuille flow with $\eta = 0.75$. From Recktenwald et al. (1993).

1.3.3 Combined eccentricity and axial flow

No one seems to have studied theoretically the combined effects of axial flow and eccentricity, but a few experimental results are available (see §4.1.5 for references). In figure 1.7, we show two graphs of the threshold of temporal growth as a function of eccentricity, for different values of the axial Reynolds number. The difference between the left-hand and right-hand graphs is the inlet conditions of the apparatus: 'smooth' or 'sharp'. Increasing axial flow at any given eccentricity has a stabilising effect. On the other hand, the effect of eccentricity at fixed axial Reynolds number is less clear, though it seems to be mostly stabilising. An important observation is the dependence of the results on the inlet conditions of the apparatus, an effect which is more visible for higher advection rates.

The flow structures emerging from temporal instability seem difficult to identify, as noted by the authors: 'there appears to be a fluctuation in the number of vortex cells occupying the length of the apparatus at any instant or in the number of turns in the vortex spirals'. In figure 1.8, we reproduce the so-called 'double-vortex system' observed by the authors and discussed in §4.4.5. The authors indicate that it is made up of two helical structures winding in opposite directions, but warn the reader of the difficulty in

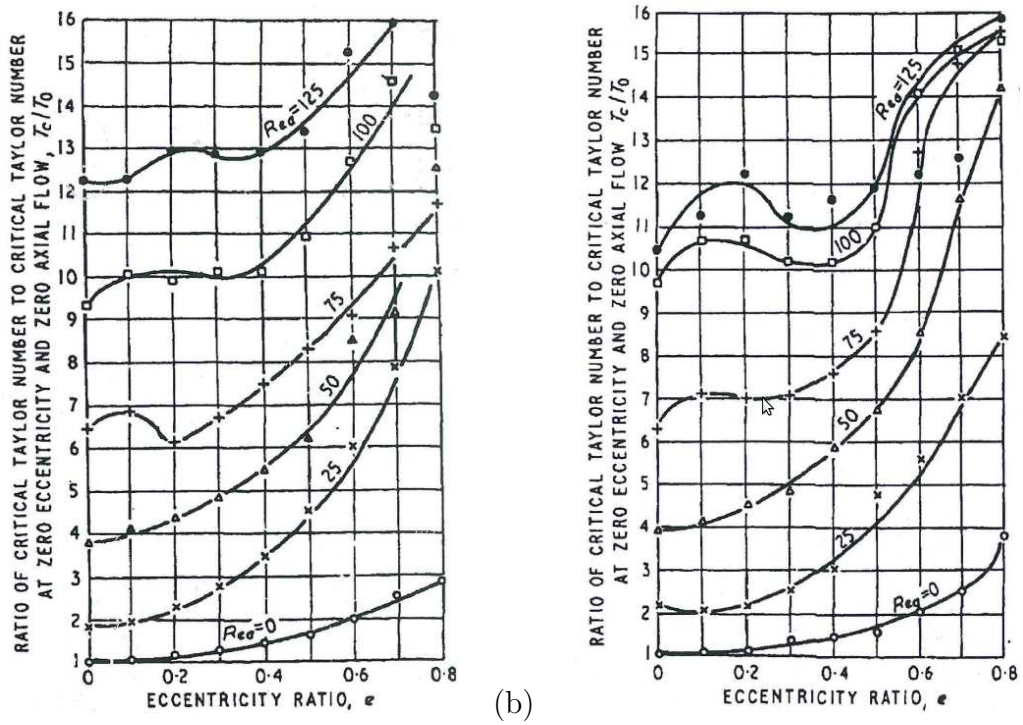

Figure 1.7 – Temporal instability threshold in eccentric Taylor–Couette–Poiseuille flow as a function of eccentricity (e), for different values of the axial Reynolds number (here denoted Re_a). Experimental results (Coney and Mobbs, 1969–70) for a (a) 'smooth' inlet, (b) 'sharp' inlet.

precisely discerning this pattern. Indeed, the identification of a double-vortex system in figure 1.8 is far from clear.

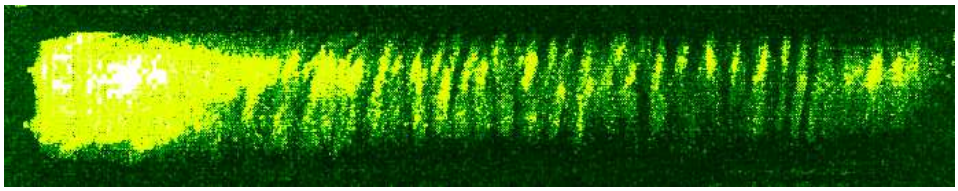

Figure 1.8 – 'Mysterious' double-vortex system (from Coney and Mobbs (1969–70), with modified colour for better contrast), discussed in §4.4.5.

1.4 Objectives and plan of the thesis

In the preceding sections, we have shown that while the stability properties of eccentric Taylor–Couette and axisymmetric Taylor–Couette–Poiseuille flows are well documented, no theoretical analysis of the joint effects of eccentricity and axial flow have been performed so far. Even though some experimental data are available, the few studies report scattered results and unexplained flow patterns. Moreover, these experimental results show no evidence of absolute instabilities, which are expected to lead to well-defined synchronized patterns rather than randomly fluctuating structures (see chapter

2). Therefore, the effect of eccentricity on absolute instabilities in the Taylor–Couette–Poiseuille flow is as yet unexplored, even from an experimental viewpoint.

The present thesis is intended to bridge these gaps, by providing a theoretical analysis of convective and absolute instabilities in the presence of eccentricity and axial flow. Parametric analyses will be carried out, taking into account the four nondimensional control parameters of the flow, which respectively measure inner cylinder rotation, axial advection, radius ratio and eccentricity. The thresholds of convective and absolute instability will be calculated and the corresponding modes of instability will be identified. The physical mechanisms associated with the instabilities will also be investigated.

The manuscript is organised in five chapters following this introduction. In chapter 2, some elements of hydrodynamic stability theory are recalled. The presentation is focused on spatio-temporal modal dynamics in open flows invariant in the streamwise direction. In chapter 3, we present the governing equations of the linear stability problem. The numerical methods used to solve this problem are also discussed in the chapter. Next, a temporal stability analysis is reported in chapter 4. The effects of axial flow and eccentricity are studied for a wide range of parameter values in both wide- and a small-gap cases. This chapter starts with a presentation of the basic flow properties, which obviously depend on the control parameters, and ends with a comparison of our stability calculations with experimental data from the literature. In chapter 5, absolute instabilities are investigated for a wide-gap case. Finally, the main results of the thesis are summarized in chapter 6, followed by a discussion of possible directions for future work.

Chapter 2

Background on convective and absolute instabilities

In this chapter, we briefly review the concepts of convective and absolute instabilities. We first define these notions by considering the response of the flow to impulsive forcing. Then we introduce the tools of modal stability theory used to study the spatio-temporal linear dynamics of any steady open flow invariant in the streamwise direction. This second section is based on the comprehensive reviews of Briggs (1964), Huerre (2000) and Schmid and Henningson (2001). In a third section, we discuss convective and absolute instabilities in the Taylor–Couette–Poiseuille flow experiment.

2.1 Definitions

In this chapter, we deal with open flows, namely flows with distinct inlet and outlet. In order to introduce concepts proper to such flows, consider what happens concretely in a perturbed Taylor–Couette system in the presence of axial flow. Figure 2.1(a) shows how a pulse perturbation at the inlet leads to a propagating Taylor-vortex wavepacket because of dispersion. Figure 2.1(b) shows a case where the wavepacket grows while being advected, indicating temporal instability of the flow. However, the perturbation eventually leaves the system, the signature of *convective instability*.

Consider now the possible ways a steady open flow, not necessarily Taylor–Couette–Poiseuille, can respond to impulsive forcing according to linear theory. The instability wavepacket can evolve in time and space in three different ways, classically represented in a space-time diagram, figure 2.2. If the wavepacket is temporally decaying, the flow is stable (see figure 2.2a). If the wavepacket is temporally growing but advected downstream of the impulse location, the flow is convectively unstable (see figure 2.2b). Finally, if a temporally amplified wavepacket is able to expand in both the downstream and upstream directions, the instability is *absolute* (see figure 2.2c). In the unstable case, there is a region of space-time in which growth occurs and which is bounded by two rays $z/t = V^{\pm}$. These rays are called *fronts* and satisfy $V^+ > 0$ (leading front) and $V^- < 0$ (trailing front) in the presence of absolute instability. As a result, absolute instability spreads through the entire system and may lead to a new flow following nonlinear saturation.

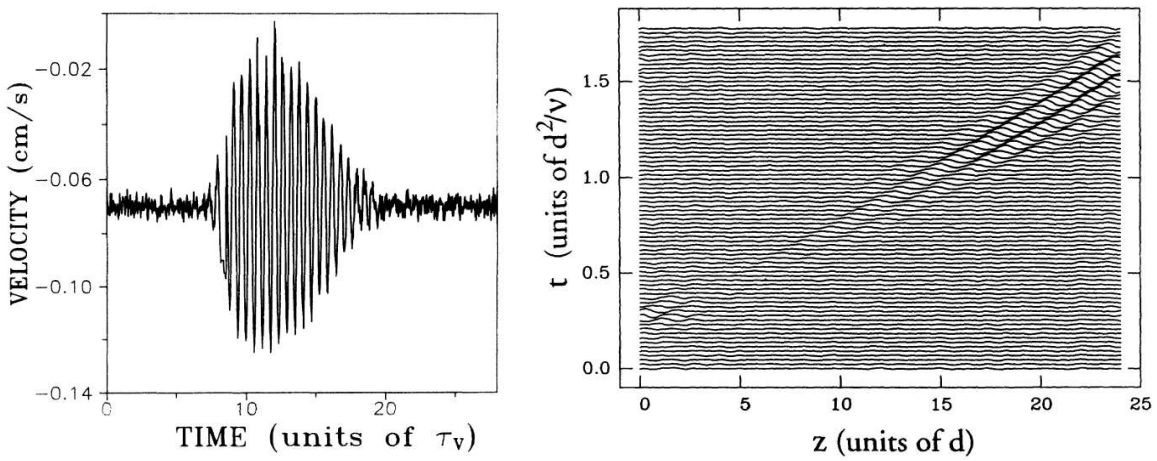

(a) (b)

Figure 2.1 – (a) Instability wavepacket in Taylor–Couette–Poiseuille flow (Tsameret and Steinberg, 1994) in the convectively unstable régime, resulting from amplification of a pulse perturbation at the inlet. (b) Space-time diagram for Taylor–Couette–Poiseuille flow (Babcock et al., 1994) showing a convective instability: a wavepacket propagates downstream while being temporally amplified.

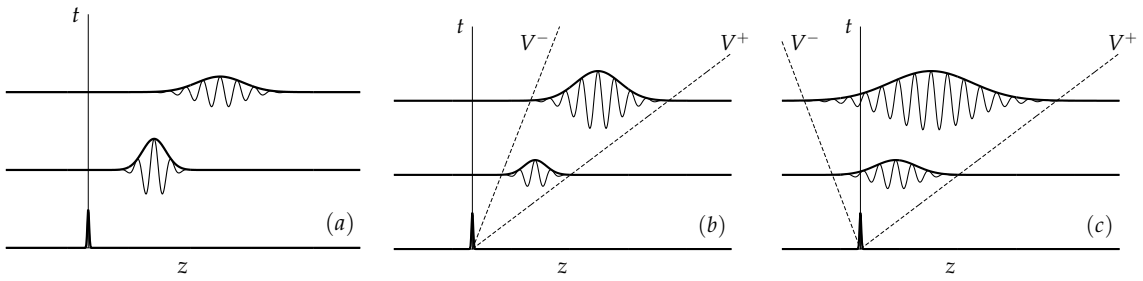

Figure 2.2 – Linear impulse response wavepacket, with basic flow advection from left to right: (a) stable, (b) convectively unstable, (c) absolutely unstable. In the temporally unstable case, $z = V^+t$ and $z = V^-t$ define the leading and trailing fronts (dashed lines) bounding the growing part of the wavepacket. After Huerre (2000).

2.2 Modal dynamics in open flows

Linear stability theory is a very general approach applicable to any dynamical system where one considers the behaviour of infinitesimal perturbations superimposed on a solution of the governing equations. These equations usually depend on at least one control parameter χ. Depending on the value of χ, perturbations will grow or decay exponentially in time. The critical value χ_c corresponds to the boundary separating these two types of behaviour. When the flow is *open*, perturbations evolve in both time and space and the distinction between convective and absolute instabilities is introduced.

The *basic flow* $\mathbf{U}$ whose stability is studied is a solution of the governing equations, assumed steady and invariant in the streamwise coordinate, z. Because of invariance of $\mathbf{U}$ with respect to z and t, the linear equations governing the evolution of the perturbation $\mathbf{u}'$ have coefficients independent of these variables. As a result, $\mathbf{u}'$ can be expressed as a

superposition of waves of the form

$$\tilde{\mathbf{u}}(x,y)\exp \mathrm{i}(kz-\omega t)+\text{c.c.},$$

where c.c. denotes complex conjugate. When boundary conditions are added, only waves satisfying a relation

$$D(k,\omega;\chi)=0,$$

called the *dispersion relation* between (possibly complex) axial wavenumber k and frequency ω, provide solutions. These waves are referred to as *normal modes*.

2.2.1 Temporal instability

As previously indicated, any perturbation may be Fourier decomposed along the streamwise direction z, and k is then a continuous real variable. For each real value of k, there are many complex values of ω satisfying the dispersion relation, corresponding to *temporal modes* and denoted $\omega(k)$. The frequency of each such mode is given by the real part ω_r of the frequency, while the temporal growth rate is given by the imaginary part ω_i [1]. If at least one temporal mode has a positive growth rate for some value of k, then the flow is unstable. At critical conditions $\chi=\chi_c$, the temporal mode with largest growth rate is neutrally stable $\omega_{\mathrm{i,max}}=0$ when $k=k_c$ (critical wavenumber) and stable $\omega_{\mathrm{i,max}}\leq 0$ otherwise. A temporally unstable flow is at least convectively unstable, because there will always exist a frame of reference where temporal growth will be observed following impulsive forcing (the maximum of the resulting wavepacket grows at a rate determined by the fastest growing mode). But the flow may also be absolutely unstable and an additional criterion is required to distinguish this type of instability.

2.2.2 Linear impulse response using integral transforms

As noted earlier, the distinction between absolute and convective instabilities can be made by considering the linear impulse response, or Green function $G(z,t)$, in the long-time limit (we suppress the $x-y$ dependence here, for clarity). A convenient approach is to use Fourier and Laplace transforms with respect to z and t to convert the original linear initial-value problem, consisting of partial differential equations, into a simple algebraic equation. The latter equation is easily solved: the impulse response in spectral space being simply the reciprocal of the dispersion relation, $1/D(k,\omega)$. To convert the solution back to physical space, inverse Fourier and Laplace transforms are applied:

$$G(z,t)=\frac{1}{4\pi^2}\int_{L_\omega}\int_{F_k}\frac{\exp \mathrm{i}(kz-\omega t)}{D(k,\omega)}\,\mathrm{d}k\,\mathrm{d}\omega, \tag{2.1}$$

where L_ω is an appropriately chosen integration contour in the complex ω-plane and F_k is the real wavenumber axis.

The integrand must be analytic above L_ω in order for the response to be zero when $t<0$, namely before impulsive forcing is applied at $t=0$. In other words, L_ω must be

1. subscripts 'r' and 'i' denote real and imaginary parts in the rest of the manuscript.

chosen so as to comply with the *causality principle*. Since the poles of the integrand are given by the temporal modes $\omega(k)$, a straight integration contour L_ω at constant ω_i can be chosen, provided ω_i is larger than the maximum growth rate $\omega_{\mathrm{i,max}}$.

Even though k is real in the Fourier transform, it is useful to allow for complex wavenumbers. This approach permits the use of powerful complex variable techniques to evaluate the integral. In the following, we will therefore consider the analytic continuation of the integrand to the complex k-plane. The residue theorem can then be applied to compute the inverse Fourier transform by closing the integration contour F_k by a semicircle at $|k| \to \infty$. The contribution of the integral along the semicircle is zero if it is chosen in the upper half k-plane for $x > 0$, and in the lower half k-plane for $x < 0$. The value of the integral is given by the contributions of the poles enclosed by the integration contour. These poles correspond to the roots $k(\omega)$ of the dispersion relation and are called *spatial modes* or *branches*. The residue theorem tells us that distinct sets of spatial modes, respectively denoted $k^+(\omega)$ and $k^-(\omega)$, contribute to the impulse response downstream and upstream of the forcing at $z = 0$. When L_ω is chosen as indicated earlier, the k^+ lie in the upper half k-plane whereas the k^- are in the lower half k-plane.

2.2.3 The pinching criterion and absolute instability

Provided the choice of L_ω complies with causality, it is in principle possible to determine the impulse response at any time and position using (2.1) and F_k on the real k-axis. However, since $\omega_\mathrm{i} > \omega_{\mathrm{i,max}}$, the integrand in (2.1) grows with t faster than any temporal mode. The distinction between convective and absolute instability arises when one considers the limit $t \to \infty$ at fixed z. In this limit, the response to the impulse cannot have exponential growth rate larger than $\omega_{\mathrm{i,max}}$ and the contributions from different ω on L_ω are asymptotically self-cancelling. For this reason, it is appropriate to adopt analytical continuation with respect to ω and progressively displace the contour L_ω downwards in the complex ω-plane, thus reducing the temporal growth rate of the integrand. As we shall see, this asymptotic method leads to a simple criterion to predict absolute instability. This criterion was originally introduced by Briggs (1964) and Bers (1983) in the context of plasma physics and later reviewed by Huerre and Monkewitz (1990) for applications in fluid dynamics.

As ω_i is decreased, the spatial branches, $k^+(\omega)$ and $k^-(\omega)$, move around in the complex k-plane. As always, these branches are roots of $D(k, \omega) = 0$ and are *defined* for $\omega_\mathrm{i} \leq \omega_{\mathrm{i,max}}$ by continuation from $\omega_\mathrm{i} > \omega_{\mathrm{i,max}}$. If one of the k-roots crosses the real k-axis, analytic continuation with respect to ω requires that F_k be deformed to avoid being traversed by the offending k-root. Thus, the distinction between $k^+(\omega)$ and $k^-(\omega)$ is maintained and the contour F_k is deformed to remain above all k^- and below all k^+. This is possible provided that a $k^-(\omega)$ and a $k^+(\omega)$ do not collide for some value of ω. Such a collision is known as a *pinch* (the contour F_k is 'pinched' by the two k-roots) and analytic continuation to smaller values of ω_i is not possible: a singularity in the complex ω-plane arises which dominates the large t asymptotics of the impulse response. If a pinch occurs in $\omega_\mathrm{i} > 0$, there is exponential growth at large t and fixed z. This is the condition for *absolute* instability, which has growth rate $\omega_{0,\mathrm{i}}$, where ω_0 is the location of the pinch of largest imaginary part in the complex ω-plane. If the flow is temporally

unstable, but the instability is not absolute, it is referred to as *convective*.

For a convectively unstable or stable flow, the contour L_ω can be lowered all the way to the real ω-axis and the integral over ω in (2.1) is a classical Fourier representation of the impulse reponse. However, in the presence of temporal instability, deformation of the contour F_k will generally have forced it off the real k-axis. If one considers the problem of localised time-harmonic (rather than impulsive) forcing, the large-t response will be at the real forcing frequency ω_f with spatial modes $k^+(\omega_f)$ downstream and $k^-(\omega_f)$ upstream of the forcing location (Huerre, 2000):

$$\mathbf{u}'_{\text{forcing}} \propto \tilde{\mathbf{u}}(x,y)\exp \mathrm{i}(k^{\pm}(\omega_f)z - \omega_f t) + \text{c.c.} \tag{2.2}$$

In this case, spatial modes represent the (possibly growing in $|z|$) streamwise evolution of the response. Note that studying such a spatial instability problem (real ω_f, complex k) only makes sense in the absence of absolute instability, otherwise absolute growth drowns out the response at the forcing frequency. Note also that the correct identification of the upstream and downstream branches, k^+ and k^-, requires analytic continuation with respect to ω_f from sufficiently large $\omega_{f,\mathrm{i}}$ (a study limited to real ω_f is insufficient).

2.2.4 Saddle points and branch points

A collision between $k^+(\omega)$ and $k^-(\omega)$ for $\omega = \omega_0$ implies at least a double root of $D(k,\omega_0)$ at $k = k_0$. This, in turn, implies $D = \partial_k D = 0$ at $k = k_0$, $\omega = \omega_0$. Another way of writing this condition is $\partial_k \omega(k_0) = 0$, where, as always, $\omega(k)$ arises from $D(k,\omega) = 0$. Thus, $\omega(k)$ has a *saddle point* (zero complex derivative) at $k = k_0$. At the same time, $k(\omega)$ has a *branch point* at $\omega = \omega_0$. Although an absolutely unstable pinch requires a saddle point in $\omega_\mathrm{i} > 0$, this purely local condition is insufficient because there is no guarantee that the colliding $k(\omega)$ correspond to the distinct spatial branches, k^+ and k^-. A pinch requires a saddle/branch point, but also that the colliding wavenumbers lie in $k_\mathrm{i}^- < 0$ and $k_\mathrm{i}^+ > 0$ when continued with respect to ω upwards to large enough ω_i. Because locating saddle/branch points can be carried out locally, it is much easier in practice than verifying that such a point represents a genuine pinch. As we shall see later, there can be many branch points which do not correspond to pinches and it is important (as far as possible) to check candidate branch points by continuation upwards in ω to large ω_i. This is illustrated in figure 2.3.

Although, as we shall see later, higher-order saddle points are possible for particular parameter values, the collision between two and only two spatial branches at k_0 corresponds to the conditions $D = \partial_k D = 0$ and $\partial_{kk}^2 D \neq 0$, which imply

$$\partial_k \omega = 0, \quad \partial_{kk}^2 \omega \neq 0 \tag{2.3}$$

when $k = k_0$. Since $\omega(k)$ is analytic, there is no local extremum of $|\omega|$ and, as noted above, this condition indicates the presence of a saddle point in the complex k-plane (see white dot in figure 2.3a). Performing a Taylor expansion in the vicinity of k_0, one finds that, as also noted above, a saddle point corresponds to a branch point singularity of $k(\omega)$, located at $\omega_0 = \omega(k_0)$:

$$|k - k_0| = O\left(|\omega - \omega_0|^{1/2}\right). \tag{2.4}$$

Indeed, the two spatial branches collide when $\omega = \omega_0$, but 'live' on two different Riemann sheets otherwise. The two sheets are connected through a *branch cut* running from ω_0 in an arbitrarily chosen direction (see thick line in figure 2.3b). If the branch point is a genuine pinch, the frequency ω_0 is called the *absolute frequency* and k_0 is the *absolute wavenumber*.

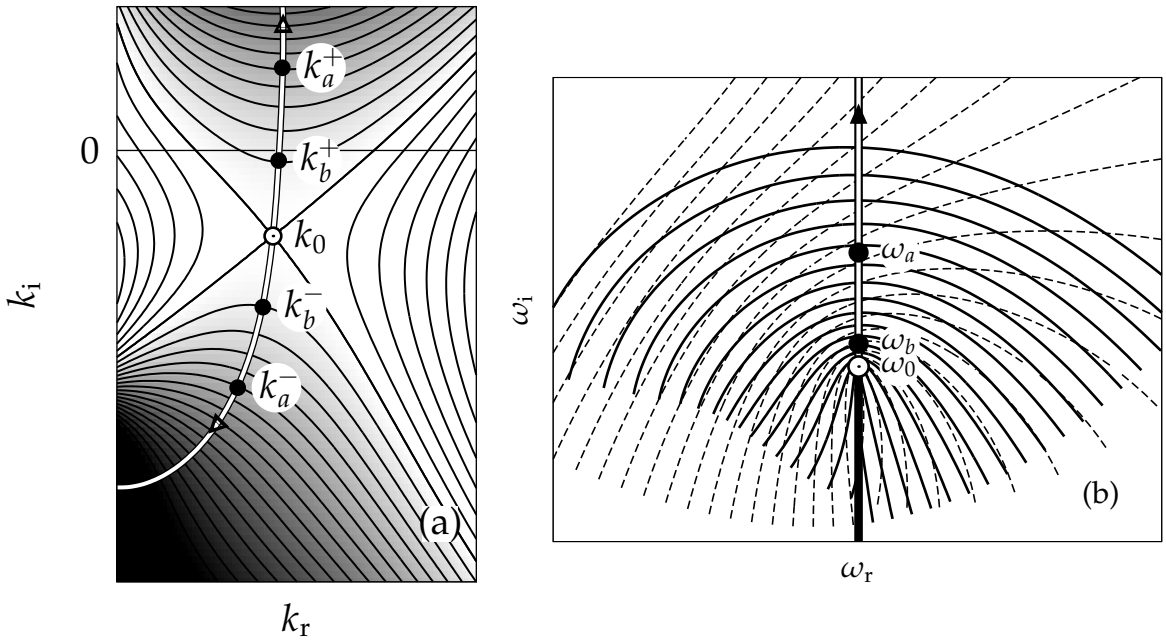

Figure 2.3 – (a) Map and isocontours of ω_i (shaded regions correspond to larger ω_i) in the complex k-plane. (b) Contours of constant k_i in the complex ω-plane for the same dispersion relation. A pinch point is indicated by a white dot: it corresponds to a saddle point at k_0 in (a) and to a branch point at ω_0 in (b). The thick black line in (b) corresponds to the branch cut associated with the branch point. Solid and dotted lines in (b) correspond to two different Riemann sheets of $k(\omega)$. The white path in (a) and (b) corresponds to the contour of constant $\omega_\mathrm{r} = \omega_{0,\mathrm{r}}$ for $\omega_\mathrm{i} \geq \omega_{0,\mathrm{i}}$. The arrows indicate increasing values of ω_i. The spatial branches $k_a^\pm$ and $k_b^\pm$ are respectively associated with the frequencies ω_a and ω_b. For large enough ω_i, when $\omega = \omega_a$ for instance, the two spatial branches on the white path separate into the upper and lower half k-planes. Thus, the saddle point at k_0 satisfies the pinching criterion.

Finally, note that the Briggs–Bers method can also be used to evaluate the impulse response along any spatio-temporal ray $V = z/t$, corresponding to an observer moving at velocity V in the laboratory frame. The procedure described above corresponds to $V = 0$, since z was held fixed while $t \to \infty$. One finds that the asymptotic dynamics for any value of V is governed by a pinch criterion applied to the modified dispersion relation $\omega'(k) \equiv \omega - Vk$. In other words, the response is dominated by the contribution of the wavepacket comoving with the observer, namely with *group-velocity* $\partial_k \omega = V$. The growth rate perceived in the moving frame is equal to $\sigma(V) = \omega_{*,\mathrm{i}} - Vk_{*,\mathrm{i}}$ (see Huerre (2000)), where k_* is the pinch point of $\omega'(k)$ and $\omega_* \equiv \omega'(k_*)$ is the associated frequency. The *fronts* of the wavepacket, as defined in the previous section (see figure 2.2), are hence given by the condition $\sigma(V^\pm) = 0$. In the case of marginal absolute instability, defined by $\omega_{0,\mathrm{i}} = \sigma(0) = 0$, one of the fronts is stationary in the laboratory frame which means that dispersion is just strong enough to compete with advection.

When $\omega_{0,\mathrm{i}} > 0$, the front propagates upstream (see figure 2.2a), permiting growth *in situ*. In this sense, the absolute instability criterion corresponds to the existence of an unstable wave with zero group velocity (and which corresponds to a genuine pinch).

2.3 Discussion of experimental results

Going back to the Taylor–Couette–Poiseuille experiment, one must be aware of some differences between the idealized description of §2.1 and what is observed in practice. For instance, no Taylor vortices are observed at the inlet even in the absolutely unstable case, for mainly two reasons. One is that the flow enters the system with no azimuthal velocity, hence becomes centrifugally unstable only after a finite distance. But even if the basic flow were fully-developed and absolutely unstable right at the inlet, perturbations could only be detected some distance downstream because their amplitude must vanish at the inlet. Indeed, a finite distance is required to allow for sufficient spatial growth leading to nonlinear saturation (Couairon and Chomaz, 1997b). Another important difference between theory and practice is that instabilities may be sustained even in the convectively unstable régime. Indeed, even in the absence of controlled forcing, noise may be sufficient to trigger instabilities that could saturate before exiting the system if their growth rate is large enough. A saturated flow may hence be observed at large time without the presence of absolute instability, because noise acts as a weak but permanent forcing.

Despite these warnings, convective and absolute instabilities may usually be clearly identified in practice. One property of absolute instability is that the 'interface' between basic and bifurcated flow remains at a well-defined position (see figure 2.4a) whereas it is fluctuating in the convectively unstable case (see figure 2.4b). Time-series taken at a

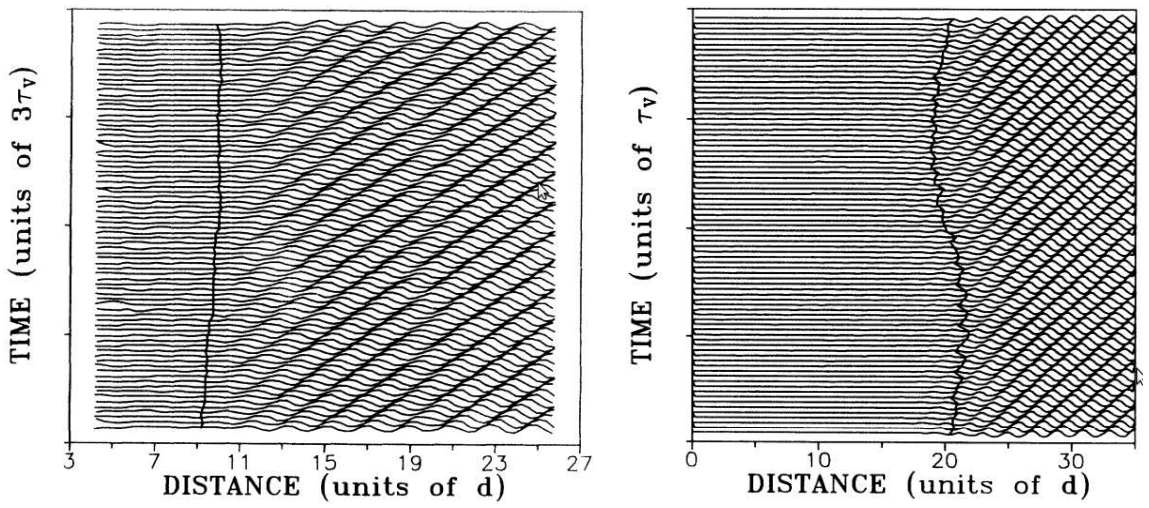

(a) (b)

Figure 2.4 – Space-time diagrams (optical signal intensity) in axisymmetric Taylor–Couette–Poiseuille flow (Tsameret and Steinberg, 1994). The fluid flows from left to right and the solid line indicates the interface between the basic flow and propagating Taylor vortices. The interface remains at a well-defined position for (a) absolute instability, whereas it moves for (b) convective instability.

fixed position downstream this 'interface' indicate the most important distinctive feature between the two types of instabilities: in cases like (a), an almost discrete spectrum with a single frequency is observed (cf. figure 2.5a) contrasting with the broadened frequency spectrum obtained in cases like (b) (see figure 2.5b). The oscillation at a well-defined frequency in case (a) is characteristic of an absolute instability, where the flow behaves largely as a *resonator*. The dynamics is *intrinsic*, explaining why the interface remains at a fixed location independent of external perturbations. In case (b), the broadband power spectrum and the moving interface indicate a great sensitivity to noise, which is typical of convectively unstable flows, sometimes called *noise amplifiers* (Huerre, 2000). The broadened spectrum is caused by phase wander of the most rapidly amplified pattern (Babcock et al., 1994) and is related to the stochastic nature of the forcing.

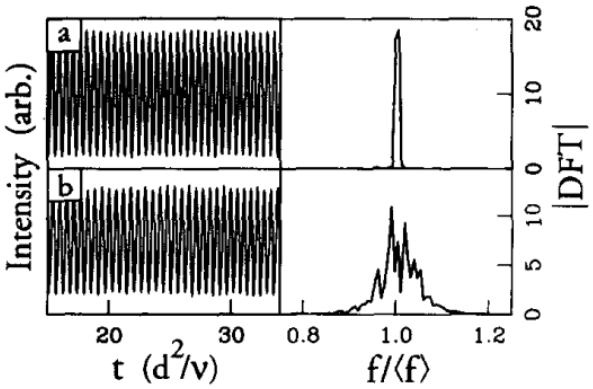

Figure 2.5 – Time-series at a fixed position in Taylor–Couette–Poiseuille flow (Babcock et al., 1994), and its discrete Fourier transform near the fundamental peak. The spectrum has a sharp peak in the presence of (a) absolute instability, but broadens if the instability is convective (b).

Chapter 3

Numerical methods

In this chapter, the numerical tools used to carry out stability analyses of eccentric Taylor–Couette–Poiseuille flow are presented. In §3.1, the geometry, control parameters and governing equations are introduced. In §3.2, the pseudospectral Fourier–Chebyshev method used to discretize the equations in space is briefly presented. A discussion of Fourier–Galerkin and Chebyshev collocation methods can be found in Appendices A.1 and A.2. Some additional formulas for implementation of the method are given in Appendix A.3. In §3.3, we explain how axially invariant and steady basic flow solutions are computed, using a projection method. In §3.4, we present the methods used to solve the generalized eigenvalue problem resulting from the linear stability problem. The problem is first reduced to a smaller standard eigenvalue problem (details in Appendix C.1). The algorithms used for numerical solution of this problem are briefly discussed to (details in Appendix C). In §3.5, we show how classical continuation techniques (explained in Appendix D) can be used to compute the boundaries of temporal and absolute instability in parameter space, as well as some other critical curves. Finally, in §3.6, some validation results are presented and commented in detail.

In short, this chapter gives the principal elements of our methodology, which is classical, and presents validation results. The reader is invited to refer to the Appendices for further theoretical background and technical details.

N.B. All the code has been developed by the author in `C++`, with the exception of the Thomas algorithm (written by B. Pier) and some mathematical libraries. These packages are FFTW [1] for fast Fourier transforms, LAPACK/BLAS [2] for linear algebra, and ARPACK++ [3] for the computation of eigenvalues.

3.1 Model

3.1.1 Geometry, control parameters

The annular geometry between eccentric cylinders is represented in figure 3.1. The

1. `http://www.fftw.org/`
2. `http://www.netlib.org/lapack/`
3. `http://www.caam.rice.edu/software/ARPACK/`

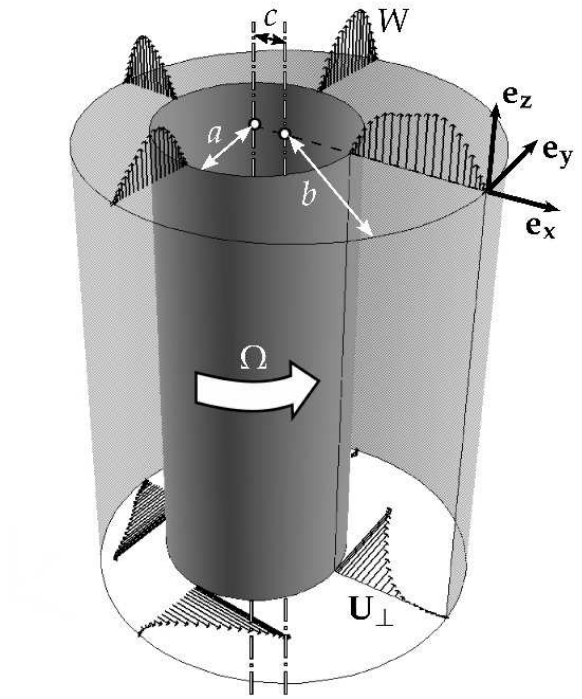

Figure 3.1 – Eccentric annulus of radius ratio $\eta = a/b = 0.5$ and basic flow $\mathbf{U} = \mathbf{U}_\perp + W\mathbf{e_z}$.

ratio between inner and outer radii is $0 < \eta = a/b < 1$. The clearance ratio $\delta = d/a$ is sometimes used instead of η, with $d = b - a$ the annular clearance. The eccentricity $0 \leq e = c/(b-a) < 1$ measures the distance between cylinder axes.

Define Ω as the inner cylinder rotation rate and ρ the density of the fluid. Physical quantities will be made non-dimensional with respect to the following length, velocity and pressure scales

$$\mathrm{L} \equiv d, \quad \mathrm{V} \equiv a\Omega, \quad \mathrm{P} \equiv \rho(a\Omega)^2.$$

The rotational/azimuthal Reynolds number $Re_\Omega = a\Omega d/\nu$ measures the ratio between centrifugal and viscous effects, with ν the kinematic viscosity. The axial Reynolds number $Re_z = \overline{W}d/\nu$, based on the mean axial velocity $\overline{W}$, characterises axial advection.

The set of all four control parameters will be denoted $\chi \equiv (\eta, e, Re_\Omega, Re_z)$.

3.1.2 Governing equations

The fluid motion is governed by the incompressible Navier–Stokes equations, for the velocity $\mathbf{u}$ and pressure p

$$\partial_t \mathbf{u} + \mathbf{u} \cdot \nabla \mathbf{u} = -\nabla p + Re_\Omega^{-1} \nabla^2 \mathbf{u}, \tag{3.1a}$$

$$\nabla \cdot \mathbf{u} = 0, \tag{3.1b}$$

with no-slip and impermeability at the walls. The rotation of the inner cylinder is thus represented through the boundary conditions. Along the axial direction z, the pressure gradient induces a constant forcing term G in the momentum equation (3.1a).

Denote by w the component of the flow in the axial direction z. Crossflow velocity is defined as the remainder $\mathbf{u}_\perp \equiv \mathbf{u} - w\mathbf{e}_z$. All terms in (3.1a) and (3.1b) can be decomposed in a similar fashion using

$$\nabla_\perp p \equiv \nabla p - \partial_z p \mathbf{e}_z \tag{3.2a}$$
$$\mathbf{u}_\perp \cdot \nabla_\perp \mathbf{u} \equiv \mathbf{u} \cdot \nabla \mathbf{u} - w\partial_z \mathbf{u} \tag{3.2b}$$
$$\nabla_\perp \cdot \mathbf{u}_\perp \equiv \nabla \cdot \mathbf{u} - \partial_z w \tag{3.2c}$$
$$\nabla_\perp^2 \mathbf{u} \equiv \nabla^2 \mathbf{u} - \partial_{zz} \mathbf{u}. \tag{3.2d}$$

Flow variables are collectively denoted $\mathbf{q} \equiv (\mathbf{u}_\perp, w, p)^T$.

Basic flow

Basic flows are defined as steady and axially invariant solutions of (3.1a)–(3.1b). They are denoted using capital letters as $\mathbf{Q} \equiv (\mathbf{U}_\perp, W, P)^T$ and satisfy the following equations

$$\mathbf{U}_\perp \cdot \nabla_\perp \mathbf{U}_\perp = -\nabla_\perp P + Re_\Omega^{-1} \nabla_\perp^2 \mathbf{U}_\perp, \tag{3.3a}$$
$$\mathbf{U}_\perp \cdot \nabla_\perp W = -G + Re_\Omega^{-1} \nabla_\perp^2 W, \tag{3.3b}$$
$$\nabla_\perp \cdot \mathbf{U}_\perp = 0. \tag{3.3c}$$

Equations (3.3a) and (3.3c) form a system of equations for $\mathbf{U}_\perp$, independent of W. However, W depends on $\mathbf{U}_\perp$ through (3.3b). In practice, $\mathbf{U}_\perp$ is determined by time-marching two-dimensional Navier–Stokes equations for $\mathbf{u}_\perp$

$$\partial_t \mathbf{u}_\perp + \mathbf{u}_\perp \cdot \nabla_\perp \mathbf{u}_\perp = -\nabla_\perp p + Re_\Omega^{-1} \nabla_\perp^2 \mathbf{u}_\perp, \tag{3.4a}$$
$$\nabla_\perp \cdot \mathbf{u}_\perp = 0, \tag{3.4b}$$

until convergence to a steady solution satisfying (3.3a) and (3.3c). A projection method is used to perform time integration, and will be explained in §3.3.1. W is then obtained by solving (3.3b), with G set to 1 without loss of generality. The axial flow field is then rescaled to match the average value $\overline{W}$, set by the ratio Re_z/Re_Ω.

Normal modes

In the linear stability framework, small-amplitude perturbations $\mathbf{q}' \equiv (\mathbf{u}'_\perp, w', p')^T$ are added to the basic flow, i.e. $\mathbf{q} = \mathbf{Q} + \mathbf{q}'$. In the limit of vanishing amplitude, these perturbations are governed by the linearized incompressible Navier–Stokes equations

$$\partial_t \mathbf{u}' + \mathbf{U} \cdot \nabla \mathbf{u}' + \mathbf{u}' \cdot \nabla \mathbf{U} = -\nabla p' + Re_\Omega^{-1} \nabla^2 \mathbf{u}', \tag{3.5a}$$
$$\nabla \cdot \mathbf{u}' = 0, \tag{3.5b}$$

with $\mathbf{u}' = 0$ at the walls.

Perturbations are decomposed as a sum of normal modes, which take the form

$$\mathbf{q}' = \tilde{\mathbf{q}} \exp \mathrm{i}(kz - \omega t) + \text{c.c.}, \tag{3.6}$$

where c.c. denotes the complex conjugate. Axial wavenumber k and frequency ω can be real or complex numbers, depending on the context. Using (3.6), the final set of equations reads

$$-\mathrm{i}\omega\tilde{\mathbf{u}}_\perp + (\mathbf{U}_\perp\cdot\nabla_\perp + \mathrm{i}kW)\tilde{\mathbf{u}}_\perp + \tilde{\mathbf{u}}_\perp\cdot\nabla_\perp\mathbf{U}_\perp = -\nabla_\perp\tilde{p} + Re_\Omega^{-1}(\nabla_\perp^2 - k^2)\tilde{\mathbf{u}}_\perp, \tag{3.7a}$$

$$-\mathrm{i}\omega\tilde{w} + (\mathbf{U}_\perp\cdot\nabla_\perp + \mathrm{i}kW)\tilde{w} + \tilde{\mathbf{u}}_\perp\cdot\nabla_\perp W = -\mathrm{i}k\tilde{p} + Re_\Omega^{-1}(\nabla_\perp^2 - k^2)\tilde{w}, \tag{3.7b}$$

$$\nabla_\perp\cdot\tilde{\mathbf{u}}_\perp + \mathrm{i}k\tilde{w} = 0, \tag{3.7c}$$

which, together with the boundary conditions, forms a generalized eigenvalue problem $\mathrm{A}\tilde{\mathbf{q}} = \lambda\mathrm{B}\tilde{\mathbf{q}}$ with $\lambda = \mathrm{i}\omega$. The linear operators A and B can be written using matrix-style notation as

$$\mathrm{A} = \begin{bmatrix} \mathrm{C} & 0 & \mathrm{E} \\ \mathrm{F} & \mathrm{G} & \mathrm{i}k \\ \mathrm{H} & \mathrm{i}k & 0 \end{bmatrix}, \quad \mathrm{B} = \begin{bmatrix} 1 & 0 & 0 \\ 0 & 1 & 0 \\ 0 & 0 & 0 \end{bmatrix}, \tag{3.8}$$

where

$$\mathrm{C} \equiv \mathbf{U}_\perp\cdot\nabla_\perp + \mathrm{i}k - Re_\Omega^{-1}(\nabla_\perp^2 - k^2) + \nabla_\perp\mathbf{U}_\perp\cdot, \tag{3.9a}$$

$$\mathrm{E} \equiv \nabla_\perp, \tag{3.9b}$$

$$\mathrm{F} \equiv \nabla_\perp W, \tag{3.9c}$$

$$\mathrm{G} \equiv \mathbf{U}_\perp\cdot\nabla_\perp + \mathrm{i}k - Re_\Omega^{-1}(\nabla_\perp^2 - k^2), \tag{3.9d}$$

$$\mathrm{H} \equiv \nabla_\perp\cdot. \tag{3.9e}$$

This eigenvalue problem leads to $D(k,\omega;\chi) = 0$, where D is the dispersion relation of instability waves. The zero entries in matrix A allow a reduction of the problem, as explained in §3.4.1.

3.1.3 Modified bipolar coordinate system

The annular geometry between eccentric cylinders is conveniently represented using a bipolar coordinate system (see figure 3.2). Wood (1957)'s modified bipolar coordinate system (ρ,ϕ) is defined by the conformal mapping of the cartesian coordinates (x,y) [4]:

$$x + \mathrm{i}y = \frac{1}{\delta}\frac{\rho\mathrm{e}^{\mathrm{i}\phi} + \gamma}{1 + \gamma\rho\mathrm{e}^{\mathrm{i}\phi}}, \tag{3.10}$$

with constants γ and β depending on the geometry through δ and e

$$\gamma = \left\{\left(\frac{2+\delta(1-e^2)}{2e}\right)^2 - 1\right\}^{1/2} - \frac{2+\delta(1-e^2)}{2e} \text{ if } e \neq 0, \text{ else } \gamma = 0. \tag{3.11}$$

The advantage of this formulation over classical bipolar coordinates is that it is not singular in the concentric limit, allowing computations in the axisymmetric case $e = 0$. The system is locally orthogonal and fits the boundaries of the domain, defined by $\rho = 1$ and $\rho = \beta$, where

$$\beta = \frac{1 + \delta(1+e) - \gamma}{1 - \gamma(1 + \delta(1+e))}. \tag{3.12}$$

4. Recall that spatial coordinates x and y are non-dimensionalized using the length scale d.

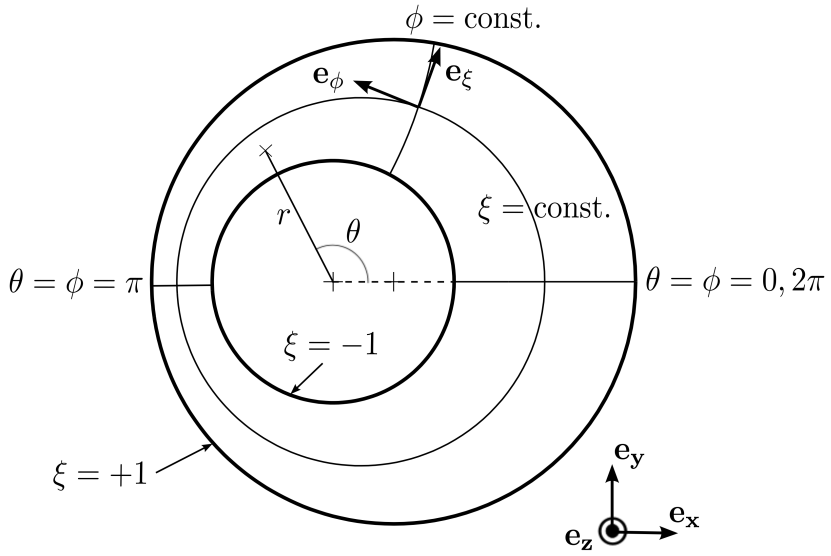

Figure 3.2 – Modified bipolar coordinate system (ξ, ϕ) fitting the eccentric annular domain. Polar coordinates (r, θ) are centered on the inner cylinder, with $\theta = \phi = 0$ along the line joining the cylinder axes.

By mapping $1 \leq \rho \leq \beta$ to $-1 \leq \xi \leq 1$ with the transformation $\xi = (2\rho - \beta - 1)/(\beta - 1)$, the computational domain is

$$\mathcal{D} = \{(\xi, \phi) \in [-1, 1] \times [0, 2\pi[\} \,.$$

The coordinates ξ and ϕ are called pseudo-radial and pseudo-azimuthal respectively.

In-plane differential operators defined in (3.2a)–(3.2d) are expressed in this coordinate system. In-plane velocity is decomposed in the local basis as $\mathbf{u}_\perp = u\mathbf{e}_\xi + v\mathbf{e}_\phi$. Following DiPrima and Stuart (1972a), the infinitesimal length element $\mathrm{d}s$ in (ξ, ϕ, z) is

$$\mathrm{d}s^2 = \frac{(\beta-1)^2}{4\delta^2 J}\mathrm{d}\xi^2 + \frac{\rho^2}{\delta^2 J}\mathrm{d}\phi^2 + \mathrm{d}z^2, \tag{3.13}$$

where J is the Jacobian of transformation (3.10), given by

$$J = \frac{\left(1 + 2\gamma\rho\cos\phi + \gamma^2\rho^2\right)^2}{\left(1-\gamma^2\right)^2}. \tag{3.14}$$

The scale factors of the coordinates ξ and ϕ are

$$\mu_\xi = \frac{2\delta\sqrt{J}}{\beta - 1},\ \mu_\phi = \frac{\delta\sqrt{J}}{\rho}. \tag{3.15}$$

It is convenient to define derivation operators

$$D_\xi \equiv \mu_\xi \partial_\xi,\ D_\phi \equiv \mu_\phi \partial_\phi, \tag{3.16}$$

and geometric factors

$$A \equiv \mu_\phi - \partial_\xi \mu_\xi\ ,\ B \equiv \partial_\phi \mu_\phi. \tag{3.17}$$

Using Whitham (1963)'s general orthogonal coordinate formulas

$$\nabla_\perp p = \begin{bmatrix} D_\xi p \\ D_\phi p \end{bmatrix}, \tag{3.18a}$$

$$\nabla_\perp \cdot \mathbf{u}_\perp = (D_\xi + A)u + (D_\phi - B)v, \tag{3.18b}$$

$$\mathbf{u}_\perp \cdot \nabla_\perp \mathbf{u}_\perp = (uD_\xi + vD_\phi) \begin{bmatrix} u \\ v \end{bmatrix} + (Av + Bu) \begin{bmatrix} -v \\ u \end{bmatrix}, \tag{3.18c}$$

$$\mathbf{u}_\perp \cdot \nabla_\perp w = (uD_\xi + vD_\phi)\, w, \tag{3.18d}$$

$$\nabla_\perp^2 \mathbf{u}_\perp = \begin{bmatrix} \nabla_\perp^2 u \\ \nabla_\perp^2 v \end{bmatrix} + \begin{bmatrix} (D_\xi A - D_\phi B)u - 2\,(AD_\phi + BD_\xi)\, v \\ (D_\xi A - D_\phi B)v + 2\,(AD_\phi + BD_\xi)\, u \end{bmatrix}, \tag{3.18e}$$

where the scalar Laplacian has the expression:

$$\nabla_\perp^2 \equiv D_\xi^2 + D_\phi^2 + (AD_\xi - BD_\phi). \tag{3.19}$$

3.2 Fourier–Chebyshev pseudospectral method

The bipolar mapping allows the use of an efficient pseudospectral method. Some theoretical aspects of Fourier–Galerkin and Chebyshev collocation methods are reviewed in Appendices A.1 and A.2. For more details, the reader is referred to Canuto et al. (1988) and Peyret (2002). Any smooth real or complex field f in $\mathcal{D}$ can be decomposed as

$$f(\xi, \phi) \approx \sum_{k=-K}^{K} \sum_{j=0}^{M} \hat{f}_{kj} q_j(\xi) \mathrm{e}^{\mathrm{i}k\phi}, \tag{3.20}$$

with q_j the Lagrange basis polynomial associated with the Gauss–Lobatto collocation point $\xi_j = -\cos[j\pi/M]$ in the pseudo-radial direction. The spectral coefficients $\hat{f}_{kj} \equiv \hat{f}_k(\xi_j)$ for each collocation point ξ_j represent Fourier modes with $|k| \leq K$. The strength of spectral methods lies in the exponential convergence of the series as K and M increase, a property which is verified in §3.6.1.

An important question regarding implementation of this method is the form of the matrices arising from the differential operators: gradient, divergence, Laplacian, etc. In particular, the projection method presented in §3.3.1 requires solution of Poisson problems, based on a discretized version of the Laplacian operator with Neumann boundary conditions. Moreover, the gradient and divergence operators, E and H, also give rise to matrices. The method used to obtain these matrices is explained in the next two subsections, and additional details are given in Appendix A.3.

Coupling between harmonics induced by the metric

Let ψ be any of the following linear operators $f \mapsto g \in \{D_\xi f, D_\phi f, Af, Bf, \nabla_\perp^2 f\}$. f and g are decomposed as infinite Fourier series in ϕ,

$$f(\xi, \phi) = \sum_{k=-\infty}^{\infty} \hat{f}_k(\xi) \mathrm{e}^{\mathrm{i}k\phi}, \quad g(\xi, \phi) = \sum_{k=-\infty}^{\infty} \hat{g}_k(\xi) \mathrm{e}^{\mathrm{i}k\phi}.$$

In order to obtain a relation between the Fourier coefficients of g and f, the factors μ_ξ, μ_ϕ, A and B are also decomposed in Fourier space. Since $\partial_\xi \mu$ and $\partial_\phi \mu$ are both proportional to $\sqrt{J}$, they can be written in the form

$$\mu_\xi = \hat{\mu}_0 + \hat{\mu}_1(\mathrm{e}^{\mathrm{i}\phi} + \mathrm{e}^{-\mathrm{i}\phi}), \quad \mu_\phi = \zeta \mu_\xi, \tag{3.21}$$

with $\hat{\mu}_0$, $\hat{\mu}_1$ and ζ functions of ξ only (see the detailed expressions in Appendix A.3). The geometric factors A and B have Fourier coefficients

$$\hat{A}_k = \zeta \hat{\mu}_k - \partial_\xi \hat{\mu}_k, \quad \hat{B}_k = \zeta \mathrm{i} k \hat{\mu}_k \tag{3.22}$$

and as a result, can be written in the form

$$A = \hat{A}_0 + \hat{A}_1(\mathrm{e}^{\mathrm{i}\phi} + \mathrm{e}^{-\mathrm{i}\phi}), \tag{3.23}$$

$$B = \hat{B}_1(\mathrm{e}^{\mathrm{i}\phi} - \mathrm{e}^{-\mathrm{i}\phi}). \tag{3.24}$$

The spectrum of μ_ξ, μ_ϕ, A and B contains harmonics 0, 1 and -1 only, therefore, $\widehat{(D_\xi f)}_k, \widehat{(D_\phi f)}_k, \widehat{(Af)}_k, \widehat{(Bf)}_k$ depend on $\hat{f}_{k-1}$, $\hat{f}_k$ and $\hat{f}_{k+1}$ for any value of k. This coupling of neighbouring Fourier components is due to the special form of the metric coefficients as functions of ϕ. For instance,

$$\begin{aligned} \widehat{(D_\xi f)}_k = \widehat{(\mu_\xi \partial_\xi f)}_k &= \sum_{l=-\infty}^{\infty} \hat{\mu}_l \partial_\xi \hat{f}_{k-l} \\ &= \hat{\mu}_0 \partial_\xi \hat{f}_k + \hat{\mu}_1 \left[\partial_\xi \hat{f}_{k+1} + \partial_\xi \hat{f}_{k-1}\right]. \end{aligned} \tag{3.25}$$

The Laplacian operator (3.19) is proportional to μ_ξ^2:

$$\begin{aligned} \nabla_\perp^2 &\equiv D_\xi^2 + D_\phi^2 + (AD_\xi - BD_\phi) \\ &= \mu_\xi^2(\partial_{\xi\xi}^2 + \zeta \partial_\xi + \zeta^2 \partial_{\phi\phi}^2). \end{aligned} \tag{3.26}$$

The metric coefficient μ_ξ^2 has five non-zero harmonics and, as a result, $\widehat{(\nabla_\perp^2 f)}_k$ is a function of $\hat{f}_{k-2}, \hat{f}_{k-1}, \hat{f}_k, \hat{f}_{k+1}, \hat{f}_{k+2}$.

Matrix form of linear operators for real fields

An important case is when both f and g are real, as this is the case for basic flow fields. In this case, the Fourier coefficients of f and g have Hermitian symmetry $\hat{f}_{-k} = \hat{f}_k^\star$ ('$\star$' denoting complex conjugation). Therefore, only the Fourier coefficients with positive k need be stored, and $\hat{f}_0$ is a real number. Discretized fields can hence be stored as real-valued vectors

$$\mathsf{f} \equiv (\hat{\mathsf{f}}_{0,\mathrm{r}}, \hat{\mathsf{f}}_{1,\mathrm{r}}, \ldots, \hat{\mathsf{f}}_{K,\mathrm{r}}, \hat{\mathsf{f}}_{1,\mathrm{i}}, \ldots, \hat{\mathsf{f}}_{K,\mathrm{i}})^T, \quad \mathsf{g} \equiv (\hat{\mathsf{g}}_{0,\mathrm{r}}, \hat{\mathsf{g}}_{1,\mathrm{r}}, \ldots, \hat{\mathsf{g}}_{K,\mathrm{r}}, \hat{\mathsf{g}}_{1,\mathrm{i}}, \ldots, \hat{\mathsf{g}}_{K,\mathrm{i}})^T,$$

where each $\hat{\mathsf{f}}_{k,\mathrm{r/i}}$ and $\hat{\mathsf{g}}_{k,\mathrm{r/i}}$ is decomposed on the collocation points as [5]

$$\hat{\mathsf{f}}_{k,\mathrm{r/i}} \equiv (\hat{f}_{k0,\mathrm{r/i}}, \hat{f}_{k1,\mathrm{r/i}}, \ldots, \hat{f}_{kM,\mathrm{r/i}}), \quad \hat{\mathsf{g}}_{k,\mathrm{r/i}} \equiv (\hat{g}_{k0,\mathrm{r/i}}, \hat{g}_{k1,\mathrm{r/i}}, \ldots, \hat{g}_{kM,\mathrm{r/i}}).$$

5. The subscripts 'r' and 'i' denote real and imaginary parts.

Given these conventions, $\psi f = g$ can be written as a linear system $\mathsf{M}\mathsf{f} = \mathsf{g}$, with a four-block matrix M

$$\mathsf{M} = \begin{pmatrix} \mathsf{M}_{\mathrm{rr}} & \mathsf{M}_{\mathrm{ri}} \\ \mathsf{M}_{\mathrm{ir}} & \mathsf{M}_{\mathrm{ii}} \end{pmatrix}, \tag{3.27}$$

and block dimensions

$$\begin{aligned} \mathsf{M}_{\mathrm{rr}} &: (M+1)(K+1) \times (M+1)(K+1) \\ \mathsf{M}_{\mathrm{ri}} &: (M+1)(K+1) \times (M+1)K \\ \mathsf{M}_{\mathrm{ir}} &: (M+1)K \times (M+1)(K+1) \\ \mathsf{M}_{\mathrm{ii}} &: (M+1)K \times (M+1)K. \end{aligned}$$

For the Laplacian operator $\mathsf{M}_{\mathrm{ri}} = 0$ and $\mathsf{M}_{\mathrm{ir}} = 0$. Because of the coupling between harmonics induced by the metric, the matrices M_{rr} and M_{ii} are block pentadiagonal, so a improved version of the Thomas algorithm (cf. Appendix B) can be used to efficiently solve Poisson and Helmholtz problems in §3.3.1.

3.3 Basic flow computation

In the preceding section, the governing equations and method of spatial discretization were given. Basic flow solutions $\mathbf{U}_\perp$ are obtained as steady solutions of an unsteady problem for the crossflow velocity field $\mathbf{u}_\perp$, so temporal discretization is also required. A *projection method* is used to time-march the momentum equation while always enforcing the incompressibility constraint. Finally, the axial velocity W is obtained in a postprocessing step.

3.3.1 Projection method

The algorithm used to solve the time-dependent incompressible Navier–Stokes equations is inspired by the projection method of Goda (1979), and the modified version proposed by Raspo et al. (2002). In the following, we consider equations discretized with respect to time, with superscript 'n' denoting evaluation at time $t_n = n\Delta t$. For stability analyses, we are only interested in steady state solutions, so emphasis is put on numerical stability and fast computation, rather than on accurate time-marching. A first order forward/backward Euler scheme is used, reading (before splitting)

$$\frac{\mathbf{u}_\perp^{n+1} - \mathbf{u}_\perp^n}{\Delta t} = -\mathbf{u}_\perp^n \cdot \nabla_\perp \mathbf{u}_\perp^n - \nabla_\perp p^{n+1} + Re_\Omega^{-1} \left[\nabla^2_{\perp,\mathrm{expl}} \mathbf{u}_\perp^n + \nabla^2_{\perp,\mathrm{impl}} \mathbf{u}_\perp^{n+1} \right], \tag{3.28a}$$

$$\nabla_\perp \cdot \mathbf{u}_\perp^{n+1} = 0, \tag{3.28b}$$

with Dirichlet boundary conditions denoted $\mathbf{u}^{n+1}_{\perp,BC}$ at the boundaries. The vectorial Laplacian operator (3.18e) has been separated into two parts $\nabla^2_\perp \equiv \nabla^2_{\perp,\mathrm{expl}} + \nabla^2_{\perp,\mathrm{impl}}$. The implicit part contains all *stiff* second order derivative terms from the scalar Laplacian of each velocity component, and is therefore applied to $\mathbf{u}_\perp^{n+1}$ to enhance stability:

$$\nabla^2_{\perp,\mathrm{impl}} \mathbf{u}_\perp \equiv \begin{bmatrix} \nabla^2_\perp u \\ \nabla^2_\perp v \end{bmatrix}. \tag{3.29}$$

The remaining terms in the Laplacian are less constraining on numerical stability, and are treated explicitly:

$$\nabla^2_{\perp,\text{expl}}\mathbf{u}_\perp \equiv \begin{bmatrix}(D_\xi A - D_\phi B)u - 2(AD_\phi + BD_\xi)v \\ (D_\xi A - D_\phi B)v + 2(AD_\phi + BD_\xi)u\end{bmatrix}. \tag{3.30}$$

The system of equations (3.28a)–(3.28b) for $(\mathbf{u}_\perp^{n+1}, p^{n+1})$ is solved in three steps:

Preliminary step

For this step, it is useful to separate the Laplacian operator into irrotational and solenoidal parts

$$\nabla^2\mathbf{u} = \underbrace{\nabla(\nabla\cdot\mathbf{u})}_{\text{irrot.}}\underbrace{-\nabla\times\nabla\times\mathbf{u}}_{\text{solen.}},$$

where the components of $\nabla\times\mathbf{u}$ in the (ξ,ϕ,z) system read

$$\nabla\times\mathbf{u} = \begin{bmatrix}D_\phi w - \partial_z v \\ \partial_z u - D_\xi w \\ \omega_z\end{bmatrix}, \text{ with } \omega_z \equiv (D_\xi + A)v - (D_\phi - B)u. \tag{3.31}$$

The crossflow curl term $\nabla_\perp\times\mathbf{u}_\perp \equiv \omega_z\mathbf{e}_z$ is obtained by setting $w\equiv 0$, $\partial_z \equiv 0$ in (3.31). Thus, the solenoidal contribution to the crossflow Laplacian operator $\nabla^2_\perp$ is

$$-\nabla_\perp\times\nabla_\perp\times\mathbf{u}_\perp \equiv \begin{bmatrix}-D_\phi\omega_z \\ D_\xi\omega_z\end{bmatrix}, \tag{3.32}$$

and the irrotational contribution is $\nabla_\perp(\nabla_\perp\cdot\mathbf{u}_\perp)$.

In the preliminary step, this decomposition is applied to the viscous term in (3.28a), which is here evaluated at time t_n. An approximate pressure $\bar{p}^{n+1}$ is computed from this momentum equation. Taking the divergence

$$\nabla_\perp\cdot\nabla_\perp\bar{p}^{n+1} = \nabla_\perp\cdot\left[-\mathbf{u}_\perp^n\cdot\nabla_\perp\mathbf{u}_\perp^n - Re_\Omega^{-1}\nabla_\perp\times\nabla_\perp\times\mathbf{u}_\perp^n\right], \tag{3.33}$$

and projecting onto the wall-normal unit vector $\mathbf{e}_\xi$ at the boundaries

$$D_\xi\bar{p}^{n+1} = \left[-\mathbf{u}_\perp^n\cdot\nabla_\perp\mathbf{u}_\perp^n - Re_\Omega^{-1}\nabla_\perp\times\nabla_\perp\times\mathbf{u}_\perp^n\right]\cdot\mathbf{e}_\xi, \tag{3.34}$$

leads to a Poisson problem for $\bar{p}^{n+1}$ with inhomogeneous Neumann boundary conditions.

A few remarks are in order:

- (3.33)–(3.34) is indeed a Poisson problem because mathematically $\nabla_\perp\cdot\nabla_\perp\bar{p}^{n+1}$ defines the Laplacian term $\nabla^2_\perp\bar{p}^{n+1}$. However, the notation $\nabla_\perp\cdot\nabla_\perp\bar{p}^{n+1}$ is preferred because in practice, the discretized version of this operator, in matrix form, is different from the matrix of $\nabla^2_\perp$, as explained in the concluding remarks of Appendix A.3. To ensure compatibility with the right-hand side of the equation, the gradient matrix should be left-multiplied by the divergence matrix to obtain the left-hand side linear operator. The expression of these matrices is given in Appendix A.3.
- No time derivative appears because of incompressibility of $\mathbf{u}_\perp^n$ and $\mathbf{u}_\perp^{n+1}$ and impermeability at the walls.

- Mathematically, for a solenoidal field $\mathbf{u}_\perp^n$, the Laplacian is zero, and no viscous term should appear in (3.33). This is indeed true to machine precision for the irrotational contribution $\nabla_\perp(\nabla_\perp \cdot \mathbf{u}_\perp^n)$. However, the 'solenoidal' term does not have zero divergence in its discretized version, because of truncation error, and it is therefore necessary to keep it.
- In an annular geometry, because of periodicity in the pseudo-azimuthal direction ϕ, (3.33)–(3.34) only define $\bar{p}^{n+1}$ up to an additive constant. This problem is solved by fixing the azimuthal mean $\hat{\bar{p}}_{00,\mathrm{r}}^{n+1} = 0$ at the inner cylinder. This replaces the Neumann constraint for this variable.
- The matrix associated with operator $\nabla_\perp \cdot \nabla_\perp$ in spectral space has $\mathsf{M}_{\mathrm{ri}} = \mathsf{M}_{\mathrm{ir}} = 0$, therefore, there is no coupling between real and imaginary parts of $\hat{\bar{p}}_{kj}^{n+1}$. Solving the Poisson problem requires solution of two linear systems of dimensions $(M+1)(K+1)$ and $(M+1)K$ instead of one single problem of size $(M+1)(2K+1)$. Each matrix M_{rr} and M_{ii} is block-pentadiagonal, so the two linear systems can be solved using an adapted version of the Thomas algorithm, described in Appendix B.

Prediction step

In the prediction step, the velocity $\mathbf{u}_\perp^{n+1}$ is approximated by a non-solenoidal field $\tilde{\mathbf{u}}_\perp^{n+1}$, obtained by time-marching the momentum equation (3.28a), with the preliminary pressure $\bar{p}^{n+1}$

$$\frac{\tilde{\mathbf{u}}_\perp^{n+1} - \mathbf{u}_\perp^n}{\Delta t} = -\mathbf{u}_\perp^n \cdot \nabla_\perp \mathbf{u}_\perp^n - \nabla_\perp \bar{p}^{n+1} + Re_\Omega^{-1}\left[\nabla_{\perp,\mathrm{expl}}^2 \mathbf{u}_\perp^n + \nabla_{\perp,\mathrm{impl}}^2 \tilde{\mathbf{u}}_\perp^{n+1}\right], \tag{3.35}$$

and Dirichlet boundary conditions.

Equation (3.35) defines two Helmholtz problems: one for $\tilde{u}$ and another one for $\tilde{v}$. The matrix operator associated with the scalar Laplacian $\nabla_\perp^2$ has $\mathsf{M}_{\mathrm{ri}} = \mathsf{M}_{\mathrm{ir}} = 0$ and $\mathsf{M}_{\mathrm{rr}}, \mathsf{M}_{\mathrm{ii}}$ are block pentadiagonal (expressions given in Appendix A.3). Hence, linear systems for the real and imaginary parts of $\hat{u}_{ki}$ and $\hat{v}_{ki}$ are solved independently using the modified Thomas algorithm.

Projection step

In the projection step, the velocity field at time t_{n+1} is made incompressible by adding a pressure correction $\Phi^{n+1} = p^{n+1} - \bar{p}^{n+1}$, such that

$$\mathbf{u}_\perp^{n+1} = \tilde{\mathbf{u}}_\perp^{n+1} - \Delta t \nabla_\perp \Phi^{n+1}. \tag{3.36}$$

Taking the divergence of (3.36), one obtains a Poisson problem to solve for Φ^{n+1}

$$\nabla_\perp \cdot \nabla_\perp \Phi^{n+1} = \frac{1}{\Delta t} \nabla_\perp \cdot \tilde{\mathbf{u}}_\perp^{n+1}, \tag{3.37}$$

with Neumann boundary conditions $\partial_\xi \Phi^{n+1} = 0$. As in the preliminary step, $\hat{\Phi}_{00}^{n+1}$ is fixed to zero, replacing the von Neumann constraint for this harmonic on the inner cylinder. The method used to solve the linear system is the same as in the preliminary step.

Additional comments

Splitting error Combining equations (3.35) and (3.36), we obtain an approximate version of (3.28a):

$$\frac{\mathbf{u}_\perp^{n+1}-\mathbf{u}_\perp^n}{\Delta t}+\mathbf{u}_\perp^n\cdot\nabla_\perp\mathbf{u}_\perp^n+\nabla_\perp p^{n+1}-Re_\Omega^{-1}\left[\nabla^2_{\perp,\text{expl}}\mathbf{u}_\perp^n+\nabla^2_{\perp,\text{impl}}\mathbf{u}_\perp^{n+1}\right]=E^{n+1}, \quad (3.38)$$

with pressure $p^{n+1}=\bar{p}^{n+1}+\Phi^{n+1}$ and residual error $E^{n+1}=\Delta t Re_\Omega^{-1}\nabla^2_{\perp,\text{impl}}\nabla_\perp\Phi^{n+1}$. The estimated pressure $\bar{p}^{n+1}$ being a first order approximation of p^{n+1} through (3.33), we have $\Phi^{n+1}=O(\Delta t)$, hence $E^{n+1}=O(\Delta t^2)$. The splitting error E^{n+1} is one order of magnitude smaller than the truncation error of the time-marching scheme (3.28a)–(3.28b), which is $O(\Delta t)$.

The preliminary pressure prediction produces an almost incompressible provisional velocity field $\tilde{\mathbf{u}}_\perp^{n+1}$, leading to a less 'brutal' projection step and enhanced numerical stability. This step, introduced by Raspo et al. (2002), also takes into account variations in the wall-normal derivative of p, which would be omitted if one were to use $\bar{p}^{n+1}=p^n$ in the prediction step, as in Goda (1979). This also has a stabilising effect on the scheme.

Slip velocity If we directly set the desired Dirichlet boundary conditions $\mathbf{u}_{\perp,BC}^{n+1}$ in the prediction step, then a slip velocity $\mathbf{u}_{\perp,s}^{n+1}=-\Delta t\nabla_\perp\phi^{n+1}$ would be introduced in the projection step. To anticipate this effect, we impose modified boundary conditions for (3.35)

$$\tilde{\mathbf{u}}_\perp^{n+1}=\mathbf{u}_{\perp,BC}^{n+1}+\Delta t\nabla_\perp\Phi^n. \quad (3.39)$$

By doing so, the final slip velocity is reduced to $\mathbf{u}_{\perp,s}^{n+1}=-\Delta t\nabla_\perp(\Phi^n-\Phi^{n+1})$, and is $O(\Delta t^3)$. Approaching steady state conditions, $\Phi^n-\Phi^{n+1}\to 0$, so the slip velocity can be driven down to zero up to machine precision.

Time step The time step is adaptively computed to ensure stability. It is initialized with a value of $\Delta t=0.01\tau_\nu$ (with $\tau_\nu\equiv d^2/\nu$ the viscous time scale), but is divided by two upon divergence of the residual, defined as $r^n=\|\mathbf{u}_\perp^n-\mathbf{u}_\perp^{n-1}\|_\infty$. When $r^n>100$, the time step is halved and the simulation restarted from the initial conditions.

Convergence criterion The simulation is automatically stopped when $r^n<10^{-8}$.

3.3.2 Axial flow

The last step of the basic flow computation is to calculate the axial velocity W as the solution of the linear problem (3.3b) with $G=1$

$$[Re_\Omega^{-1}\nabla^2_\perp-(UD_\xi+VD_\phi)]W=1. \quad (3.40)$$

The matrix associated with the Laplacian operator in spectral space is already known (see Appendix A.3), but now the convective term also needs to be written in matrix

form. The relation between the coefficients $\widehat{W}_{ki}$ of W and those, $\hat{g}_{ki}$, of $(UD_\xi + VD_\phi)W$ is

$$\hat{g}_{ki} = \sum_l \sum_j \sum_m \left[\widehat{U}_{(k-l-m)i} \hat{\mu}_m d^{(1)}_{ij} + \widehat{V}_{(k-l-m)i} \mathrm{i} l \zeta_i \hat{\mu}_m \delta_{ij} \right] \widehat{W}_{lj}, \tag{3.41}$$

where $|k|, |l|, |k-l-m| \leq K$, $-1 \leq m \leq 1$, $0 \leq i, j \leq M$ and $\hat{\mu}_{-1} \equiv \hat{\mu}_1$. It is much easier here to store all discretized fields f as complex-valued vectors f

$$\mathsf{f} \equiv (\hat{\mathsf{f}}_{-K}, \hat{\mathsf{f}}_{-K+1}, \ldots, \hat{\mathsf{f}}_K)^T,$$

where each block $\hat{\mathsf{f}}_k$ contains the values of the corresponding harmonic k at all collocation points

$$\hat{\mathsf{f}}_k \equiv (\hat{f}_{k0}, \hat{f}_{k1}, \ldots, \hat{f}_{kM}).$$

Using these conventions, the matrix of linear system (3.40) is full, but it needs to be solved only once for a given set of parameters (η, e, Re_Ω). A multiplicative factor is then applied to the solution W, to match the average value $\overline{W} = Re_z/Re_\Omega$.

3.4 Normal modes computation

In this brief section, we summarize the approach for computing the eigenvalues and associated normal modes of the linear stability problem. In §3.4.1, we give an overview of a reduction technique to transform the generalized eigenvalue problem to a much smaller standard eigenvalue problem. Details of numerical implementation are given in Appendix C. Two methods are used to solve the resulting eigenvalue problem: QR iteration (see Appendix C.3), yielding the full spectrum, and the Arnoldi method (see Appendix C.4) to obtain a small subset of eigenvalues efficiently. The principle of these methods is described in Appendices. Freely available libraries were used for the computations. The specific parameter values used with the ARnoldi PACKage (ARPACK++ [6]) are given in §3.4.2.

3.4.1 Reduction of the eigenvalue problem

We recall that normal modes of the form $\tilde{\mathbf{q}} \exp \mathrm{i}(kz - \omega t) + \text{c.c.}$, with $\tilde{\mathbf{q}} = (\tilde{\mathbf{u}}_\perp, \tilde{w}, \tilde{p})^T$, are solutions of the generalized eigenvalue problem $\mathrm{A}\tilde{\mathbf{q}} = \lambda \mathrm{B}\tilde{\mathbf{q}}$, with $\lambda = \mathrm{i}\omega$ and linear operators A and B:

$$\mathrm{A} = \begin{bmatrix} \mathrm{C} & 0 & \mathrm{E} \\ \mathrm{F} & \mathrm{G} & \mathrm{i}k \\ \mathrm{H} & \mathrm{i}k & 0 \end{bmatrix}, \quad \mathrm{B} = \begin{bmatrix} 1 & 0 & 0 \\ 0 & 1 & 0 \\ 0 & 0 & 0 \end{bmatrix}. \tag{3.8}$$

The last equation (incompressibility),

$$\mathrm{H}\tilde{\mathbf{u}}_\perp + \mathrm{i}k\tilde{w} = 0, \tag{3.42}$$

does not involve λ and is therefore an algebraic constraint that can be used to eliminate $\tilde{w}$ from the eigenvalue problem. Another algebraic constraint can be obtained by

6. http://www.caam.rice.edu/software/ARPACK/

left-multiplying the first line ('in-plane' momentum equation) by H, the second (axial momentum equation) by ik and the third by λ, then summing the three resulting equations yields:

$$(\mathrm{HC} + \mathrm{i}k\mathrm{F})\tilde{\mathbf{u}}_\perp + \mathrm{i}k\mathrm{G}\tilde{w} + (\mathrm{HE} - k^2)\tilde{p} = 0. \tag{3.43}$$

This last equation can be used to eliminate $\tilde{p}$ from the eigenvalue problem. In practice, the problem has boundary conditions that do not explicitly appear above, but also need to be taken into account to solve for $\tilde{p}$ as a function of $\tilde{w}$ and $\tilde{\mathbf{u}}_\perp$ (this is a Poisson problem since $\mathrm{HE} - k^2 = \nabla_\perp^2$ is the scalar Laplacian operator). The reduction is performed after discretization of the equations and all details are given in Appendix C.1. The boundary conditions are no-slip $\tilde{v} = \tilde{w} = 0$, impermeability $\tilde{u} = 0$ and incompressibility at the walls. Using these constraints on the discretized problem allows further reduction of the problem by eliminating boundary points (see Appendix C.1).

3.4.2 Solving the eigenvalue problem

The interested reader will find a short description of the numerical methods used to solve the eigenvalue problem (of standard type after reduction) in Appendix C. The QR method (routine zgeev in LAPACK [7], see Appendix C.3) was used for full spectrum computations, while the implicitly restarted Arnoldi method with shift-invert transformation (see Appendix C.4) was used to compute a few eigenvalues efficiently (ARPACK++). The following paragraph gives specific parameter values used with ARPACK++.

The ARPACK++ class 'ARdsNonSymMatrix' was used to store the dense complex-valued matrix (A_1) of the standard eigenvalue problem. The class 'ARluCompStdEig' was used to define the eigenvalue problem, with the following input parameters:

- **nev**=1 or 5; the number of required eigenvalues.
- **which**='LM'; the selected part of the spectrum, here 'Larger Magnitude' since the shift-invert transformation is used, see Appendix C.4,
- **ncv**=15; the number of Arnoldi vectors. This corresponds to the dimension of the Arnoldi decomposition or Krylov subspace in Appendix C.4,
- **tol**=10^{-10}; the convergence tolerance for the Ritz values,
- **maxit**=500; the maximum number of iterations,
- **resid**=NULL; randomly selected starting vector for Arnoldi iteration,
- **AutoShift**=true; exact shifts are being used.

The routine performs a LU decomposition of the dense matrix $\mathsf{A}_1 - \sigma\mathsf{I}$ (with σ the given complex shift), using LAPACK, before proceeding to Arnoldi iteration.

3.5 Continuation and Newton–Raphson solvers

In stability analyses, we are often interested in computing critical curves which divide the parameter space into stable, convectively unstable or absolutely unstable regions. Once a point on the critical manifold has been found, small steps in the control parameters allow the critical curve to be followed (see Appendix D for details). At each step one needs to solve an equation of the form $\mathbf{f}(\mathbf{x}) = 0$, where the precise definitions of

7. `http://www.netlib.org/lapack/`

the vector $\mathbf{x}$ and function $\mathbf{f}$ depend on which of the various criticality conditions are considered. Solution of $\mathbf{f}(\mathbf{x}) = 0$ is carried out using Newton–Raphson iteration (see Appendix D):

$$\mathbf{x}^{n+1} = \mathbf{x}^n - (\mathbf{Df})^{-1}(\mathbf{x}^n)\mathbf{f}(\mathbf{x}^n), \tag{3.44}$$

where $\mathbf{Df}$ is the Jacobian matrix associated with $\mathbf{f}$: $(Df)_{ij} = \partial f_i/\partial x_j$.

The main Newton–Raphson solvers used in the stability analyses are listed below:

- Temporal instability threshold: $\omega_\mathrm{i} = \partial_k\omega_\mathrm{i} = 0,\ k \in \mathbb{R}$, so

$$\mathbf{x} \equiv \begin{bmatrix} k \\ Re_\Omega \end{bmatrix}, \quad \mathbf{f}(\mathbf{x}) \equiv \begin{bmatrix} \omega_\mathrm{i} \\ \partial_k\omega_\mathrm{i} \end{bmatrix}, \quad \mathbf{Df}(\mathbf{x}) = \begin{bmatrix} \partial_k\omega_\mathrm{i} & \partial_{Re_\Omega}\omega_\mathrm{i} \\ \partial^2_{kk}\omega_\mathrm{i} & \partial^2_{kRe_\Omega}\omega_\mathrm{i} \end{bmatrix}. \tag{3.45}$$

  Control parameters: e, Re_z.
- Absolute instability threshold: $\omega_\mathrm{i} = \partial_k\omega = 0,\ k \in \mathbb{C}$.
  Assuming $\omega(k)$ is an analytic function, the Cauchy–Riemann relations hold:

$$\partial_{k_\mathrm{r}}\omega_\mathrm{r} = \partial_{k_\mathrm{i}}\omega_\mathrm{i}, \quad \partial_{k_\mathrm{r}}\omega_\mathrm{i} = -\partial_{k_\mathrm{i}}\omega_\mathrm{r}. \tag{3.46}$$

  Therefore, the zero-group-velocity constraint $\partial_k\omega = 0$ is equivalent to $\partial_{k_\mathrm{r}}\omega = 0$, thus

$$\mathbf{x} \equiv \begin{bmatrix} k_\mathrm{r} \\ k_\mathrm{i} \\ Re_\Omega \end{bmatrix}, \quad \mathbf{f}(\mathbf{x}) \equiv \begin{bmatrix} \omega_\mathrm{i} \\ \partial_{k_\mathrm{r}}\omega_\mathrm{i} \\ \partial_{k_\mathrm{r}}\omega_\mathrm{r} \end{bmatrix}. \tag{3.47}$$

  Differentiating the Cauchy–Riemann relations (3.46) with respect to k_r and k_i:

$$\partial^2_{k_\mathrm{r}k_\mathrm{r}}\omega_\mathrm{r} = \partial^2_{k_\mathrm{r}k_\mathrm{i}}\omega_\mathrm{i} = -\partial^2_{k_\mathrm{i}k_\mathrm{i}}\omega_\mathrm{r}, \quad \partial^2_{k_\mathrm{r}k_\mathrm{r}}\omega_\mathrm{i} = -\partial^2_{k_\mathrm{r}k_\mathrm{i}}\omega_\mathrm{r} = -\partial^2_{k_\mathrm{i}k_\mathrm{i}}\omega_\mathrm{i}. \tag{3.48}$$

  Hence,

$$\mathbf{Df}(\mathbf{x}) = \begin{bmatrix} \partial_{k_\mathrm{r}}\omega_\mathrm{i} & \partial_{k_\mathrm{r}}\omega_\mathrm{r} & \partial_{Re_\Omega}\omega_\mathrm{i} \\ \partial^2_{k_\mathrm{r}k_\mathrm{r}}\omega_\mathrm{i} & \partial^2_{k_\mathrm{r}k_\mathrm{r}}\omega_\mathrm{r} & \partial^2_{k_\mathrm{r}Re_\Omega}\omega_\mathrm{i} \\ \partial^2_{k_\mathrm{r}k_\mathrm{r}}\omega_\mathrm{r} & -\partial^2_{k_\mathrm{r}k_\mathrm{r}}\omega_\mathrm{i} & \partial^2_{k_\mathrm{r}Re_\Omega}\omega_\mathrm{r} \end{bmatrix}. \tag{3.49}$$

  Control parameters: e, Re_z.
- Absolute instability threshold in the (Re_Ω, Re_z)-plane at fixed e, using continuation with respect to a pseudo-arclength variable s defined along the critical curve:

$$\omega_\mathrm{i} = \partial_k\omega = \partial_s Re_\Omega \Delta Re_\Omega + \partial_s Re_z \Delta Re_z - \delta s = 0,\ k \in \mathbb{C}, \tag{3.50}$$

  where δs is the step between two computed values on the critical curve and ΔRe_Ω is defined as follows. Let $Re^+_{\Omega,0}$ be the converged value of Re_Ω at $s + \delta s$ and Re^n_Ω be an approximation of $Re^+_{\Omega,0}$ at step n of the Newton iteration, then ΔRe_Ω designates the variation $Re^n_\Omega - Re_{\Omega,0}$. A similar definition applies to ΔRe_z. With these definitions, finally:

$$\mathbf{x} \equiv \begin{bmatrix} k_\mathrm{r} \\ k_\mathrm{i} \\ Re_\Omega \\ Re_z \end{bmatrix}, \quad \mathbf{f}(\mathbf{x}) \equiv \begin{bmatrix} \omega_\mathrm{i} \\ \partial_{k_\mathrm{r}}\omega_\mathrm{i} \\ \partial_{k_\mathrm{r}}\omega_\mathrm{r} \\ \partial_s Re_\Omega \Delta Re_\Omega + \partial_s Re_z \Delta Re_z - \delta s \end{bmatrix}, \tag{3.51}$$

$$\mathbf{Df}(\mathbf{x}) = \begin{bmatrix} \partial_{k_\mathrm{r}}\omega_\mathrm{i} & \partial_{k_\mathrm{r}}\omega_\mathrm{r} & \partial_{Re_\Omega}\omega_\mathrm{i} & \partial_{Re_z}\omega_\mathrm{i} \\ \partial^2_{k_\mathrm{r}k_\mathrm{r}}\omega_\mathrm{i} & \partial^2_{k_\mathrm{r}k_\mathrm{r}}\omega_\mathrm{r} & \partial^2_{k_\mathrm{r}Re_\Omega}\omega_\mathrm{i} & \partial^2_{k_\mathrm{r}Re_z}\omega_\mathrm{i} \\ \partial^2_{k_\mathrm{r}k_\mathrm{r}}\omega_\mathrm{r} & -\partial^2_{k_\mathrm{r}k_\mathrm{r}}\omega_\mathrm{i} & \partial^2_{k_\mathrm{r}Re_\Omega}\omega_\mathrm{r} & \partial^2_{k_\mathrm{r}Re_z}\omega_\mathrm{r} \\ 0 & 0 & \partial_s Re_\Omega & \partial_s Re_z \end{bmatrix}. \tag{3.52}$$

Newton–Raphson iteration was also used for purposes (described below) other than continuation of the critical manifolds:

- Third-order neutral saddle point: $\omega_\mathrm{i} = \partial_k\omega = \partial^2_{kk}\omega = 0,\ k \in \mathbb{C}$, so

$$\mathbf{x} \equiv \begin{bmatrix} k_\mathrm{r} \\ k_\mathrm{i} \\ Re_\Omega \\ Re_z \\ e \end{bmatrix}, \quad \mathbf{f}(\mathbf{x}) \equiv \begin{bmatrix} \omega_\mathrm{i} \\ \partial_{k_\mathrm{r}}\omega_\mathrm{i} \\ \partial_{k_\mathrm{r}}\omega_\mathrm{r} \\ \partial^2_{k_\mathrm{r}k_\mathrm{r}}\omega_\mathrm{i} \\ \partial^2_{k_\mathrm{r}k_\mathrm{r}}\omega_\mathrm{r} \end{bmatrix}, \tag{3.53}$$

$$\mathbf{Df}(\mathbf{x}) = \begin{bmatrix} \partial_{k_\mathrm{r}}\omega_\mathrm{i} & \partial_{k_\mathrm{r}}\omega_\mathrm{r} & \partial_{Re_\Omega}\omega_\mathrm{i} & \partial_{Re_z}\omega_\mathrm{i} & \partial_e\omega_\mathrm{i} \\ \partial^2_{k_\mathrm{r}k_\mathrm{r}}\omega_\mathrm{i} & \partial^2_{k_\mathrm{r}k_\mathrm{r}}\omega_\mathrm{r} & \partial^2_{k_\mathrm{r}Re_\Omega}\omega_\mathrm{i} & \partial^2_{k_\mathrm{r}Re_z}\omega_\mathrm{i} & \partial^2_{k_\mathrm{r}e}\omega_\mathrm{i} \\ \partial^2_{k_\mathrm{r}k_\mathrm{r}}\omega_\mathrm{r} & -\partial^2_{k_\mathrm{r}k_\mathrm{r}}\omega_\mathrm{i} & \partial^2_{k_\mathrm{r}Re_\Omega}\omega_\mathrm{r} & \partial^2_{k_\mathrm{r}Re_z}\omega_\mathrm{r} & \partial^2_{k_\mathrm{r}e}\omega_\mathrm{r} \\ \partial^3_{k_\mathrm{r}k_\mathrm{r}k_\mathrm{r}}\omega_\mathrm{i} & \partial^3_{k_\mathrm{r}k_\mathrm{r}k_\mathrm{r}}\omega_\mathrm{r} & \partial^3_{k_\mathrm{r}k_\mathrm{r}Re_\Omega}\omega_\mathrm{i} & \partial^3_{k_\mathrm{r}k_\mathrm{r}Re_z}\omega_\mathrm{i} & \partial^3_{k_\mathrm{r}k_\mathrm{r}e}\omega_\mathrm{i} \\ \partial^3_{k_\mathrm{r}k_\mathrm{r}k_\mathrm{r}}\omega_\mathrm{r} & -\partial^3_{k_\mathrm{r}k_\mathrm{r}k_\mathrm{r}}\omega_\mathrm{i} & \partial^3_{k_\mathrm{r}k_\mathrm{r}Re_\Omega}\omega_\mathrm{r} & \partial^3_{k_\mathrm{r}k_\mathrm{r}Re_z}\omega_\mathrm{r} & \partial^3_{k_\mathrm{r}k_\mathrm{r}e}\omega_\mathrm{r} \end{bmatrix}. \tag{3.54}$$

- Inversion of the dispersion relation $k = K(\omega),\ k, \omega \in \mathbb{C}$:

$$\mathbf{x} \equiv \begin{bmatrix} k_\mathrm{r} \\ k_\mathrm{i} \end{bmatrix}, \quad \mathbf{f}(\mathbf{x}) \equiv \begin{bmatrix} \omega_\mathrm{r} - \omega_{\mathrm{r,target}} \\ \omega_\mathrm{i} - \omega_{\mathrm{i,target}} \end{bmatrix}, \quad \mathbf{Df}(\mathbf{x}) = \begin{bmatrix} \partial_{k_\mathrm{r}}\omega_\mathrm{r} & -\partial_{k_\mathrm{r}}\omega_\mathrm{i} \\ \partial_{k_\mathrm{r}}\omega_\mathrm{i} & \partial_{k_\mathrm{r}}\omega_\mathrm{r} \end{bmatrix}. \tag{3.55}$$

Newton–Raphson iteration requires the derivatives appearing in the Jacobian $\partial f_i/\partial x_j$ and inversion of the resulting matrix $\mathbf{Df}$ at each iteration. Matrix inversion is cheap since the dimension of the largest system considered is only five. Derivatives are most easily approximated using finite differences and small variations in $\mathbf{x}$. In practice, steps of δk, δRe_Ω, δRe_z and δe of 10^{-4} were taken to compute the derivatives.

3.6 Validation

Many validation results are given in §4.2.6 and §5.3.5. The aim of the present section is to give a more detailed presentation, along with some additional tests which will not be mentioned again in later chapters.

3.6.1 Basic flow

We start by defining a number of basic-flow quantities used for validation

- F_x and F_y, the x- and y-components of the force (per unit length) on the inner cylinder,
- T, the torque on the inner cylinder,
- $f \equiv d|G|/(1/2\rho\overline{W}^2)$ (using dimensional quantities), the Fanning friction factor characterising the resistance to axial motion due to viscosity,
- Q_ϕ, the azimuthal volume flux (per unit length). It is defined as the flux of in-plane velocity through any path joining the two cylinders.

The torque and forces on the inner cylinder are obtained by integration of the wall stresses. The stress tensor $\overline{\overline{\sigma}}$ has pressure and viscous contributions, with $\overline{\overline{\tau}}$ the viscous-stress tensor

$$\overline{\overline{\sigma}} = -p\overline{\overline{I}} + \overline{\overline{\tau}}. \tag{3.56}$$

For an incompressible Newtonian flow, $\overline{\overline{\tau}}$ is given in non-dimensional form by

$$\overline{\overline{\tau}} = 2Re_\Omega^{-1}\overline{\overline{e}}, \tag{3.57}$$

with the strain-rate tensor $\overline{\overline{e}}$:

$$\begin{cases} e_{\xi\xi} &= D_\xi u - Bv, \\ e_{\phi\phi} &= D_\phi v + Au, \\ e_{\phi\xi} &= e_{\xi\phi} = \frac{1}{2}(D_\xi v + D_\phi u + Bu - Av). \end{cases} \tag{3.58}$$

The infinitesimal force (per unit length) on the inner cylinder of outward unit normal $\mathbf{e}_\xi$ is

$$\mathrm{d}\mathbf{F} = \frac{\overline{\overline{\sigma}} \cdot \mathbf{e}_\xi}{\mu_\phi}\mathrm{d}\phi = \frac{e_{\xi\xi}\mathbf{e}_\xi + e_{\xi\phi}\mathbf{e}_\phi}{\mu_\phi}\mathrm{d}\phi, \tag{3.59}$$

therefore, the components F_x and F_y of the force, and the torque T (all per unit length) are

$$F_x = \oint \mathrm{d}\mathbf{F} \cdot \mathbf{e}_x, \quad F_y = \oint \mathrm{d}\mathbf{F} \cdot \mathbf{e}_y, \quad T = \frac{1}{\delta}\oint \mathrm{d}\mathbf{F} \cdot \mathbf{e}_\phi. \tag{3.60}$$

On the inner cylinder, $\mathbf{e}_\xi$ and $\mathbf{e}_\phi$ are respectively equal to $\mathbf{e}_r$ and $\mathbf{e}_\theta$ (polar coordinates). Thus, the projections $\cos\theta = \mathbf{e}_\xi \cdot \mathbf{e}_x = \mathbf{e}_\phi \cdot \mathbf{e}_y$ and $\sin\theta = \mathbf{e}_\xi \cdot \mathbf{e}_y = -\mathbf{e}_\phi \cdot \mathbf{e}_x$ are given by $\cos\theta = x\delta$ and $\sin\theta = y\delta$. The cartesian coordinates (x, y) centered on the inner cylinder are related to (ξ, ϕ) via the conformal transformation (3.10)–(3.12).

Stokes régime

The first step is to validate basic flow against analytical solutions. This is trivially done for the concentric Taylor–Couette flow. Analytical solutions are also available for the crossflow components of the eccentric case in the Stokes limit, $Re_\Omega \to 0$. Indeed, Wannier (1950) derived analytical formulas for the Stokes problem between eccentric cylinders, with rotation of the inner one (see Appendix E). Analytical expressions for F_y and T (E.15) and (E.16) show an explicit scaling with Re_Ω^{-1}, expected from the fact that both the viscous stresses τ and pressure P have this scaling. The azimuthal volume flux Q_ϕ can also be calculated by evaluating the stream function on the inner and outer cylinders, with expressions given in Appendix E.

Tests were performed by computing $F_y Re_\Omega$, $T Re_\Omega$ and Q_ϕ for $\eta = 0.5$ and eccentricities close to one, with various resolutions. Results are compared with the analytical values. The code was adapted to eliminate the nonlinear terms in the Navier–Stokes equations. Time-stepping was stopped when residuals reach a plateau. Computed values are reported in table 3.1, with sixteen significant digits, and the relative errors are plotted in figure 3.3.

For $e = 0.9$, machine accuracy is approached (relative error $\sim 10^{-13}$) for Q_ϕ and $T Re_\Omega$ when $(M+1) \times K = 32 \times 128$. For $e = 0.99$, machine accuracy is not reached and a larger number of Fourier components would be needed to attain it. Spectral accuracy with respect to the Fourier decomposition is clear in figure 3.3(c). The exponential rate of convergence with respect to the number of collocation points can also be seen for low values of M, typically $M + 1 \leq 16$, but the error reaches a plateau for higher values (figures 3.3c,d): Stokes flow varies 'smoothly' with respect to the pseudo-radial direction.

e	$(M+1)\times K$	$F_y Re_\Omega$	$T Re_\Omega$	Q_ϕ
0.9	exact	−39.3203945895357	−40.8448766630907	0.0656030515284698
	32×16	−39.3202241544768	−40.8449043568617	0.0654495222319055
	32×32	−39.3203945741966	−40.8448766634296	0.0656029020330217
	32×64	−39.3203945788530	−40.8448766631289	0.0656030515279514
	32×128	−39.3203945909704	−40.8448766630927	0.0656030515284725
	24×128	−39.3203945860874	−40.8448766630826	0.0656030515284609
	16×128	−39.3203945880031	−40.8448766630939	0.0656030515302144
	12×128	−39.3203945986371	−40.8448766627354	0.0656030587195854
	8×128	−39.3204600917767	−40.8448688312408	0.0656329804433483
0.99	exact	−125.603824106706	−126.028454301705	0.00665661245732574
	32×16	−122.101899226183	−126.203967010802	−0.0416554215879224
	32×32	−125.232258991428	−126.03091393078	0.00158221631455449
	32×64	−125.602938338639	−126.028454791607	0.00660166275020455
	32×128	−125.603849809656	−126.028454299078	0.00665659498501146
	24×128	−125.603822023761	−126.028454300413	0.00665659497850345
	16×128	−125.603826662920	−126.028454301725	0.00665659505480074
	12×128	−125.603822560541	−126.028454301037	0.00665665830767067
	8×128	−125.603792313892	−126.028444865078	0.00675984911901183

Table 3.1 – Torque T and y-component of the force on the inner cylinder F_y for Stokes flow between eccentric cylinder with rotation of the inner one, $\eta = 0.5$. Exact solution from analytical formulas of Wannier (1950) and numerical results for various resolutions.

Comparison with experiments

For eccentric Taylor–Couette–Poiseuille flow, no analytical solution exists, so validation can only be done against experimental and numerical results. Escudier and Gouldson (1997) reported LDA measurements of eccentric Taylor–Couette–Poiseuille flow, below onset of the Taylor vortices. The apparatus has a radius ratio of $\eta = 0.506$, and cross-sections A, B, C and D are defined in figure 3.4. Our computations are compared with these measurements in figure 3.5, for $e = 0.2, 0.5, 0.8$ and azimuthal Reynolds numbers $Re_\Omega \approx 55$ (the precise values indicated in the caption). $U_{\tilde{\theta}}$ is the azimuthal velocity in the polar coordinate system centered on the outer cylinder $(\tilde{r}, \tilde{\theta})$.

Agreement is excellent, except for the axial velocity component when $e = 0.8$ (see figure 3.5(2c)). The mismatch is likely due to an imprecise measurement of the experimental flow rate. Indeed, rescaling our data by a multiplicative factor of 0.95 leads to excellent matching, as for all other curves. A 5% inaccuracy in the measured flow rate may well explain this discrepancy, since W is non-dimensionalized with respect to the mean axial velocity $\overline{W}$. Profile D in figure 3.5(3a) is also poorly fitted for $\sigma < 0.6$. The same discrepancy was reported in Escudier et al. (2000), whose numerical calculations agree with our results more closely than with the experiment. In this case again, an experimental bias is plausible.

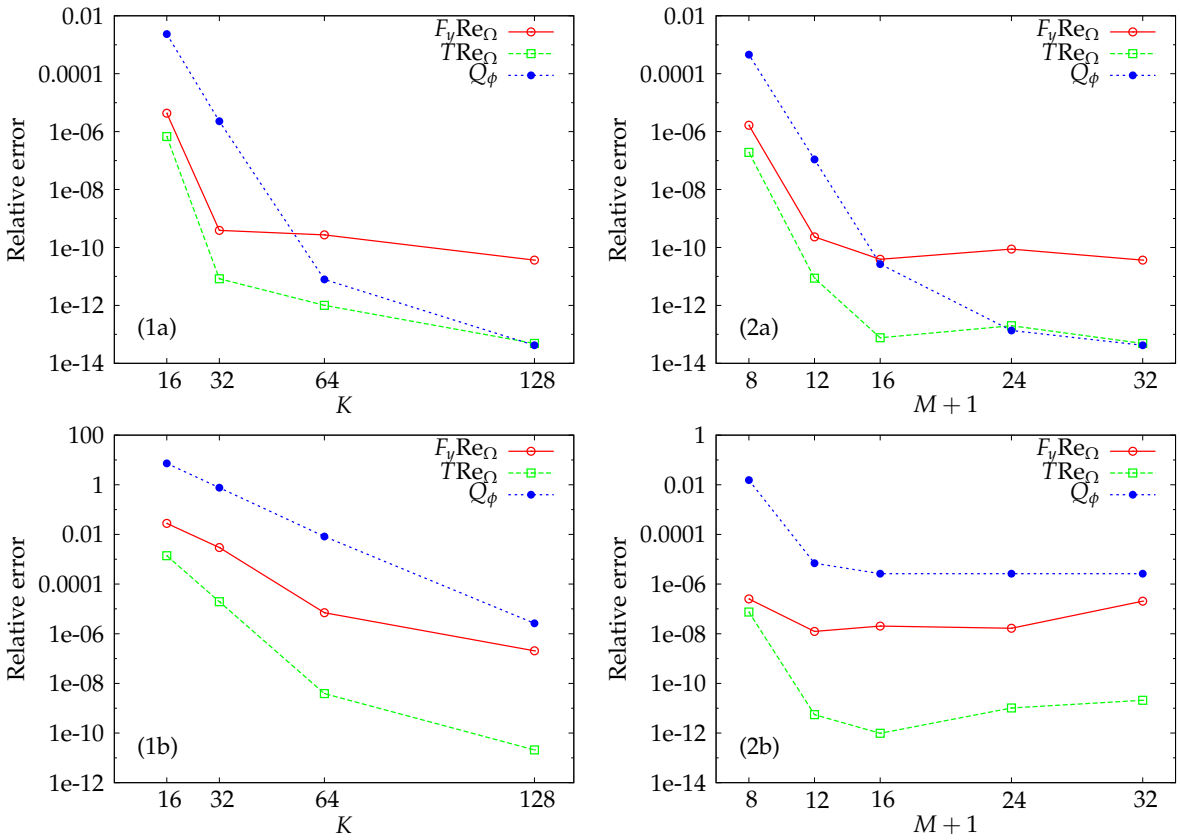

Figure 3.3 – Relative error as a function of resolution for Stokes flow between eccentric cylinders with rotation of the inner one, $\eta = 0.5$. (a) $e = 0.9$, (b) $e = 0.99$; (1) $M+1 = 32$, (2) $K = 128$.

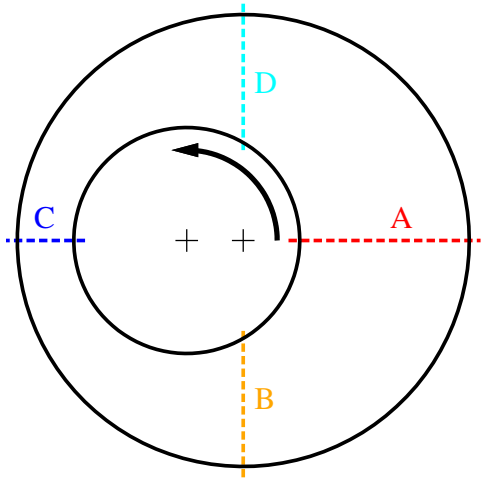

Figure 3.4 – Definition of cross-sections A, B, C and D for velocity measurements by Escudier and Gouldson (1997).

Fanning friction factor

As mentioned earlier, the Fanning friction factor characterizes the resistance to axial flow due to viscous effects. Escudier et al. (2000) made a thorough investigation of the effect of rotation of the inner cylinder on the axial flow between eccentric cylinders, and

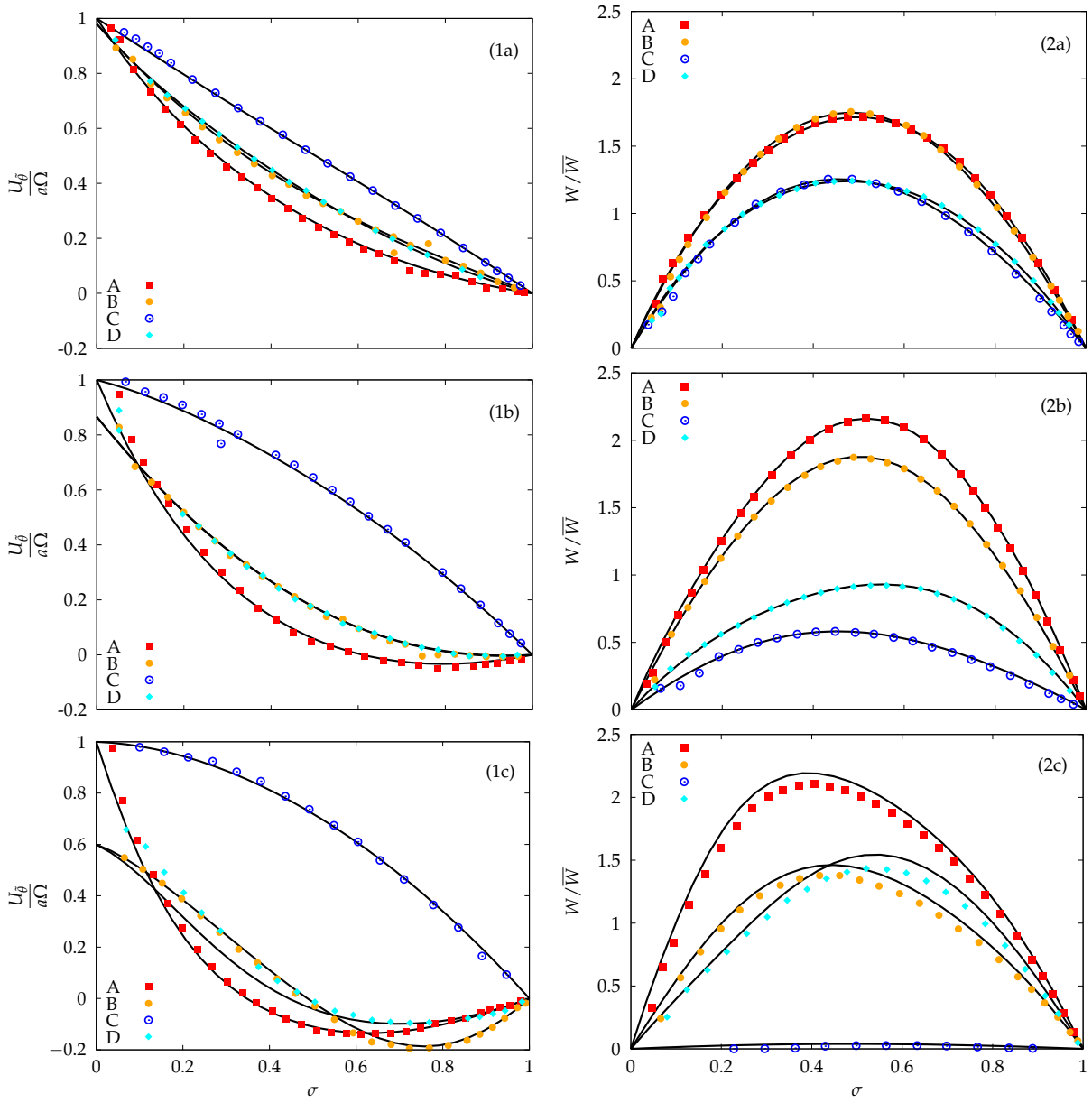

Figure 3.5 – (1) Azimuthal $U_{\tilde{\theta}}$ and (2) axial velocity W in a cylindrical coordinate system centered on the inner cylinder. $U_{\tilde{\theta}}$ and W are respectively non-dimensionalized with $a\Omega$ and the average axial velocity $\overline{W}$. Cross-sections A,B,C,D shown in figure 3.4 are defined by $\tilde{\theta} = 0, \pi/2, \pi, 3\pi/2$. Along a given cross-section, σ is defined by $\sigma \equiv (\tilde{r} - \tilde{r}_i)/(\tilde{r}_o - \tilde{r}_i)$, with $\tilde{r}_i$ and $\tilde{r}_o$ the values of $\tilde{r}$ on the inner and outer cylinders. Symbols represent experimental data from Escudier and Gouldson (1997). Lines correspond to our simulations. (a) $e = 0.2$, $Re_\Omega = 53.70$, (b) $e = 0.5$, $Re_\Omega = 55.65$, (c) $e = 0.8$, $Re_\Omega = 54.67$.

reported computed values of the friction factor for various values of η, e and Ta (Taylor number defined as $\mathrm{Ta} = Re_\Omega^2 \delta$). Computations were made using a finite-difference solver cast in polar coordinates centered on the inner cylinder. The authors validated their code against their own experimental data (Escudier and Gouldson, 1997) (see figure 3.5). Figure 3.6 shows our results together with those of Escudier et al. (2000) for the wide-gap case $\eta = 0.5$. Our results lie within 0.67% of their values.

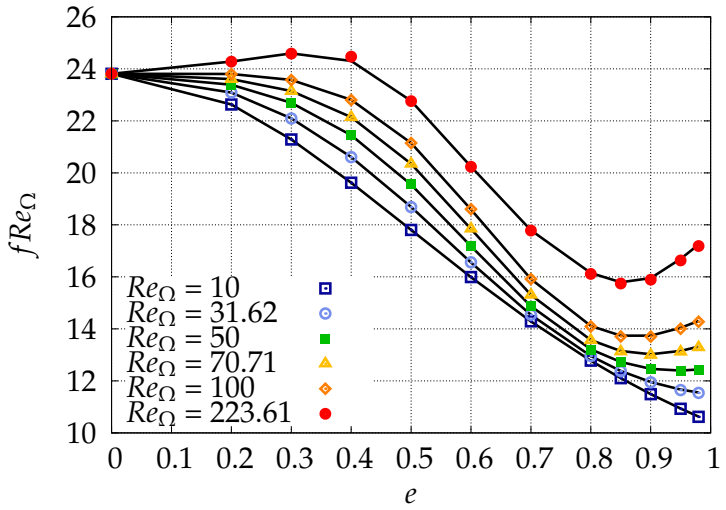

Figure 3.6 – Comparison of Fanning friction factor with numerical values of Escudier et al. (2000), for $\eta = 0.5$. The values of Re_Ω correspond to Taylor numbers $Ta = Re_\Omega^2 \delta = 1000, 2500, 5000, 10000, 50000$. Lines: present results; symbols: Escudier et al. (2000).

Forces on the inner cylinder

The calculation of the tangential viscous stress on the inner cylinder is validated (see figure 3.7) against a curve given in Oikawa et al. (1989a). The contributions of the

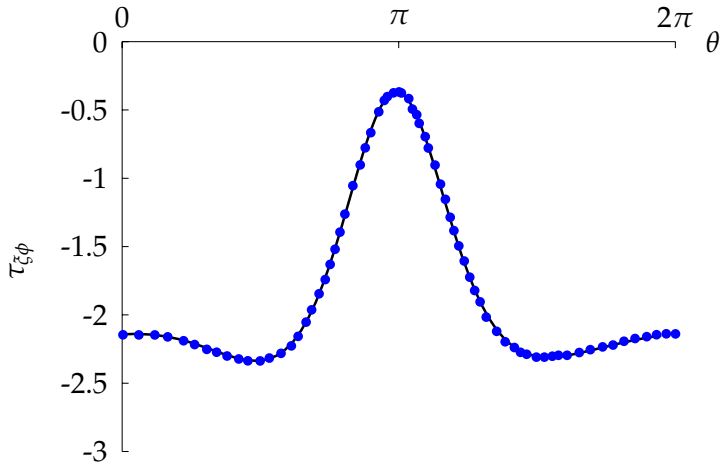

Figure 3.7 – Shear stress $\tau_{\xi\phi}$ acting on the inner cylinder non-dimensionalized by $\mu a\Omega/d$, for $\delta = 0.205$, $e = 0.5$, $Re_\Omega = 155$. Comparison with figure 8 in Oikawa et al. (1989a). Lines: present results; symbols: Oikawa et al. (1989a).

viscous and pressure terms to the x and y components of the force are then computed for various eccentricities up to $e = 0.98$, $\eta = 0.5$ and $Re_\Omega = 125$, and compared with numerical results of Feng et al. (2007) (see figure 3.8). The relative difference with these authors' values is always less than 1.80%, and 0.76% on average, when at least four digits are provided by Feng et al. (2007). Comparisons were also made against numerical results of Podryabinkin and Rudyak (2011) and are shown in figure 3.9. Radius ratios $\eta = 0.2$ and $\eta = 0.85$ were used, with $Re_\Omega = 100$. Matching is good in all cases, except for F_y in

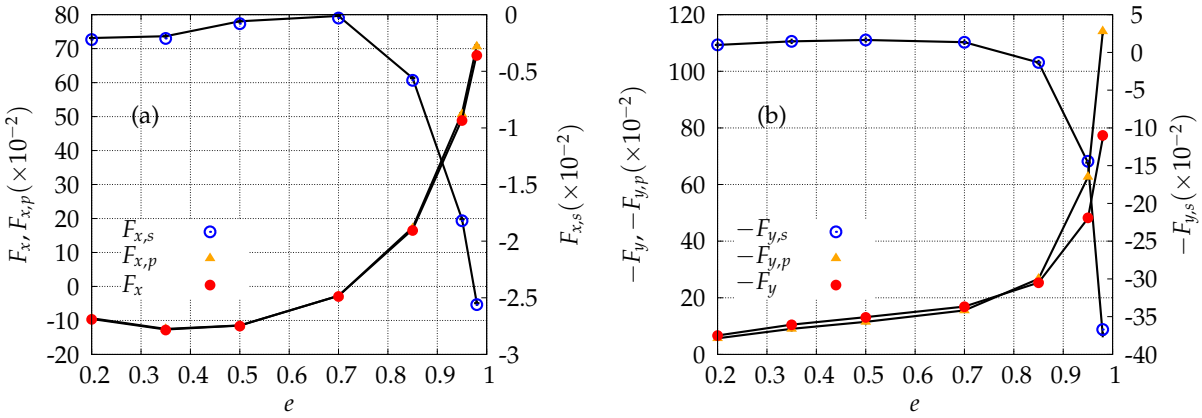

Figure 3.8 – Pressure F_p and viscous F_s contributions to the (a) x and (b) y components of the force on the inner cylinder. Comparison with values computed by Feng et al. (2007). Lines: present results; symbols: Feng et al. (2007).

the very wide gap case $\eta = 0.2$ for $e \geq 0.9$. The authors observe a change of sign in F_y that is not found for $\eta = 0.5$ and $\eta = 0.85$. No mention is made of the spatial resolution used in their article. For the case $e = 0.99$, the resolution we used was $M + 1 = 32$ and $K = 128$, which we will show to be acceptable for the case $\eta = 0.5$ (see resolution tests in the next subsection and figure 3.10 in particular). Given the convincing results obtained otherwise with our code, we suspect a convergence issue in the computations of Podryabinkin and Rudyak (2011).

Resolution tests

Resolution tests were performed to define the appropriate number of Fourier components/collocation points for $\eta = 0.5$ in the ranges $e \leq 0.99$ and $Re_\Omega \leq 250$. Table 3.2 shows meshes necessary to achieve convergence up to the sixth significant digit simultaneously on different scalar quantities obtained by numerical integration of the flow field: azimuthal flowrate Q_ϕ, Fanning friction factor f, torque and the x-y components of the viscous and pressure forces on the inner and outer cylinders.

Increasing the number of Chebyshev polynomials from 32 to 64 was found to have a small effect on the sixth significant digit only for $e \geq 0.95$ and $Re_\Omega \geq 250$. For such high values of eccentricity, the mesh concentrates in the narrow gap, leaving the wider gap coarsely meshed, explaining the need for a significantly higher number of Fourier modes. $N = 128$ is the maximum number of Fourier modes considered, and seems to be sufficient to well represent the flow in conditions as stringent as $e = 0.98$ and $Re_\Omega = 223.61$ (see figure 3.10 which shows a comparison with Escudier et al. (2000)).

3.6.2 Normal modes and continuation

Eigenmode calculation

The eigenmode stucture was compared with literature results in a very simple case: concentric Taylor–Couette flow with $\eta = 0.5$ at the onset of temporal instability. Excel-

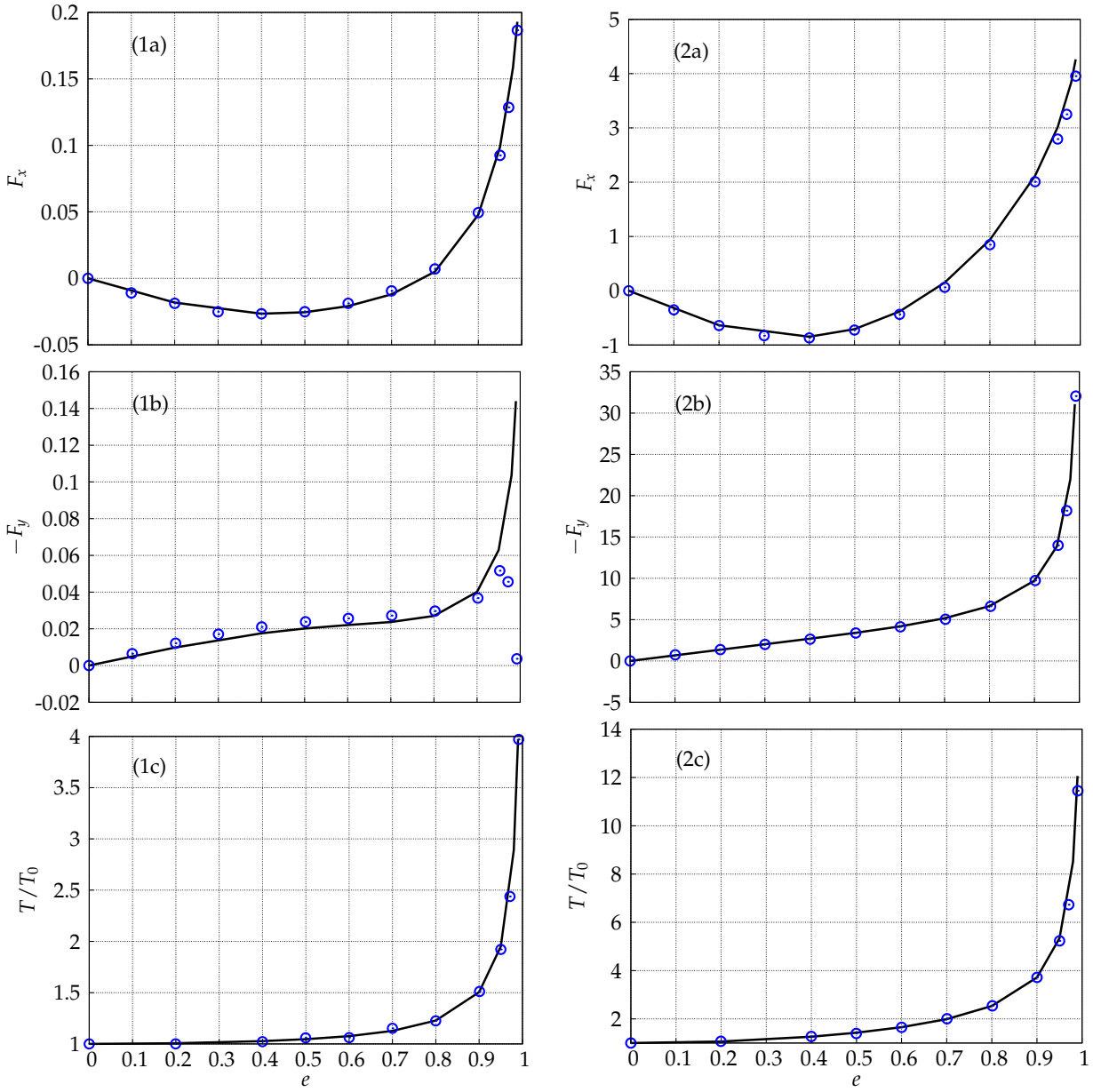

Figure 3.9 – Comparison of forces and torque computation with numerical values of Podryabinkin and Rudyak (2011), $Re_\Omega = 100$. (1) $\eta = 0.2$; (2) $\eta = 0.85$. (a) F_x; (b) $-F_y$; (c) T/T_0, with T_0 the torque for $e = 0$. Lines: present results; open circles: Podryabinkin and Rudyak (2011).

lent matching is shown in figure 3.11.

Temporal stability threshold

The temporal stability threshold calculations were validated first for the case of concentric Taylor–Couette–Poiseuille flow with $\eta = 0.5$, against numerical results of Takeuchi and Jankowski (1981) (see figure 3.12). Numerical values given by the authors are matched with all significant digits (except for the case $Re_z = 90$, where only the last digit in the values of k and phase speed $c = \omega/k$ differed from our result by one).

e \ Re_Ω	10	50	100	150	200	250
0	16×0					
0.1						
0.2	16×8					
0.3						
0.4			32×16			
0.5						
0.6	16×16					
0.7						
0.8				32×32		
0.9	16×32			32×64		
0.95	32×64					
0.98			32×128			
0.99						

Table 3.2 – Minimum mesh size $(M+1) \times K$ to achieve 6-digit accuracy simultaneously for Q_ϕ, f, torque and forces on the inner and outer cylinders.

In the eccentric case with no axial flow, comparisons with numerical results for two different radius ratios $\eta = 0.912$ (Dai et al., 1992, Chawda and Avgousti, 1996) and $\eta = 0.5$ (Oikawa et al., 1989a) show good agreement (see figure 4.6). More details are given in §4.2.6.

Convective/absolute instability threshold

The absolute instability thresholds in concentric Taylor–Couette–Poiseuille flow were computed for a few modes with largest absolute growth rate by Pinter et al. (2003), Altmeyer et al. (2011). In the axisymmetric case, the normal modes have the form $\mathbf{q}' = \tilde{\mathbf{q}}(r) \exp[\mathrm{i}(kz + m\theta - \omega t)] + \text{c.c.}$, characterised by an azimuthal integer wavenumber m. For $m = 0, 1$, agreement is excellent between our computations and the results of Pinter et al. (2003). More details can be found in §5.3.5.

For $m = 2$ and $e = 0$, Altmeyer et al. (2011) found absolute instability to occur over a closed domain in the (Re_Ω, Re_z)-plane, which the authors called an 'island of instability' [8]. This closed boundary is accurately reproduced by our code, see figure 3.14.

8. The study is however incomplete since the authors considered only one saddle point in their calculations, more details can be found in chapter 5.

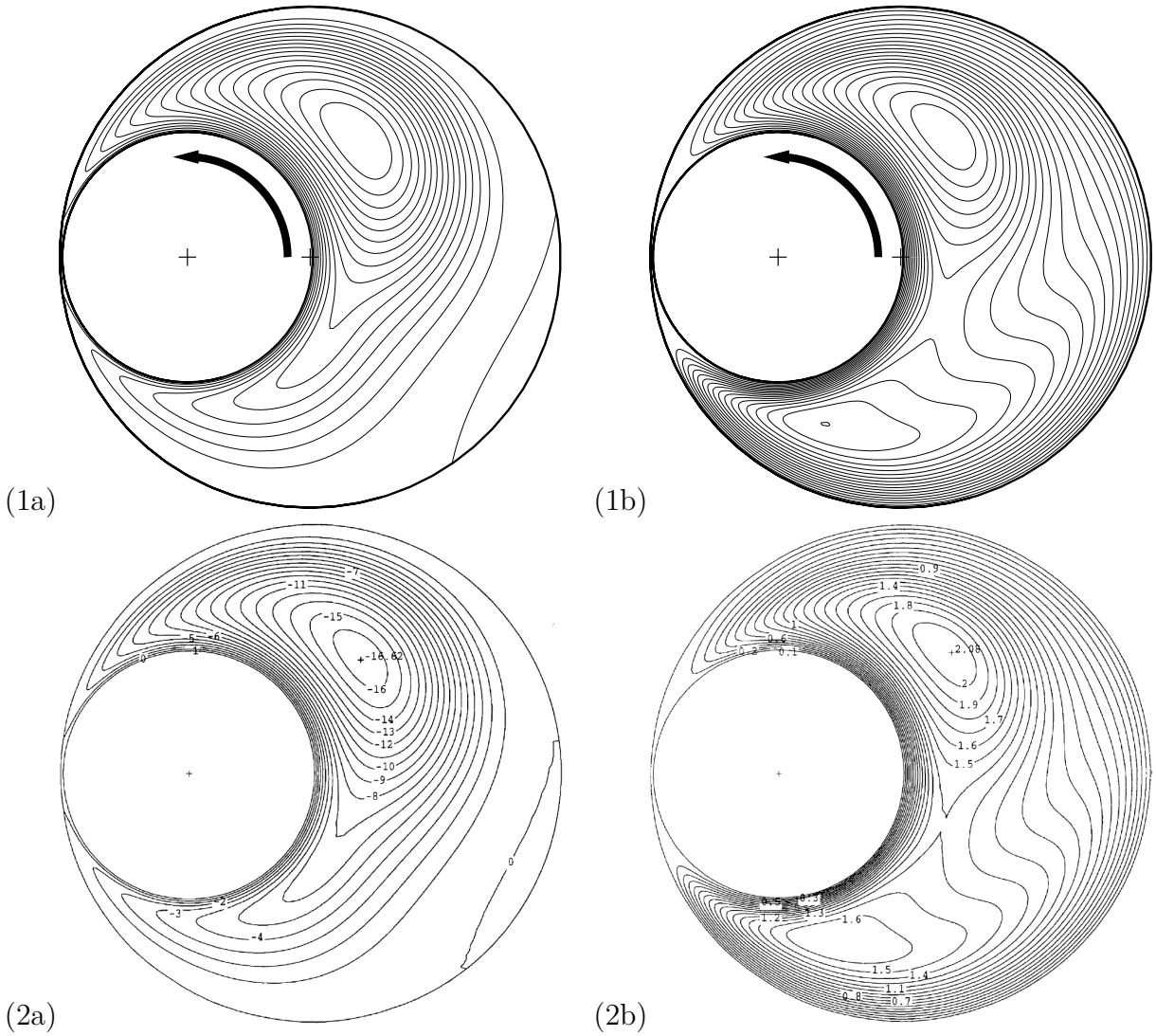

Figure 3.10 – Streamlines (a) and axial flow isocontours (b) for $\eta = 0.5$, $e = 0.98$ and $Re_\Omega = 223.61$. Comparison of (1) present calculations using $(M + 1) \times N = 32 \times 257$ ($K = 128$) with (2) Escudier et al. (2000). The calculation recovers the secondary recirculation region in the wide gap and the two distorted maxima in axial velocity. The numerical values of the isolines match those of Escudier et al. (2000).

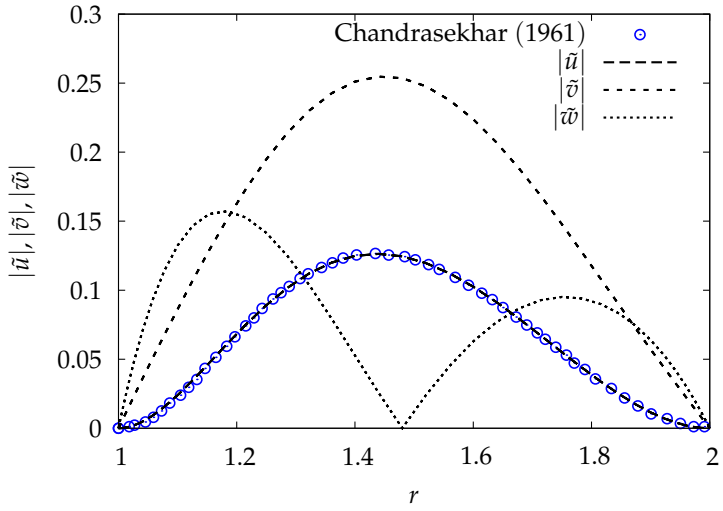

Figure 3.11 – Mode structure as a function of radial coordinate r for Taylor–Couette flow with $\eta = 0.5$, at onset of instability: $k = 3.2$, $Re_\Omega = 68.19$. Comparison with Chandrasekhar (1981) (open circles) for the radial component $\tilde{u}$.

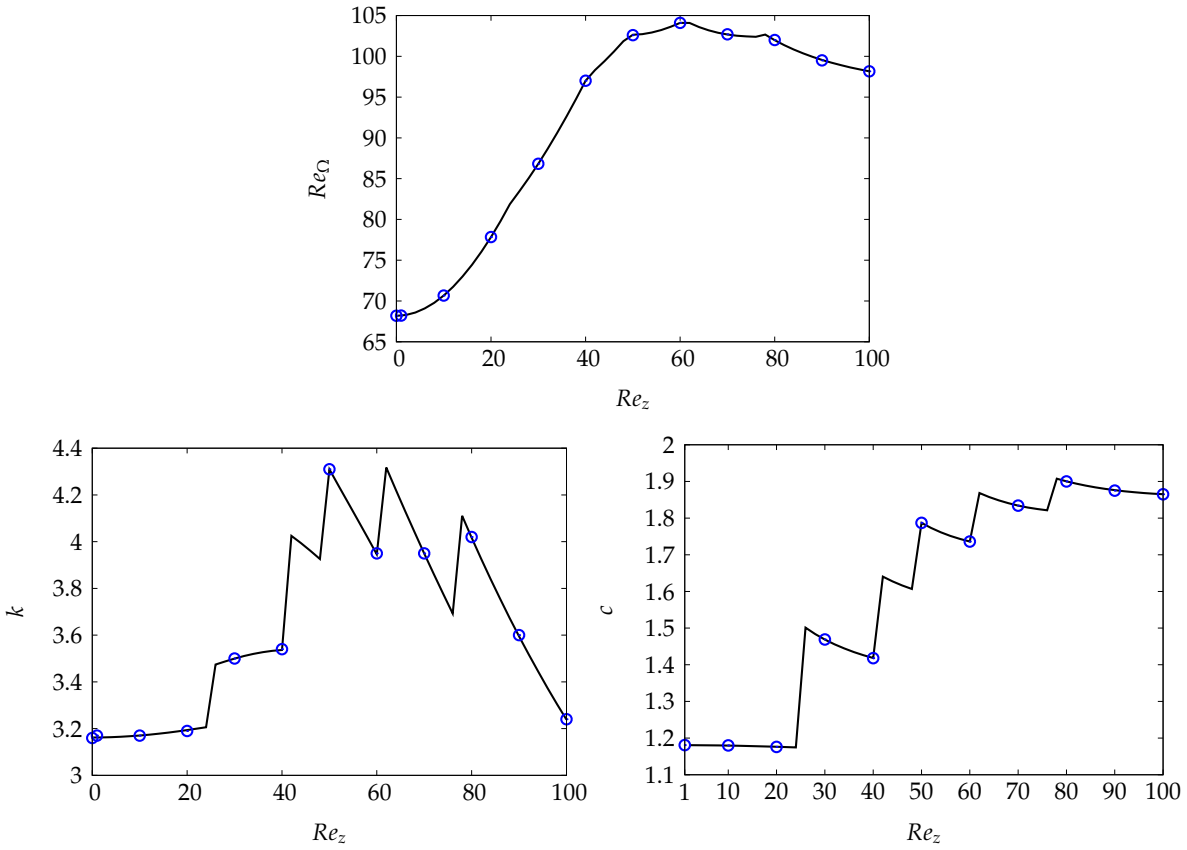

Figure 3.12 – Critical azimuthal Reynolds number Re_Ω, wavenumber k, and phase speed c (normalized by $\overline{W}$ as a function of advection Re_z, for $\eta = 0.5$, in the concentric Taylor–Couette–Poiseuille flow. Lines: present results; open circles: Takeuchi and Jankowski (1981).

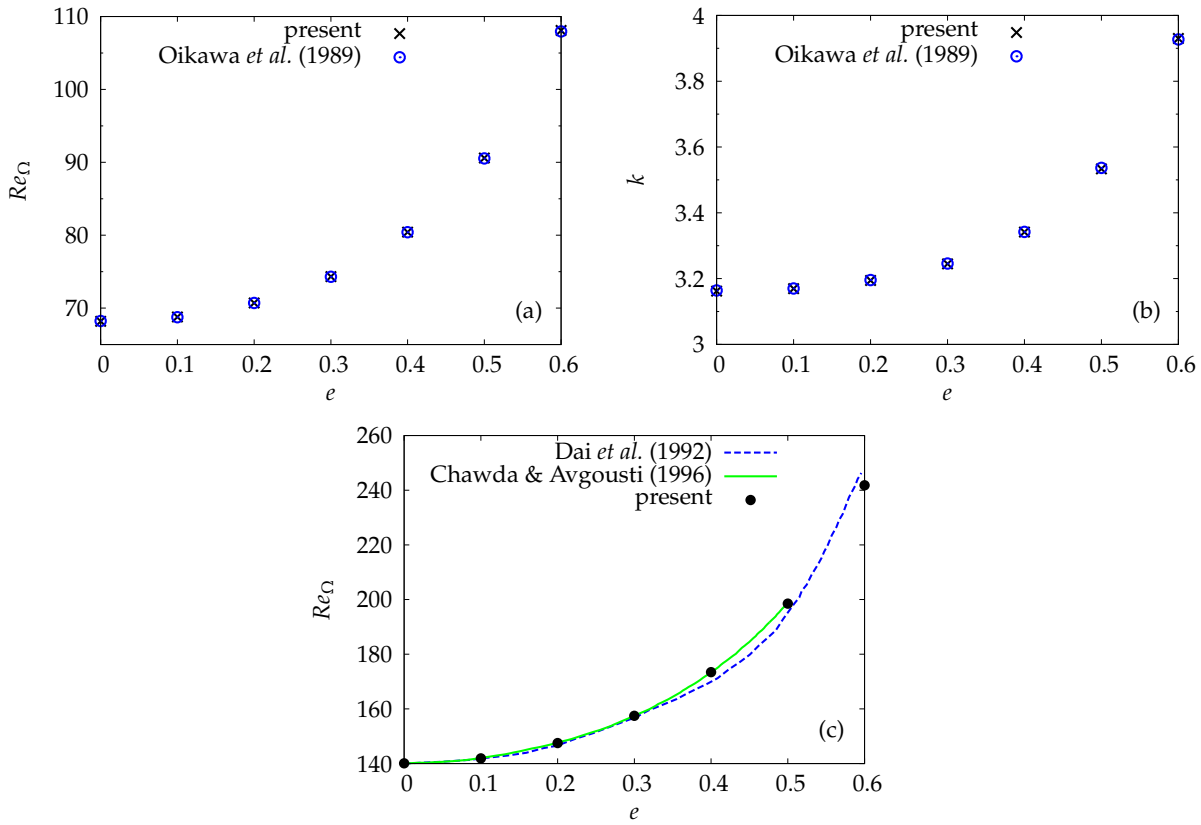

Figure 3.13 – (a) Critical azimuthal Reynolds number Re_Ω and (b) axial wavenumber k vs. eccentricity e for $\eta = 0.5$: comparison with Oikawa et al. (1989a). (c) Critical azimuthal Reynolds number for $\eta = 0.912$, $k = 3.17$, comparison with Dai et al. (1992), Chawda and Avgousti (1996).

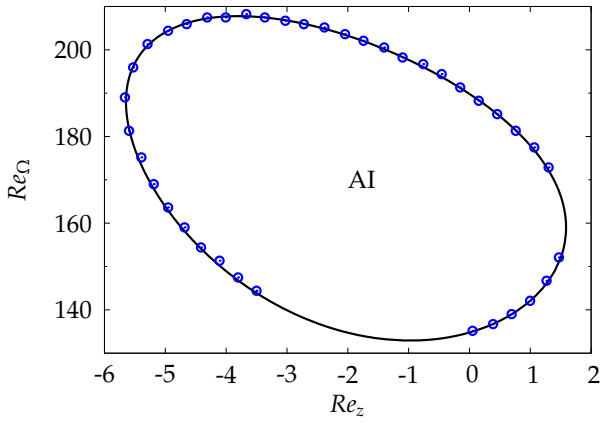

Figure 3.14 – 'Island of instability' for helical mode $m = 2$ in the concentric Taylor–Couette–Poiseuille flow, $\eta = 0.5$. Line: present calculations, dots: Altmeyer et al. (2011).

Chapter 4

Temporal stability

Before proceeding to any stability analysis, the first step is to investigate the basic flow solution, defined as the hypothetical flow with the maximum number of symmetries. In this chapter, we review the basic flow properties and study the temporal dynamics of superimposed infinitesimal perturbations. Perturbations are decomposed as a sum of normal modes and the properties of the fastest growing ones are studied. In particular, the effect of eccentricity and axial advection on the instability threshold is investigated for a wide gap and a small gap configurations. For the small gap configuration, comparison is made against experimental data obtained in the seventies, the only available data of which we are aware. The chapter starts with a review of previous studies on eccentric Taylor–Couette flow, axisymmetric Taylor–Couette–Poiseuille flow, and finally eccentric Taylor–Couette–Poiseuille flow. We show that little is known about the combined effects of eccentricity and axial flow, and the originality of our analysis is to perform a systematic temporal stability analysis incorporating the two effects. The results are reported in the form of an article published in the *Journal of Fluid Mechanics* (Leclercq et al., 2013). Slight notation changes have been introduced to ensure coherence with the rest of the present manuscript, but the text and figures are otherwise identical to the original article. Sections, figures, tables and equations were also relabelled to fit with the manuscript structure. At the end of the chapter, a small section is added, giving further results concerning the wall stresses on the inner cylinder. This section illustrates statements made in §4.2.4 and helps to understand the evolution of the forces and torque on the inner cylinder when parameters are varied.

Temporal stability of eccentric Taylor–Couette–Poiseuille flow

Colin Leclercq, Benoît Pier and Julian F. Scott

Laboratoire de mécanique des fluides et d'acoustique, École centrale de Lyon—CNRS—Université Claude-Bernard Lyon 1—INSA Lyon, 36 avenue Guy-de-Collongue, 69134 Écully cedex, France

Published in J. Fluid Mech. (2013), ***733****, pp. 68–99.*

The combined effects of axial flow and eccentricity on the temporal stability properties of the Taylor–Couette system are investigated using a pseudospectral method. Eccentricity is found to stabilize the Couette flow regardless of axial advection intensity. As the axial Reynolds number Re_z is increased for any fixed eccentricity $e \leq 0.7$, the critical mode switches from deformed toroidal Taylor vortices to helical structures with an increasing number of waves, and with helicity opposed to the inner cylinder rotation. For a wide gap configuration of radius ratio $\eta = 0.5$, increasing axial advection has a stabilising effect for low Re_z, then a weak destabilising effect for high enough Re_z. Centrifugal effects are always destabilising, but axial shear is responsible for dominance of helical modes of increasing azimuthal complexity. The modes localise in the converging gap region, and the energy concentrates increasingly into axial motion for larger Re_z. Critical quantities are also computed for a small gap case, and similar trends are observed, even though no destabilising effect of advection is observed within the range of Re_z considered. Comparison with the experiment of Coney and Mobbs (1969–70) for $\eta = 0.89$ shows good agreement, despite small discrepancies attributed to finite length effects.

4.1 Introduction

More than 40 years ago, Coney and Mobbs (1969–70) wrote: 'a linear stability theory solution for the case of eccentric rotating cylinders with a superimposed axial flow [...] is not available and the difficulties in the way of such a solution are formidable'. Indeed, while the flow between rotating cylinders is one of the benchmarks of hydrodynamic stability since the path breaking work of Taylor (1923), the computational cost associated with more complex versions of this flow has long been considered a show stopper, and still remains a major challenge as we try to bridge the gap with engineering applications. In this paper, we study the temporal stability of cylindrical Couette flow with two additional effects: eccentricity of the cylinder axes and axial flow. Taken separately, the two effects have already been the subject of numerous studies which we will briefly review in this introductory section. But to the best of our knowledge, no one has yet undertaken the complete theoretical study of the combination of both, and very limited experimental data is available in this case.

4.1.1 Control parameters

This problem is governed by four control parameters. The geometry is defined by the ratio of radii $0 < \eta \equiv a/b < 1$ and eccentricity $0 \leq e \equiv c/(b-a) \leq 1$, with a and b the inner and outer cylinder radii and c the distance between centers. Introducing the clearance $d = b - a$, one can also use the clearance ratio $\delta \equiv d/a = (1-\eta)/\eta$ instead of η.

The azimuthal Reynolds number $Re_\Omega = a\Omega d/\nu$, based on the inner cylinder rotation rate Ω, compares centrifugal and viscous effects, while the axial Reynolds number $Re_z = \overline{W}d/\nu$, based on the mean axial velocity $\overline{W}$, measures the importance of axial advection.

4.1.2 Industrial applications: wellbore drilling and high-speed journal bearings

This model flow is of interest to the oil industry as a first step towards understanding the dynamics of the complex annular flow of mud in wellbore drilling operations. For drilling applications, a drillstring is rotated inside the well in order to drive a drillbit that cuts the rock at the bottom of the well. Mud is injected through the drillstring and flows back to the surface through the annular gap, ensuring several engineering functions, among which (Escudier et al., 2002): carry the rock cuttings out of the well, cool and clean the drillbit, support the wellbore, avoid inflow of formation fluids and prevent settling of the cuttings when circulation is stopped. The annular flow of mud can be modeled in first approximation by an eccentric Taylor–Couette–Poiseuille flow because of the rotation of the drillstring, the pressure-driven axial flow and eccentricity caused by flexibility of the drillstring.

For typical industrial configurations (Escudier et al., 2002, Guo and Liu, 2011), the ratio between drillstring and outer-wall radii ranges from 0.2 at the top to 0.8 at the bottom, and eccentricity can go all the way to the limit of touching cylinders. The gap between the drillstring and the outer wall is of order $10^{-2} - 10^{-1}$m. The velocity of the inner cylinder in rotation is comparable to the mean axial velocity of the flow, of the order of 1m.s^{-1}. Finally, mud density is of order 10^3kg.m^{-3}, with equivalent dynamic viscosity between $10^{-3} - 10^{-1}$Pa.s (note that viscosity is a function of local strain rate for non-Newtonian fluids). As a result, equivalent Reynolds numbers Re_Ω and Re_z of the order of $10^2 - 10^5$ are expected.

Limitations of the model for this application include non-Newtonian effects (viscoelasticity and thixotropicity), motion of the inner cylinder position inside the well, contamination of the fluid by cuttings and 'formation fluid', variable eccentricity and outer wall radius with depth, and imperfect circularity of the wellbore wall. However, the consideration of both eccentricity and axial flow in a systematic way is already a significant improvement on existing theory.

Eccentric Taylor–Couette–Poiseuille flow is also of interest in the field of high-speed journal bearings where 'the damaging effect of impurities contained in oil can be considerably reduced when they are quickly removed from the friction contact area [...] by intensifying axial oil flow' (Sep, 2008). In high-speed journal bearings, Huggins (1966–67) quotes a value of $Re_z = 100$ during tests on a 24-in diameter journal bearing. And

instabilities are expected to arise as noted by Coney and Mobbs (1969–70): 'in the large-diameter journal bearings, which may be expected to operate in the Taylor vortex régime, there is [...] a considerable superimposed axial flow of lubricant'.

4.1.3 Eccentric Taylor–Couette flow

The effect of eccentricity on the Taylor–Couette flow has been investigated by many researchers, covering a wide range of ratio of radii and eccentricities, starting with the experimental work of Cole (1957). Using torque measurements, flow visualisation (dye injection, aluminum flakes, etc.) and hot wire probes, Cole (1957, 1967, 1969), Kamal (1966), Vohr (1968), Koschmieder (1976) and later Karasudani (1987), Xiao et al. (1997) and Lim and Lim (2008) found a stabilizing effect of eccentricity on the appearance of Taylor vortices. On the other hand Castle and Mobbs (1967), Versteegen and Jankowski (1969) and Frêne and Godet (1971) found a slight destabilization at weak eccentricities, followed by stabilization at higher values. The vortices of the first type, confined to the inner cylinder neighbourhood, were later found to be caused by end wall effects by Mobbs and Ozogan (1984), El-Dujaily and Mobbs (1990). For the second type of vortices, an increase in critical wavenumber at higher eccentricities was reported in the early work of Cole (1967) and quantified by subsequent authors.

The first theoretical analyses were made by DiPrima (1963) and Ritchie (1968), using *local* stability theory (as implied by the *parallel-flow* approximation in the 'pseudo-azimuthal' direction) and asymptotic analyses in the small gap, small eccentricity limit. The first *global* stability analyses of the problem, considering fully two-dimensional basic flows, were performed a decade later by DiPrima and Stuart (1972b), DiPrima and Stuart (1975) and Eagles et al. (1978), demonstrating a stabilising effect of eccentricity and the weakness of the *local* approach to model this flow. More recently, Oikawa et al. (1989b,a) and Dai et al. (1992) were able to relax the small gap–small eccentricity constraint (e up to $0.6 - 0.7$, η as low as 0.5), using numerical methods to solve the two-dimensional stability problem.

Finally, most recent numerical and experimental stability analyses seem to have been concerned mostly with the effect of non-Newtonian fluids (e.g. Chawda and Avgousti (1996), Dris and Shaqfeh (1998)), with applications to oil drilling and polymeric processing.

4.1.4 Taylor–Couette–Poiseuille flow

The effect of a pressure driven axial flow on the concentric Taylor–Couette system with fixed outer cylinder has been the object of even more investigations. The first analytical studies were restricted to the narrow gap limit and axisymmetric perturbations (e.g. Chandrasekhar (1960), DiPrima (1960)), reaching (after some controversy) the conclusion that advection stabilizes the Couette flow. The first correct numerical studies of the finite gap geometry, with non-axisymmetric disturbances, are due to Takeuchi and Jankowski (1981) and Ng and Turner (1982). Considering axial Reynolds number $Re_z \leq 100 - 150$ (theoretical – experimental), and a wide gap value $\eta = 0.5$, Takeuchi and Jankowski (1981) confirmed numerically and experimentally the results from Snyder

(1962, 1965)'s experiments showing that toroidal vortices are replaced by helical vortices for larger advection rates. Ng and Turner (1982) extended the results to $Re_z \leq 6000$ for $\eta = 0.77$ and $\eta = 0.95$, with fair agreement with experiments. They also considered axisymmetric disturbances for $\eta = 0.95$ up to the value of $Re_z = 7739.5$ where annular Poiseuille flow becomes unstable with respect to Tollmien–Schlichting (TS) like disturbances. They showed a connection between the centrifugal instability and the shear instability at high advection rates, as conjectured by Reid (1961). More recently Cotrell and Pearlstein (2004), Cotrell et al. (2004) extended the analysis of Ng and Turner (1982) to non-axisymmetric disturbances for $\eta = 0.5, 0.77, 0.95$. Before the transition to shear instability, these authors noted the existence of a plateau in critical Re_Ω, for which the associated critical axial wavenumber drops with increasing Re_z. For the case $\eta = 0.5$, they also noticed the existence of a maximum critical Re_Ω for a specific value of Re_z. Heaton (2008) complemented their analyses by assessing the importance of non-modal effects, and showed their relevance at moderate and large $Re_z \sim 10^2$–10^4. Other recent studies concern rotation of the outer cylinder (Meseguer and Marques, 2002), absolute/convective instabilities (Altmeyer et al., 2011), supercritical states (Hwang and Yang, 2004), time-periodic flow (Marques and Lopez (2000), additional radial flow (e.g. Martinand et al. (2009)), etc. A comprehensive review of the large panel of work on this topic, though not completely up to date, is available in Cotrell and Pearlstein (2004).

4.1.5 Eccentric Taylor–Couette–Poiseuille flow

As already mentioned, some experimental data is available in the case of combined eccentricity and axial flow. To the best of the authors' knowledge, only one experiment has been undertaken, at a radius ratio of $\eta = 0.89$ (Coney and Mobbs, 1969–70, Coney, 1971, Younes, 1972, Younes et al., 1972, Mobbs and Younes, 1974, Coney and Atkinson, 1978). In Coney and Mobbs (1969–70) and Younes et al. (1972) the critical Taylor number is reported as a function of $e \leq 0.8$ and Re_z up to 125, using flow visualisation and torque measurements. It is found that axial flow always stabilises the Couette flow. At fixed eccentricity, stabilisation due to advection is less marked than in the concentric case. The critical curves have complicated forms for $Re_z \geq 75$ but the effect of eccentricity is generally stabilising. However, the results display considerable scatter and are very sensitive to the instability criterion, as shown in Coney and Atkinson (1978). Moreover, attempts at determining the critical wavenumber of the perturbations proved abortive, because of the complex flow structure observed. For $e > 0.2$, $Re_z > 20$, there seems to be coexistence of two helical structures winding in opposite directions, with 'fluctuations in the number of vortex cells occupying the length of the apparatus at any instant or in the number of turns in the vortex spirals' (Coney and Mobbs, 1969–70, Mobbs and Younes, 1974). These experiments will be discussed further in §4.4.

On the theoretical side, apart from the semi-empiral *local stability* theory of Coney and Mobbs (1969–70), inspired by the work of DiPrima (1963), no stability analysis has been attempted so far. Modal stability analysis is the object of the present article and is a first step towards understanding the complex behaviour exhibited by this flow.

4.1.6 Plan of the article

The paper is organised in four parts. §4.2 introduces the linear stability problem, including governing equations and numerical methods for basic flow and normal modes computations. The main properties of the basic flow and dominant eigenmodes are presented. In §4.3, a parametric temporal stability study is performed for $\eta = 0.5$: critical quantities are computed and stability diagrams are given. The instability mechanism is investigated by examining the spatial structure of the critical modes, and variations of growth rates with control parameters. In §4.4, critical values are computed for a small gap case $\eta = 0.89$, for which comparison with experimental data is possible. A concluding section then summarizes our main findings and paves the way for future work.

4.2 Linear stability framework

Recall that a, b are the inner and outer cylinder radii, $d = b - a$ is the clearance and Ω is the rotation rate of the inner cylinder. ρ and ν are the density and the kinematic viscosity. In the following, quantities will be made non-dimensional with respect to the reference scales $\mathrm{L} \equiv d$, $\mathrm{V} \equiv a\Omega$ and $\mathrm{P} \equiv \rho \mathrm{V}^2$ for length, velocity and pressure.

An azimuthal/rotational Reynolds number, defined as $Re_\Omega \equiv \mathrm{VL}/\nu = a\Omega d/\nu$ will be used to measure competition between centrifugal effects and viscosity. Note that this type of definition is preferred in recent numerical work (e.g. Oikawa et al. (1989a), Feng et al. (2007), Martinand et al. (2009)) rather than using Taylor numbers of the form $\mathrm{Ta} \sim \delta {Re_\Omega}^2$, which naturally appeared in the pioneering analytical studies of the small-gap limit $\delta \to 0$ (e.g. Taylor (1923), DiPrima (1959), Chandrasekhar (1981)).

Axial advection is characterised by an axial Reynolds number $Re_z \equiv \overline{W} d/\nu$, based on the mean axial velocity $\overline{W}$. The ratio Re_z/Re_Ω represents the mean axial velocity in units of rotation velocity, and conveniently measures competition between advection and rotation. Because of this, using an azimuthal Reynolds number instead of a 'classical' Taylor number seems particularly appropriate when axial flow is considered.

Finally, geometry is characterised by the ratio of radii $0 < \eta \equiv a/b < 1$, or equivalently the clearance ratio $\delta \equiv d/a = (1-\eta)/\eta$. c being the distance between centers (cf. figure 4.1), eccentricity is measured by the non-dimensional number $0 \leq e = c/d \leq 1$.

4.2.1 Governing equations

The incompressible Navier–Stokes equations governing velocity $\mathbf{u}$ and pressure p read

$$\left.\begin{aligned} \partial_t \mathbf{u} + \mathbf{u}\cdot\nabla\mathbf{u} &= -\nabla p + Re_\Omega^{-1}\nabla^2\mathbf{u}, \\ \nabla\cdot\mathbf{u} &= 0, \end{aligned}\right\} \tag{4.1}$$

with impermeability and no-slip boundary conditions at the walls (rotating inner cylinder, fixed outer one). Basic flows for stability analyses are axially invariant, steady solutions of (5.1). Because of the vanishing derivatives in the axial direction $\mathbf{e_z}$, velocity

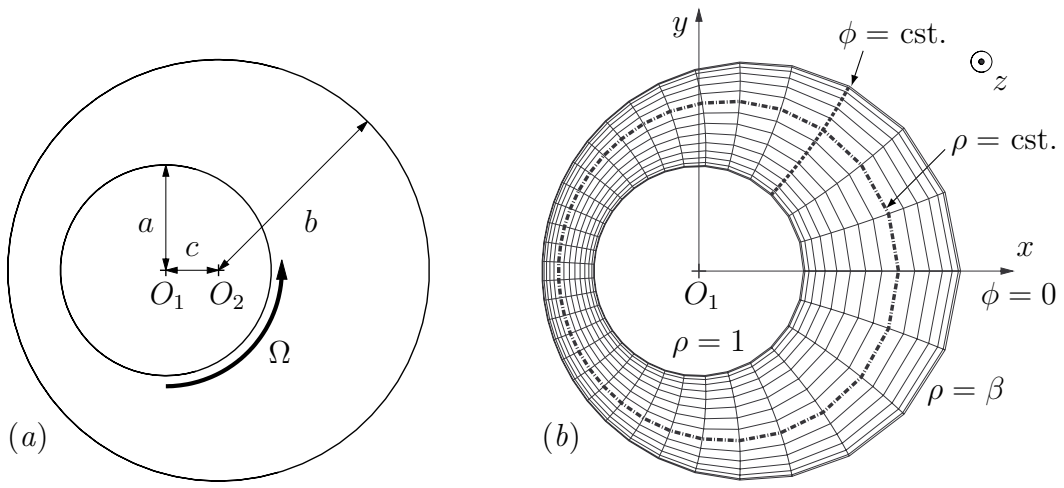

Figure 4.1 – Eccentric annular domain for radius ratio $\eta = 0.5$ and eccentricity $e = 0.5$. (a) Geometry definition. (b) Typical bipolar mesh used for calculations with $M + 1 = K = 16$.

components $\mathbf{u}_\perp = \mathbf{u} - w\mathbf{e_z}$ perpendicular to the axis are decoupled from the axial component w. Letting the subscript '$\perp$' denote projection perpendicular to $\mathbf{e_z}$, $\mathbf{u}_\perp$ satisfies

$$\left.\begin{aligned} \partial_t \mathbf{u}_\perp + \mathbf{u}_\perp \cdot \nabla_\perp \mathbf{u}_\perp &= -\nabla_\perp p + Re_\Omega^{-1} \nabla_\perp^2 \mathbf{u}_\perp, \\ \nabla_\perp \cdot \mathbf{u}_\perp &= 0. \end{aligned}\right\} \tag{4.2}$$

Steady solutions of (5.2), with boundary conditions, yield 'in-plane' components $\mathbf{U}_\perp$ of basic flows, denoted hereon as $\mathbf{U} = (\mathbf{U}_\perp, W)$. Basic axial velocity can then be calculated by simply solving a linear system

$$\mathbf{U}_\perp \cdot \nabla_\perp W = -G + Re_\Omega^{-1} \nabla_\perp^2 W, \tag{4.3}$$

with G the imposed axial pressure gradient. Wood (1957)'s modified bipolar coordinate system (ρ, ϕ), fitting the annular domain (see figure 4.1) with the following conformal transformation, is appropriate for the present configuration

$$x + \mathrm{i}y = \frac{1}{\delta} \frac{\rho \mathrm{e}^{\mathrm{i}\phi} + \gamma}{1 + \gamma\rho \mathrm{e}^{\mathrm{i}\phi}}, \tag{4.4}$$

with constants γ and β depending on the geometry through δ and e

$$\gamma = \left\{ \left(\frac{2 + \delta(1 - e^2)}{2e} \right)^2 - 1 \right\}^{1/2} - \frac{2 + \delta(1 - e^2)}{2e} \text{ if } e \neq 0, \text{ else } \gamma = 0, \tag{4.5}$$

$$\beta = \frac{1 + \delta(1 + e) - \gamma}{1 - \gamma(1 + \delta(1 + e))}. \tag{4.6}$$

Unlike classical bipolar coordinates, this system is non-singular in the concentric limit, allowing computations in the axisymmetric case. Local orthogonality ensures separation of the variables in the expression of the Laplacian operator. An additional transformation maps the non-dimensional 'pseudo-radius' $1 \leq \rho \leq \beta$ to $-1 \leq \xi \leq 1$,

with $\xi = (2\rho - \beta - 1)/(\beta - 1)$. In the local frame, in-plane velocity is decomposed as $\mathbf{u}_\perp = u\mathbf{e}_\xi + v\mathbf{e}_\phi$. Expressions for operators in equations (5.2-5.3), written in the (ξ, ϕ) coordinate system, are given in the Appendix.

Linear stability theory predicts the behaviour of small-amplitude perturbations $\mathbf{q}'(\xi, \phi, z, t) \equiv (u', v', w', p')^T$ superimposed on the basic flow, $\mathbf{Q}(\xi, \phi) \equiv (U, V, W, P)^T$.The system being homogeneous along the axial direction z, small perturbations can be written in normal-mode form

$$\mathbf{q}'(\xi, \phi, z, t) = \tilde{\mathbf{q}}(\xi, \phi) \exp[\mathrm{i}(kz - \omega t)]. \tag{4.7}$$

As usual in temporal stability analyses, the axial wavenumber k is real, and the frequency is a complex number $\omega = \omega_\mathrm{r} + \mathrm{i}\omega_\mathrm{i}$. The *phase speed* $c \equiv \omega_\mathrm{r}/k$ characterises axial propagation, and the *growth rate* ω_i indicates temporal growth/decay (resp. $\omega_\mathrm{i} > 0$ and $\omega_\mathrm{i} < 0$). Linearizing the Navier–Stokes equations about the basic flow and using the normal-mode form (4.7) gives the system of differential equations $\mathrm{A}\tilde{\mathbf{q}} = \mathrm{i}\omega\mathrm{B}\tilde{\mathbf{q}}$, expressed in the (ξ, ϕ) coordinate system as

$$\mathrm{A} = \begin{bmatrix} A_{11} & A_{12} & 0 & D_\xi \\ A_{21} & A_{22} & 0 & D_\phi \\ D_\xi W & D_\phi W & A_{33} & \mathrm{i}k \\ D_\xi + A & D_\phi - B & \mathrm{i}k & 0 \end{bmatrix}, \ \mathrm{B} = \begin{bmatrix} 1 & 0 & 0 & 0 \\ 0 & 1 & 0 & 0 \\ 0 & 0 & 1 & 0 \\ 0 & 0 & 0 & 0 \end{bmatrix}, \tag{4.8}$$

$$\left.\begin{aligned} A_{11} &= (UD_\xi + D_\xi U) + V(D_\phi - B) + \mathrm{i}kW - Re_\Omega^{-1}(\nabla_\perp^2 - k^2 + C), \\ A_{22} &= (VD_\phi + D_\phi V) + U(D_\xi + A) + \mathrm{i}kW - Re_\Omega^{-1}(\nabla_\perp^2 - k^2 + C), \\ A_{33} &= (UD_\xi + VD_\phi) + \mathrm{i}kW - Re_\Omega^{-1}(\nabla_\perp^2 - k^2), \\ A_{12} &= -2AV + (D_\phi - B)U + 2Re_\Omega^{-1}\left(AD_\phi + BD_\xi\right), \\ A_{21} &= 2BU + (D_\xi + A)V - 2Re_\Omega^{-1}\left(AD_\phi + BD_\xi\right). \end{aligned}\right\} \tag{4.9}$$

D_ξ, D_ϕ are differential operators given in the Appendix, together with the spatially dependent factors A, B and C. At the walls, impermeability $u = 0$, no-slip $v = w = 0$ and incompressibility $D_\xi u = 0$ conditions apply. For each value of k, the solution of this eigenvalue problem yields a spectrum of temporal modes $\omega = \Omega(k; \eta, e, Re_z, Re_\Omega)$. The *critical azimuthal Reynolds number* is such that the mode with largest growth rate is at most *neutrally stable* ($\omega_{\mathrm{i,max}} = 0$). The value of k for which it is neutrally stable is called *critical wavenumber*.

The eigenvalue problem is invariant under complex conjugation (denoted by $\star$) $(k, \omega, \tilde{\mathbf{q}}) \mapsto (-k, -\omega^\star, \mathbf{q}^\star)$, so only $k > 0$ need be considered. In the absence of axial flow, the problem is also invariant to axial reflection, implying, with conjugation symmetry, that the spectrum is symmetric with respect to the imaginary axis ($\omega \mapsto -\omega^\star$). When axial flow is added, mirror symmetry of the system in the axial direction and the resulting symmetry of the spectrum is lost.

4.2.2 Numerical method

A spectral decomposition of the fields was implemented, as in Oikawa et al. (1989a) and Chawda and Avgousti (1996), using a Fourier–Chebyshev decomposition

$$\mathbf{u}(\xi,\phi) = \sum_{i=0}^{M} \sum_{j=-K}^{K} \hat{\mathbf{u}}_{ij} \mathrm{e}^{\mathrm{i}j\phi} T_i(\xi), \tag{4.10}$$

with T_i the Chebyshev polynomial of order i. A pseudospectral collocation method is used in the pseudo-radial direction, using a Gauss–Lobatto distribution $\xi_i = \cos[i\pi/M]$, with $0 \leq i \leq M$. K is the number of Fourier components, corresponding to $N = 2K+1$ points on the physical grid (figure 4.1), after inverse discrete Fourier transform.

Steady solutions $\mathbf{U}_\perp$ of (5.2) are calculated using a time-marching procedure, then the axial flow W is obtained by solving the linear system (5.3). Thanks to linearity of (5.3) with respect to W, the axial pressure gradient G is just a multiplying factor on the axial velocity, so G can be set to 1 without loss of generality. W is then rescaled to yield the required axial Reynolds number Re_z.

Integration of (5.2) is performed using a projection method enhanced with a preliminary pressure-prediction step (Goda (1979), Raspo et al. (2002)). A simple and robust first-order temporal scheme is used since only steady solutions are of interest here. The stiff viscous terms of the vectorial Laplacian operator involving the scalar Laplacian $\nabla^2_\perp$ (see the Appendix) are treated implicitly, while all other terms are extrapolated from the previous time step. The Poisson and Helmholtz problems involve block pentadiagonal matrices, and are efficiently solved using the Thomas algorithm. The choice of time step was automated in order to achieve convergence. When velocity residuals in the physical space $\max_{i,j} |u^n_{i,j} - u^{n-1}_{i,j}|$ or $\max_{i,j} |v^n_{i,j} - v^{n-1}_{i,j}|$ diverged, the time step was divided by 2: resulting time steps ranged from 1 for the concentric case to 10^{-2} for $Re_\Omega = 250$, $e \geq 0.8$, and $M+1 = K = 32$. The convergence tolerance on the residuals was set to 10^{-8}.

Approximating normal modes (4.7) with the same Fourier–Chebyshev expansion as the basic flow leads to a generalised eigenvalue problem, with matrix versions of linear operators (4.8)–(4.9), of size $4N(M+1)$. This generalized eigenvalue problem can be reduced to a standard eigenvalue problem $\mathsf{A}_1\tilde{\mathsf{q}}_1 = \mathrm{i}\omega\tilde{\mathsf{q}}_1$ of size $2N(M-2)$, after eliminating w, p, and boundary points of u and v. The reduction is performed numerically and allows significant time savings in full spectrum calculation, as well as avoiding spurious eigenvalues. A similar approach seems to have been used in Oikawa et al. (1989a).

Full spectrum computations were performed using the standard QR procedure available in the free software package LAPACK (www.netlib.org/lapack). When the region of interest in the spectrum was known beforehand, we used the Arnoldi (1951) method to compute a few eigenvalues efficiently. The shift-invert spectral transformation was used to enhance convergence, where the initial problem was replaced by $(\mathsf{A}_1 - \sigma\mathsf{I})^{-1}\tilde{\mathsf{q}}_1 = \nu\tilde{\mathsf{q}}_1$. The eigenvalues $\nu = 1/(\lambda - \sigma)$ of largest magnitude give the corresponding eigenvalues $\lambda = \mathrm{i}\omega$ of the original problem closest to the given shift σ. The eigenvectors $\tilde{\mathsf{q}}_1$ of the new problem are those of the initial one. The method requires solving linear systems involving the non-sparse matrix $\mathsf{A}_1 - \sigma\mathsf{I}$, which is factorized in LU form in an initialisa-

tion step. The calculations were performed using the ARPACK++ class for non-sparse matrices (www.caam.rice.edu/software/ARPACK), based on LAPACK routines.

For a given mode, *critical curves* were calculated using a Newton–Raphson iteration: k and Re_Ω were varied simultaneously so as to reach $|\omega_\mathrm{i}|$ and $|\partial_k \omega_\mathrm{i}|$ less than 10^{-6}. Initial estimates for the critical k and Re_Ω were obtained by linear extrapolation with respect to Re_z. Identification of the most unstable modes is discussed in §4.2.5.

4.2.3 Spatial resolution

A systematic grid refinement study was performed for the basic flow with $16 \leq M+1 \leq 64$ and $0 \leq K \leq 128$ ($K = 0$ for $e = 0$), for $e \leq 0.99$ and $Re_\Omega \leq 250$. The minimal resolution achieving convergence of 6 significant digits of a number of integral quantities (forces and torque on inner cylinder, Fanning friction factor $f \equiv d|G|/(1/2\rho\overline{W}^2)$, azimuthal volume flux) was found for each set of parameters, and used for the computations in §4.2.4. It appears that refining the number of collocation points much above $m = 32$ is unnecessary for $Re_\Omega \leq 250$, and the dependence on eccentricity is weak. On the other hand, if eccentricities close to 1 are considered, a large number of Fourier modes is required as ϕ varies extremely slowly in the wide gap then. For $e = 0.98$ and $Re_\Omega = 223.61$, a resolution of $(M+1) \times K = 32 \times 128$ achieves excellent results, as can be seen in figure 4.2, showing a comparison with Escudier et al. (2000)'s calculations.

In parametric stability analyses though (§4.3 & §4.4), a fixed resolution of $M + 1 = K = 16$ was systematically used for both basic flow and normal modes, for practical reasons and computational cost. Tests were performed *a posteriori* to check that these values provided reliable results, and are reported in table 4.1. With the chosen resolution, 3 significant digits of the critical Re_Ω are converged in most cases. However, larger inaccuracies occur for high e and Re_z, and critical curves are truncated below $Re_\Omega = 200$ (resp. $Re_\Omega = 250$) for $\eta = 0.5$ (resp. $\eta = 0.89$), as remeshing above this limit becomes quickly prohibitive.

4.2.4 Basic flow

The most striking feature of the basic flow is the occurrence of a recirculation eddy for eccentricities larger than a certain threshold value of about 0.3 for $\eta = 0.5$ (see figure 5.3), which only depends weakly on Re_Ω. This behaviour, exists even for Stokes flow and Kamal (1966) was the first to study the influence of inertial effects. The recirculation is due to the adverse pressure gradient caused by the large expansion of annulus clearance, downstream the 'bottleneck' at $\phi = \pi$. Figure 4.4*(d)* represents the evolution of the azimuthal volume flux (per unit length) Q_ϕ with eccentricity, for $\eta = 0.5$ and azimuthal Reynolds numbers Re_Ω up to 250. Q_ϕ is obtained by integration of the azimuthal velocity along the radial path $\phi = 0$ joining the cylinders. As the inner cylinder gets closer to the outer one, the azimuthal flow becomes progressively 'choked', and Q_ϕ seems to be controlled by the smaller gap width. Indeed, the flow in the vicinity of the inner cylinder resembles a circular Couette flow of clearance ratio controlled by the smaller gap, while the wide gap region hosts a low velocity recirculation zone contributing no net azimuthal volume flux. A comparison is made with the value of Q_ϕ in the Stokes régime, using

	e	0.5				0.6				0.7			
	$(M+1)\times K$	16×16		32×32		16×16		32×32		16×16		32×32	
η	Re_z	Re_Ω	k	Re_Ω	k	Re_Ω	k	Re_Ω	k	Re_Ω	k	Re_Ω	k
0.5	50	127.41	3.34	127.41	3.35	147.52	3.45	147.52	3.45	184.99	4.26	185.13	4.23
	100	151.61	3.17	151.63	3.17	171.59	2.67	171.76	2.69	212.78	3.21	213.19	3.20
	150	156.73	2.86	156.76	2.86	187.61	2.76	188.25	2.76	231.15	2.57	230.28	2.77
	180	156.91	2.78	157.02	2.79	191.58	2.53	191.94	2.58	238.15	2.94	243.96	3.02
	200	156.15	2.53	156.28	2.54	194.73	2.42	193.98	2.49	237.85	2.74	246.89	2.91
0.8907	32	247.82	2.98	247.82	2.98	–	–	–	–	–	–	–	–
	50	296.19	2.74	296.20	2.74	–	–	–	–	–	–	–	–
	17	–	–	–	–	247.40	3.40	247.46	3.40	–	–	–	–
	30	–	–	–	–	283.26	3.11	284.04	3.13	–	–	–	–

Table 4.1 – Resolution tests for $\eta = 0.5$ and $\eta = 0.8907$, with $(M+1)\times K = 16\times 16, 32\times 32$. Critical Re_Ω and k are given for various e and Re_z.

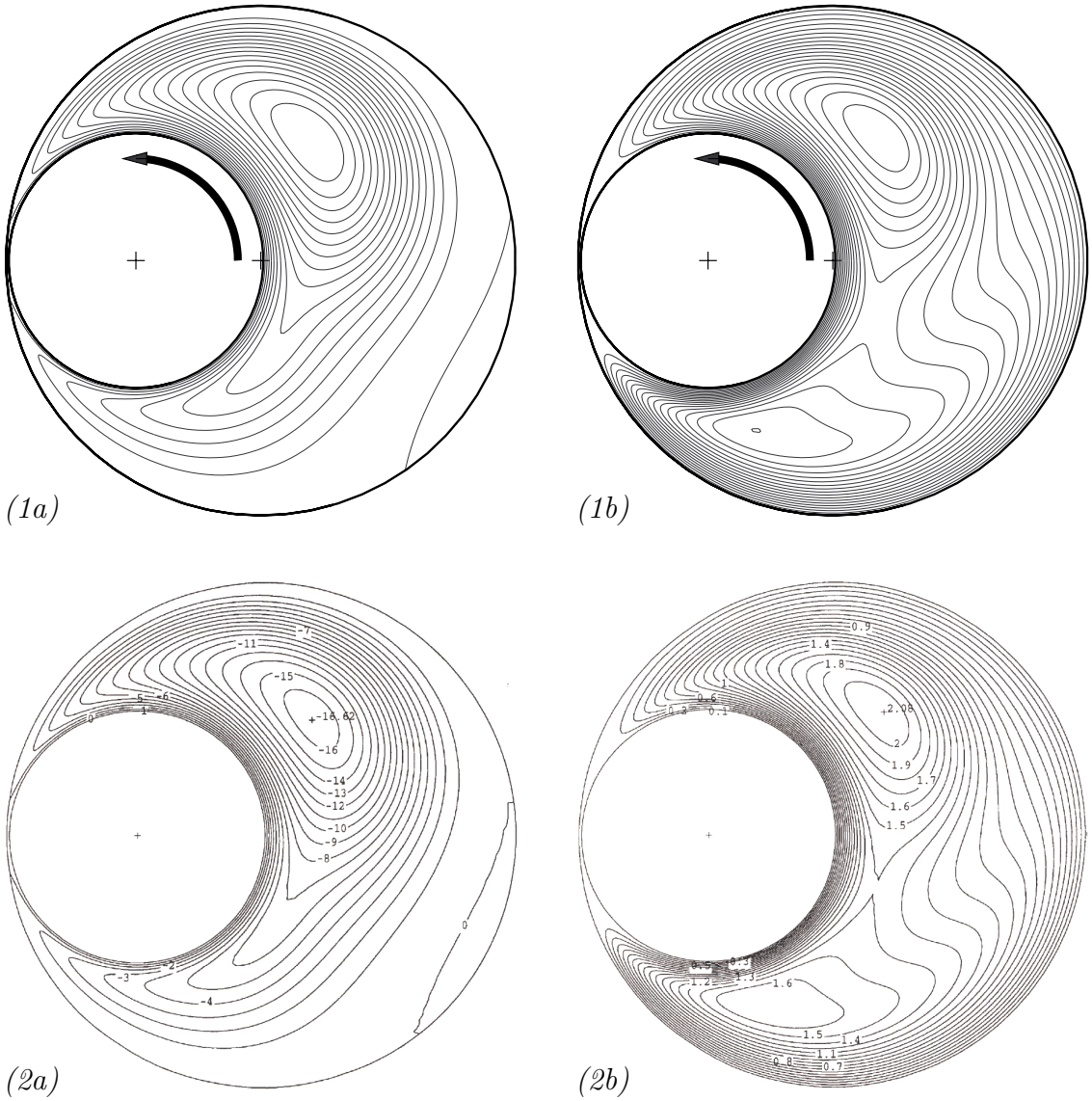

Figure 4.2 – Basic flow for $\eta = 0.5$, $e = 0.98$ and $Re_\Omega = 223.61$: *(1)* present calculation using $(M + 1) \times N = 32 \times 257$ ($K = 128$), *(2)* Escudier et al. (2000) with a 40×256 grid. *(a)* streamlines, *(b)* isolines of axial velocity normalized by mean velocity $\overline{W}$. The calculation recovers the secondary recirculation region in the wide gap and the two distorted maxima in axial velocity. The numerical values of the isolines match those of Escudier et al. (2000).

Wannier (1950)'s exact formula for the in-plane stream function. Inertial effects only have a weak impact on Q_ϕ, which could be expected from the fact that the fluid is entrained in rotation by viscous forces.

Maximum axial velocity occurs in the wide gap region. Indeed, in the absence of rotation, eccentric annular Poiseuille flow is nearly parabolic in the pseudo-radial direction, and for any fixed value of ϕ, the maximum velocity scales as the 'local clearance' squared. However, the position of maximum axial velocity is not exactly located at $\phi = 0$, because of convective transport of W by crossflow components $\mathbf{U}_\perp$ (see equation

(5.3)). In fact, these nonlinear effects distort the whole flowfield, and Escudier et al. (2000) performed a thorough computational/experimental analysis of the effects of eccentricity and inner-cylinder rotation, on annular Poiseuille flow. At low eccentricity, the maximum axial velocity was shown to be advected towards the narrowing-gap region, inducing a slight increase in Fanning friction factor (defined in §4.2.3) with e. For moderate eccentricities $0.3 \leq e \leq 0.8$, the maximum moves back to the wide-gap region, with a subsequent decrease in friction factor. For larger eccentricities, the maximum is located in the diverging-gap region, and the friction factor increases again. At very high eccentricities and rotation rates, a second peak in axial velocity appears in the wide gap, while a secondary recirculation is observed at the outer cylinder wall. This complex pattern is successfully obtained with our code, as illustrated in figure 4.2.

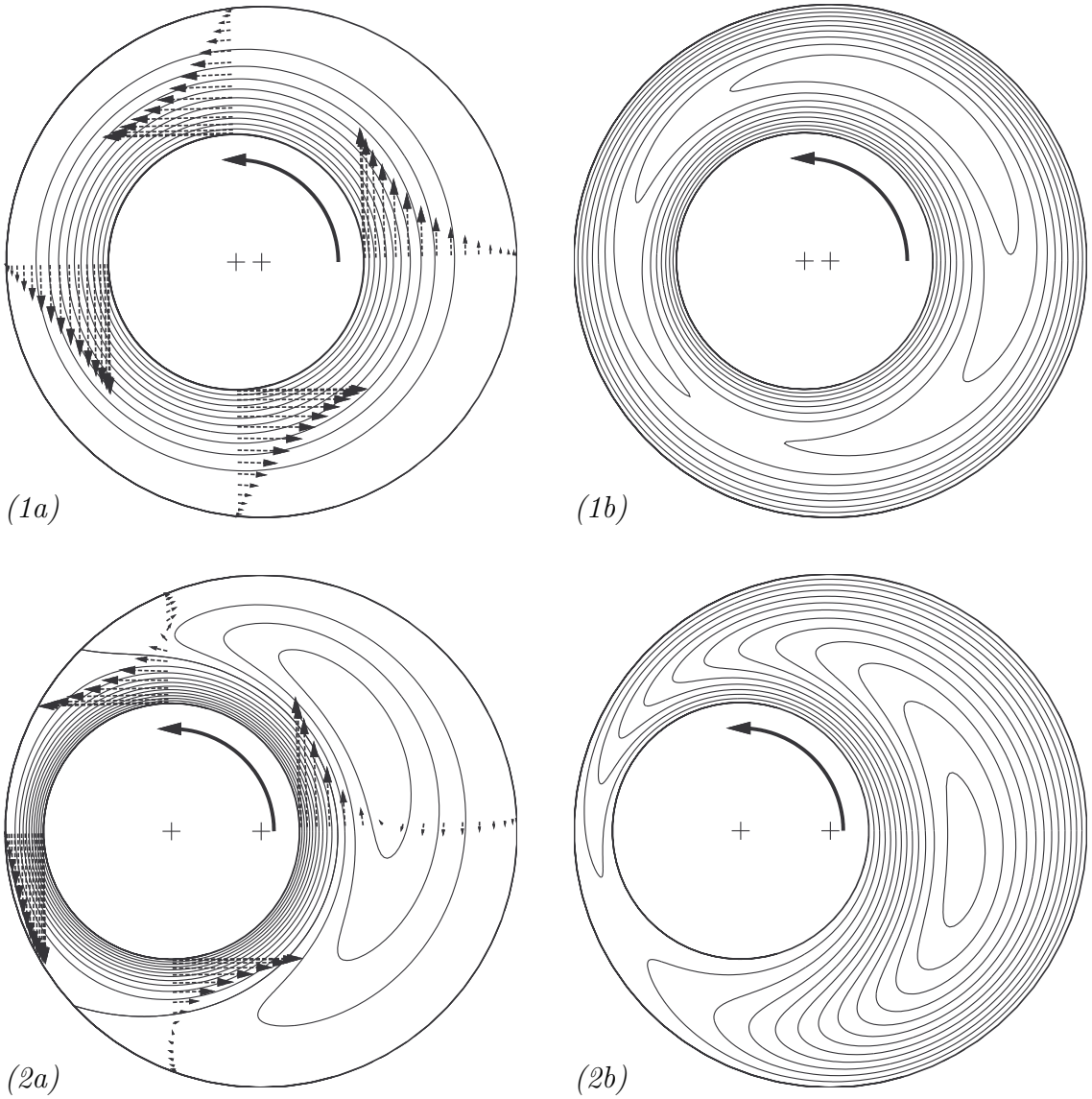

Figure 4.3 – Basic flows for $\eta = 0.5$, $Re_\Omega = 100$: *(1)* weak eccentricity $e = 0.2$, *(2)* high eccentricity $e = 0.7$. *(a)* Contours of equispaced in-plane streamfunction with superimposed in-plane velocity profiles at $\theta = 0, \pi/2, \pi, 3\pi/2$ (polar angle with respect to the inner cylinder). *(b)* Equispaced contours of axial velocity.

Forces on the inner cylinder can be easily computed by integration of the pressure and viscous stresses at the wall. The expression of the strain tensor components in our coordinate system are given in the Appendix. Figure 4.4 shows a systematic study of the effect of Re_Ω and e on the loads, for $\eta = 0.5$. A comparison is made with the Stokes régime, using analytical formulas derived by Wannier (1950). In this limit, the velocity and pressure distributions are anti-symmetric with respect to the symmetry plane of the annulus. Therefore, the x-component of the force is exactly 0. At the inner cylinder surface, the pressure increases with ϕ on the wide gap side up to $0 < \phi_{\max} < \pi$, and decreases on the small gap side up to $\phi_{\min} = -\phi_{\max}$. As e increases, the pressure extrema both tend to the same limit $\phi_{\min/\max} \to \pi$. Because $0 < \phi_{\max} < \pi$, the y-component of the force F_y is negative. The viscous torque T is obviously opposed to the sense of rotation, so $T < 0$. In the Stokes limit, T and F_y both scale as Re_Ω^{-1}. Indeed, the torque T is induced by shear stresses τ, which scale as $\tau \sim \mu \mathrm{V/L}$ in dimensional form, with μ the dynamic viscosity. Non-dimensionalising with respect to the pressure scale $\mathrm{P} \equiv \rho \mathrm{V}^2$, one obtains $T \sim \tau \sim Re_\Omega^{-1}$. In the absence of inertial terms, the pressure P also scales as τ, so $F_y \sim P \sim \tau \sim Re_\Omega^{-1}$.

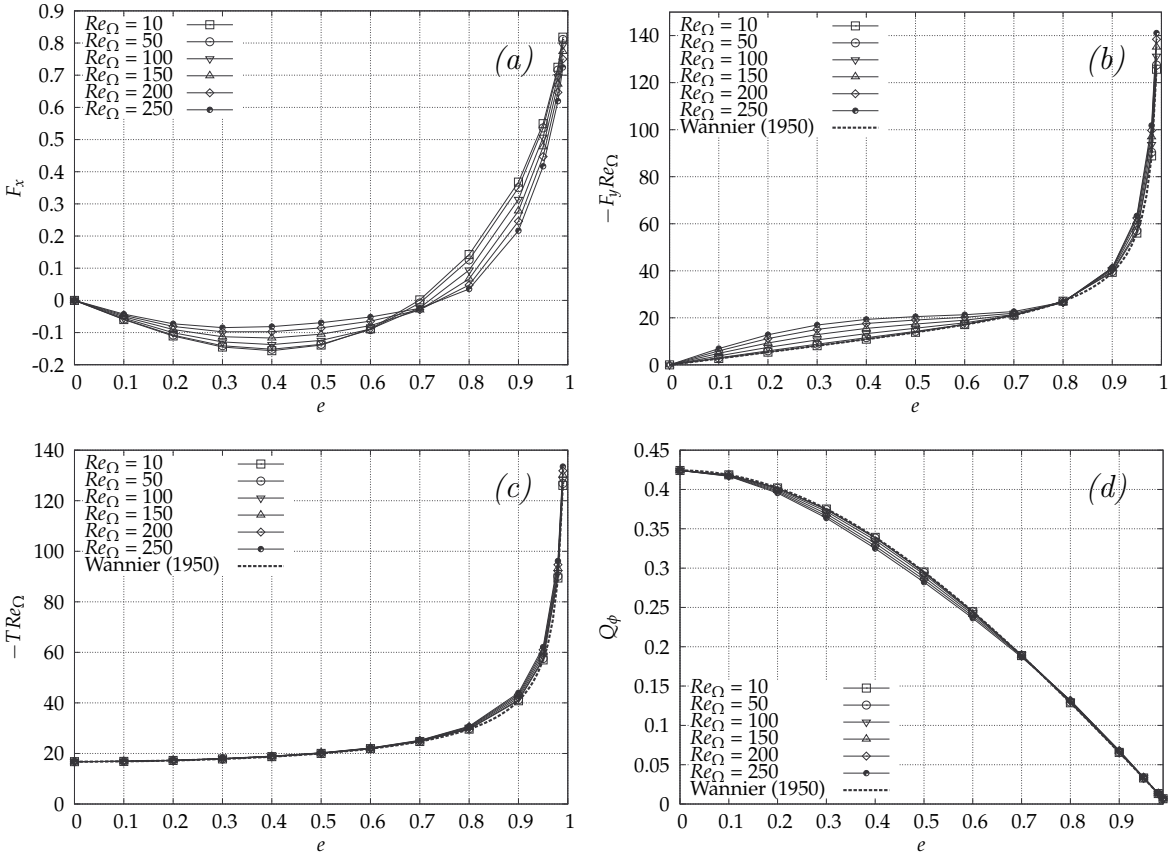

Figure 4.4 – Forces, torque and azimuthal flow rate (per unit length) for $e = 0, \ldots, 0.7$ and $Re_\Omega = 10, \ldots, 250$. *(a)* x-component F_x, *(b)* y-component F_y of the force on the inner cylinder. *(c)* torque T on inner cylinder. *(d)* azimuthal flow rate Q_ϕ. Dotted lines in *(b),(c)* and *(d)* correspond to the exact value in the Stokes régime, taken from Wannier (1950).

When inertial effects are added, this scaling still holds and only small deviations

to the Stokes limit are observed. Larger variations occur for an eccentricity of about $0.3 - 0.4$, where the value of $F_y Re_\Omega$ at $Re_\Omega = 250$ is almost twice the purely viscous one. At $e \approx 0.8$, variations of $F_y Re_\Omega$ with Re_Ω are almost non existent. Similarly, the formula for the torque in the Stokes régime applies quite robustly for all the range of eccentricities and Re_Ω up to 250. Again, this close agreement is attributed to the fact that the flow in the vicinity of the inner cylinder is similar to a circular Couette flow where inertial effects are weak (and non existent in the purely axisymmetric case). For e close to 1, F_y and T increase sharply because of lubrication effects.

When $Re_\Omega \neq 0$, the flow anti-symmetry is broken, and F_x is non-zero. For low eccentricities, F_x is negative, but for high e, F_x is negative, as expected from lubrication theory. The change of sign of F_x is located about a critical eccentricity of $e \approx 0.7 - 0.75$ for $\eta = 0.5$ and $Re_\Omega \leq 250$, as already discussed by Feng et al. (2007) and Podryabinkin and Rudyak (2011). Small eccentricity perturbations about this point tend to push the inner cylinder back to its initial position. However, pressure-induced precession prevents any stable equilibrium for this value of eccentricity, explaining the complex motion of drillstrings in wellbores. The intensity of F_x is determined by the magnitude of the convective term, so the pressure scaling $\mathrm{P} \equiv \rho \mathrm{V}^2$ is appropriate in this case.

4.2.5 Critical modes

The first step of linear stability analysis is to identify a reduced set of leading modes, with largest growth rates. Full spectrum computations were used to find the most unstable eigenvalue at each point of a coarse grid in (e, Re_Ω, Re_z), for $\eta = 0.5$. k was varied between 1 and 7, a range containing all the critical wavenumbers for the concentric case with $Re_z \leq 200$ ($1.5 \lesssim k \lesssim 4.5$ from the graph in Cotrell and Pearlstein (2004)), with large steps of 0.5 for computational efficiency. Approximate critical curves were obtained, and it was found that the modes at criticality are always either propagating 'Taylor-like' vortices or deformed left-handed helical modes. These pseudo-toroidal and pseudo-helical modes correspond to the same family of critical modes found in Taylor–Couette–Poiseuille flow (Takeuchi and Jankowski, 1981), but distorted by eccentricity (cf. figure 4.10). In the axisymmetric case, these modes can be assigned an integer azimuthal wavenumber m corresponding to a normal-mode decomposition of the form $\mathbf{q}' = \tilde{\mathbf{q}}(r) \exp[\mathrm{i}(kz + m\theta - \omega t)]$, using the usual cylindrical coordinates (r, θ, z). Considering $k > 0$, $m = 0$ correspond to Taylor vortices and $m > 0$ (resp. $m < 0$) are left-handed (resp. right-handed) helical vortices, with helicity opposed to (resp. matching) that of the basic flow. Following these modes by continuity, pseudo-helices are also assigned a 'pseudo-azimuthal wavenumber' equal to the corresponding value of m in the concentric case. Henceforth, TV will denote 'Taylor-like' vortices while LH$|m|$ and RH$|m|$ will correspond to left- (resp. right-) handed helical vortices of order m. The symmetry of the spectrum for $Re_z = 0$ implies that LH and RH of equal order m, have the same growth rate and oppositely signed phase speeds. As Re_z is increased, LH modes become more unstable than TV and RH, and form the family of critical modes, as in the axisymmetric case (cf. figure 4.5). The critical value of m increases steadily with Re_z.

Additional families of modes such as wall modes related to a shear instability mechanism were not found to be critically unstable in the range of parameters considered. Center modes of *Sp* type, such as described by Merzari et al. (2008), and critical in

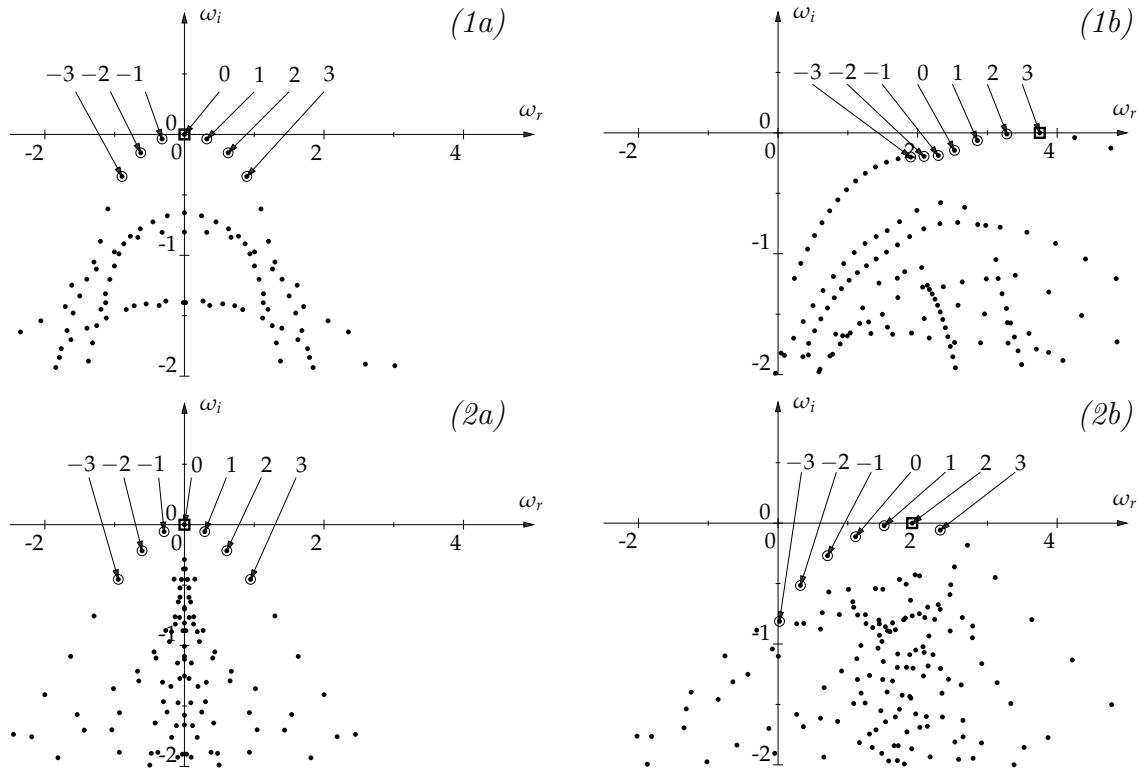

Figure 4.5 – Spectra of eigenvalues $\omega = \Omega(k; e, Re_\Omega, Re_z)$ with (k, Re_Ω) at critical conditions. Rows: *(1)* $e = 0$, *(2)* $e = 0.5$. Columns: *(a)* $Re_z = 0$, *(2)* $Re_z = 50$. Numbers indicate the azimuthal wavenumber m of the eigenmode (or pseudo-wavenumber if eccentric). Positive ω_i indicates instability. Positive (negative) m correspond to left-(right-)handed helix-like modes. The eigenvalue in the square box corresponds to the most unstable mode.

highly eccentric annular Poiseuille flow for high values of Re_z, were not found to be critical in our configuration either.

In axisymmetric Taylor–Couette–Poiseuille flow with $\eta = 0.5$, the maximum value of m at criticality is 7 (Cotrell and Pearlstein, 2004). Hence, in the subsequent parametric study at $\eta = 0.5$ (§4.3), critical curves were calculated for TV, LH modes with $m \leq 7$, and RH of order 1 and 2 as a check.

4.2.6 Validation

Extensive validation of basic flow and stability calculations have been performed. In the Stokes limit $Re_\Omega \ll 1$, Wannier (1950) derived analytical expressions for torque and forces on the inner cylinder, that were matched by our code up to machine precision. Using his analytical solution of the stream function, azimuthal volume flux Q_ϕ calculations were also successfully validated. Escudier et al. (2000) provided fourth-order accurate values of the Fanning friction factor (defined in §4.2.3) in the eccentric Taylor–Couette flow, for $10 \leq Re_\Omega \leq 223.61$ and eccentricities up to 0.98. The present numerical results all lay within 0.67% of their values. Feng et al. (2007) gave numerical values for the

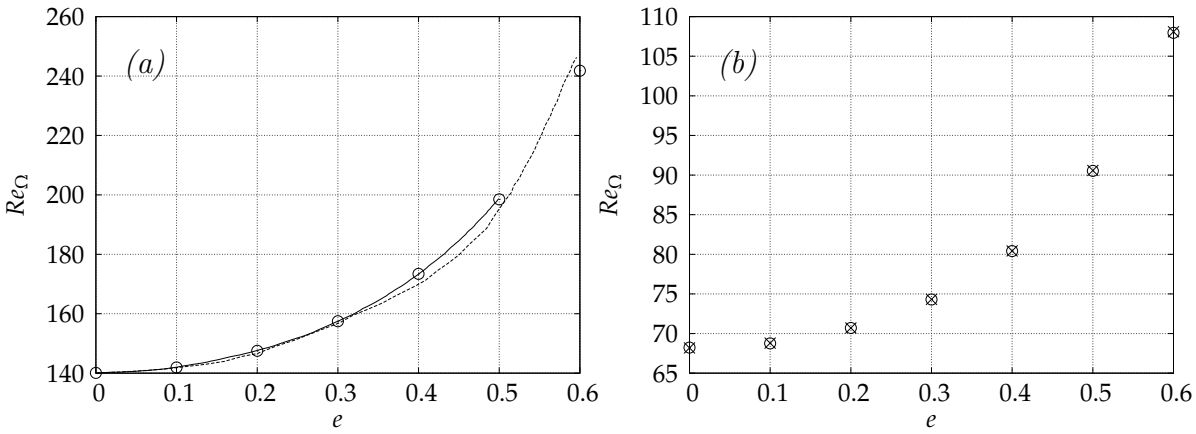

Figure 4.6 – Validation of critical azimuthal Reynolds number Re_Ω against eccentricity e. *(a)* $\eta = 0.912$, $k = 3.17$, solid line: Chawda and Avgousti (1996), dotted line: Dai et al. (1992), ∘: present calculation. *(b)* $\eta = 0.5$, ×: Oikawa et al. (1989a), ∘: present calculation.

pressure and stress contributions to the x and y components of the force on the inner cylinder for $Re_\Omega = 125$ and eccentricities up to $e = 0.98$. For these parameters, our calculations match their results, with less than 1.80% of relative difference, and 0.76% on average when at least 4 significant digits were provided by the authors.

In the axisymmetric configuration with axial throughflow, Takeuchi and Jankowski (1981) performed the first numerical prediction of the critical curves for Re_z up to 100. In their article, they provide data for the critical values of Re_Ω, k, and wave speed $c = \omega_\mathrm{r}/k$ for $Re_z = 0, 10, \ldots, 100$. The critical values are exactly matched by our code in all cases except for $Re_z = 90$, where only the last significant digit given by the authors for k and c differs from our values by one.

In the eccentric configuration with no axial flow, Oikawa et al. (1989a) reported a critical azimuthal Reynolds number of 307.59 for an axial wavenumber of 4.126 and $\delta = 0.1$, $e = 0.7$. With the same spatial resolution $(M + 1) \times K = 21 \times 24$, our corresponding critical values are $Re_\Omega = 307.71$ and $k = 4.127$, which gives relative errors of 0.04% and 0.02% respectively. Additional tests were performed using a graph of critical Re_Ω versus eccentricity for $\eta = 0.5$ from a second article of Oikawa et al. (1989b), and for $\eta = 0.912$ and $k = 3.17$ against graphical results from Chawda and Avgousti (1996) and Dai et al. (1992). Figure 4.6 shows excellent agreement with the data of Oikawa et al. (1989b), and Chawda and Avgousti (1996) who both used the same spectral decomposition of the modes as us. Values from Dai et al. (1992) are close, but discrepancies may be attributed to their relatively coarse meshing ($N = 16$ points only in the 'pseudo-azimuthal' direction) and the use of piecewise polynomials to approximate the fully nonlinear fields in their bifurcation analysis.

4.3 Parametric study for a wide gap $\eta = 0.5$

In this section, we give results for the case $\eta = 0.5$, representative of industrial configurations in oil drilling. A resolution of $M + 1 = K = 16$ allows satisfactory accuracy for $e \leq 0.7$ and Re_Ω, Re_z up to 200 as shown in the previous section.

4.3.1 Critical azimuthal Reynolds number

For an eccentricity of $e = 0.5$, figure 4.7*(a)* shows the critical curves of the TV ($m = 0$), LH ($m > 0$) and RH ($m < 0$) modes labeled from $m = -2$ to 5. The solid thick line indicates the stability boundary, switching from one m to the next as Re_z is increased. Similar behaviour was found in the axisymmetric case by Takeuchi and Jankowski (1981).

Similar results were obtained for all eccentricities and figure 4.7*(b)* superimposes on a single figure all the results concerning the stability boundary for $e = 0, 0.1, \ldots, 0.7$. The main result of this study is clear from this figure: eccentricity always has a stabilizing effect, regardless of axial advection. The origin of this stabilization, as hinted at by Karasudani (1987) for the eccentric Taylor–Couette flow without axial flow, seems to lie in the weakening of centrifugal effects by eccentricity. Indeed, as already mentioned in §4.2.4, azimuthal flow gets 'choked' with increasing eccentricity (see Q_ϕ in figure 4.4*(d)*), and the basic flow becomes similar to an axisymmetric Couette flow of clearance ratio δ' controlled by the small gap $\delta' \sim \delta(1 - e)$, next to a 'dead' recirculating flow zone. Decreasing the clearance ratio, or equivalently, increasing the radius ratio of a circular Couette flow, reduces curvature effects, and has a stabilising effect, as shown by DiPrima et al. (1984).

The effect of axial advection on the axisymmetric case is two-fold: first it stabilizes the Couette flow up to $Re_z = 61.08$ and then it slightly destabilizes it as Re_z is further increased, while maintaining the threshold above the value for $Re_z = 0$. The change in behaviour corresponds exactly to the intersection between the increasing critical curve corresponding to mode $m = 3$ and the decreasing curve for $m = 4$, hence maximal stability is achieved when the two modes exchange stability. The value of Re_z corresponding to the maximum in critical Re_Ω increases with eccentricity. Above $e = 0.5$, maximum stability occurs beyond $Re_z = 200$.

At fixed Re_z above 50, increasing eccentricity tends to select critical modes of lower m: the stabilizing effect of eccentricity is even more important for higher azimuthal wavenumbers. On the contrary, at small Re_z, eccentricity favours the dominance of the LH1 over TV. For large enough eccentricities, one can expect helices with $m = 1$ to dominate TV even without axial flow. In the absence of axial flow, this feature was found experimentally by Vohr (1968) ($\delta = 0.099$ and $e > 0.707$) and Karasudani (1987) ($\eta = 0.83$, $e > 0.6$). Oikawa et al. (1989a) found a complex conjugate pair of eigenvalues $\lambda = \mathrm{i}\omega$ at criticality for $\delta = 0.1$, $e = 0.7$ (LH & RH), confirming numerically Vohr (1968)'s findings.

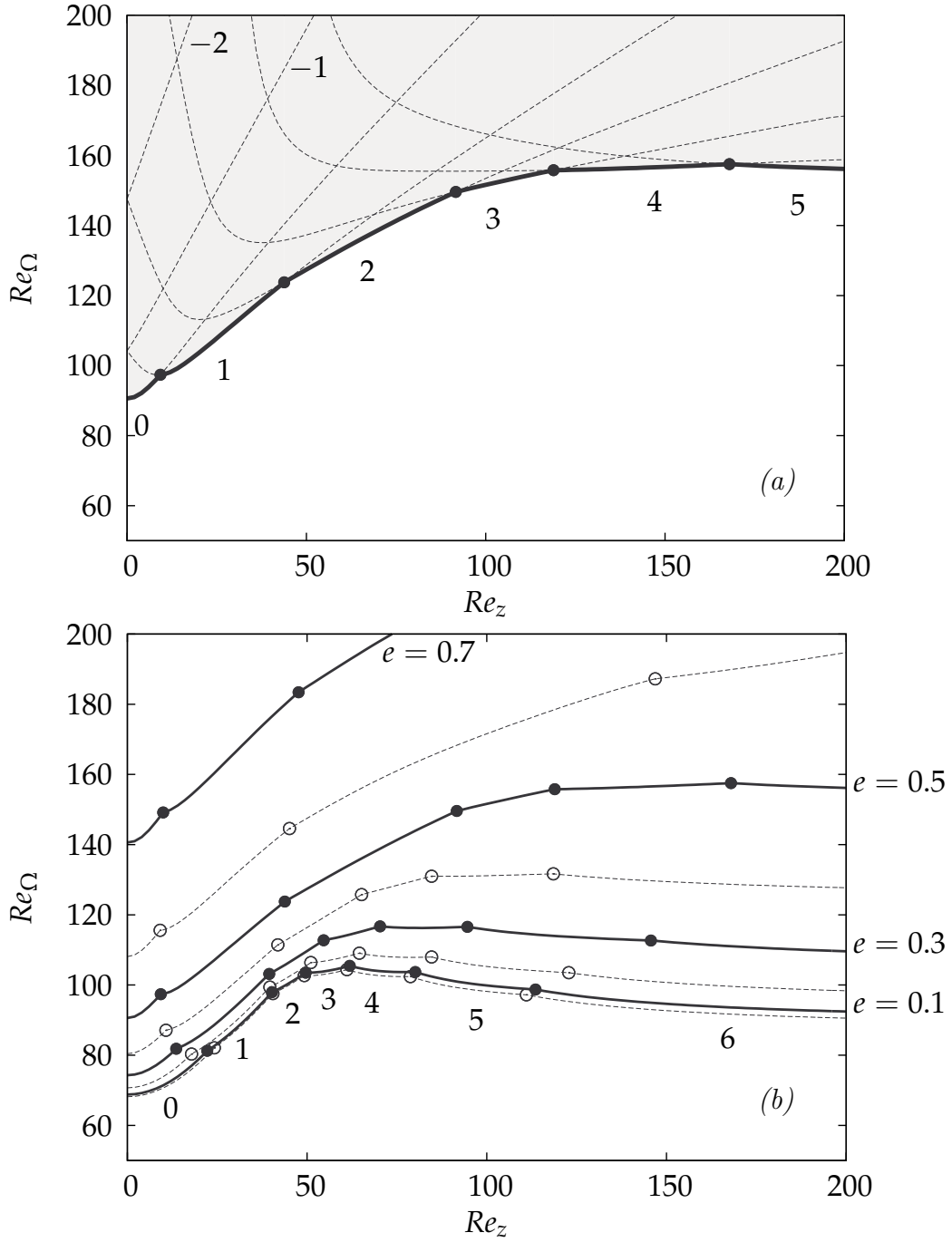

Figure 4.7 – *(a)* Critical curves $Re_\Omega = f(Re_z)$ for $e = 0.5$ and modes $m = -2, \ldots, 5$. The thick solid line indicates the instability threshold taking into account all the modes. The shaded area corresponds to instability. *(b)* Solid (resp. dotted) lines: critical curves taking into account all the modes, for $e = 0.1, 0.3, 0.5, 0.7$ (resp. $e = 0, 0.2, 0.4, 0.6$). In both *(a)* and *(b)*, filled/open circles indicate a switch in critical m, and the associated 'pseudo-azimuthal' wavenumber is indicated by annotation.

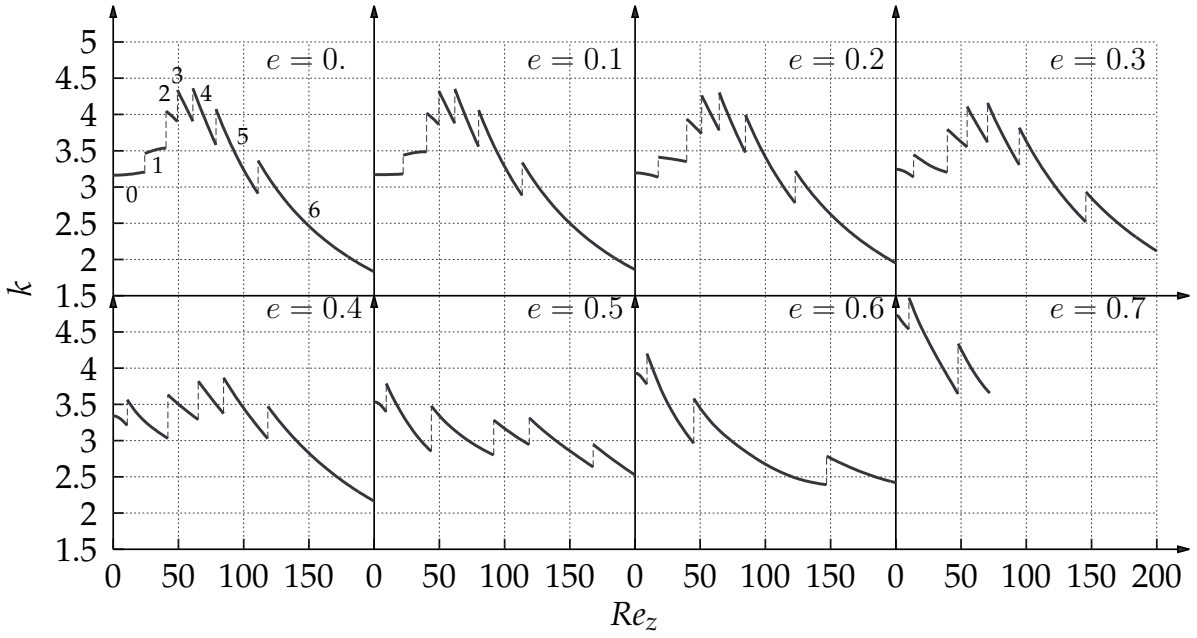

Figure 4.8 – Critical wavenumber k against axial Reynolds number Re_z for eccentricities $e = 0, 0.1, \ldots, 0.7$. Discontinuities correspond to a switch in critical m (values indicated by annotation for $e = 0$).

4.3.2 Critical axial wavenumber

Figure 4.8 shows the evolution of the critical wavenumber. The curves display jumps at points where modes exchange stability, and these discontinuities always correspond to a positive jump in k. When axial flow is increased, k usually decreases as long as the critical mode doesn't switch. The order of magnitude of k is always the same regardless of eccentricity, and remains between 1.5 and 5, which indicates that the axial wavelength of the critical perturbations is always of the same order of magnitude as the clearance $d = b - a$. These observations may explain the pattern selection process: increasing Re_z tends to elongate the modes in the axial direction, so a switch to higher 'pseudo-azimuthal' wavenumber mode occurs to reach a vortical structure that better fits the annular domain, and is thus amplified faster.

4.3.3 Critical phase speed

Figure 4.9 shows the evolution of the phase speed at criticality. As in figure 4.8, the curves are discontinuous as critical m switches with increasing Re_z. The phase speed always remains between 0.6 times and twice the average axial velocity of the basic flow. It decreases with increasing Re_z for each mode, but discontinuities always correpond to a jump to a larger value. Interestingly, except for LH1 (LH with $m = 1$) at the point of stability exchange with TV, all the critical modes see their phase speed decrease with eccentricity, this effect being more noticeable for $e \geq 0.3$. Most critical pertubations propagate somewhat faster than the average axial flow velocity, but see their propagation hindered by increasing Re_z.

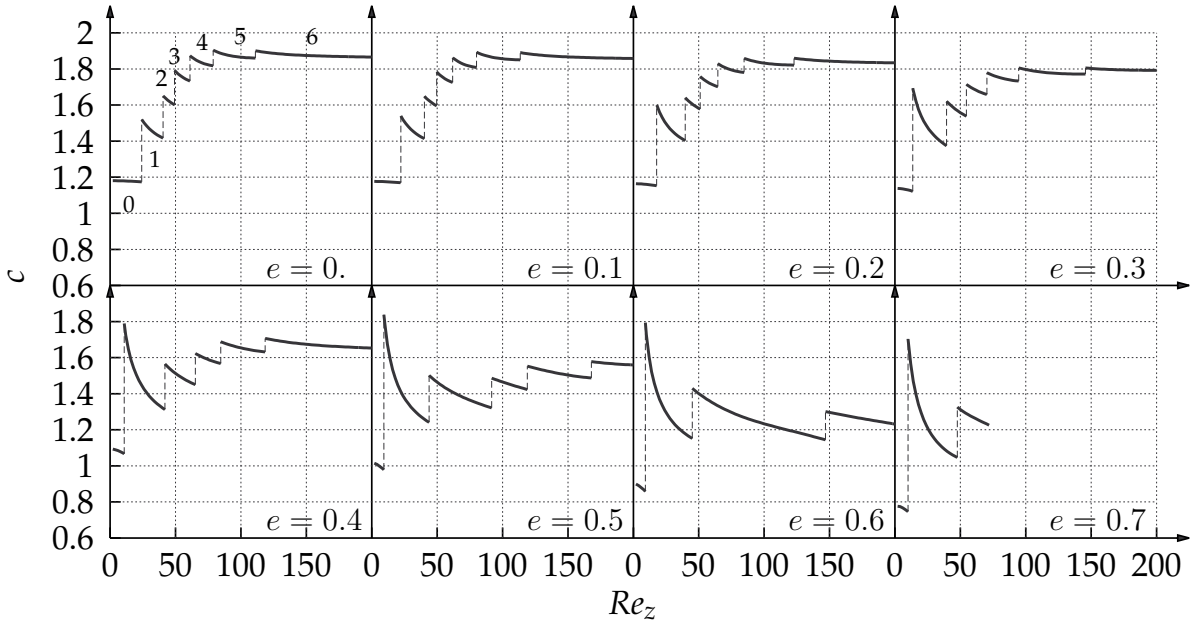

Figure 4.9 – Critical phase speed c against axial Reynolds number Re_z at critical conditions for eccentricities $e = 0, 0.1, \ldots, 0.7$. Discontinuities correspond to a switch in m (values indicated by annotation for $e = 0$). Unit is the average axial basic flow velocity $\overline{W}$.

4.3.4 Critical eigenmodes structure

A systematic study of the spatial structure of the critical eigenmodes has been performed. Figure 4.10 shows a deformed LH1 for $e = 0.5$, $Re_z = 40$. Figure 4.10*(e)* clearly represents the helical structure while figure 4.10*(b)* shows the $m = 1$ azimuthal order. In-plane motion of the mode (figure 4.10*(a)*) can be quite complicated and difficult to interpret for higher-order modes.

It is interesting to look at the disturbance kinetic energy distribution to see where the mode localizes within the annulus. Figure 4.10*(c)* shows concentration of the energy in the converging gap region, consistent with observations of Oikawa for TV perturbations in both the small and wide gap eccentric Taylor–Couette flow (and the numerous theoretical and experimental studies cited in the introduction, either calculating or observing the so-called 'maximum vortex activity' in the saturated régime). It is also possible to track the position of the maximum of the total disturbance energy. It is found that both in the axisymmetric and the $e = 0.5$ cases, the perturbation localizes closer and closer to the inner wall as advection is increased, at a radius (with respect to inner cylinder) of about 1.2–1.5 times the inner cylinder radius. In the eccentric case, this maximum also moves azimuthally to the small gap region, with jumps as the critical mode switches. At $Re_z = 0$ ($m = 0$), it is located at a polar angle (centered on inner cylinder) of $\theta = 79°$, while at $Re_z = 200$ ($m = 5$), it is at $\theta = 121°$. From the energy density maps, it is also clear that as Re_z is increased, the energy is less and less spread out in the annular region and peaks around some radial position. For $Re_z = 0$, the ratio between the maximum of the total disturbance energy and the average is 5.7, whereas it is 16.3 for $Re_z = 200$.

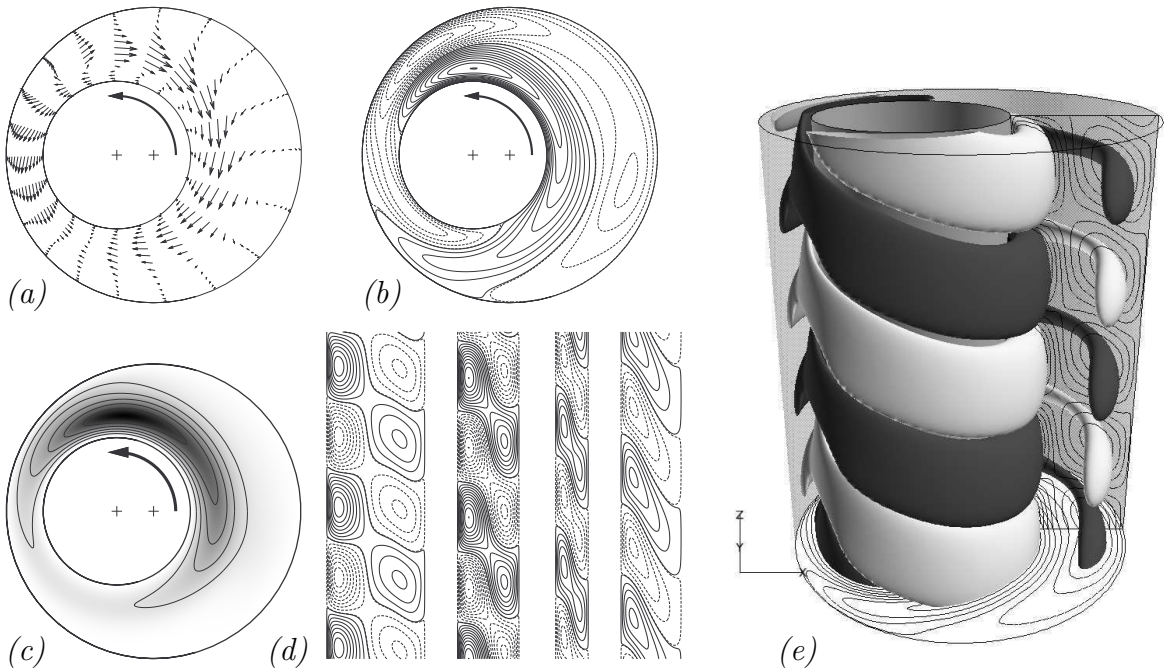

Figure 4.10 – Structure of the critical eigenmode for $e = 0.5$, $Re_z = 40$. *(a)* Real part of the in-plane perturbation velocity $\tilde{\mathbf{u}}_\perp = (\tilde{u}, \tilde{v})$. *(b)* Equispaced contours of real part of the axial perturbation velocity $\tilde{w}$. Solid (dotted) lines indicate positive (negative) values. *(c)* disturbance energy density $E_\perp + E_z$ map and (equispaced) contours. Dark grey correpond to high values. *(d)* Vertical cuts (equispaced contours) of real part of the axial perturbation velocity $\tilde{w}$ for $\theta = 0, \pi/2, \pi, 3\pi/2$ (from left to right) in a polar coordinate system centered on the inner cylinder. *(e)* Iso-surfaces of $\mathrm{Re}(\tilde{w})$ showing the 3D structure of the mode. Dark (light) shades of grey indicate positive (negative) value respectively.

Define the in-plane and axial disturbance energy contributions of a mode as the integral quantities over the annular domain $\mathcal{A}$:

$$E_\perp = \frac{1}{2}\int_{\mathcal{A}} (|u|^2 + |v|^2)\mathrm{d}\mathcal{A}, \quad E_z = \frac{1}{2}\int_{\mathcal{A}} |w|^2 \mathrm{d}\mathcal{A}. \tag{4.11}$$

Figure 4.11 shows the contributions to the total disturbance energy of the critical mode as a function of Re_z for $e = 0$ and $e = 0.5$. The graphs show in both cases how the energy transfers from dominantly in-plane motion to dominantly axial motion as advection is increased, regardless of the ('pseudo-') azimuthal wavenumber involved. There is a tendency of the modes to become more and more two-dimensional with suppressed spanwise (here azimuthal) motion, as for TS waves on a flat-plate or in channel flow. This suggests that viscosity plays an important role in the destabilization of the modes at high Re_z. This hypothesis is consistent with the fact that the modes localize more and more in high shear regions: closer to the inner wall at smaller clearance. It is also consistent with the decrease in critical axial wavenumber k with increasing Re_z (figure 4.8). Interestingly, in the case $e = 0.5$, the critical axial Reynolds number above which advection becomes destabilizing corresponds to the switch from dominantly in-plane disturbance energy to dominantly axial disturbance energy (this is less clear for $e = 0$). Note, however, that these modes are distinct from the 'pure' viscous wall modes referred

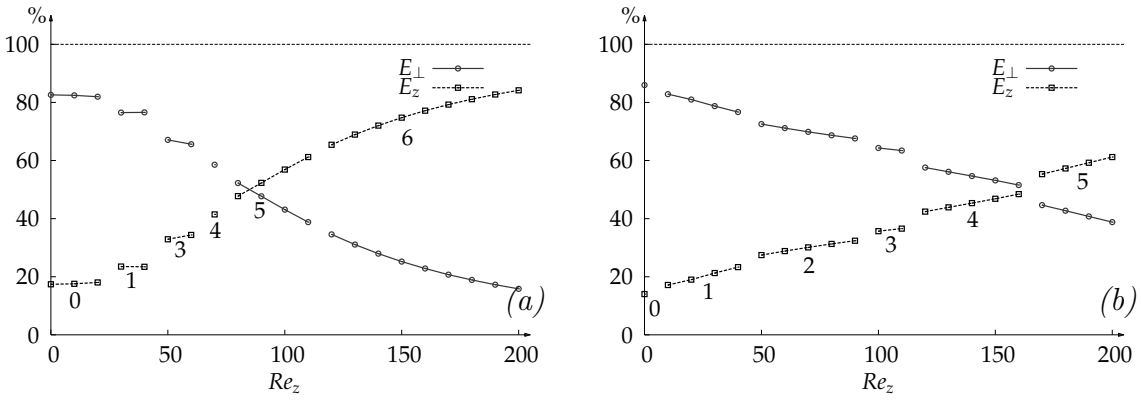

Figure 4.11 – In-plane $E_\perp$ and axial E_z contributions to the total disturbance energy of the critical mode as a function of Re_z. *(a)* $e = 0$. *(b)* $e = 0.5$. Numbers indicate the ('pseudo-') azimuthal wavenumber of the critical mode.

to as modes A in Merzari et al. (2008) for eccentric Poiseuille flow, or TS-like modes in axisymmetric Taylor–Couette–Poiseuille flow (Cotrell and Pearlstein, 2004). Those latter modes are localised about critical layers, and are expected to become critical at higher values of Re_z, typically of the order of 10^4 in the axisymmetric Taylor–Couette–Poiseuille flow with $\eta = 0.5$ (Cotrell and Pearlstein, 2004).

4.3.5 Growth rate maps and stability diagrams

In the concentric and $e = 0.5$ cases, a more complete study of the dispersion relation was carried out. Figure 4.12 shows maps of the maximum growth rate $\omega_{\mathrm{i,max}}$ in the (Re_Ω, Re_z) space for modes 2 and 4 and $e = 0.5$. For 'higher-order' modes like $m = 4$ one can clearly distinguish two zones. For low Re_z, there is a sharp increase in $\omega_{\mathrm{i,max}}$ with advection and rotation only has a minor effect on stability. For higher axial flow rates, the tendency is reversed: advection has only a weak effect on stability and centrifugal effects govern the stability of the mode. This trend was also observed in the concentric case for high-order left helices. For 'low-order' modes like $m = 2$, the separation of the two effects is less clear: the increase of $\omega_{\mathrm{i,max}}$ for weak axial advection is also observed, though less markedly, and at higher axial flow rates, the stabilizing effect of advection is comparable in magnitude to the destabilizing effect of rotation.

It is also possible to calculate the regions in which each m dominates the instability, as shown in figure 4.13. In both the cases of no eccentricity and $e = 0.5$, it appears that frontiers between these regions are always close to straight lines parallel to the Re_Ω axis. This illustrates again the importance of advection in the destabilization of the helical modes. While the instability mechanism is centrifugal in nature, there is a need for a minimum axial flow rate for this instability to operate on higher-order LH modes.

This importance of both shear and centrifugal effects in the destabilisation process at high Re_z as noticed here and in the preceding sub-section is not a complete surprise. Indeed, as pointed out in Meseguer and Marques (2002), Hagen–Poiseuille flow

is linearly stable for any Re_z, however, a slow rotation may destabilize the basic flow (Mackrodt, 1976). Conversely, rigid-body rotation is linearly stable for any rotation rate but the superposition of axial flow can also destabilize the flow. The same mechanism was observed for an axisymmetric Couette flow (Meseguer and Marques, 2000) with axial motion of the inner cylinder, where both shear and centrifugal effects were needed to make the basic flow unstable. It is clear from figure 4.12*(b)* that this is here the case for higher-order helical modes: the region of instability is bounded by a threshold in both rotation and advection rates.

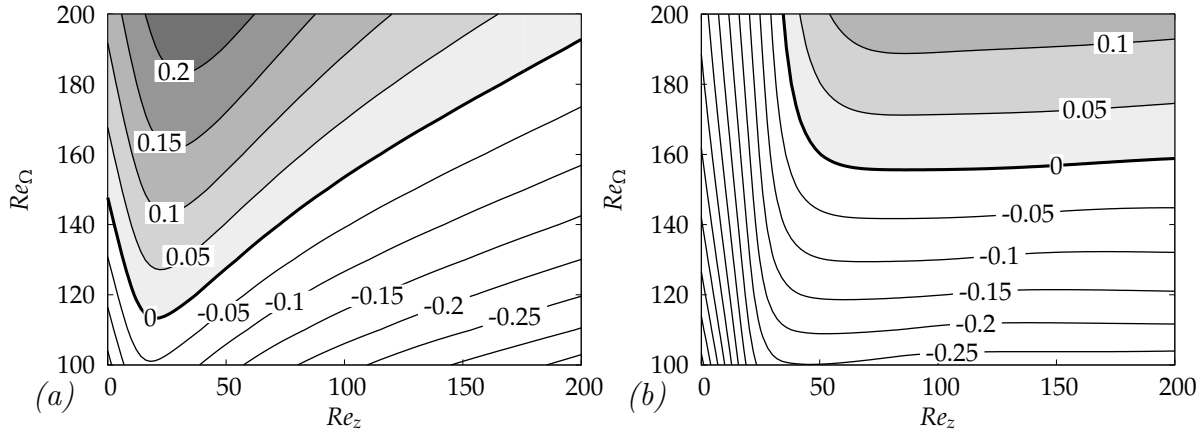

Figure 4.12 – Growth rate map for an eccentricity of $e = 0.5$. *(a)* mode $m = 2$, *(b)* mode $m = 4$.

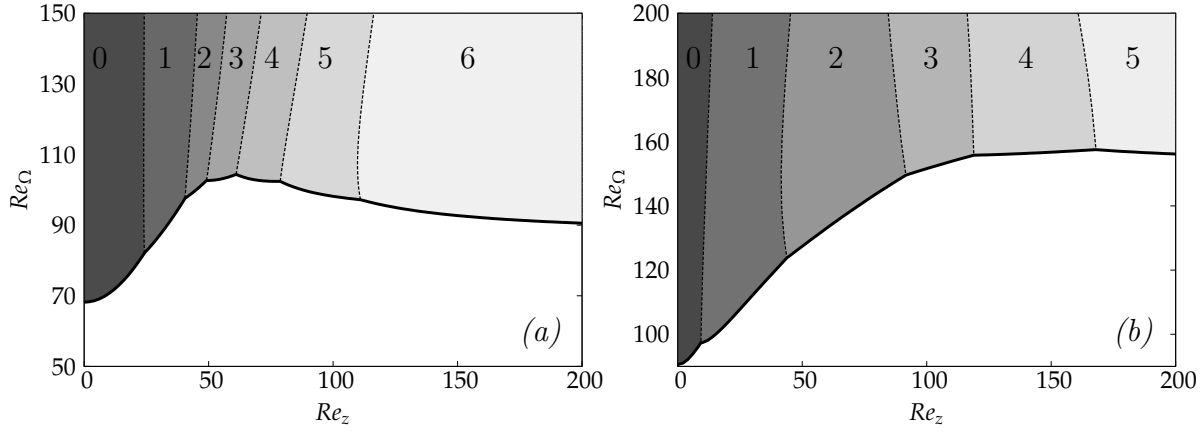

Figure 4.13 – Dominant unstable modes in (Re_z, Re_Ω) space with and without eccentricity. *(a)* $e = 0$, *(b)* $e = 0.5$. Numbers indicate the azimuthal or 'pseudo-azimuthal' wavenumber of the fastest growing mode.

4.4 Parametric study for a small gap $\eta = 0.89$

As mentioned in the introduction, very little work has been done on the experimental study of eccentric Taylor–Couette–Poiseuille flow. However, some experimental data is available for radius ratios close to $\eta = 0.9$. We study the case $\eta = 0.89$ ($\eta = 0.8907$ to be exact), corresponding to the sharp entry apparatus in Coney and Mobbs (1969–70) (comparable results were obtained for the smooth entry). In the same fashion as in section 4.3, we obtain results for e up to 0.6, Re_z up to 50 and Re_Ω up to 250, reaching reasonable accuracy with $M + 1 = K = 16$, as indicated in table 4.1.

4.4.1 Critical azimuthal Reynolds number

Compared to the wide gap case, the critical Re_Ω are higher, as expected because the curvature of the gap is less important. The transition to higher-order LH modes happens at much lower advection rates, and $m = 5$ becomes critical before $Re_z = 50$ for some eccentricities. Unlike for $\eta = 0.5$, increasing the eccentricity at a fixed Re_z results in the selection of higher-order m. For the wide gap, this was the case only for TV and LH1 (for low e), and otherwise selection of lower order m was observed. Figure 4.14*(a)* shows how the critical curves for the different m lie close to each other ($e = 0.2$ here), including the first RH modes. Complex behaviour is expected in the supercritical régime from the competition of the different helices. Notice that no weak destabilising effect of advection is noticed for any value of $Re_z \leq 50$ at any eccentricity. Indeed, this effect is expected to be pushed towards much higher values of Re_z, as in the concentric case. In this case, Ng and Turner (1982) found such an effect to occur at about $Re_z \sim 10^3$ for $\eta = 0.77$ (extremely weak effect), and did not observe it at all for $\eta = 0.95$ and $Re_z \leq 6000$.

4.4.2 Critical axial wavenumber

The range of critical axial wavenumbers (figure 4.15) is almost the same as in the wide gap case. This means that the clearance is still controlling the size of the vortices. The most noticeable difference with $\eta = 0.5$ is the fact that for weak eccentricities ($e \leq 0.2$) and low order modes, k increases continuously with Re_z. This was observed only for TV and LH1 in the previous case, but is now seen for more modes. This observation, together with the previous subsection, shows that the behaviour is globally the same as for $\eta = 0.5$, but variation in critical m is much faster as Re_z increases and more modes are involved. This behaviour is consistent with the results of Ng and Turner (1982) who found a critical azimuthal wavenumber of 12 at $Re_z = 100$ for $\eta = 0.77$, and of 35 for $\eta = 0.95$.

4.4.3 Critical phase speed

As for the case $\eta = 0.5$, the phase speed is around $1 - 2$ times the average axial speed of the base flow (figure 4.16). As eccentricity is increased, the jump in phase speed

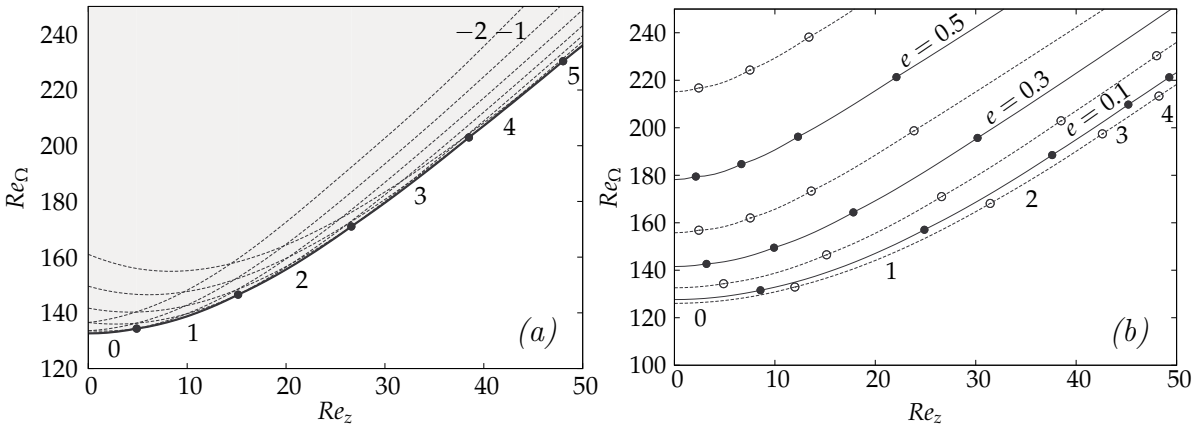

Figure 4.14 – *(a)* Critical curves $Re_\Omega = f(Re_z)$ for $\eta = 0.8907$, $e = 0.2$ and modes $m = -2, \ldots, 5$. The thick solid line indicates the instability threshold taking into account all the modes. Shaded area corresponds to instability. *(b)* Critical curves taking into account all the modes, for different eccentricities $e = 0, 0.1, \ldots, 0.6$ and $\eta = 0.8907$. In both *(a)* and *(b)*, dots indicate a switch in critical m, and the associated 'pseudo-azimuthal' wavenumber is indicated below.

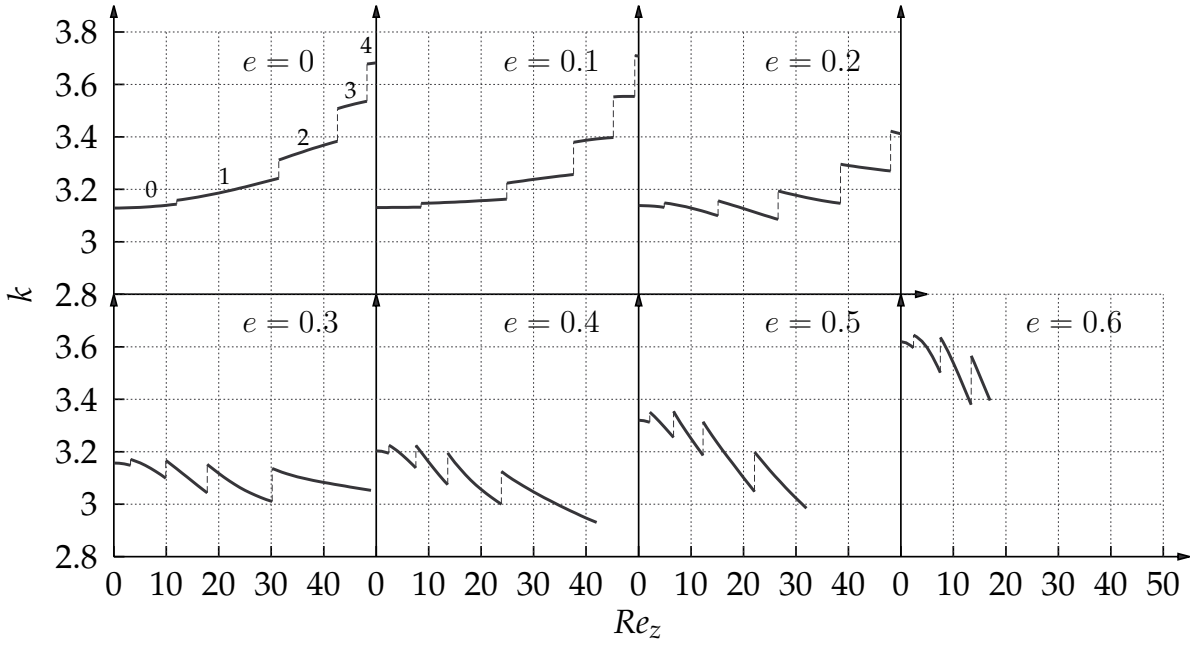

Figure 4.15 – Critical wavenumber k against axial Reynolds number Re_z for eccentricities $e = 0, 0.1, \ldots, 0.6$. Discontinuities correspond to a switch in critical m (values indicated by annotation for $e = 0$).

between consecutive critical modes becomes larger. For high enough eccentricities, the peak phase speed is that of the LH1.

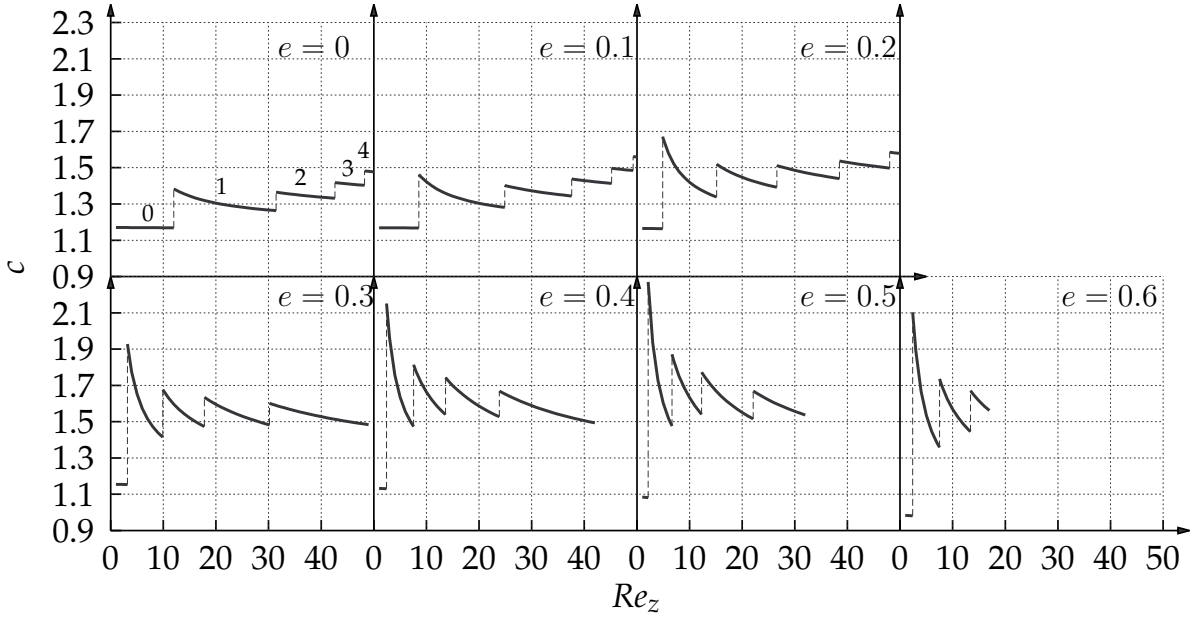

Figure 4.16 – Critical phase speed c (in base flow axial speed unit $\overline{W}$) against axial Reynolds number Re_z for eccentricities $e = 0, 0.1, \ldots, 0.6$. Discontinuities correspond to a switch in critical m (values indicated by annotation for $e = 0$).

4.4.4 Comparison with experiments

In this section, we compare numerical results with a series of experiments performed on a single apparatus of radius ratio $\eta = 0.89$ and aspect ratio (length over clearance) $L = 71.8$. Figure 4.17 compares experimental data from Coney and Mobbs (1969–70) (sharp entry case) against our calculations, after converting their graphical data into our system of control parameters. Agreement is quite good when there is no axial flow, and for $e < 0.5$. At higher eccentricities though, we predict transition at higher rotation rates. It is likely that the difference is due to boundary effects, causing early transition to a Taylor 'pre-vortex' flow as reported in Mobbs and Ozogan (1984).

As soon as axial flow is added, the predicted critical Re_Ω is significantly lower than the experimental values, at any eccentricity, though trends are the same. The experimental data lie between $10 - 20\%$ above the calculated threshold. Discrepancies as high as 20% were also noticed between the numerical predictions of Ng and Turner (1982) and the experimental data of Nagib (1972) for the Taylor–Couette–Poiseuille flow of radius ratio $\eta = 0.77$. Takeuchi and Jankowski (1981) reported divergent trends between thoretical predictions and experimental data for $\eta = 0.5$ and Re_z as low as 40. Takeuchi and Jankowski (1981) claimed that the length of the apparatus was responsible for the supercritical Taylor numbers. Indeed, they invoked the idea of a 'vortex development length', defined as 'the length needed for a moving disturbance to reach an amplitude that is observable by the visualization method'. With more recent theory, it would be said that the instability is convective and is triggered by noise at the inlet of the apparatus (sharp or smooth). Indeed, the apparatus used by Coney and Mobbs (1969–70) is quite compact compared to other experiments. The length to gap ratio L is 71.8, whereas it

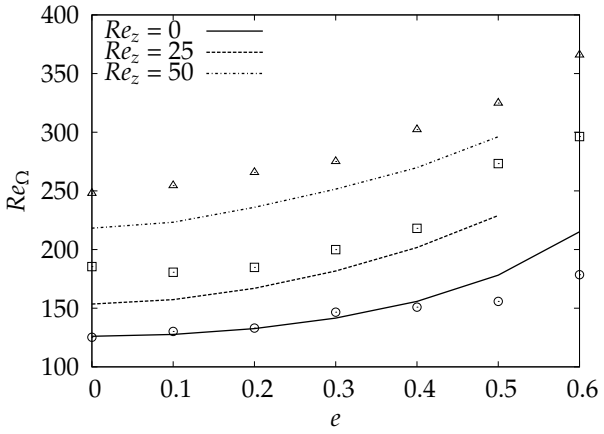

Figure 4.17 – Comparison of the critical curves $Re_\Omega = f(e)$ for $Re_z = 0, 25, 50$: present results (lines) and experimental results (points) of Coney and Mobbs (1969–70) for the sharp entry apparatus.

Re_z	torque [1]	visual [1]	visual [1]	visual [2]	visual [3]	present work
0	145	175	166	162	164	178
25	208	269	219	249	301	229
50	281	349	303	334	319	296

Table 4.2 – Critical Re_Ω for $e = 0.5$, $\eta = 0.89$: [1] Younes (1972), [2] Coney and Mobbs (1969–70), Coney (1971), [3] Coney and Atkinson (1978).

was respectively 160 for Nagib (1972) and 110 for Takeuchi and Jankowski (1981). In comparison, for a radius ratio of $\eta = 0.95$ and a length to gap ratio of 290, Snyder (1962) obtained experimental data matching very closely Ng and Turner (1982), supporting the idea of the importance of the vortex development length. As advection is increased, perturbations travel faster as they grow, and might not be detected for large Re_z, also explaining why results diverge for larger Re_z.

In table 4.2, numerical values are given for the critical Re_Ω at $e = 0.5$, from visual observations and torque measurements, compared to our values. The table shows significant scatter of the experimental data, even when using the same technique, e.g. visual observations. Values obtained via torque measurements always give lower values than those from visualisation, as the method is essentially more sensitive to the 'pre-vortex' flow located near the inner cylinder and difficult to visualise. Overall, theoretical values always lie within (or very close to) the bounds given by the experiments.

4.4.5 The 'double-vortex' pattern

More surprising are the complex patterns observed by Coney and Mobbs (1969–70), with apparent random axial wavenumber. For an eccentricity of $e = 0.3$ and an axial Reynolds number of $Re_z = 50$, they described a system of two vortices co-existing in the annulus: respectively a left and a right helix. Looking at their graph, the azimuthal Reynolds number associated with this state has a supercritical value of $Re_\Omega \approx 275$.

For this set of parameters, it is possible to calculate the maximum growth rate of all unstable modes. Results are reported in table 4.3, including axial wavenumber, phase speed and group velocity $c_g \equiv \partial\omega_\mathrm{r}/\partial k$. Modes $m = -1$ to 6 are all linearly unstable, so theory allows for a RH to grow at these operating conditions. However, the growth rates associated with higher-order LH are much higher, and $m = 5$ is dominant, closely followed by $m = 4$. The wavenumbers of these latter modes lie in the lower range of what was experimentally observed: $3.25 - 5.20$. Temporal stability theory offers no obvious explanation for the larger wavenumber perturbations observed in the experiment.

In table 4.3, we also give the equivalent spatial amplification properties of the unstable modes, following Gaster (1962). For near critical perturbations, the spatial amplification rate $-k_\mathrm{i}$ can be related to the temporal growth rate ω_i, via the group velocity of the perturbation, with the simple relation $-k_\mathrm{i} \approx \omega_\mathrm{i}/c_g$. In the spatial stability framework (meaningful for convective instabilities), the resulting amplification of the perturbations over the length L of the apparatus is given by $\exp[-k_\mathrm{i}L]$. According to this theory, the spatial amplification of higher-order spirals is very fast due to the large growth rate and the moderate group velocity. On the other hand RH spiral $m = -1$ is barely amplified through the apparatus and is very unlikely to saturate before exiting the system.

One could then think of this unexpected pattern as a consequence of transient growth due to non-modal effects (see Chomaz (2005) for a review). Heaton (2008) assessed the importance of these effects in axisymmetric Taylor–Couette–Poiseuille flow, and showed that they could also potentially explain deviations from modal stability predictions at moderate Re_z, typically of the order of a few hundreds. For lower Re_z however, transient growth is not significant, and modal theory alone was shown (Cotrell et al., 2004) to match experimental results accurately. Hence, for $Re_z = 50$, it seems unlikely that transient effects might be important, even though no results are currently available for the eccentric case.

Owing to the supercritical operating conditions and the variety of unstable modes, nonlinear simulations would surely help to understand the double-vortex pattern. As in the case with no advection, end effects might have an impact on stability properties as well. Finally, phase noise may prevent a clear identification of the convectively amplified pattern (Babcock et al., 1991, 1992).

4.5 Conclusions and perspectives

Temporal stability of eccentric Taylor–Couette–Poiseuille flow with fixed outer cylinder has been investigated for a large range of parameter space. Parametric studies have been performed for a wide gap case $\eta = 0.5$ with $Re_z \leq 200$ and $e \leq 0.7$, and a small gap case $\eta = 0.89$ with $Re_z \leq 50$ and $e \leq 0.6$. Taylor vortices give way to helical structures of increasing azimuthal complexity as advection is increased. The helicity of these structures is always opposed to the inner cylinder rotation, and are termed left helices, as in the Taylor–Couette–Poiseuille flow. Broken axisymmetry changes the thresholds and distorts the critical modes, but was not found to trigger any new instability mechanism for the parameter range considered.

Eccentricity is always stabilising, regardless of axial flow rate, and this effect becomes even more important for higher values of e. Indeed, centrifugal effects are weakened

m	k	$\omega_{\mathrm{i,max}}$	c	c_g	$-k_\mathrm{i}$	$\exp[-k_\mathrm{i}L]$
-1	2.60	1.95×10^{-4}	0.89	1.08	0.0010	1.1
0	2.70	9.04×10^{-3}	1.03	1.09	0.0455	26.3
1	2.82	1.55×10^{-2}	1.16	1.10	0.0774	258.3
2	2.94	2.00×10^{-2}	1.28	1.12	0.0986	1187.6
3	3.08	2.28×10^{-2}	1.39	1.13	0.1112	2943.3
4	3.21	2.43×10^{-2}	1.50	1.14	0.1169	4429.7
5	3.37	2.46×10^{-2}	1.60	1.16	0.1171	4488.0
6	3.53	2.40×10^{-2}	1.69	1.17	0.1131	3356.9

Table 4.3 – Properties of the unstable modes $m = -1, \ldots, 6$ for $e = 0.3$, $Re_z = 50$ and $Re_\Omega = 275$. k and $\omega_{\mathrm{i,max}}$ are calculated from the temporal stability problem. Phase and group velocities c and c_g are relative to average axial flow velocity $\overline{W}$. k_i is the spatial amplification rate from Gaster (1962)'s relation. $\exp[-k_\mathrm{i}L]$ is the amplification factor from the inlet to the outlet of the apparatus (Coney and Mobbs, 1969–70).

at $e \geq 0.3$, as a low speed recirculation region forms in the base flow and less fluid is driven in rotation around the inner cylinder. The effect of axial advection at fixed eccentricities is more subtle. For the small gap case, the critical Re_Ω increases steadily with Re_z. For the wide gap case $\eta = 0.5$, the critical Re_Ω increases for weak values of Re_z, but decreases slightly as axial advection is increased further. The maximum value of the critical Re_Ω is obtained for a value of Re_z that increases with eccentricity. Despite the destabilising effect of advection above this specific value of Re_z, the case with no advection always remains the most unstable. For the wider gap $\eta = 0.5$, increasing e at fixed Re_z tends to lower the critical pseudo-azimuthal wavenumber m (except for LH1 over TV), whereas 'higher-order' modes seem to be selected for $\eta = 0.89$. The critical axial wavelength is always of the order of the clearance d. For $\eta = 0.5$, the axial wavenumber k decreases continuously for a given m (except for TV and LH1 at small eccentricities) with increasing Re_z, but positive jumps are seen as higher and higher pseudo-azimuthal wavenumber m are selected at criticality. For $\eta = 0.89$, the behaviour is similar except that the increase of k for small m and small e is seen for more modes. For both radius ratios, the critical phase speed c of the travelling waves varies between 0.8 and 2.2 times the axial mean velocity of the base flow. c decreases with Re_z, except when the critical azimuthal wavenumber switches, in which case there is a discontinuous jump to a higher phase speed. For the small gap case $\eta = 0.89$, the range of Re_z for which a critical fixed m dominates is much smaller than for $\eta = 0.5$ and transition to higher-order modes happens in a smoother way as Re_z increases. Mode competition is more pronounced for the small gap case because modes of different m lie closer to each other in the (Re_Ω, Re_z) plane.

Whereas the instability mechanism for TV is only centrifugal, with a stabilising effect of Re_z, the destabilisation of helical modes $m > 0$ is strongly influenced by axial advection. Indeed, higher-order LH modes require a minimum amount of axial shear to become unstable, and this effect dominates the centrifugal mechanism for low Re_z. For large enough Re_z, the effect of axial advection becomes minor, compared to centrifugal destabilisation with increasing Re_Ω. Maximum vortex activity, measured here by the maximum of the disturbance kinetic energy, is localised in the converging gap

and moves towards the small gap and inner cylinder as Re_z is increased. At the same time, the disturbance energy concentrates increasingly into axial motion, recalling the two-dimensional structure of TS waves generated by axial shear. However, the so-called TS-like disturbances, involving a critical layer close to the wall, are not found in the range of the computations and are only expected to appear at larger advection rates (Cotrell and Pearlstein, 2004). Center modes of Sp type, found in eccentric annular Poiseuille flow by Merzari et al. (2008), are expected to exist in eccentric Taylor–Couette–Poiseuille flow at sufficiently large values of Re_z, but would require prohibitively fine meshing to be explored thoroughly with the method used here.

Comparison with the experiment of Coney and Mobbs (1969–70) for the small gap case shows agreement within 20% and matching trends. However, transition is found to occur below the linear threshold for $e \geq 0.5$ and $Re_z = 0$, and above for $Re_z = 25$ and 50 regardless of e. These differences are thought to be due to finite length effects. In the eccentric case with no axial flow, end effects may be responsible for the onset of toroidal vortices below the limit of infinite-cylinder theory. When axial flow is added, delayed onset is probably caused by the 'vortex development length' invoked by Takeuchi and Jankowski (1981). In the framework of convective instabilities, the system needs to be of appropriate length for the perturbations to reach an amplitude detectable by experiments. The apparatus being quite compact, it is plausible that high rotation rates would be needed to amplify perturbations before they exit the system. Despite overall encouraging results, modal stability analysis cannot fully explain the complex pattern observed for $e = 0.3$, $Re_z = 50$, involving a double-vortex structure. Non-modal effects, potentially responsible for transient amplification of this unexpected structure, are likely to be weak for such a low advection rate. According to Heaton (2008), these effects become important for Re_z of the order of a few hundreds in the concentric case, and might contribute to discrepancies in onset of instability. Assuming non-modal effects are also important at high Re_z for the eccentric case, we leave the calculation of optimal perturbations as a perspective. The double-vortex structure may result from nonlinear interactions between modes, and fully nonlinear simulations, including end effects and inlet noise, would be very helpful to understand formation of this pattern. More experimental data would also be appreciable to ensure reproducibility of the observations.

Though the experiments of Coney and Mobbs (1969–70) suggest that instability is triggered by noise at the inlet and amplified convectively, the effect of eccentricity on absolute instabilities (Huerre and Monkewitz, 1985, 1990) remains an open problem. This aspect is currently being investigated and will be addressed in a future article. A weakly nonlinear study is also required to determine whether the bifurcation remains supercritical over the whole parameter space, or if subcritical transition can occur. Possible steps towards a better understanding of annular flows of drilling muds include non-Newtonian effects and motion of the inner cylinder, as complex effects are expected (Escudier et al., 2002, Feng et al., 2007, Feng and Fu, 2007). To fully document the linear stability properties of this flow, it would also be interesting to investigate the connection with eccentric annular Poiseuille flow at high Re_z, analysed by Cotrell and Pearlstein (2004), Cotrell et al. (2004) in the concentric case. At high Re_z, three families of modes of very different structure are expected to compete (Merzari et al., 2008) and make the problem even more computationally challenging.

4.6 Appendix

This appendix contains, in non-dimensional form, the expression of some differential operators using Wood (1957)'s modified bipolar coordinate system defined by equations (4.4–4.6). As in §5.3.4, the 'stretched' variable defined by $\xi = (2\rho - \alpha - 2)/\alpha$ (where $\alpha = \beta - 1$) is used instead of ρ to transform the flow domain to $-1 \leq \xi \leq 1$. Following DiPrima and Stuart (1972a), the infinitesimal length element $\mathrm{d}s$ in (ξ, ϕ, z) is:

$$\mathrm{d}s^2 = \frac{\alpha^2}{4\delta^2 J}\mathrm{d}\xi^2 + \frac{\rho^2}{\delta^2 J}\mathrm{d}\phi^2 + \mathrm{d}z^2, \tag{4.12}$$

with J the Jacobian of the transformation 4.4 given by:

$$J = \frac{\left(1 + 2\gamma\rho\cos\phi + \gamma^2\rho^2\right)^2}{\left(1 - \gamma^2\right)^2}. \tag{4.13}$$

Introducing the inverse scale factors μ_ξ and μ_ϕ associated to the coordinates ξ and ϕ respectively:

$$\mu_\xi = \frac{2\delta\sqrt{J}}{\alpha},\ \mu_\phi = \frac{\delta\sqrt{J}}{\rho}, \tag{4.14}$$

one can define the following operators:

$$D_\xi \equiv \mu_\xi\partial_\xi,\ D_\phi \equiv \mu_\phi\partial_\phi, \tag{4.15}$$

and factors:

$$A \equiv \mu_\phi - \partial_\xi\mu_\xi\ ,\ B \equiv \partial_\phi\mu_\phi\ ,\ C \equiv D_\xi A - D_\phi B. \tag{4.16}$$

Using Whitham (1963)'s general orthogonal coordinate formulas, the different terms in equations (5.2-5.3) can be written (recall that $\partial_z \equiv 0$ for the basic flow):

$$\nabla_\perp p \equiv \begin{bmatrix} D_\xi p \\ D_\phi p \end{bmatrix}, \tag{4.17}$$

$$\nabla_\perp \cdot \mathbf{u}_\perp \equiv (D_\xi + A)u + (D_\phi - B)v, \tag{4.18}$$

$$\mathbf{u}_\perp \cdot \nabla_\perp \mathbf{u}_\perp \equiv (uD_\xi + vD_\phi)\,\mathbf{u} + (Av + Bu)\begin{bmatrix} -v \\ u \end{bmatrix}, \tag{4.19}$$

$$\mathbf{u}_\perp \cdot \nabla_\perp w \equiv (uD_\xi + vD_\phi)\,w, \tag{4.20}$$

$$\nabla_\perp^2 \mathbf{u}_\perp \ \equiv\ \begin{bmatrix} \nabla_\perp^2\ u \\ \nabla_\perp^2\ v \end{bmatrix} + \begin{bmatrix} Cu - 2\left(AD_\phi + BD_\xi\right)v \\ Cv + 2\left(AD_\phi + BD_\xi\right)u \end{bmatrix}, \tag{4.21}$$

where the scalar Laplacian has the expression:

$$\nabla_\perp^2 \equiv D_\xi^2 + D_\phi^2 + (AD_\xi - BD_\phi). \tag{4.22}$$

Finally, we give the expression for the rate-of-strain tensor in-plane components used for forces/torque calculations:

$$\begin{cases} e_{\xi\xi} &= D_\xi u - Bv, \\ e_{\phi\phi} &= D_\phi v + Au, \\ e_{\phi\xi} &= e_{\xi\phi} = \frac{1}{2}(D_\xi v + D_\phi u + Bu - Av). \end{cases} \tag{4.23}$$

4.7 Complement: wall stresses

To illustrate the discussion of the forces and torque in §4.2.4, we show the distribution of wall stress on the inner cylinder in figure 4.18. For $Re_\Omega = 10$ (figure 4.18 1a & 1b),

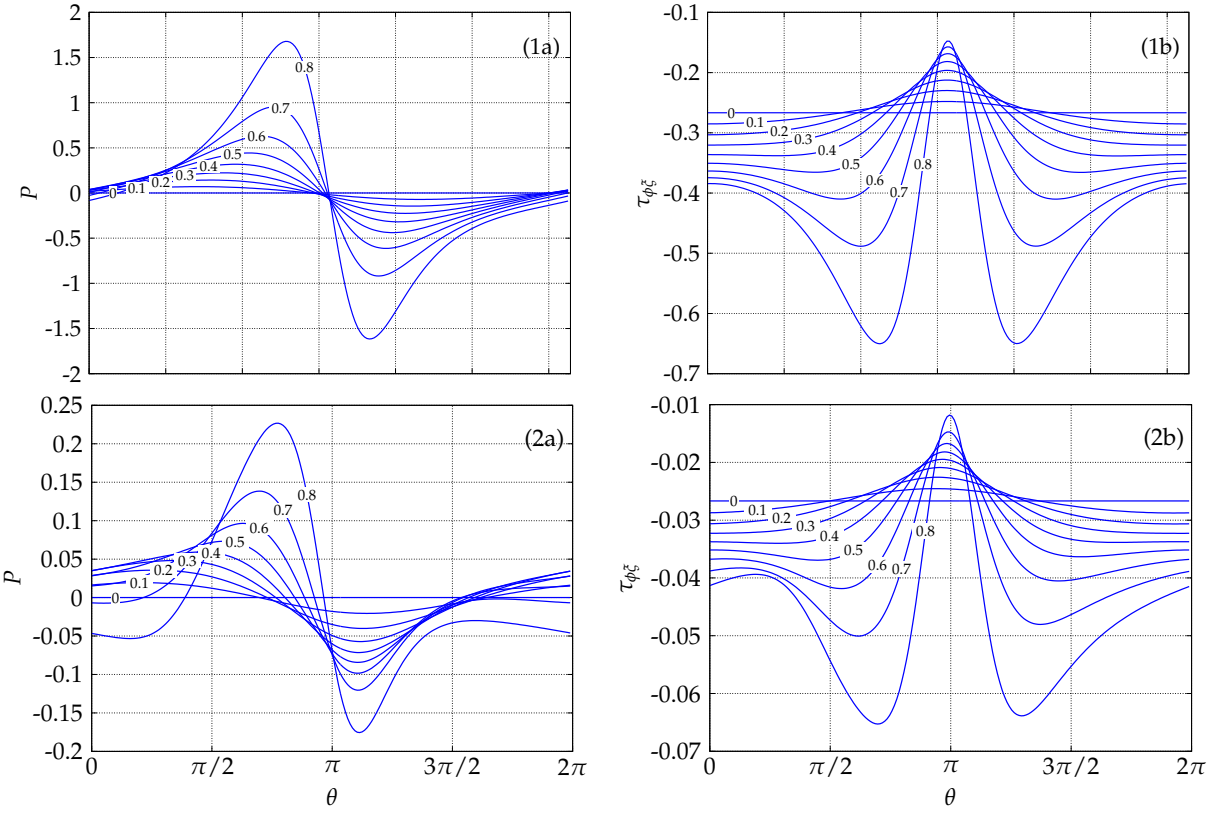

Figure 4.18 – (a) Pressure P and (b) shear stress $\tau_{\xi\phi}$ acting on the inner cylinder, as a function of θ, the polar angle centered on the inner cylinder, for eccentricities $e = 0, 0.1, \ldots, 0.8$ and (1) $Re_\Omega = 10$, (2) $Re_\Omega = 100$.

we notice the quasi-symmetry of the viscous stresses and quasi-antisymmetry of the pressure with respect to the line joining the centers. The symmetry is in fact lost for non-zero Re_Ω (a fact apparent for $Re_\Omega = 100$, see figures 4.18(2a,2b)), leading to a component of the force in the x-direction caused by inertial effects. We also notice that P and $\tau_{\phi\xi}$ scale approximately as ${Re_\Omega}^{-1}$, indicating the weakness of inertial effects on the wall stresses (cf. §4.2.4). The pressure term is dominant for $e \leq 0.8$. Figures 4.18(1a,2a) show how the pressure increases on the converging gap side and decreases sharply upon passing through the 'bottleneck' at $\theta = \pi$. As a result, the inner cylinder is pushed in the $-y$-direction. Both the pressure and shear stresses have two extrema, located in the vicinity of $\theta = \pi$. As e increases, the extrema approach $\theta = \pi$ more and more.

Chapter 5

Absolute instabilities

The preceding chapter was concerned with temporal growth of infinitesimal perturbations. In the present one, we go a step further and investigate the spatio-temporal dynamics of infinitesimal perturbations. Any initial perturbation of small amplitude can be decomposed as a sum of normal modes, which evolve in the form of a wavepacket carried by the flow. Each wave grows in time at its own rate and propagates with its own speed, without interacting with other waves. Temporal stability theory predicts the growth rate and phase speed of each mode, but does not directly predict the behaviour of the wavepacket at a fixed location in the long term. Indeed, even if a localized perturbation is amplified because of modal growth, the wavepacket may eventually be blown away if advection is strong enough. As a result, the flow would relax to its initial state in the long term. On the other hand, growth may occur in both the downstream and upstream directions and cause the entire flow to bifurcate to a new state. The two types of dynamics, respectively *convective* and *absolute*, are qualitatively very different.

Secondary flows caused by an instability would typically cause an increase in frictional torque and pressure drop, and even trigger transition to turbulence. Convective instabilities are highly dependent on the level of noise and may only affect the system downstream of external perturbations. On the other hand, absolute instabilities may lead to synchronized oscillatory states in the entire medium, which may in turn cause harmful resonance without the need for sustained forcing. We expect this second type of dynamics to be even more 'dangerous' in industrial systems associated with this flow, and therefore it is particularly important to be able to predict absolute instabilities.

Hydrodynamic resonance occurs if a wave with zero group velocity $\partial_k \omega = 0$ is temporally growing. This apparently simple criterion, due to Briggs (1964) & Bers (1983), and popularized in fluid mechanics by Huerre and Monkewitz (1990), requires analytic continuation of the dispersion relation to the complex plane of wavenumbers. Care must be exercised to check that zero-group-velocity waves, represented by *saddle points* in the complex k-plane, do not violate the causality principle, which makes spatio-temporal analysis far more intricate than temporal analysis.

This section is devoted to absolute instabilities in eccentric Taylor–Couette–Poiseuille flow. We will show that the trends found in the framework of temporal stability theory do not hold in the presence of absolute instability. The results are reported in the form of an article currently under review by the *Journal of Fluid Mechanics*. As in the

last chapter, a few notations (and the numbering of sections, figures, tables and equations) have been modified in order to ensure coherence with the rest of the manuscript, but the text and figures have not been otherwise changed. The article is followed by a few additional results falling beyond the scope of the article. In particular, we introduce a theoretical criterion to predict the validity (with respect to the causality principle) of two saddle points, in the vicinity of a 'third-order saddle point' where they 'collide'. The analysis was motivated by the fact that collisions between saddle points occur in practice for relevant modes, very close to critical conditions. Despite limited practical interest due to a small range of validity, the criterion provides valuable theoretical insight regarding this situation. Additional figures showing results on subdominant modes, alluded to in the article are given for completeness.

Absolute instabilities in eccentric Taylor–Couette–Poiseuille flow

Colin Leclercq, Benoît Pier and Julian F. Scott

Laboratoire de mécanique des fluides et d'acoustique, École centrale de Lyon—CNRS—Université Claude-Bernard Lyon 1—INSA Lyon, 36 avenue Guy-de-Collongue, 69134 Écully cedex, France

Submitted to J. Fluid Mech.

The effect of eccentricity on absolute instabilities (AI) in the Taylor–Couette system with pressure-driven axial flow is investigated. Five modes of instability are considered, characterised by a pseudo-azimuthal wavenumber m. They correspond to deformed toroidal ($m = 0$) and left-/right-handed helical structures ($m > 0/m < 0$) made of one or two waves ($|m| = 1, 2$). The most absolutely unstable mode always corresponds to Taylor-like vortices, with $m = 0$. However, AI properties of other m are close for highly eccentric configurations, with large enough axial flow. Axial advection, characterised by a Reynolds number Re_z, carries perturbations away from their source, and has a strong stabilising effect on AI. On the other hand, the effect of eccentricity e is complex: increasing e generally delays AI, except for a range of moderate eccentricites $0.3 \lesssim e \lesssim 0.6$, where it favours AI. This striking behaviour is in contrast with temporal instabilities, always inhibited by eccentricity, and where left helical modes of increasing $m > 0$ dominate for larger Re_z. The instability mechanism of AI is clearly centrifugal, even for the larger values of Re_z considered, as indicated by an energy analysis. For large enough Re_z, critical modes localise in the wide gap for low e, but their energy distribution is shifted towards the diverging section of the annulus for moderate e. For highly eccentric geometries, instabilities are controlled by the minimal annular clearance, and critical modes are confined in the vicinity of the inner cylinder. Untangling the AI properties of each m requires consideration of multiple saddle points for each dispersion relation.

5.1 Introduction

The flow between rotating cylinders has attracted attention since the end of the 19$^{\text{th}}$ century, starting with the experiments of Couette (1888a,b) and Mallock (1888), and the landmark work by Taylor (1923), who first predicted theoretically the threshold for centrifugal instability. Taylor characterised centrifugal effects using a non-dimensional number appropriate in the limit of small clearance, $d = (b - a) \ll a$, with a and b the inner and outer cylinder radii (see figure 5.1). In this paper, a wide gap geometry with radii ratio $\eta = a/b = 0.5$ will be considered, and centrifugal effects will be conveniently measured by an azimuthal Reynolds number $Re_\Omega = a\Omega d/\nu$, with Ω the inner cylinder rotation rate and ν the kinematic viscosity.

Adding axial flow to this system, one obtains a simple prototype for the study of pattern formation in real open flows. The effect of axial advection can also be measured

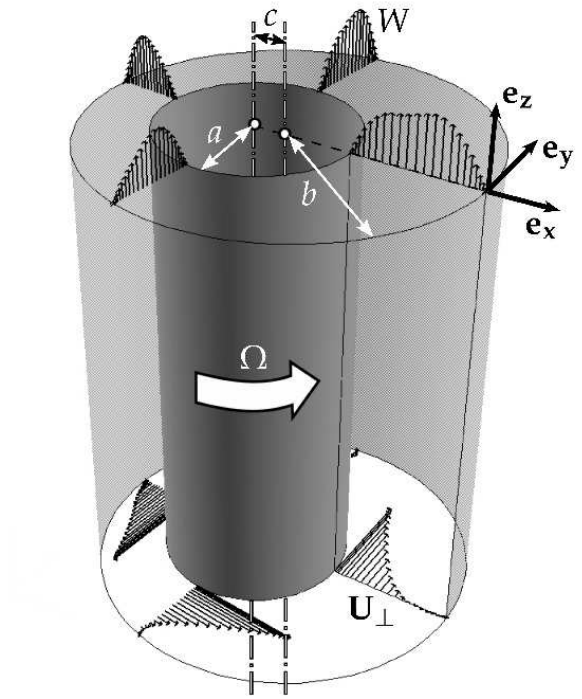

Figure 5.1 – Eccentric annulus of radius ratio $\eta = a/b = 0.5$ and basic flow $\mathbf{U} = \mathbf{U}_\perp + W\mathbf{e_z}$.

by a Reynolds number $Re_z = \overline{W}d/\nu$, based on the mean axial velocity $\overline{W}$. First theoretical predictions of the absolute instability (AI) threshold were obtained by Tsameret and Steinberg (1991b) with a criterion based on a one-dimensional Ginzburg-Landau equation (with coefficients determined by two-dimensional numerical simulations), and then by Babcock et al. (1991, 1992), using the full set of hydrodynamic equations and a saddle-point criterion (Briggs, 1964, Bers, 1983) that will be discussed in §5.3. They showed that upon crossing the AI threshold, periodic self-sustained vortices appear, in contrast with the irregular patterns emerging from noise amplification in the convectively unstable régime. In these papers and subsequent work (Tsameret and Steinberg, 1991a, Babcock et al., 1992, Lücke and Recktenwald, 1993, Swift et al., 1994, Babcock et al., 1994, Tsameret and Steinberg, 1994), effort was dedicated to identifying the noise sources (inlet noise versus thermal noise) which sustain the convective instability (CI). These studies were restricted to small axial Reynolds numbers Re_z, typically below 4, and it was found that the most unstable (fastest growing) perturbations were in the form of propagating Taylor vortices. For higher values of axial advection, Takeuchi and Jankowski (1981) and Ng and Turner (1982) had previously shown numerically (and also experimentally for the former reference) that critical modes consisted in propagating helical vortices, with helicity opposite that of the basic flow, and with azimuthal order m increasing with Re_z. However, the concept of AI was not widespread in fluid mechanics back then, and these studies were restricted to CI. Theoretical prediction of AI of helical modes was investigated only recently (Hoffmann 2004, Altmeyer 2011). In these papers, the authors studied the effect of axial through-flow on the spatio-temporal properties of toroidal and helical wavepackets with angular orders $|m| \leq 2$, for $Re_z \leq 20$. For $|m| \leq 1$, it was shown that critical azimuthal Reynolds numbers Re_Ω are higher for AI than for CI, and that the difference between the two thresholds increases with Re_z.

For $|m| = 2$ and a stationary outer cylinder, AI was found to occur in a closed region of the Re_z-Re_Ω plane, considering only the saddle point originating at the critical conditions for CI with $Re_z = 0$ (detailed in §5.3.5). However, the authors mentioned other saddle points expected to destabilise these modes in other regions of parameter space and which will be taken into account in the present article. More recent work on AI in the Taylor–Couette–Poiseuille flow concerned the effect of radial flow at the inner cylinder, representative of filtration devices (Martinand et al., 2009). In this analysis, it was shown that axisymmetric modes become absolutely unstable for inward radial flow, while helical modes with helicity identical to that of the basic flow dominate at high enough Re_z, for outward radial flow.

When the two cylinder axes do not coincide, axisymmetry is broken and the stability properties of the flow are modified. Eccentricity is generally measured by the non-dimensional distance between the two cylinders $e = c/d$ (see figure 5.1). Adding eccentricity to the Taylor–Couette flow with axial advection, one obtains a basic model for annular mud flows in oil-well drilling, or lubrication flows present in high-speed journal bearings. In the first case, mud is injected in a rotating drillstring, and flows back to the surface through the annular domain between the drillstring and the rock face, with several engineering functions: carry the rock cuttings out, lubricate, prevent inflow of formation gases and wellbore collapse, etc. (Escudier et al., 2002, Guo and Liu, 2011). For deep wells, the drillstring inevitably bends along its axis, on a typical length scale much larger than the well diameter. As a result, a parallel-flow assumption is reasonable, and the flow can be locally described as a Taylor–Couette–Poiseuille flow between eccentric cylinders. In high-speed turbomachinery, a similar configuration is found: oil is contained in eccentric journal bearings for lubrication purposes, and a pressure gradient is imposed along the shaft to evacuate damaging impurities (Sep, 2008). Aside from its fundamental interest, these industrial applications motivate the present analysis. In both applications, transition to complex hydrodynamic régimes would result in increased frictional losses, detrimental to the system efficiency. If the basic flow advection is weak compared to the rotation rate, hydrodynamic resonance may occur and the entire flow would bifurcate to an undesired self-sustained oscillatory state. This specific behaviour, called *absolute instability*, is particularly 'dangerous', because it does not require a permanent forcing: once the instability is triggered, it will propagate in both the downstream and upstream directions, and amplify using energy from the basic flow. On the other hand, *convective instabilities* correspond to wavepackets propagating only in the downstream direction: in the absence of forcing, the system eventually relaxes to its initial state at any fixed location, after perturbations have been 'blown away' from the source. The most temporally amplified perturbations are given by a classical *temporal stability analysis*, and such a study was recently carried out for this flow (Leclercq et al., 2013). It was shown that the physics is essentially similar to the axisymmetric case (Takeuchi and Jankowski, 1981, Ng and Turner, 1982), with propagating toroidal vortices replaced by helical structures of increasing azimuthal complexity as Re_z is increased. Eccentricity deforms the critical modes, but does not introduce new instabilities to the problem. The effect of eccentricity is stabilising for all values of Re_z, and this result is interpreted as a consequence of the reduction of centrifugal effects in the basic flow. Indeed, as eccentricity increases, the azimuthal flow rate decreases for a fixed inner cylinder rotation rate, resulting in weaker driving of the instability. This is a consequence of the appearance of a recirculation region in the wide gap which does not contribute to the net azimuthal flow rate. Outside this zone, in the vicinity of

the inner cylinder, the flow resembles an axisymmetric Taylor–Couette flow with clearance scaling with the inner gap $d(1-e)$. The reduction of the 'effective' clearance ratio $\delta = d/a$ with eccentricity, or increase in 'effective' radius ratio η, also explains stabilisation (see DiPrima (1960) for the effect of η on the Taylor–Couette flow). To date, it is, to the authors' knowledge, the only available theoretical study of eccentric Taylor–Couette–Poiseuille flow. The only known series of experiments were performed by Coney and Mobbs (1969–70), Coney (1971), Younes (1972), Younes et al. (1972), Mobbs and Younes (1974), Coney and Atkinson (1978) and show good agreement with our *a posteriori* predictions, despite small discrepancies attributed to finite-length effects. For a brief review of other theoretical and experimental results on eccentric Taylor–Couette flow on the one hand, and axisymmetric Taylor–Couette–Poiseuille flow on the other hand, we refer to Leclercq et al. (2013).

The present paper extends this previous linear stability analysis by considering the case of AI. In §5.2, the linear stability framework is presented. The governing equations and numerical methods are briefly described, and the main properties of the basic flow and normal modes are recalled. In §5.3, the methods used to investigate AI, based on the Briggs (1964)–Bers (1983) pinching criterion, are described. In §5.4, results are presented for the 5 modes of instability with angular orders $|m| \leq 2$, which include the fastest growing temporally unstable modes for $Re_z \leq 50$.

5.2 Linear stability framework

In the following, the geometry will be described using the ratio $0 < \eta = a/b < 1$ between the inner and outer cylinder radii a and b (see figure 5.1), and the eccentricity $0 \leq e = c/(b-a) < 1$, based on the distance c between centers, divided by the clearance $d = b - a$. The radii ratio will be fixed at the value $\eta = 0.5$ throughout this paper. Rotation and axial advection will be quantified using the two Reynolds numbers given in introduction: $Re_\Omega = a\Omega d/\nu$ and $Re_z = \overline{W}d/\nu$, with Ω the inner cylinder rotation rate, $\overline{W}$ the basic flow mean axial velocity and ν the kinematic viscosity.

The velocity $\mathbf{u}$ will be made non-dimensional with the rotation speed $\mathrm{V} \equiv a\Omega$. The clearance d will be taken as the reference length scale L. Finally, the pressure p will be in units of $\mathrm{P} \equiv \rho V^2$, with ρ the density of the fluid. All equations and physical quantities will be written in non-dimensional form, using V, L and P.

5.2.1 Basic flow

The velocity $\mathbf{u}$ can be decomposed into a component w parallel to the axis $\mathbf{e}_z$, and a component $\mathbf{u}_\perp = \mathbf{u} - w\mathbf{e}_z$ in a plane perpendicular to the axis. The axial flow is driven by a pressure gradient G in the z-direction. Denoting the in-plane pressure gradient as $\nabla_\perp p = \nabla p - G\mathbf{e}_z$, the incompressible Navier–Stokes equations read:

$$\left.\begin{aligned} (\partial_t + \mathbf{u}\cdot\nabla)\begin{bmatrix}\mathbf{u}_\perp \\ w\end{bmatrix} &= -\begin{bmatrix}\nabla_\perp p \\ G\end{bmatrix} + Re_\Omega^{-1}\nabla^2\begin{bmatrix}\mathbf{u}_\perp \\ w\end{bmatrix}, \\ \nabla\cdot\mathbf{u} &= 0, \end{aligned}\right\} \tag{5.1}$$

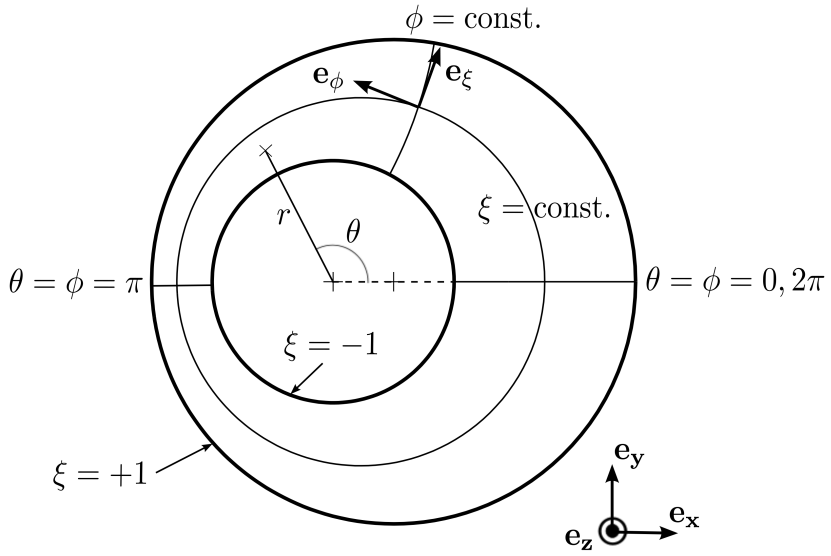

Figure 5.2 – Modified bipolar coordinate system (ξ, ϕ) fitting the eccentric annular domain. Polar coordinates (r, θ) are centered on the inner cylinder, with $\theta = \phi = 0$ along the line joining the cylinder axes.

with impermeability and no-slip boundary conditions on the fixed outer cylinder and on the inner cylinder, whose rotational velocity is 1. In-plane and axial derivatives can be separated, using convenient notations: $\mathbf{u}_\perp \cdot \nabla_\perp \equiv \mathbf{u} \cdot \nabla - w\partial_z$, $\nabla^2_\perp \equiv \nabla^2 - \partial^2_{zz}$ and $\nabla_\perp \cdot \mathbf{u}_\perp \equiv \nabla \cdot \mathbf{u} - \partial_z w$. Assuming an axially invariant flow, the problem is two-dimensional and $\mathbf{u}_\perp$ becomes independent of w:

$$\left.\begin{aligned} \partial_t \mathbf{u}_\perp + \mathbf{u}_\perp \cdot \nabla_\perp \mathbf{u}_\perp &= -\nabla_\perp p + Re_\Omega^{-1} \nabla^2_\perp \mathbf{u}_\perp, \\ \nabla_\perp \cdot \mathbf{u}_\perp &= 0. \end{aligned}\right\} \tag{5.2}$$

Basic flows $\mathbf{Q} \equiv (\mathbf{U}, P)$, denoted with capital letters, are defined as axially invariant, steady solutions of (5.1). Such solutions are found by integrating forwards in time equation (5.2) until convergence of $\mathbf{U}_\perp$ is attained, and then solving for the corresponding axial velocity W, given by:

$$\mathbf{U}_\perp \cdot \nabla_\perp W = -G + Re_\Omega^{-1} \nabla^2_\perp W. \tag{5.3}$$

Note that because of linearity of (5.3), the magnitude of W is proportional to G. Therefore, G can be set to a value of 1 without loss of generality. W can then be rescaled in a postprocessing step to match the average value $\overline{W} = Re_z/Re_\Omega$. In order to drive $\partial \mathbf{u}_\perp / \partial t$ to zero, a time-marching procedure based on a projection method (Goda, 1979, Raspo et al., 2002) is implemented. Equations are cast in a set of locally orthogonal, body-fitted coordinate system, using a conformal transformation given by Wood (1957). Full equations for the modified bipolar coordinates (ξ, ϕ) and the operators in (5.2–5.3) can be found in Leclercq et al. (2013). In the local frame $(\mathbf{e}_\xi, \mathbf{e}_\phi)$, the in-plane velocity vector is decomposed as $\mathbf{u}_\perp = (u, v)$. The pseudo-radial coordinate $-1 \leq \xi \leq 1$ spans the gap between the two cylinders while the pseudo-azimuthal coordinate $0 \leq \phi < 2\pi$ winds around the inner cylinder (see figure 5.2). In this coordinate system, a Fourier–Chebyshev pseudospectral method can be implemented. Fields $\mathbf{q} \equiv (\mathbf{u}, p)$ are decomposed onto $N = 2K + 1$ azimuthal modes, and $M + 1$ Chebyshev polynomials T_i,

with $0 \leq i \leq M$:

$$\mathbf{q}(\xi, \phi) = \sum_{i=0}^{M} \sum_{j=-K}^{K} \hat{\mathbf{q}}_{ij} \mathrm{e}^{\mathrm{i}j\phi} T_i(\xi). \tag{5.4}$$

A classical collocation method using a Gauss–Lobatto distribution $\xi_i = \cos[i\pi/M]$ is implemented in the pseudo-radial direction. We refer to Leclercq et al. (2013) for more details on the numerical procedure, mesh resolution and validation.

For an axisymmetric flow, the basic in-plane motion results from diffusion of azimuthal momentum from the rotating inner cylinder to the fixed outer cylinder. In cylindrical coordinates (r, θ), it takes the well-known form $\mathbf{U}_\perp = (0, Ar + B/r)$, with A and B two constants depending on the geometry. For low eccentricities, the result is quite similar, as can be seen in figure 5.3*(1a)*. However, for higher eccentricities, a low-speed recirculation region forms in the wide gap (figure 5.3*(2a)*). For the relatively high value of $Re_\Omega = 500$ presented here, small recirculation can already be seen for $e = 0.2$, whereas in Leclercq et al. (2013), figure 3, it was not present for $Re_\Omega = 100$ and appeared around $e \approx 0.3$ for that lower value of Re_Ω.

In the axisymmetric case, W is independent of $\mathbf{U}_\perp$, and the axial flow is very similar to a parabolic Poiseuille flow, with small corrections due the annular geometry. As eccentricity is increased, W decreases in the small gap, because of viscous effects, and most of the volume flux passes through the wide gap (see figure 5.3*(2b)*). Distortion also occurs, due to coupling with $\mathbf{U}_\perp$, and the peak velocity is no longer in the symmetry plane. For high rotation rates, the nonlinear interaction term $\mathbf{U}_\perp \cdot \nabla_\perp W$ can locally dominate the viscous term $Re_\Omega^{-1} \nabla_\perp^2 W$, and there is significant transport of W by in-plane components.

5.2.2 Normal modes

Let $\mathbf{q}' \equiv \mathbf{q} - \mathbf{Q}$ be three-dimensional perturbations of small amplitude superimposed onto the two-dimensional basic flow $\mathbf{Q}$. Injecting this decomposition of $\mathbf{q}$ into equations (5.1), and linearizing with respect to $\mathbf{q}'$, one obtains the evolution equations:

$$\left.\begin{aligned} \partial_t \mathbf{u}' + \mathbf{u}' \cdot \nabla \mathbf{U} + \mathbf{U} \cdot \nabla \mathbf{u}' &= -\nabla p' + Re_\Omega^{-1} \nabla^2 \mathbf{u}', \\ \nabla \cdot \mathbf{u}' &= 0, \end{aligned}\right\} \tag{5.5}$$

with impermeability and no-slip boundary conditions. The basic flow being invariant in the axial direction, perturbations can be written as normal modes

$$\mathbf{q}' = \tilde{\mathbf{q}}(\xi, \phi) \exp \mathrm{i}(kz - \omega t) + c.c., \tag{5.6}$$

where *c.c.* denotes the complex conjugate. In a general framework, k is the complex axial wavenumber and ω is the complex frequency. $\omega_\mathrm{r} \equiv \mathrm{Re}(\omega)$ is the temporal frequency and $\omega_\mathrm{i} \equiv \mathrm{Im}(\omega)$ is the temporal growth rate. Equivalently, $k_\mathrm{r} \equiv \mathrm{Re}(k)$ is the wavenumber of the mode, and $-k_\mathrm{i} \equiv -\mathrm{Im}(k)$ is the spatial growth rate. Injecting the modal form (5.6) into (5.5) with boundary conditions, one obtains a problem of the form $(\mathrm{A} - \mathrm{i}\omega \mathrm{B})\tilde{\mathbf{q}} = 0$, where (A, B) are two linear operators, with A depending on k. Expressions for A and B are given in Leclercq et al. (2013), in the modified bipolar coordinate system. The set of wavenumbers k and frequencies ω satisfying this problem for non-zero $\tilde{\mathbf{q}}$ define the dispersion relation $D(k, \omega) = 0$. Using a Fourier–Chebyshev decomposition of $\tilde{\mathbf{q}}$,

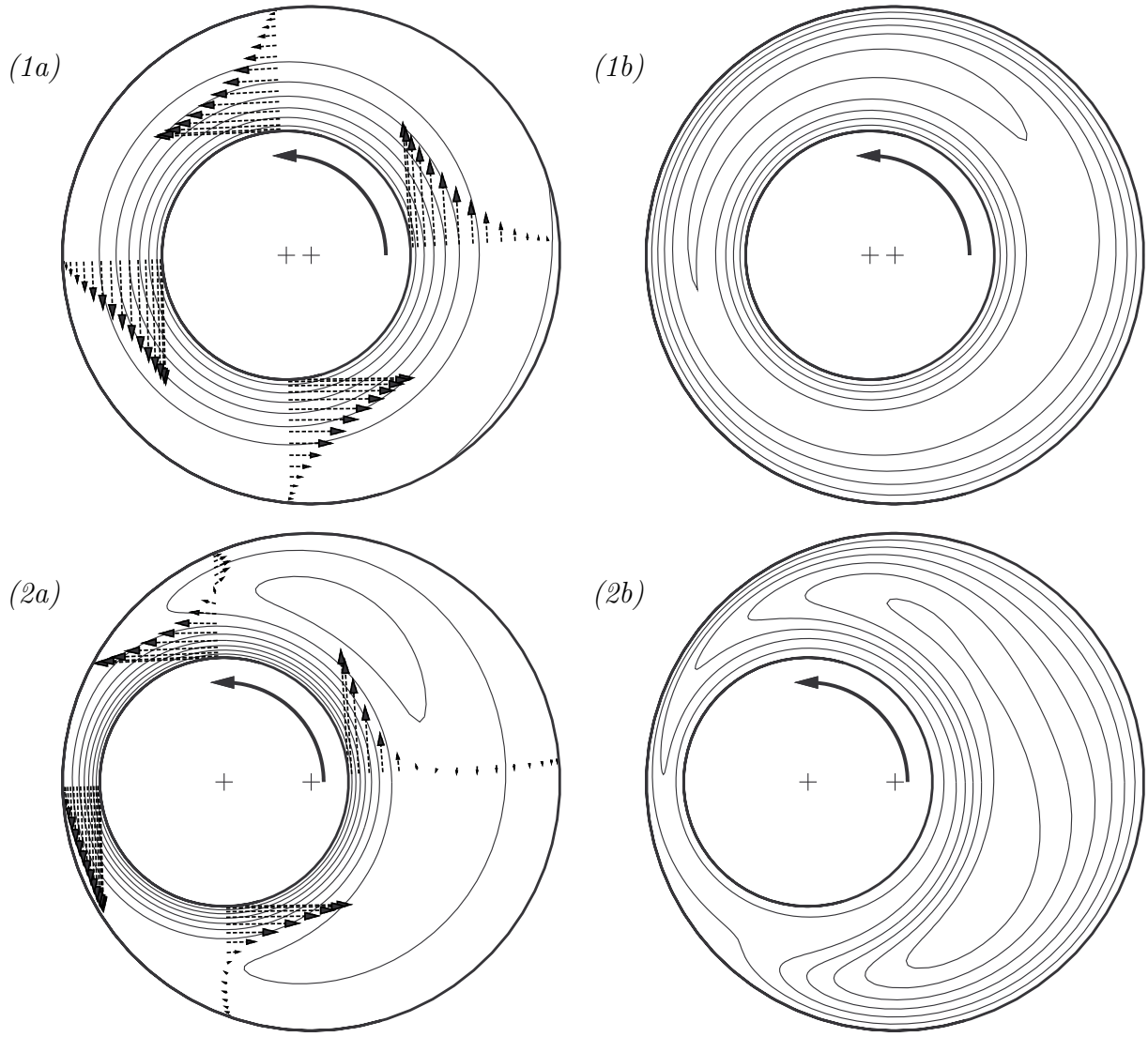

Figure 5.3 – Basic flows for $Re_\Omega = 500$: *(1)* weak eccentricity $e = 0.2$, *(2)* high eccentricity $e = 0.7$. *(a)* Contours of equispaced in-plane streamfunction with superimposed $\mathbf{U}_\perp$ profiles at $\theta = 0, \pi/2, \pi, 3\pi/2$ (polar angle with respect to the inner cylinder). *(b)* Equispaced contours of W.

as in (5.4), the linear problem is converted into a generalized eigenvalue problem for ω, with eigenvectors $\tilde{\mathbf{q}}$. This problem can be reduced by eliminating both $\tilde{w}$, $\tilde{p}$ and the boundary points, resulting in significantly smaller eigenvalue problems, thus requiring less numerical resources. The reduction is done numerically and yields a standard eigenvalue problem, which can readily be solved using the QR algorithm implemented in the free software package LAPACK (www.netlib.org/lapack). However, only a few eigenvalues are of interest in this problem, and an iterative method based on a small Krylov subspace is more efficient. Here, the implicit restarted Arnoldi algorithm from the open-source package ARPACK++ (Lehoucq et al., 1997) is used. A shift-invert transformation is applied to converge eigenvalues in the vicinity of a given complex shift. More details on the procedure, validation and resolution can be found in Leclercq et al. (2013).

In this previous study, a temporal stability analysis was carried out to predict the fastest growing perturbations with k real. It was found that among the large set of temporal modes, the most unstable ones were in the form of deformed toroidal vortices for low Re_z, or complex helical structure for higher Re_z. The modes were labelled according to a pseudo-azimuthal-integer-wavenumber m, or angular order. The labelling was made in accordance to the axisymmetric case, where normal modes can be written as $\mathbf{q}' = \tilde{\mathbf{q}}(r)\exp \mathrm{i}(kz + m\theta - \omega t)$ in polar coordinates (r, θ) (see figure 5.2). Restricting attention to positive k, because of symmetry arguments to be discussed in the next paragraph, positive values of m (resp. negative) correspond to helical structures winding clockwise (resp. counter-clockwise) around the inner cylinder, and were called left-helical (resp. right-helical), or LH$|m|$ (resp. RH$|m|$) modes. The case $m = 0$ corresponds to the classical toroidal Taylor vortex flow (TV). By following these modes as eccentricity is continuously varied, one obtains the corresponding pseudo-angular-order m for $e \neq 0$. Figure 5.4 shows the structure of modes $m = -2, \ldots, 2$ for the classical Taylor–Couette flow. When e increases, the modes are deformed and the final three-dimensional structure can be quite complex to describe.

Note that the symmetry $\Pi_0 \equiv (m, \omega, w) \rightarrow (-m, -\omega^\star, -w)$ (with * denoting the complex conjugate) between RH and LH in figure 5.4 is broken when axial flow is added, or when k is complex. Indeed, by taking the complex conjugate of the axisymmetric modal form, the general symmetry $\Pi_1 \equiv (k, m, \omega) \rightarrow (-k^\star, -m, -\omega^\star)$ appears, also valid for $e \neq 0$. By considering the mirror image of the system $(z \rightarrow -z)$, one obtains a second symmetry of (5.5), $\Pi_2 \equiv (Re_z, k, w) \rightarrow (-Re_z, -k, -w)$. Combining Π_1 and Π_2, one gets

$$\Pi_3 \equiv (Re_z, k, m, \omega, w) \rightarrow (-Re_z, k^\star, -m, -\omega^\star, -w). \tag{5.7}$$

Setting Re_z to zero and k real in Π_3, one recovers Π_0. In the general case, because of Π_3, one can choose to study only $m \geq 0$, or only $Re_z \geq 0$, without loss of generality. Π_1 also indicates that it is possible to restrict computations to $k_\mathrm{r} \geq 0$.

5.3 Criterion for absolute instability

This section is intended to recall concepts reviewed comprehensively by Huerre and Monkewitz (1990), Huerre (2000), Chomaz (2005), but essential to the rest of this paper. In this analysis we are concerned with the spatio-temporal behaviour of the wavepacket $G(z, t)$, or Green function, generated by a localised impulse forcing $\delta(z)\delta(t)$. The linear stability problem being axially invariant, the Green function can be Fourier-decomposed in z, with wavenumber k real. Because this is an initial value problem, G is Laplace-transformed in time, and ω needs to be taken complex. Using standard complex-variable techniques, the impulse response can be expressed as a superposition of temporal modes $\omega_j(k)$, for all real wavenumbers k:

$$G(z, t) = \sum_j -\frac{\mathrm{i}}{2\pi} \int_{-\infty}^{+\infty} \frac{\exp[\mathrm{i}(kz - \omega_j(k)t)]}{(\partial D/\partial\omega)[k, \omega_j(k)]} \mathrm{d}k. \tag{5.8}$$

Three situations then arise. (i) If all the modes are decaying, the flow is linearly *stable*. (ii) If at least one mode is growing but advection is strong, instabilities will develop while being convected away from the source: the flow is only *convectively* unstable. (iii)

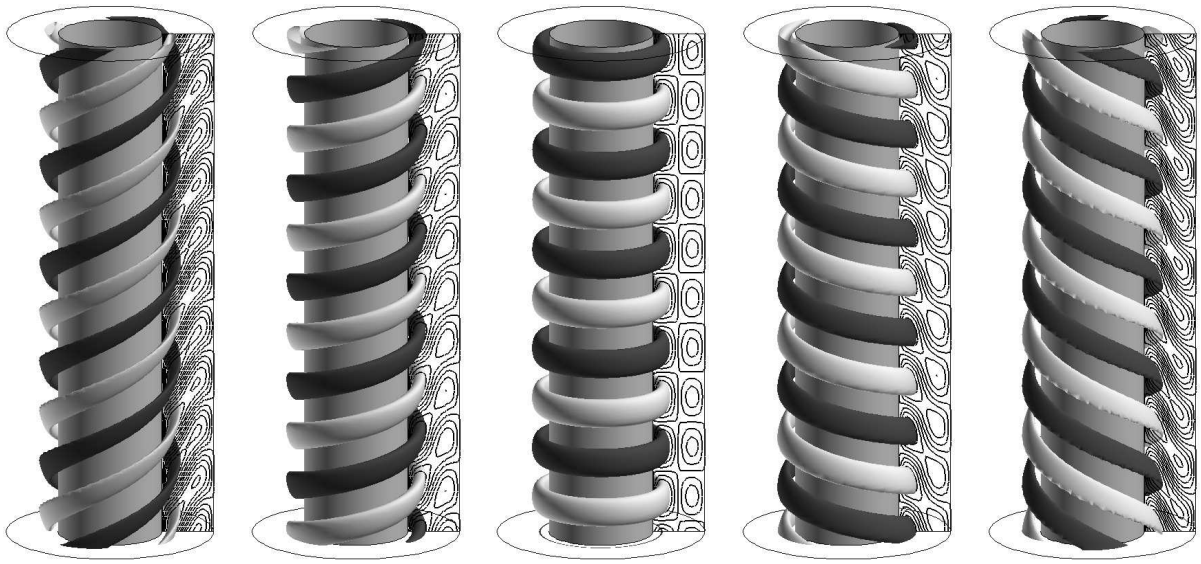

Figure 5.4 – Structure (isovalues of axial velocity) of the five modes of interest $m = -2, \ldots, 2$, from left to right. For this example, $e = 0$, $Re_\Omega = 68.19$, $Re_z = 0$ and $k = 3.16$, corresponding to the critical conditions for temporal instability of the axisymmetric Taylor–Couette flow (see DiPrima and Swinney (1985) for a review).

If at least one growing mode remains stationary in the laboratory frame, perturbations will grow in both the upstream and downstream directions, and eventually invade the whole medium at large times: the flow is said to be *absolutely* unstable.

5.3.1 Zero-group velocity condition

In order to distinguish between these 3 possibilities, one can evaluate the Green function at the point of impulse for very large times. The limit is easily calculated by considering the analytic continuation of the integrand in equation (5.8) to the complex k-plane. Cauchy's theorem implies that the value of the integral remains unchanged, if the integration path initially lying on the k_r axis is deformed into the complex k-plane. This property holds as long as the new path F_k joins the k_r axis when $|k_\mathrm{r}| \to \infty$, and hits no singularity or branch cut in the deformation process. Considering the contribution from a single temporal mode $\omega(k)$, the integral can be evaluated by following the so-called 'steepest-descent' path through stationary points, which are defined by the zero-group-velocity condition

$$\frac{\partial \omega}{\partial k} = 0. \tag{5.9}$$

This condition defines *saddle points* of $\omega(k)$, rather than local extrema, because of analycity of the dispersion relation. By following the steepest-descent path, we ensure that ω_i is maximum at the saddle point, so its contribution dominates the whole integral over F_k for large times. The wavenumber k_0 where (5.9) applies with the largest value of ω_i is called the *absolute wavenumber*, and the associated frequency $\omega_0 = \Omega(k_0)$ is called the *absolute frequency*. Using the asymptotic procedure described above, in the

long-time limit, the response at the point of impulse $z = 0$ takes the form of a plane wave

$$G(z,t) \sim A(t) \exp \mathrm{i}(k_0 z - \omega_0 t). \tag{5.10}$$

Given this expression, a condition for AI is that the *absolute growth rate* $\omega_{0,\mathrm{i}}$ be positive.

5.3.2 Fronts

In the general case, the wavepacket can be approximated by an expression similar to (5.10) along any spatio-temporal ray $z/t = V$, when $t \to \infty$. The 'local' wavenumber k_* and frequency $\omega_* = \Omega(k_*)$ in (5.10) are then given by the stationarity-condition (5.9) applied to $\omega - kV$, the apparent frequency in a reference frame translated at velocity V. In this case, (5.9) is replaced by $\partial\omega/\partial k|_{k_*} = V$. If the apparent temporal growth rate $\sigma \equiv \omega_{*,\mathrm{i}} - k_{*,\mathrm{i}} V$ is zero, V defines a *front* of the wavepacket. Any unstable wavepacket is bounded by a *leading front* with group velocity V_+, and a *trailing front* with group velocity $V_- < V_+$. In the absolutely unstable case, $V_+ > 0$ and $V_- < 0$.

5.3.3 The pinching criterion

Despite the apparent simplicity of the AI criterion given in §5.3.1, one must examine very carefully which saddle point will dominate the impulse response, among the potentially large set of stationary points of $\omega(k)$. One extra condition applies, and is known as the Briggs (1964)–Bers (1983) *pinching criterion*. Using a Taylor expansion in the vicinity of a saddle point, it is easily shown that the stationarity condition corresponds to a 'collision' between two *spatial branches*, denoted as $k^{\pm}$:

$$k^{\pm}(\omega) = k_0 \pm \left(\frac{2}{\omega_{kk}}\right)^{1/2} (\omega - \omega_0)^{1/2}, \text{ with } \omega_{kk} = \left.\frac{\partial^2 \omega}{\partial k^2}\right|_{k_0} \tag{5.11}$$

Physically, these solutions of the dispersion relation correspond to the spatial responses to a localised forcing at $z = 0$, with complex frequency ω. Causality requires that if the temporal growth rate of the forcing is larger than that of all the temporal modes, then the spatial response should decay away from the source. In practice, it means that if one follows the two spatial branches by increasing the temporal growth rate of the forcing, one solution should eventually lie in the upper-half k-plane, while the other should be in the lower-half k-plane. Indeed, the solution with $k_\mathrm{i} > 0$ will decay for $z > 0$, while the other one will decay for $z < 0$. The branch contributing to the spatial response for $z > 0$ (resp. $z < 0$) is usually denoted k^+ (resp. k^-). The 'pinching' of a k^+ and a k^- corresponds to a spatial response smoothly varying from $z = -\infty$ to $z = +\infty$, in the form of equation (5.10), with no necessity of a forcing at $z = 0$ to accomodate a discontinuity: the system behaves as a *resonator*. In many cases, saddle points do not satisfy the pinching criterion and correspond to the coalescence of two upstream or downstream propagating branches. These 'spurious' saddle points should be discarded on physical grounds. In practice, including them in the integration path F_k would violate the steepest-descent method: in order to join the k_r axis at infinity, a 'hill' of the function $\omega_\mathrm{i} = \Omega_\mathrm{i}(k)$ has to be crossed, and the saddle point would not dominate the response for large times.

5.3.4 Numerical method

In order to determine the border of the absolutely unstable domain, it is necessary to follow all the neutrally stable saddle points. This is done by performing Newton–Raphson iterations, varying simultaneously k_r, k_i and Re_Ω until $|\omega_\mathrm{i}|$, $|\mathrm{Re}(\partial\omega/\partial k)|$ and $|\mathrm{Im}(\partial\omega/\partial k)|$ are below 10^{-6}. Estimated values for the independent variables are obtained by linear extrapolation with respect to the parameter being varied, e. g. e, Re_Ω or Re_z. For $|m| = 2$, critical curves display folds, and it is necessary to implement a continuation scheme based on an arclength variable (Keller, 1977).

In a second step, extensive checks are made to determine when saddle points remain valid. This is done by numerically tracking the two spatial branches coalescing at a saddle point, and checking that they separate into the upper- and lower-half k-plane when ω_i is increased. Spatial k-branches are obtained by numerically inverting the relation $\omega = \Omega(k)$ with a Newton–Raphson iteration.

5.3.5 Validation

To validate the numerical procedure, critical curves in the axisymmetric case were computed and compared with literature results. For $m = 0$ and 1, Pinter et al. (2003) provide the coefficients of fourth-order polynomials f_m fitting their data in the range $-20 \leq Re_z \leq 20$, with step $\delta Re_z = 1$. The same procedure was applied here, and our calculated values $\tilde{g}_m$ at the same points were fitted by polynomials g_m. To compare our results, the residual $\sum_{-20}^{20} |f_m(Re_z) - g_m(Re_z)|^2$ between the two fits was divided by the residual $\sum_{-20}^{20} |g_m(Re_z) - \tilde{g}_m(Re_z)|^2$ between our fit and our calculated values. For $m = 0$ and 1, this ratio is respectively 1.16×10^{-2} and 1.10×10^{-2}, showing agreement with the authors' calculations. For $m = 2$, only graphical data was available, and figure 5.5 shows excellent agreement with the 'island' of instability found by Altmeyer et al. (2011) in Re_Ω-Re_z plane. In their analysis, the authors considered only the saddle points originating at the real critical wavenumber k_c of temporal instability with $Re_z = 0$, as will be explained now. At critical conditions for temporal instability $(k_c, Re_{\Omega,c})$, the leading and trailing fronts (see section §5.3.2 for definition) of the impulse response wavepacket are degenerate. For Re_Ω slightly above $Re_{\Omega,c}$ however, the medium is convectively unstable and two fronts can be defined, that bound the temporally growing region of the wavepacket. Each front has a complex wavenumber $k_* \approx k_c$ and a velocity $V_\pm \approx \partial\omega/\partial k|_{k_c}$. By increasing Re_Ω further, one front changes propagation direction, which corresponds formally to the saddle-point condition (5.9), and defines the threshold of AI. When other parameters are varied, typically when $Re_z < 0$, the other front can also satisfy (5.9) and cause a CI/AI or AI/CI transition. In Altmeyer et al. (2011), only the two fronts bounding the convectively unstable wavepacket at Re_Ω slightly above $Re_{\Omega,c}$ and $Re_z = 0$ were considered. These specific fronts were followed as Re_Ω and Re_z were varied, and the AI boundary in figure 5.5 corresponds to points where one of the fronts was stationary. Saddle points corresponding to other stationary fronts were ignored in figure 5.5, even though the authors mentioned the existence of other relevant ones. Note that validation for $m \geq 0$ is sufficient because of the Π_3-symmetry (5.7).

In this study, only values of $|m| \leq 2$ will be considered and a small number of Fourier modes $K = 8$ is deemed satisfactory, as can be seen in table 5.1. A higher number of

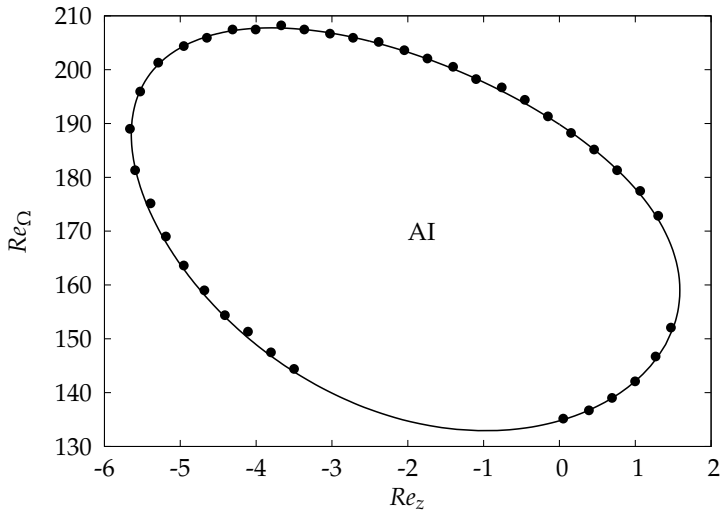

Figure 5.5 – 'Island' of AI in the axisymmetric case, for mode LH2. Line: present calculation; dots: figure 8*(b)* in Altmeyer et al. (2011).

m	0		1		-1		2		-2	
e	0.3	0.7	0.3	0.7	0.3	0.7	0.45	0.7	0.45	0.7
16×8	402.59	283.22	475.66	285.22	431.88	300.21	465.54	305.73	472.77	347.83
16×16	402.59	283.32	475.66	285.70	431.88	300.22	465.54	306.79	472.77	347.90
32×32	402.59	283.33	475.65	285.71	431.88	300.29	465.52	306.80	472.46	348.34

Table 5.1 – Critical azimuthal Reynolds number Re_Ω for $Re_z = 50$ and different resolutions $(M+1) \times K$.

Chebyshev polynomials $M + 1 = 16$ is however required for accuracy at large Re_Ω.

5.4 Results

A parametric study has been performed within the ranges $e \leq 0.7$, $0 \leq Re_z \leq 60$ and $0 \leq Re_\Omega \leq 500$. Within these bounds, modes $m = 0, 1, 2$ are always the most temporally unstable, except for a small range $e \leq 0.3$, $50 \leq Re_z \leq 60$, where $m = 3$ has the largest temporal growth rate (Leclercq et al., 2013). It will be assumed that the absolute growth rate of these modes will be higher than that of $|m| \geq 3$. However, right helical modes RH1 and RH2 will be retained in the analysis, as RH are known to be more absolutely unstable than TV and LH in some cases (e. g. high Re_z, outward radial flow, $e = 0$, cf. Martinand et al. (2009)). Because we are considering both positive and negative m, it is unnecessary to consider negative Re_z, because of the Π_3-symmetry (5.7).

5.4.1 Reference saddle point

The bifurcation to (pseudo-)toroidal vortices without axial flow is a steady one, $\omega_\mathrm{r}(m = 0) = 0$, so CI and AI thresholds, respectively denoted here $Re_{\Omega,c}$ and $Re_{\Omega,c-a}$,

coincide in this case. For modes $m \neq 0$, CI occurs through Hopf bifurcations at $Re_z = 0$, so AI only occurs above a higher threshold: $Re_{\Omega,c-a} > Re_{\Omega,c}$. For these modes, $Re_{\Omega,c-a}(Re_z = 0)$ is found by locating the saddle point with k_0 closest to k_c, the real critical wavenumber of CI. This neutral saddle point corresponds to a stationary front of the impulse response wavepacket for Re_Ω just above $Re_{\Omega,c}$, as explained in detail in section §5.3.5. For $m = 1, 2$, the stationary front is the trailing one: $V_- = 0$, $k_{0,\mathrm{i}} < 0$. For negative m, $k_{0,\mathrm{i}} > 0$ because of the Π_3-symmetry (5.7), and the stationary front is the leading one: $V_+ = 0$. The present paragraph defined the *reference saddle point* for each m, obtained for $Re_z = 0$ and $e = 0$. These saddle points are systematically followed in parameter space to define critical curves of AI. However, as will be seen in the next paragraph, other saddle points are also relevant to the spatio-temporal dynamics.

5.4.2 Multiplicity of saddle points

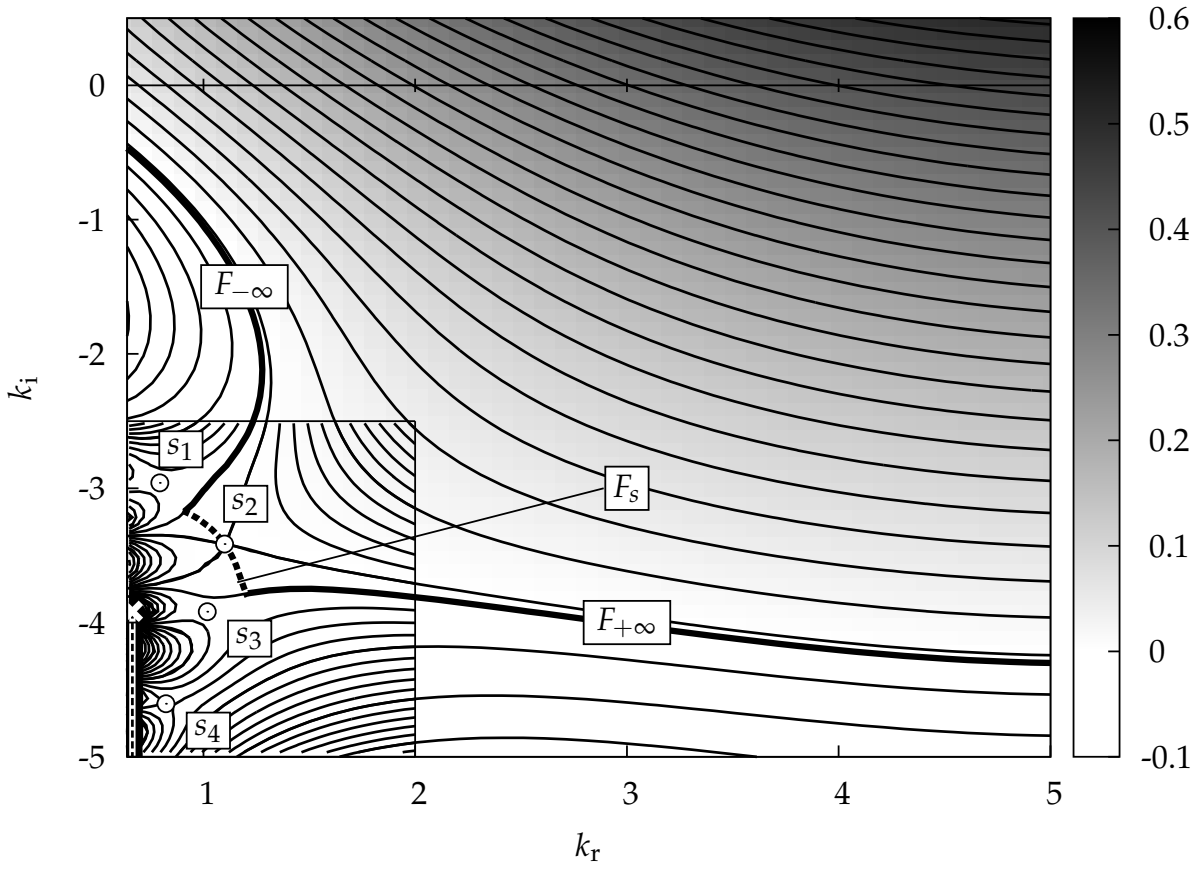

Figure 5.6 – Contours of constant growth rate for $m = 0$ at criticality; $e = 0.3075$, $Re_z = 60$ ($Re_\Omega = 472.24$). Saddles are indicated by white dots, labelled $s_{1,2,3,4}$. The integration path (thick line) passes through 'pinch point' s_2 on the steepest descent path F_s, and joins the k_r axis at $\pm\infty$ through contours $F_{\pm\infty}$ of constant $\omega_\mathrm{i} = -0.004$. The white cross indicates a branch point $\partial k/\partial\omega = 0$, associated to a branch cut (straight dotted line).

In the light of the theoretical elements recalled in section §5.3, let us examine closely the dispersion relation of mode $m = 0$ for a strong axial advection $Re_z = 60$, and three eccentricities around $e = 0.3$. Figure 5.6, similar to figure 2 in Juniper (2006), shows isocountours of the function $\omega_\mathrm{i} = \Omega_\mathrm{i}(k)$, for the case $e = 0.3075$ (and $Re_\Omega =$

472.24). Dark shade indicates a 'hill', or a region of high ω_i, while 'valleys' (low ω_i) are indicated in lighter shades. Saddle points are indicated by white dots. Four saddle points, labelled $s_1, \ldots, s_4$, are seen in the range $0.6 \leq k_\mathrm{r} \leq 5$, $-5 \leq k_\mathrm{i} \leq 0.5$. There is a branch point, indicated with a white cross near $k = 0.7 - 4\mathrm{i}$, and corresponding to a collision of temporal modes for that specific value of k. Its associated branch cut, oriented towards negative k_i, is represented with a dotted white line. The thick black line indicates the chosen integration path F_k for this case, made up of three different curves: $F_{-\infty}, F_s, F_{+\infty}$. F_s (thick dashed line) follows the steepest-descent path passing through saddle s_2, namely keeping ω_r constant and equal to its value on s_2. $F_{\pm\infty}$ connects F_s to the k_r axis at $|k_\mathrm{r}| \to \infty$ following lines of constant $\omega_\mathrm{i} = -0.004$. For the given parameter values, the growth rate associated with saddle s_2 is zero, hence $F_{\pm\infty}$ add subdominant contributions to the impulse response at $z = 0$. By zooming on the lower-left-hand corner (cf. figure 5.7*(b)*), we notice that both s_1 and s_2 satisfy the pinching condition, whereas s_3 and s_4 do not. Indeed, increasing the value of ω_i from a saddle point and following the coalescing spatial branches requires 'climbing' up the two dark 'hills' surrounding the white dot. The direction of 'climb' is perpendicular to the isovalues of ω_i, because $\omega(k)$ is analytic. For high values of ω_i, we see graphically that s_1 and s_2 will share a common downstream propagating branch k^+, but each saddle will have its own upstream propagating branch k_1^-/k_2^-. On the other hand, s_3 and s_4 are of k^-/k^--type. s_3 shares one k^- branch with s_2, and the other one with s_4. The saddle s_2 has a zero growth rate, but s_1 has a negative growth rate for these conditions, hence s_2 is the dominant 'pinch point', which is confirmed by the appropriate choice of the integration path F_k. For the chosen control parameter values, s_2 sets the frontier between CI and AI. If the rotation rate is increased further, then the absolute growth rate will be positive and the entire flow will bifurcate to a new state for large times.

Now if we vary the eccentricity about $e = 0.3075$, while keeping Re_z constant, and imposing the criticality condition $\omega_{0,\mathrm{i}} = 0$, we obtain figures 5.7*(a)* for $e = 0.285$ and 5.7*(c)* for $e = 0.33$. For $e = 0.285$, s_1 is the dominant 'pinch point', whereas for $e = 0.33$, s_3 dictates the long-term dynamics. Interestingly, figure 5.7 shows that there is a switch of critical saddle point when eccentricity is varied about $e \approx 0.3$. This example clearly shows that not only the ranking of the 'pinch points', in terms of absolute growth rate, can change, but also the nature of saddle points can vary, e. g. invalid saddle point versus 'pinch point'. This makes the application of the Briggs–Bers criterion quite tricky in this situation.

Maps similar to figure 5.6 are drawn for each m, and a large number of saddle points are identified each time. Saddle points with growth rate close to the *reference-saddle-point*'s are systematically identified, and followed in parameter space. As indicated in §5.3.4, the final critical curves are based on the most unstable saddle point satisfying the pinching criterion. Over the whole range of parameters, three different 'pinch points' are found to be relevant for TV, two for LH1, LH2 and RH2, but surprisingly, just one for RH1, despite numerous candidate saddle points.

5.4.3 Critical azimuthal Reynolds number

In figure 5.8, the critical azimuthal Reynolds number is represented as a function of eccentricity, for $Re_z = 0, 10, \ldots, 60$. We start by describing the curves in terms of m.

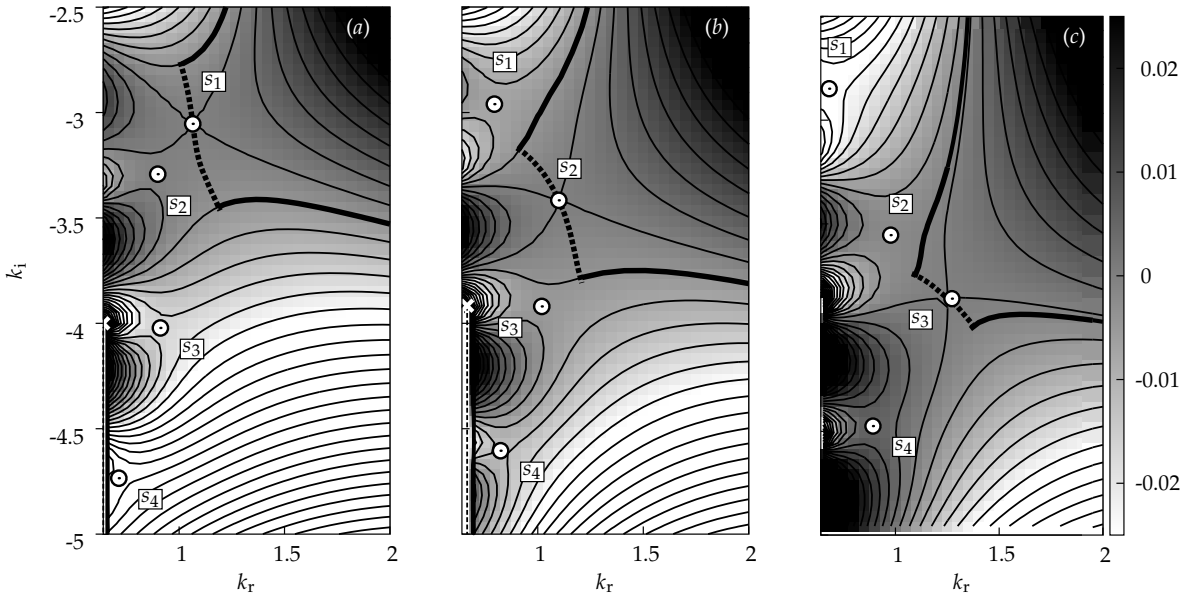

Figure 5.7 – Magnification of the bottom-left corner of figure 5.6 for the same value of Re_z, three eccentricities around $e \approx 0.3$ and their associated critical Re_Ω; *(a)* $e = 0.285, Re_\Omega = 471.65$, F_s passes through s_1, *(b)* zoom of previous figure, F_s passes through s_2, *(c)* $e = 0.33, Re_\Omega = 468.00$, F_s passes through s_3 (contours $F_{\pm\infty}$ defined by $\omega_i = -0.001$ here).

Solid lines correspond to $m \geq 0$, and dotted lines are for $m < 0$. Changes of critical saddle point are indicated with a filled (resp. open) circle for $m \geq 0$ (resp. $m < 0$). The most important result is that for any value of e and Re_z, $m = 0$ always has the lowest critical Re_Ω, followed by $|m| = 1$, and finally $|m| = 2$. This observation gives credence to the assumption that modes with $|m| \geq 3$ can be ignored in the analysis. Curves 5.8*(b)* and 5.8*(c)* also prove the importance of considering both positive and negative m, as LH are not always more absolutely unstable than RH. Indeed, for low eccentricities, RH1 is slightly more unstable than LH1, but the converse is true for high eccentricities. The dynamics is even more subtle for $|m| = 2$, as LH2 are generally more unstable than RH2, except for a small range of eccentricities that varies with Re_z.

The effect of axial advection is to stabilize all the modes. For high enough Re_z, the critical Re_Ω seems to increase almost linearly with Re_z. The rate of increase is much stronger for low eccentricities than for high eccentricities, regardless of the value of m, as already mentioned. Critical Re_Ω are typically one order of magnitude higher than Re_z, which means that the inner cylinder must be rotated much faster than the mean axial velocity to have self-sustained oscillations. Indeed, axial flow prevents AI by carrying perturbations downstream while rotation amplifies them.

The effect of eccentricity is more complex than that of Re_z. For low eccentricities, Re_Ω increases slowly for $m = 0, 1$, but decreases for all other modes. For high enough e, all the curves have the same shape: Re_Ω decreases before reaching a minimum and then increases again beyond this minimum. TV and LH1 display another similarity: they switch critical saddle point between $0.2 \leq e \leq 0.4$, for high enough Re_z. This change of saddle point coincides with the change in sign of the slope: critical Re_Ω increases with e for the first saddle point, but decreases for the second one. As was already mentioned

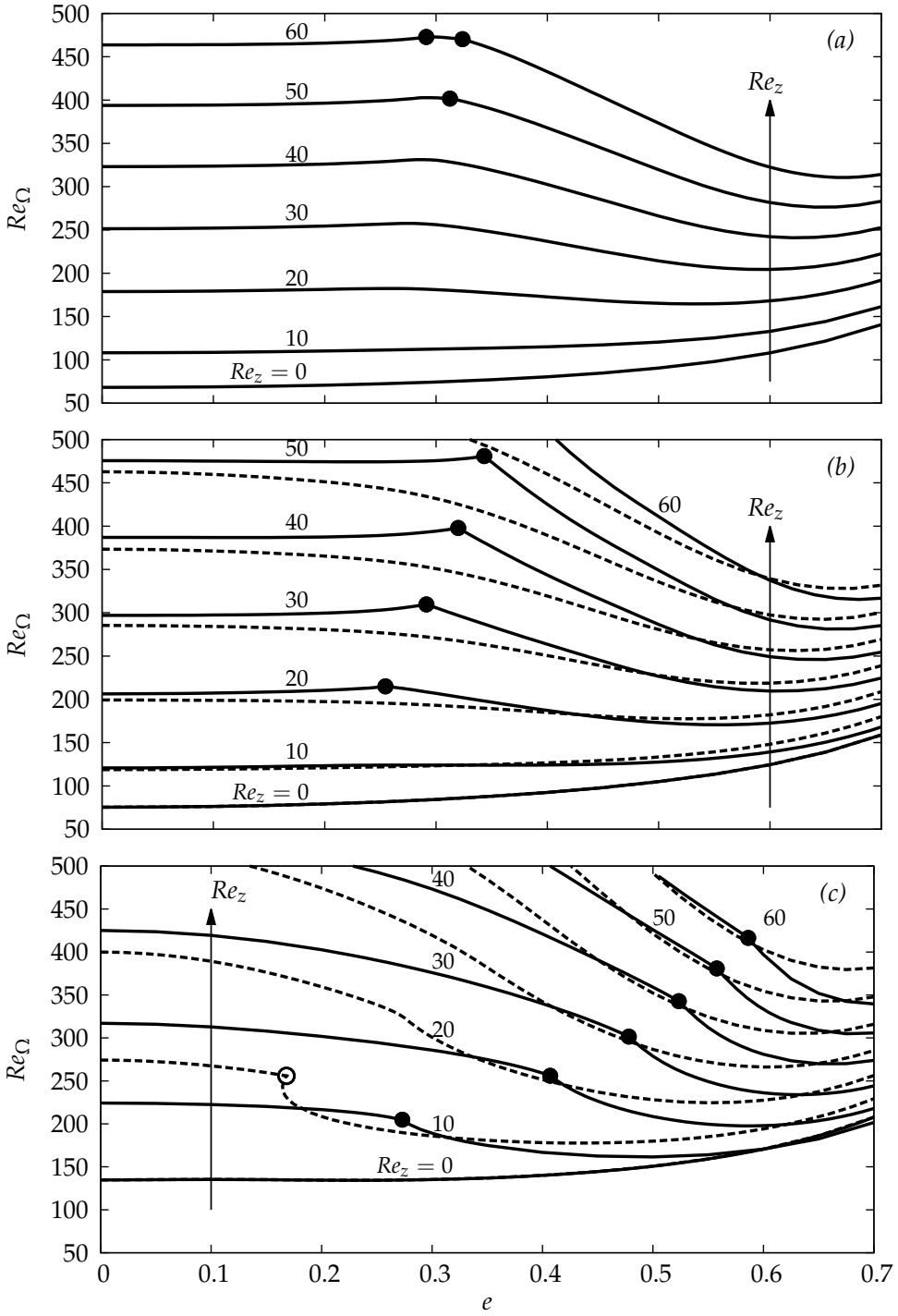

Figure 5.8 – Critical azimuthal Reynolds number Re_Ω versus eccentricity e for *(a)* $m = 0$, *(b)* $|m| = 1$ and *(c)* $|m| = 2$. Curves are drawn for $Re_z = 0, 10, \ldots, 60$. Solid lines are for $m \geq 0$, and dotted lines for $m < 0$. Filled/open dots indicate a change of saddle point.

in paragraph §5.4.2, TV even changes twice 'pinch point' for $Re_z = 60$. On the other hand, the critical curves for RH1 are smooth, because they are obtained by continuously following a single saddle point. Finally, two saddle points define the critical curves of LH2 and RH2. For low values of Re_z and e, the AI threshold is quite complex, and the curves display folds. Folds in the critical curves mean that there are finite ranges of AI in parameter space, surrounded by CI. This unusual behaviour has already been

pointed out by Altmeyer et al. (2011) in the concentric case, but it seems important here to underline the fact that for high enough Re_Ω, all the modes eventually become absolutely unstable, regardless of any 'island' of AI occurring at lower Re_Ω (cf. figure 5.5).

5.4.4 Critical absolute wavenumber $k_{0,\mathrm{r}}$

Figure 5.9 shows the evolution of the absolute wavenumber $k_{0,\mathrm{r}}$, spatial growth rate $-k_{0,\mathrm{i}}$ and frequency $\omega_{0,\mathrm{r}}$ associated with the dominant mode $m = 0$, at critical conditions. As before, curves are plotted as functions of e, for $Re_z = 0, 10, \ldots, 60$. The absolute wavenumber $k_{0,\mathrm{r}}$ (figure 5.9*(a)*) evolves in different ways below and above $e \approx 0.3$. Below $e \approx 0.3$, critical modes have longer wavelengths as Re_z increases, spanning up to 6 times the clearance for $Re_z = 60$ and $e \approx 0.3$. When e is high enough, the trend is the opposite, and critical modes have shorter wavelengths as Re_z increases. Below $e \approx 0.3$, $k_{0,\mathrm{r}}$ is almost constant, or slightly decreasing with e, whereas above $e \approx 0.3$, it is clearly increasing with e. For large enough e, the critical wavelength seems to be controlled by the smaller clearance $d(1 - e)$. Small discontinuities in $k_{0,\mathrm{r}}$ around $e \approx 0.3$ indicate a change of critical saddle point.

Comments on the curves obtained for other m, although not displayed here for clarity, can be made. First, curves of $k_{0,\mathrm{r}}$ for LH1 are very similar to those of TV, except that LH1 only changes once saddle point for $Re_z = 60$ instead of twice for TV. Ignoring the change of saddle point, they are also qualitatively similar to those of RH1. For all m, $k_{0,\mathrm{r}}$ always increases with e for high enough eccentricities, showing that all modes scale with the small gap at critical conditions. For $|m| = 2$, large values of $k_{0,\mathrm{r}}$ up to 8 and more are obtained for low eccentricites as well, provided Re_z is high enough. This behaviour is not found for other modes, where $k_{0,\mathrm{r}}$ is always between 1 and 3.5 when $e \lesssim 0.3$. For LH2 and RH2, a large discontinuity of axial wavenumber is observed upon switching saddle point. For example, $k_{0,\mathrm{r}}$ of LH2 varies from about 7.5 to about 3.5 for $Re_z = 60$ and $e \approx 0.6$.

5.4.5 Critical absolute spatial growth rate $-k_{0,\mathrm{i}}$

The absolute spatial growth rate $-k_{0,\mathrm{i}}$ (figure 5.9*(b)*) measures the 'steepness' of the stationary front of the impulse response wavepacket. For $e \lesssim 0.3$, it is slightly increasing with e. It varies quickly for $Re_z \lesssim 20$, and then slowly varies in the range $2.5 \lesssim -k_{0,\mathrm{i}} \lesssim 4$ for higher Re_z. For $e \gtrsim 0.3$, $-k_{0,\mathrm{i}}$ increases with e, reaches a maximum value, and then decreases again. For high enough e, $-k_{0,\mathrm{i}}$ increases steadily with Re_z.

Similar trends are noticed for LH1 and RH1, with comparable ranges of values. For LH2 and RH2 however, the curves are quite different. For low eccentricities, $-k_{0,\mathrm{i}}$ increases significantly with Re_z, whereas it is almost constant for other m. Therefore, extreme front steepness occurs for LH2 at low e, with $-k_{0,\mathrm{i}} > 12$ for $Re_z = 60$.

For RH1 and RH2 at low Re_z, $-k_{0,\mathrm{i}}$ can be negative over the whole range of eccentricities. Physically, this means that the stationary front is the leading one in this case $V_+ = 0$ (cf. section §5.3.2), and that the most temporally unstable RH wave has a negative group velocity.

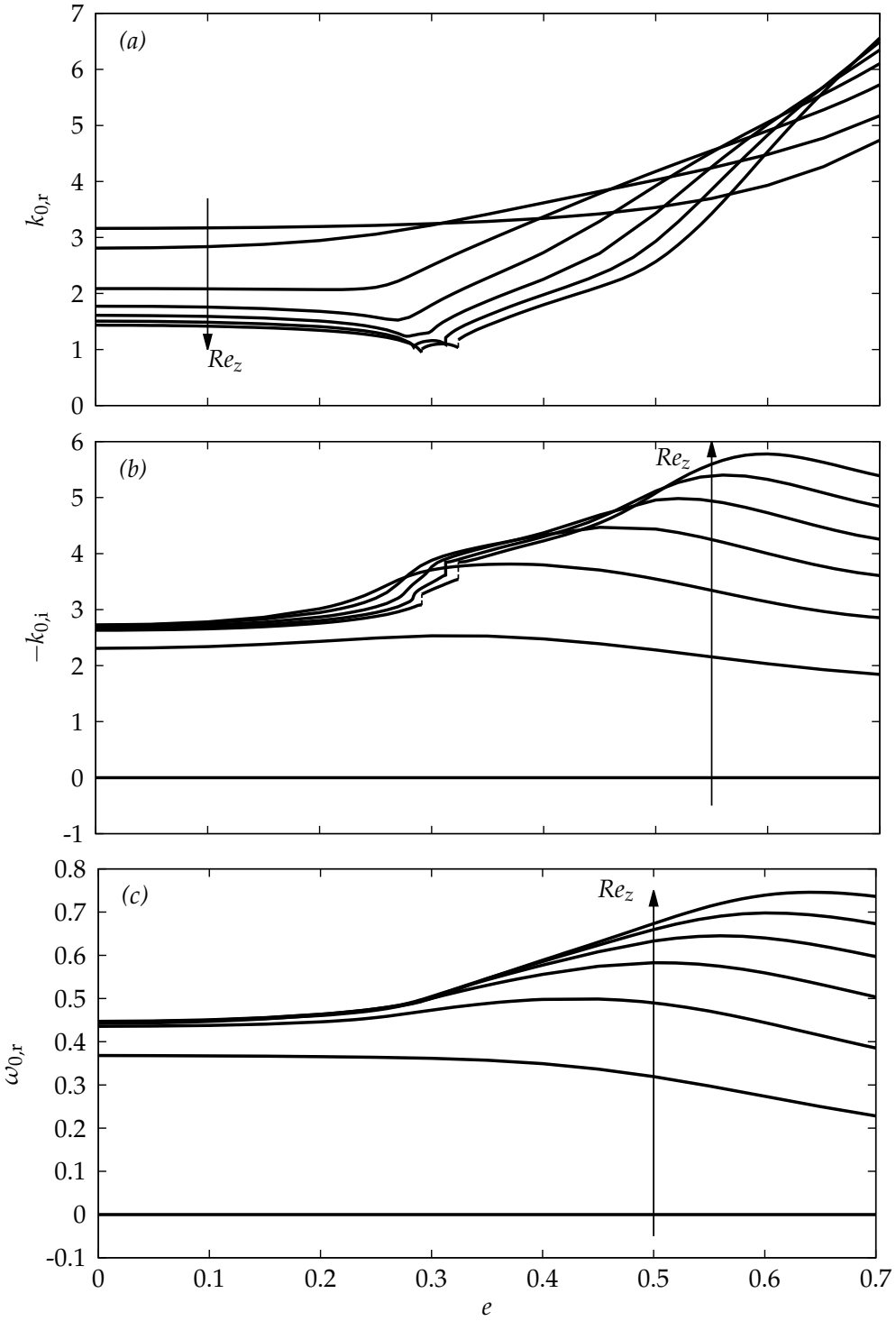

Figure 5.9 – *(a)* Absolute wavenumber $k_{0,\mathrm{r}}$, *(b)* spatial growth rate $-k_{0,\mathrm{i}}$ and *(c)* frequency $\omega_{0,\mathrm{r}}$ for $m = 0$ at critical conditions, versus eccentricity e. Curves are given for $Re_z = 0, 10, \ldots, 60$.

Finally, a common feature of all m is that $-k_{0,\mathrm{i}}$ has a maximum as a function of e.

5.4.6 Critical absolute frequency $\omega_{0,\mathrm{r}}$

The absolute frequency $\omega_{0,\mathrm{r}}$ (figure 5.9*(c)*) is given here for reference. After nonlinear saturation of the instability, self-sustained oscillations with frequency close to $\omega_{0,\mathrm{r}}$ are expected for a supercritical transition. Therefore, the values of $\omega_{0,\mathrm{r}}$ can be used as a good estimate of the hydrodynamic resonance frequency of the flow, and may be of interest for engineering applications. The trends of the curves are very similar to those obtained for the spatial growth rate. The frequency range is shifted towards higher values as m increases. For RH1 and RH2, $\omega_{0,\mathrm{r}}$ can be negative (always the case for RH2), indicating that the absolute phase speed $c_0 \equiv \omega_{0,\mathrm{r}}/k_{0,\mathrm{r}}$ of the mode is negative in this case. Finally, discontinuities in the absolute frequency occur for all modes but RH1, because of changes in critical saddle point. Discontinuities are not clearly visible for $m = 0$ and the change of saddle point is 'smooth', as will be discussed later in §5.5.4.

5.4.7 Absolute temporal growth rate $\omega_{0,\mathrm{i}}$ maps

Critical curves in §5.4.3 indicate the AI domain for each m. However, they do not indicate which mode will be the most absolutely unstable if Re_Ω is above two or more thresholds. Indeed, the mode which bifurcates first as Re_Ω is increased does not necessarily have the highest absolute growth rate $\omega_{0,\mathrm{i}}$ for larger driving. Figure 5.10 represents isocontours of $\omega_{0,\mathrm{i}}$ in Re_Ω-Re_z plane for $m = 0, 1, 2$, and $e = 0, 0.2, 0.7$. Curves for $m = -1, -2$ can be recovered upon applying the Π_3-symmetry (5.7).

The first conclusion is that $m = 0$ remains the most unstable mode over the whole range of parameters. However, for $e = 0.7$, isocontours of $m = 1$ are very close to those for $m = 0$, and one may expect LH1 to become more absolutely unstable than TV for larger eccentricities and large Re_z.

Isocontours of $\omega_{0,\mathrm{i}}$ for $m = 1$ and $m = -1$ (using Π_3-symmetry) are generally close. For low eccentricity, RH1 is always more unstable than LH1, but for high eccentricity, the converse is true. For a moderate eccentricity of $e \approx 0.5$ (not shown here), the dominant mode depends on the specific values of Re_Ω and Re_z.

For $m = 1, 2$, some isocontours have discontinuous slopes, as a consequence of a change of dominant saddle point. In figure 5.10*(3a)*, the 'island' of instability previously presented in figure 5.5 is shown to be connected to a 'continent', for higher values of Re_Ω, via a change of critical saddle point. Indeed, in their analysis of $m = 2$ in the axisymmetric case, Altmeyer et al. (2011) restricted their analysis to the *reference saddle point* defined in §5.4.1, even though the authors mentioned the existence of other saddle points. Figure 5.10*(3a)* gives the complete AI boundary for this case. For higher eccentricities, the 'continent' of instability absorbs the 'island', and for $e = 0.7$, the saddle point associated to the 'island' is always sub-dominant. When considering the saddle point associated with the 'continent', LH2 is generally more unstable than RH2. On the other hand, for low e and very low Re_z, RH2 can be more unstable than LH2 because of the 'island' of instability. For moderate eccentricities, the ordering depends on the specific values of Re_Ω and Re_z.

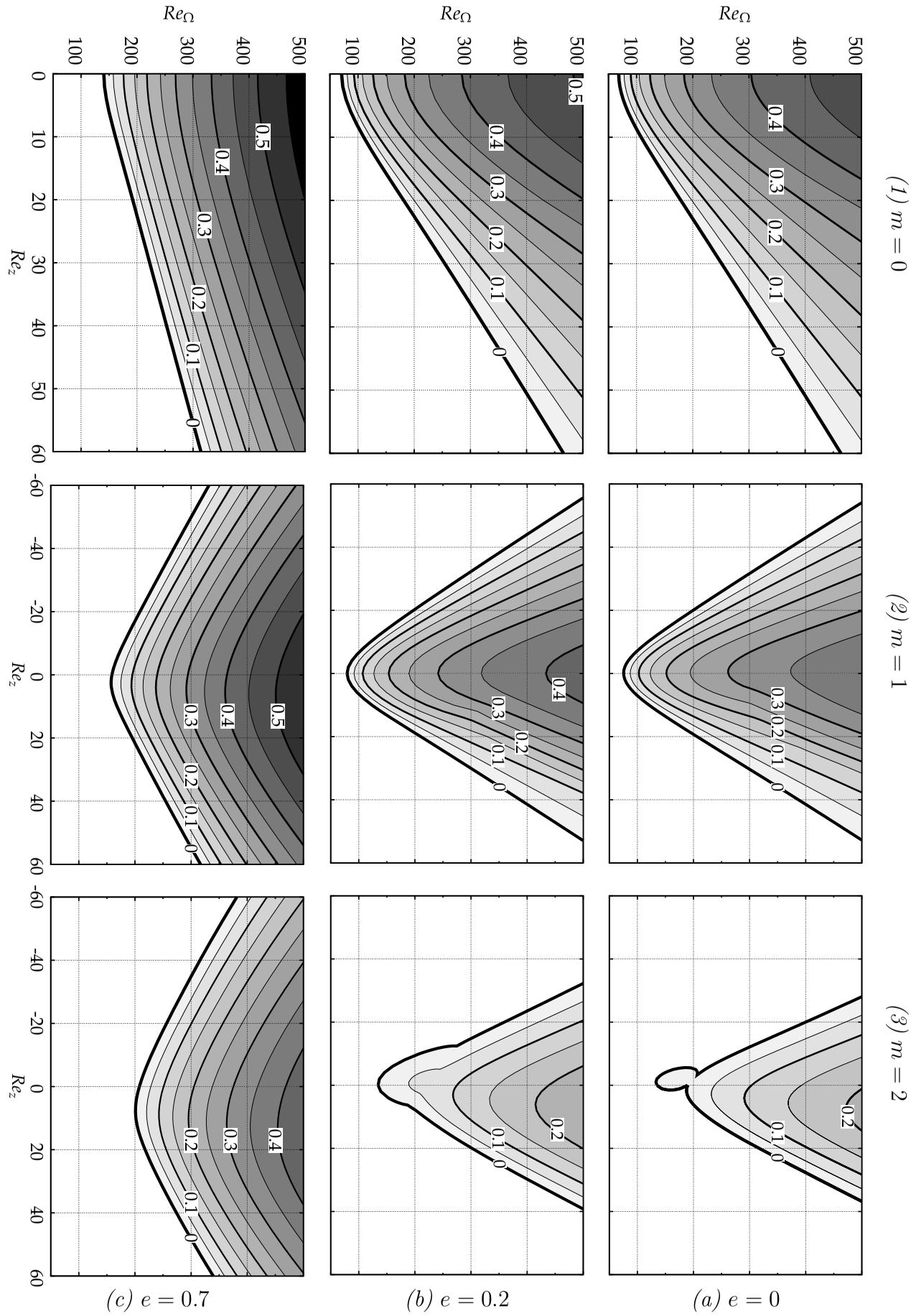

Figure 5.10 – Absolute growth rate $\omega_{0,\mathrm{i}}$ maps for $e = 0, 0.2, 0.7$, $m = 0, 1, 2$.

5.5 Discussion

In this section, we study the critical modes and the production of perturbation kinetic energy. We discuss the results and the instability mechanism in the light of these elements. Identification of third-order saddle points in the dispersion relations, and implications for the results is then discussed. Finally, a comparison between CI and AI thresholds is provided.

5.5.1 Critical modes

Examining the critical mode associated with $m = 0$ for $Re_z = 60$, we notice that localisation of the mode depends strongly on eccentricity. In figure 5.11*(1)*, we plot isocontours and isosurfaces of the axial perturbation velocity for $e = 0.2, 0.4, 0.7$, and the corresponding distribution of perturbation kinetic energy $\mathcal{E} = \frac{1}{2}(|\tilde{u}|^2 + |\tilde{v}|^2 + |\tilde{w}|^2)$ (figure 5.11*(2)*). These three eccentricities correspond to distinct evolutions of the critical Re_Ω with respect to e: slight increase for $e = 0.2$, clear decrease for $e = 0.4$ and increase for $e = 0.7$.

Consider the polar angle θ of the maximum of energy, with respect to the inner cylinder center, indicated in figure 5.2. For low eccentricities or low Re_z, the mode is localised in the wide gap, at positive θ. However, for larger e or Re_z, this maximum is shifted upstream to the region $-90° \leq \theta \leq 0°$. For $e = 0.7$, the mode concentrates in the vicinity of the inner cylinder, on the wide gap side, but has a radial extent scaling with the small gap. When e increases for $Re_z = 60$, the ratio between the maximum, and the average value increases from less than 2 for $e = 0$ to almost 14 for $e = 0.7$, indicating confinement of the mode into a smaller region of the annulus. Finally, the only contribution of $\tilde{\mathbf{u}}_\perp$ to $\mathcal{E}$ accounts for 65% to 85% of the total perturbation energy when e increases from 0 to 0.7.

Similar behaviour is found for LH1 at $Re_z = 60$, with localisation of the mode in the wide gap for low e, close to the symmetry plane, then a shift towards negative θ upon switching saddle point, and finally, concentration of the mode in the vicinity of the inner cylinder, in the wide gap region. For RH1 however, the energy is less concentrated at a specific peak. The maximum of $\mathcal{E}$ still occurs at negative angles, but does not go beyond $-45°$ in this case. It is concluded that the appareance of the peak of perturbation energy at strong negative angles is associated with the change of saddle point occuring for both TV and LH1.

Surprisingly, the critical modes of AI and CI peak at completely different regions of the annulus for moderate eccentricities and high Re_z. In comparison (cf. Leclercq et al. (2013)), the maximum energy of the critical mode of CI for $e = 0.5$ was always localised at large positive values: 79° for $Re_z = 0$ ($m = 0$), and 121° for $Re_z = 200$ ($m = 5$). No direct comparison should be made with AI because critical modes of CI are obtained for different threshold values of Re_Ω. It is nonetheless interesting to observe that modes can be localised at either positive or negative polar angles depending on the situation.

Finally, we enumerate characteristics common to all m. First, in-plane motion accounts for the larger contribution to the total perturbation kinetic energy of all m for $Re_z = 60$. Also, as e approaches 0.7 for $Re_z = 60$, all m tend to have similar distributions

of energy, with strong localisation close to the inner cylinder, over a radial extent scaling with the small gap. In addition, we recall that the critical wavenumber of all modes takes on large values $k_{0,\mathrm{r}} \sim 6.5 - 8$ when $e = 0.7$ and $Re_z = 60$. These observations indicate that for high eccentricities, the critical modes for all m scale with the small gap.

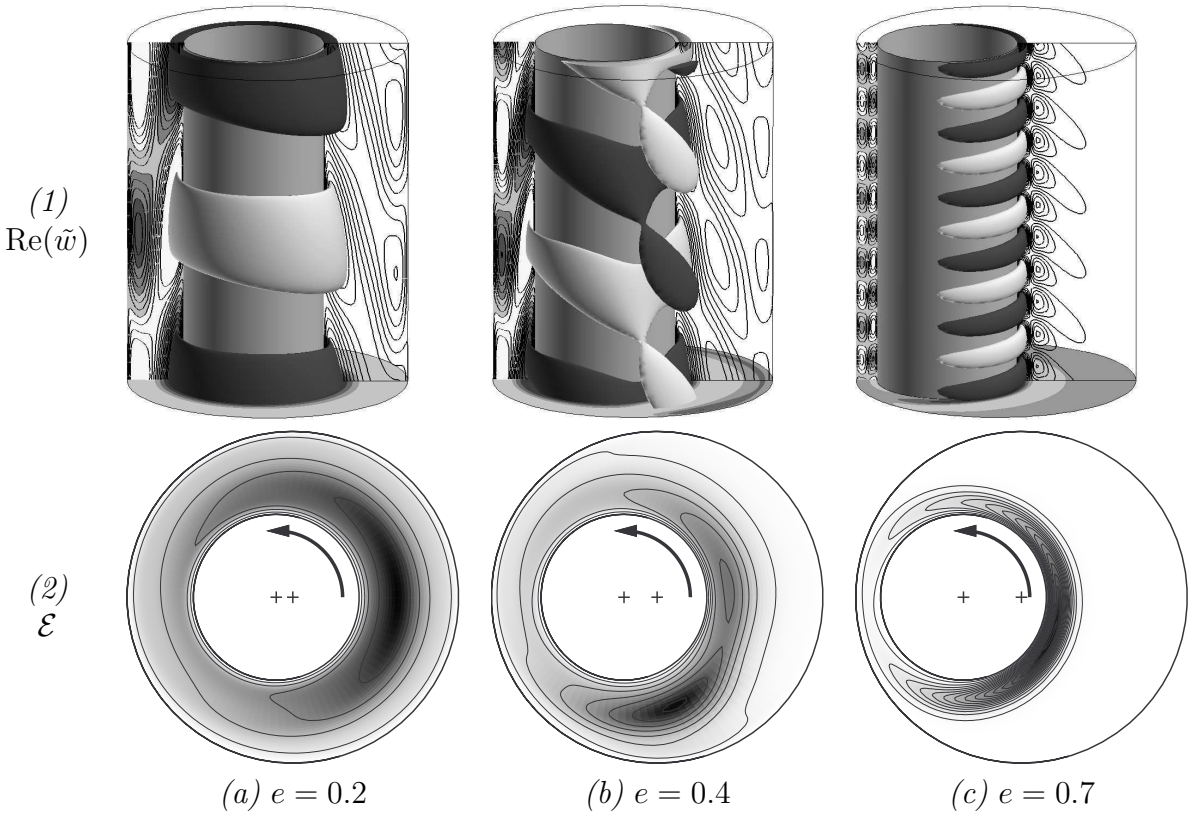

Figure 5.11 – Critical mode $m = 0$ for $Re_z = 60$, *(a)* $e = 0.2$, $Re_\Omega = 465.82$, *(b)* $e = 0.4$, $Re_\Omega = 432.74$, *(c)* $e = 0.7$, $Re_\Omega = 314.16$. *(1)* Distribution of axial perturbation velocity Re($\tilde{w}$). Dark (resp. light) grey is for positive (resp. negative) values. *(2)* Distribution of perturbation kinetic energy $\mathcal{E} = \frac{1}{2}(|\tilde{u}|^2 + |\tilde{v}|^2 + |\tilde{w}|^2)$. Dark grey indicates high values, and isocontours are equispaced.

5.5.2 Production of perturbation kinetic energy

To further investigate the instability mechanism, the production of perturbation kinetic energy is calculated. In the well-known Reynolds–Orr equation, the local rate of production of $\mathcal{E}$ is given by $-\mathbf{u}' \cdot (\mathbf{u}' \cdot \nabla \mathbf{U})$. Averaging in the axial direction, ignoring the temporal exponential dependence and separating velocities into in-plane and axial components, one can define two contributions

$$\mathcal{P}_\perp = -\frac{1}{2}\mathrm{Re}\left\{\tilde{\mathbf{u}}_\perp^\star \cdot (\tilde{\mathbf{u}}_\perp \cdot \nabla_\perp \mathbf{U}_\perp)\right\}, \text{ and } \mathcal{P}_z = -\frac{1}{2}\mathrm{Re}\left\{\tilde{w}^\star (\tilde{\mathbf{u}}_\perp \cdot \nabla_\perp W)\right\}, \tag{5.12}$$

corresponding to the work of the Reynolds stresses against the in-plane and axial shear respectively. Expressions for the nonlinear terms in the modified bipolar coordinate

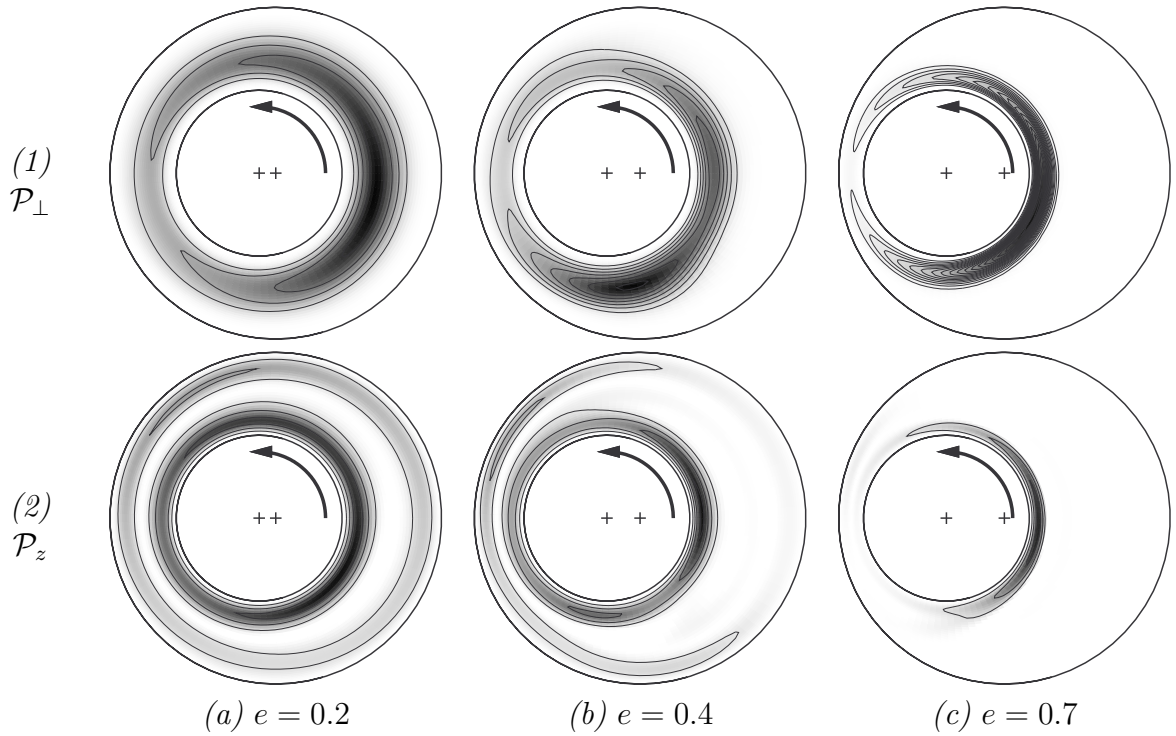

Figure 5.12 – Distribution of kinetic energy production for $m = 0$ and $Re_z = 60$, at critical conditions. *(1)* $\mathcal{P}_\perp$ and *(2)* $\mathcal{P}_z$. *(a)* $e = 0.2, Re_\Omega = 465.82$, *(b)* $e = 0.4, Re_\Omega = 432.74$, *(c)* $e = 0.7, Re_\Omega = 314.16$. Dark grey indicates large contributions and white corresponds to zero or negative contribution. Isocontours are equispaced.

system are given in Leclercq et al. (2013). Because the basic flow is axially invariant, these two terms are the only contributions to the production of $\mathcal{E}$.

Figure 5.12 represents the distribution of $\mathcal{P}_\perp$ and $\mathcal{P}_z$ for $m = 0$ and $Re_z = 60$, at $e = 0.2, 0.4, 0.7$, as in figure 5.11. Only positive contributions are shown in grey shades, as negative contributions inhibit temporal growth. Distributions of $\mathcal{P}_\perp$ and $\mathcal{E}$ look very similar. $\mathcal{P}_\perp$ is maximum in the wide gap for low e, then at negative polar angles for moderate e, then close to the inner cylinder on the wide gap side for e close to 1. The dominant contribution to $\mathcal{P}_\perp$ comes from the Reynolds stress term $-\frac{1}{2}\mathrm{Re}\{\tilde{u}\tilde{v}^\star\}$ multiplying the pseudo-radial derivative of the azimuthal velocity V. In fact, the spatial distribution of $-\frac{1}{2}\mathrm{Re}\{\tilde{u}\tilde{v}^\star\}$ is very similar to that of $\mathcal{P}_\perp$, so the region where axial oscillations of u' and v' are in phase corresponds to the peak of production of kinetic energy. The same calculation of $\mathcal{P}_\perp$ and $\mathcal{P}_z$ has been performed for the critical mode of the CI at $Re_z = 60$ and $e = 0.5$ ($m = 2$). $\mathcal{P}_\perp$ was also found to account for most of the kinetic energy production (81%), but the peak was located at a positive polar angle of 92°. This large positive value correlates well with the value of maximum kinetic energy at 99°, and noticeably contrasts with the almost opposite angles obtained for the critical mode of AI.

Distributions of $\mathcal{P}_z$ show larger contributions near the walls, where $\|\nabla_\perp W\|$ is larger. As eccentricity increases, production of kinetic energy close to the outer cylinder decreases, as the mode concentrates in the vicinity of the inner cylinder. For $e = 0.7$, $\mathcal{P}_z$ peaks almost in the same region as $\mathcal{P}_\perp$ and $\mathcal{E}$, namely close to the inner cylinder in the wide gap.

Integration of $\mathcal{P}_\perp$ and $\mathcal{P}_z$ over the annular domain for $Re_z = 60$ indicates that in-plane shear dominates the production of kinetic energy, $\mathcal{P}_\perp$ always accounting for more than 85% of the total amount, and even more than 97% for $e = 0.7$. The dominant contribution comes from the term involving pseudo-radial variations of pseudo-azimuthal velocity, characteristic of a centrifugal instability.

5.5.3 Instability mechanism

The striking destabilisation occuring at moderate eccentricities remains difficult to explain even after examining the basic flow, the critical mode and the production of kinetic energy. The transition from a stabilising to a destabilising effect of eccentricity occurs around $0.2 \leq e \leq 0.4$ for both TV and LH1, through a change of critical saddle point when Re_z is large enough. The recirculation region appears for $e \approx 0.2$ for $Re_\Omega \approx 500$ so it seems that the change of behaviour occurs after the recirculation zone has reached a critical size. The basic flow is then significantly different from a classical Couette flow. Indeed, while energy of the mode mostly localises in the vicinity of the inner cylinder, it also partially spans over the recirculation region for moderate eccentricities (cf. figure 5.11*(b)*). Surprisingly, a region of the flow located at negative polar angles seems to drive AI for moderate eccentricities, whereas kinetic energy production always peaks at positive angles for CI at criticality. Arguments based on *local stability* of the flow, however tempting in a quest of explanation, should be avoided here because of strong non-parallelism of the basic flow in the pseudo-azimuthal direction. Indeed, assuming the flow locally parallel in ϕ leads to completely wrong predictions of instability thresholds of eccentric Taylor–Couette flow (DiPrima, 1963, Ritchie, 1968). The most temporally unstable velocity profile, theoretically located at $\phi = \theta = 0°$, does not coincide with the location of maximum vortex activity found in the experiments (Vohr, 1968). On the other hand, global analyses yield good results in this geometry (DiPrima and Stuart, 1972b, 1975, Eagles et al., 1978), showing the limits of the local approach. Therefore, localisation of the modes and kinetic energy production at moderate eccentricities should be regarded as a global property of the entire flow field.

As e approaches 1, all m tend to behave in a similar way. After reaching a minimum value, the critical Re_Ω increases again as e becomes larger. Instability thresholds of all $m \geq 0$, and even their respective absolute growth rate for any Re_z-Re_Ω combination, become close at high e and less sensistive to variations of Re_z. More similarities are found by inspecting the critical modes. For $Re_z = 60$, all m have absolute wavenumbers $k_{0,\mathrm{r}}$ in the range 6.5-8, indicating a similar length scale. Indeed, the kinetic energy of all these modes is localised around the inner cylinder, on a radial extent corresponding to the smaller clearance of the eccentric annulus, consistent with a small wavelength. The localisation is so strong that the difference between toroidal or helical structure of the modes is partially 'blurred'. These similarities between m at high e is reminiscent of small gap Taylor–Couette–Poiseuille flow, where critical thresholds associated with different m are very close (Ng and Turner, 1982, Leclercq et al., 2013). Indeed, as eccentricity increases, the Couette-like flow associated with rotation of the inner cylinder scales with the smaller clearance $d(1 - e)$, curvature effects become less important, and m behaves more and more like a continuous real wavenumber, as when $\eta \to 1$. Matching between localisation of the modes and the Couette-like part of the basic flow may also explain the weaker effect of axial advection on the instability thresholds. Indeed, for

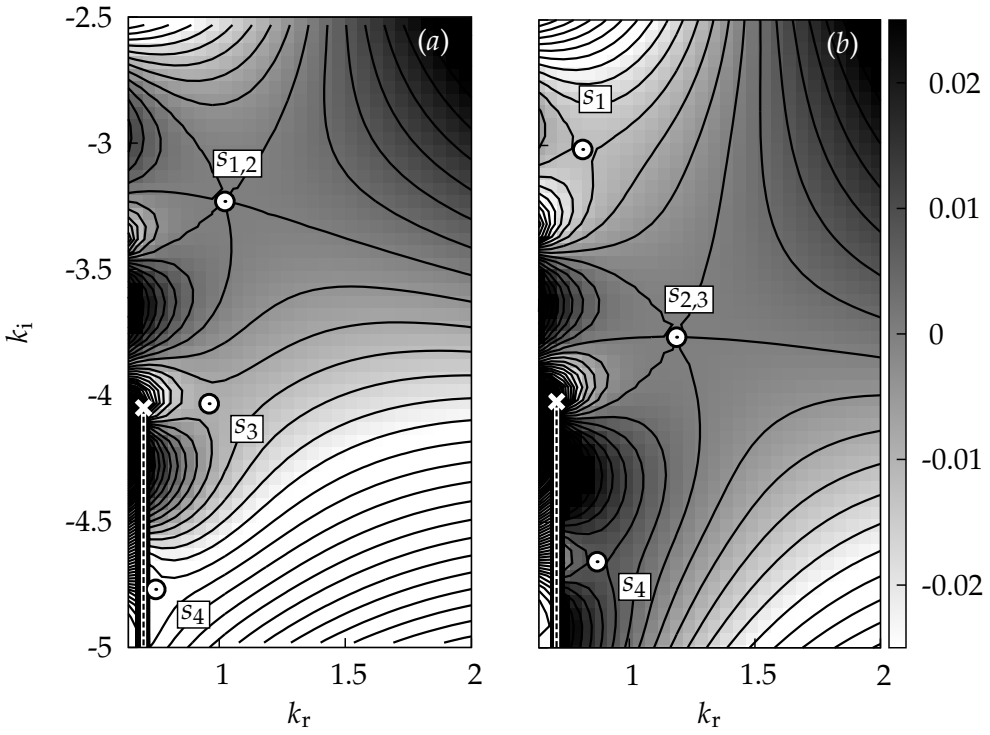

Figure 5.13 – Collision of saddle points with $\omega_{0,\mathrm{i}} = 0$ for $m = 0$: (a) $s_1\&s_2$ at $k_0 = 1.0223 - 3.2310\mathrm{i}$ for $e = 0.2839$, $Re_\Omega = 403.21$, $Re_z = 50.115$.(b) $s_2\&s_3$ at $k_0 = 1.1882 - 3.7630\mathrm{i}$ for $e = 0.3032$, $Re_\Omega = 353.60$, $Re_z = 43.188$.

large eccentricities, most of the axial volume flux passes through the wide gap, and the maximum value of W is located in the recirculation region, far from the inner cylinder. Hence, the region where perturbations are most amplified is spatially separated from the region where they are most rapidly 'blown away'. This observation could explain why critical Re_Ω are less sensitive to Re_z for e close to one.

5.5.4 Third-order saddle points

In figure 5.7, saddle points s_1, s_2 and s_3 are seen to lie very close to each other in the k-plane, with similar values of $\omega_{0,\mathrm{i}}$. By simultaneously varying the three control parameters e, Re_Ω, Re_z and the complex wavenumber k, it is possible to locate collisions between two neutral saddle points, defined by the five real-valued constraints

$$\omega_{0,\mathrm{i}} = 0, \ \partial\omega/\partial k = 0, \ \partial^2\omega/\partial k^2 = 0. \tag{5.13}$$

These 'double saddle points', 'third-order saddle points' (Davies, 1989) or 'super branch points' (Healey, 2004) correspond to the collision of three spatial branches, as can be seen by performing a Taylor expansion, as in equation (5.11), but now up to the third order. Looking at figure 5.13, it appears that the double saddle point $s_{1,2}$ corresponds to the coalescence of one k^+-branch, and the two distinct k^--branches associated to saddle points s_1 and s_2. $s_{2,3}$ also corresponds to a $k^+/k^-/k^-$ collision. When control parameters are varied in the vicinity of a double saddle point, the three spatial branches collide by pairs, and form the two separate saddle points s_1 and s_2 (resp. s_2 and s_3) for two distinct values of k. For some parameter values, one of the saddle points is formed

m	e	Re_Ω	Re_z	$k_{0,\mathrm{r}}$	$-k_{0,\mathrm{i}}$	$\omega_{0,\mathrm{r}}$	$\omega_{0,\mathrm{i}}$
0	0.2839	403.21	50.115	1.0223	3.2310	0.49075	0
	0.3032	353.60	43.188	1.1882	3.7630	0.50689	0
1	0.2412	180.20	16.448	1.8937	3.6287	0.79675	0
2	0.2325	202.54	5.8911	4.9163	3.7277	0.98521	0.03570
−2	0.2710	321.49	19.599	4.9062	0.0506	-0.48475	0

Table 5.2 – Parameter values at neutral third-order saddle points, satisfying equations (5.13) except for $m = 2$ as $\omega_{0,\mathrm{i}} > 0$. In this last case, the neutrality constraint is replaced by the minimisation of $\omega_{0,\mathrm{i}}$.

by the collision of the two k^--branches, and does not comply with causality. Therefore, careful examination is necessary in the vicinity of third-order saddle points.

Note that both double saddle points are neutral for $Re_z = 43.188$ and $Re_z = 50.115$ respectively, hence almost lie on the critical curves computed for $Re_z = 40$ and $Re_z = 50$. Therefore, no discontinuity in absolute wavenumber and frequency is observed in figure 5.9. Because of proximity of the two saddle points exchanging stability, their associated critical modes are quite similar in the vicinity of $e \approx 0.3$. As a consequence, the physical interpretation of the change of critical saddle point is unclear. For reference, the parameter values corresponding to neutral third-order saddle points are given in table 5.2 for other m. When $m = 2$, the temporal growth is always positive so the control parameters are chosen so as to minimise $\omega_{0,\mathrm{i}}$. In all cases, it appears that eccentricity is always in the range $0.2 \leq e \leq 0.3$, which, again, coincides surprisingly well with the appearance of the recirculation in the wide gap. The complexity of the dispersion relations for moderate eccentricities is remarkable. Note that many saddle points were also found for RH1, but only one of them satisfied the pinching criterion.

5.5.5 Convective versus absolute instability

We conclude this section by comparing the thresholds of CI (Leclercq et al., 2013) and AI in the eccentric Taylor–Couette–Poiseuille flow. Figure 5.14 represents the critical Re_Ω for CI (dotted lines), and for AI (solid lines), as a function of Re_z for $e = 0, 0.1, \ldots, 0.7$. For $Re_z = 0$, the two thresholds for $m = 0$ coincide, as expected for a steady bifurcation. The critical Re_Ω increases with Re_z for both CI and AI, but with a much larger rate for AI. This was expected as axial advection tends to carry the perturbations away from the source, so a larger driving is required to reach AI. The critical mode is always $m = 0$ for AI, corresponding to closed pseudo-toroidal Taylor vortices, propagating when $Re_z \neq 0$. For CI, LH modes of increasing m become critically unstable as Re_z increases. Open circles indicate a change of critical m on the CI thresholds. The effect of eccentricity is clearly stabilising for CI, but the effect on AI is more complex. For high enough Re_z, as eccentricity increases, the critical Re_Ω of AI slightly increases for low e, but then decreases before reaching a minimum and increases again for larger values of e.

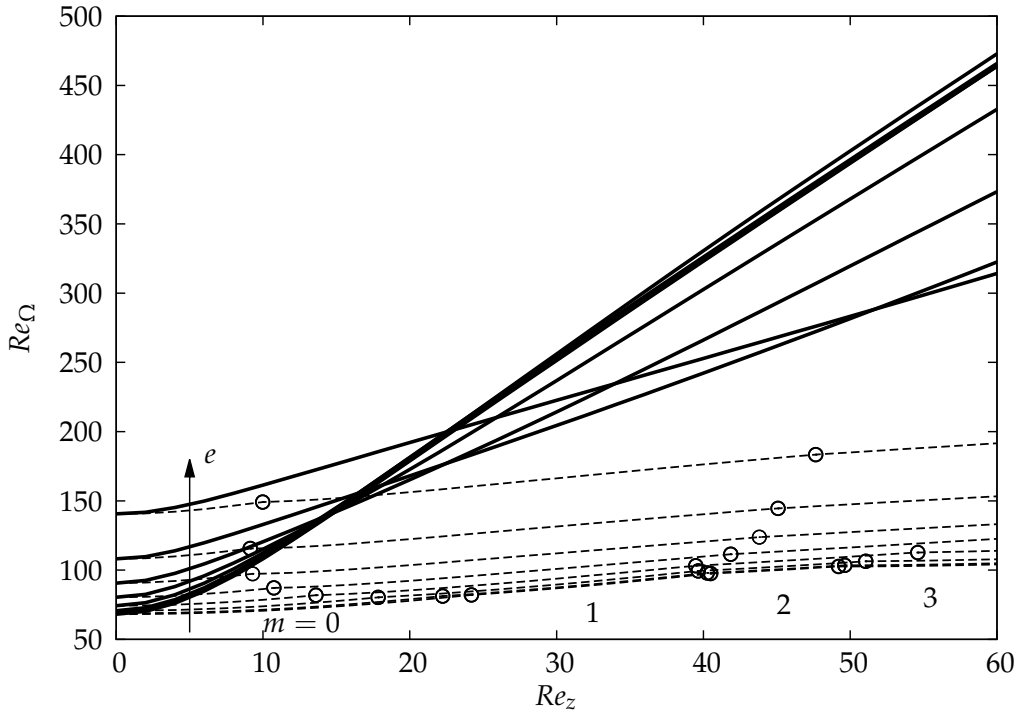

Figure 5.14 – Absolute (solid lines) and convective (dotted lines) instability thresholds: critical Re_Ω versus Re_z, for $e = 0, 0.1, \ldots, 0.7$. Open circles indicate a change of critical m for CI. For AI, the critical mode is always $m = 0$.

5.6 Conclusions

In this paper, an AI analysis has been performed for the flow between eccentric cylinders, with rotation of the inner one and a superimposed pressure-driven axial flow. The ratio between cylinder radii was fixed at $\eta = 0.5$, a value representative of an oil-well-drilling configuration. The eccentricity was varied from $e = 0$ to 0.7 with reasonable accuracy for $K = 8$ Fourier modes in the pseudo-azimuthal direction. The axial Reynolds number was varied in the range $0 \leq Re_z \leq 60$, requiring azimuthal Reynolds number one order of magnitude greater, $0 \leq Re_\Omega \leq 500$, to capture AI. This theoretical problem has concrete applications in oil-well drilling or lubrication bearings for high-speed turbomachinery. Transition to complex hydrodynamic régimes in these flows could have detrimental impact on the performance, with increased pressure losses or damaging resonance in the case of AI. The present analysis complements the recent linear stability analysis of this flow in the temporal framework (Leclercq et al., 2013), that determined thresholds of CI. In this previous paper, it was shown that modes with pseudo-azimuthal angular order $0 \leq m \leq 2$, corresponding to pseudo-toroidal (TV, $m = 0$) or left-helical (LH, $m = 1, 2$) vortices, were the most temporally unstable for $Re_z \leq 50$. LH modes with $m \geq 3$ were shown to become unstable for higher Re_z, while right helices (RH, $m < 0$) are always more temporally stable than TV and all LH. Therefore, only modes $m = 0, 1, 2$ were considered in the present analysis, together with $m = -1, -2$, assuming modes $|m| \geq 3$ always have lower absolute growth rates.

The most important result is that mode $m = 0$, corresponding to pseudo-toroidal Taylor-like vortices, is always the most absolutely unstable, for any e, Re_z, Re_Ω in the range of the present analysis. However, for large e and large Re_z, the absolute growth rate

associated with LH1 is very close to TV, and one may expect this latter mode to become the most absolutely unstable for $e > 0.7$. Another surprising result is that right helices $m < 0$ are not always more stable than left helices $m > 0$ with regards to AI. Despite lower temporal growth rates, RH can be somewhat more resistant to axial advection than LH in some cases. To be more specific, RH1 is always more absolutely unstable than LH1 for low e, but the converse is true for high e. For moderate eccentricities, the ordering depends on the three parameters e, Re_z, Re_Ω. LH2 is generally more absolutely unstable than RH2, but for low and moderate eccentricities, RH2 can sometimes be more absolutely unstable depending on the values of Re_z and Re_Ω.

Axial advection always has a stabilising effect on AI, as expected, because it carries perturbations away from their origin. The driving mechanism of the instability is clearly centrifugal, even for a moderate value of $Re_z = 60$. Indeed, almost all of the kinetic energy production is due to pseudo-radial variation of pseudo-azimuthal velocity. On the other hand, the effect of eccentricity is subtle when Re_z is high enough: for TV and LH1, one may distinguish low eccentricities $e \lesssim 0.3$, moderate eccentricities $0.3 \lesssim e \lesssim 0.6$ and large eccentricities $e \gtrsim 0.6$. For low eccentricities, the critical Re_Ω slightly increases with e, then clearly decreases in the range of moderate eccentricities, before increasing again for large eccentricities, after a minimum value is reached. By contrast, eccentricity destabilises RH1, LH2 and RH2 at low values of e as well, for large enough Re_z. At large enough Re_z, the critical Re_Ω of all m has a minimum as a function of e and Re_z.

As $e \to 1$, the critical modes associated with the different m share a number of properties. As just mentioned, critical curves start to increase after a minimum is reached for large enough e. Instability thresholds and absolute growth rates are less sensitive to variations of Re_z. LH modes are then more absolutely unstable than the corresponding RH, as in the temporal framework. Moreover, the absolute growth rate of the different $m \geq 0$ become close as e becomes large. Critical modes localise in the vicinity of the inner cylinder for all m, on a radial extent set by the smaller clearance $d(1-e)$. Because of localisation, the difference between pseudo-toroidal $m = 0$ and pseudo-helical $m \neq 0$ patterns is 'blurred', and it is not surprising that their associated AI characteristics become similar. In the large eccentricity case, the wide gap recirculation region does not seem to have a significant impact on the AI properties. Most of the axial volume flux passes through this zone, explaining the weaker effect of Re_z when e approaches one. Indeed, in this case the region of amplification of the perturbations is in the vicinity of the inner cylinder, and does not intersect with this region of advection of the perturbations. As e approaches one, the smaller clearance $d(1-e)$ decreases, curvature effects become weaker in the Couette-like part of the basic flow, and m behaves more and more like a continuous real wavenumber, as in Ng and Turner (1982) and Leclercq et al. (2013) when η increases.

When e is not large, TV and LH1 still share many similarities. For high enough Re_z, their critical Re_Ω is slightly increasing with e, before undergoing a change of critical saddle point, then Re_Ω decreases with e until a minimum is reached for $0.5 \leq e \leq 0.7$. Both modes change critical saddle point in the range $0.2 \leq e \leq 0.4$, after the recirculation region has reached a critical size. TV, however, changes critical saddle point twice for $Re_z = 60$ while LH1 changes only once. The associated critical quantities evolve in similar ways for the two modes. For low e, The critical wavenumber $k_{0,\mathrm{r}}$ is low, quasi-constant with e, and decreasing with Re_z as for critical CI. When $e \gtrsim 0.3$, $k_{0,\mathrm{r}}$ increases with e and reaches high values for $e \approx 0.7$, indicating a scaling of the vortices

with the smaller clearance. Surprisingly, for high e, $k_{0,\mathrm{r}}$ increases with Re_z.

The complete computation of critical curves for $m = 2$ has revealed the existence of a 'continent' of instability, in addition to the 'island' of AI found by Altmeyer et al. (2011). The two domains are related to different saddle points, and they exchange stability through large discontinuities in critical absolute wavenumber. Altmeyer et al. (2011) indicated the relevance of multiple saddle points but considered only the one issuing from the critical wavenumber k_c of the CI with $Re_z = 0$. The 'new' AI domain, unbounded for large values of Re_Ω, was to be expected as the destabilising mechanism is centrifugal.

In the present stability analysis, a remarkably large number of saddle points were found to be relevant to the long-term dynamics, for all m except $m = -1$, and recalls the necessity of a thorough investigation of the dispersion relation in AI analyses. In particular, for each saddle point of high enough temporal growth rate, it is essential to check the validity of the causality condition. This tedious numerical verification is absolutely necessary in the vicinity of third-order saddle points, where three spatial branches collide by pairs, and where relevant 'pinch points' can become spurious k^-/k^- saddle points (or potentially k^+/k^+ for other problems) upon varying control parameters. Because there is no general criterion to anticipate the nature of the saddle points and because the analysis of the dispersion relation is necessarily performed on bounded domains of k_r and k_i, experimental investigations or direct numerical simulations would be highly valuable to confirm the present predictions.

Finally we briefly summarize the most noticeable differences between AI and temporal instability for this flow. The $m = 0$ mode is always the most absolutely unstable while LH modes of increasing m dominate the temporal dynamics when Re_z increases. In both cases, axial advection has a stabilising effect for $Re_z \leq 60$, but the critical Re_Ω increases much faster for AI, than for CI. For zero axial advection, the two thresholds are identical as the flow bifurcates to steady Taylor vortices. For non-zero axial flow rate, perturbations are convected away from the source while growing in time, explaining much larger values of critical Re_Ω for AI. While eccentricity is clearly stabilising with regards to temporal instability, the effect on AI is complex, and the effect of e can be destabilising for moderate eccentricities, at high enough Re_z. Surprisingly, the production of perturbation kinetic energy of the critical mode peaks at negative polar angles in this case, whereas it peaks on the other side of the annulus for critical CI. For moderate eccentricities, the flow is strongly non-parallel, the position of this maximum is a global property of the complete flow field, and local stability arguments fail to explain these differences.

We believe that the most crucial perspective for this work is additional experiments to confirm our findings on CI and AI, since the last measurements made on such a configuration (Cole, 1969, Coney, 1971, Younes, 1972, Younes et al., 1972, Mobbs and Younes, 1974, Coney and Atkinson, 1978) are older than the introduction of AI theory to fluid mechanics (Huerre and Monkewitz, 1985)! Even in the convectively unstable régime, the literature is very lean, and only one apparatus seems to have ever existed, whereas the domain of application is vast. On a theoretical viewpoint, it would be particularly interesting to investigate the properties of nonlinear global modes, partly based on local AI properties (Pier et al., 2001), when eccentricity varies slowly along the axis. Indeed, because of bending of a thin drillstring in deep oil wells, including variable eccentricity would yield a more realistic model. Moreover, such weakly non-parallel open flows are

believed (Pier and Huerre, 2001) to be good candidates to confirm the potential existence of *hat modes*, theoretically predicted for model equations, but yet to be identified in a real configuration.

5.7 Additional results

5.7.1 Theoretical analysis of third-order saddle points

In this subsection, a theoretical criterion is derived to analyse the vicinity of third-order saddle points, using asymptotic matching techniques. The criterion is successfully applied to $s_{1,2}$ and $s_{2,3}$, defined in §5.5.4. The question we ask is the following: is it possible to predict the nature (spurious or representing a genuine pinch) of saddle points s_1 and s_2 (resp. s_2 and s_3), using asymptotic analysis in the vicinity of $s_{1,2}$ (resp. $s_{2,3}$)?

Let k_0, ω_0, χ_0 be such that $D^0 = D^0_k = D^0_{kk} = 0$, $D^0_\omega \neq 0$ and $D^0_{kkk} \neq 0$. We examine the limit $\chi \to \chi_0$, formally expressed by writing

$$\chi = \chi_0 + \epsilon\mu, \tag{5.14}$$

where $\epsilon \to 0^+$ is a small parameter and μ a fixed vector.

The complex ω-plane can be divided into three asymptotic regions:

Outer region

This is when ω is not near ω_0 (formally, fixed $\omega \neq \omega_0$ and $\epsilon \to 0$). The k-roots of $D(k, \omega; \chi) = 0$ have expansions in powers of ϵ:

$$k = k^{(0)} + \epsilon k^{(1)} + \dots . \tag{5.15}$$

The leading-order term satisfies

$$D(k^{(0)}, \omega; \chi_0) = 0 \tag{5.16}$$

and higher-order ones can be obtained by Taylor expansion of $D(k, \omega; \chi)$ about $\chi = \chi_0$ and $k = k^{(0)}$. The leading-order term will suffice for present purposes.

Inner region: $|\omega - \omega_0| = O(\epsilon)$

This region is described by the rescaled variable

$$\hat{\omega} = \frac{\omega - \omega_0}{\epsilon} \tag{5.17}$$

and the expansion in powers of $\epsilon^{1/3}$:

$$k = k_0 + \epsilon^{1/3}\hat{k}^{(1)} + \epsilon^{2/3}\hat{k}^{(2)} + \cdots . \tag{5.18}$$

It will suffice to consider $\hat{k}^{(1)}$, which is one of the three roots of

$$\frac{1}{6}D^0_{kkk}\hat{k}^{(1)^3} + D^0_\omega\hat{\omega} + \mu \cdot (\nabla_\chi D)^0 = 0 \tag{5.19}$$

and depends on ω and μ, as do the higher-order coefficients in (5.18). Note that all three roots of (5.19) coalesce when $D^0_\omega\hat{\omega} + \mu \cdot (\nabla_\chi D)^0 = 0$. This indicates the need for an even smaller region in the ω-plane.

Inner-inner region

This region is described by

$$\overline{\omega} = \epsilon^{-1/2}\left(\hat{\omega} + \frac{\mu\cdot(\nabla_\chi D)^0}{D^0_\omega}\right) \tag{5.20}$$

It is $O(\epsilon^{1/2})$ smaller than the previous region (i.e. of size $O(\epsilon^{3/2})$) and centred on

$$\omega = \omega_0 - \epsilon\frac{\mu\cdot(\nabla_\chi D)^0}{D^0_\omega}. \tag{5.21}$$

The k-roots expansion has the form

$$k = k_0 + \epsilon^{1/2}\overline{k}^{(1)} + \ldots, \tag{5.22}$$

where

$$\frac{1}{6}D^0_{kkk}\overline{k}^{(1)^3} + \left(\mu\cdot(\nabla_\chi D_k)^0 - \frac{\mu\cdot(\nabla_\chi D)^0 D^0_{k\omega}}{D^0_\omega}\right) + D^0_\omega\overline{\omega} = 0. \tag{5.23}$$

The notation can be simplified by introducing

$$\alpha = \left(\frac{2}{D^0_{kkk}}\left(\frac{\mu\cdot(\nabla_\chi D)^0 D^0_{k\omega}}{D^0_\omega} - \mu\cdot(\nabla_\chi D_k)^0\right)\right)^{1/2}, \tag{5.24}$$

$$K = \frac{\overline{k}^{(1)}}{\alpha}, \tag{5.25}$$

$$\Delta = -\frac{3D^0_\omega}{\alpha^3 D^0_{kkk}}\overline{\omega}, \tag{5.26}$$

leading to

$$K^3 - 3K - 2\Delta = 0. \tag{5.27}$$

Note that, in writing (5.25) and (5.26), we suppose that $\alpha \neq 0$ from here on. $\alpha = 0$ is a local (near χ_0) representation of the codimension 2 subspace of χ-space for which all three roots coalesce. (5.27) has a double root at $K = \pm 1$ when $\Delta = \mp 1$. Thus, there are saddle points at

$$\omega = \omega_0 - \epsilon\frac{\mu\cdot(\nabla_\chi D)^0}{D^0_\omega} \pm \epsilon^{3/2}\frac{\alpha^3 D^0_{kkk}}{3D^0_\omega} + \cdots. \tag{5.28}$$

The roots of (5.27) are $K_n = W_n + 1/W_n$ $(n = 1, 2, 3)$, where

$$W_1 = \left(\Delta + \mathrm{i}(1-\Delta^2)^{1/2}\right)^{1/3}, \tag{5.29a}$$

$$W_2 = \mathrm{e}^{\mathrm{i}2\pi/3}\left(\Delta + \mathrm{i}(1-\Delta^2)^{1/2}\right)^{1/3}, \tag{5.29b}$$

$$W_3 = \mathrm{e}^{-\mathrm{i}2\pi/3}\left(\Delta + \mathrm{i}(1-\Delta^2)^{1/2}\right)^{1/3}, \tag{5.29c}$$

where the cube and square roots are principal values. As functions of complex Δ, (5.29a)–(5.29c) are analytic, apart from branch cuts running along the negative real axis from $\Delta = -\infty$ to $\Delta = -1$ and $\Delta = 1$ to $\Delta = +\infty$. $K_2(\Delta)$ inherits both branch cuts, whereas

$K_1(\Delta)$ only has the cut from $\Delta = -\infty$ to $\Delta = -1$ and $K_3(\Delta)$ only has the one from $\Delta = 1$ to $\Delta = +\infty$. $K_1(\Delta)$ and $K_2(\Delta)$ coalesce when $\Delta = -1$ and $K_2(\Delta)$ and $K_3(\Delta)$ when $\Delta = 1$.

From here on the square root in (5.24) is chosen such that $\mathrm{Re}(\alpha^3 D^0_{kkk}/D^0_\omega) \leq 0$. The picture in the complex ω-plane is as shown in figure 5.15. In this figure, the dots

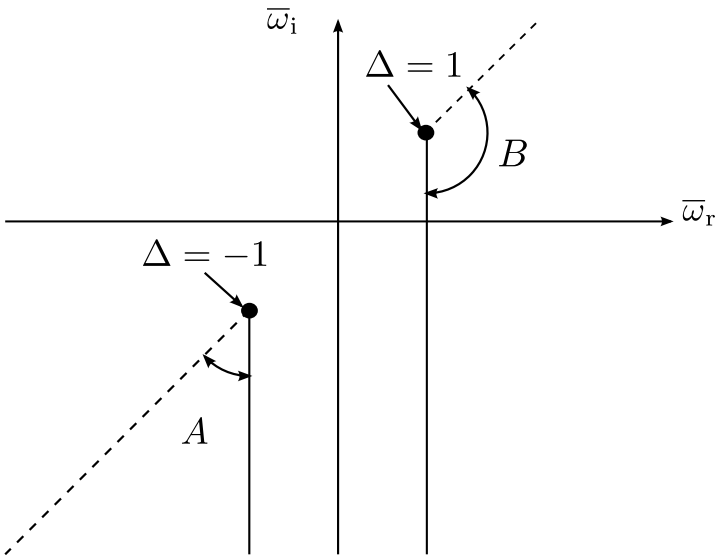

Figure 5.15 – Branch points (dots) and branch cuts of $K(\overline{\omega})$ (dashed lines), $\overline{K}(\overline{\omega})$ (solid lines).

represent the branch points,

$$\overline{\omega} = \mp \frac{\alpha^3 D^0_{kkk}}{3 D^0_\omega} \ (\Delta = \pm 1) \tag{5.30}$$

and the dashed lines are the branch cuts of $K_n(\overline{\omega})$, running radially outwards from the origin. Because $\mathrm{Re}\,(\alpha^3 D^0_{kkk}/D^0_\omega) \leq 0$, $\Delta = 1$ lies in $\overline{\omega}_\mathrm{r} \geq 0$ and $\Delta = -1$ in $\overline{\omega}_\mathrm{r} \leq 0$. We want to move the branch cuts to the locations indicated by the bold lines in the above figure. Define $\overline{K}_n(\overline{\omega})$ $(n = 1, 2, 3)$ as follows:

a) outside the regions A and B, $\overline{K}_n(\overline{\omega}) = K_n(\overline{\omega})$;

b) in region A, $\overline{K}_1(\overline{\omega}) = K_2(\overline{\omega})$, $\overline{K}_2(\overline{\omega}) = K_1(\overline{\omega})$ and $\overline{K}_3(\overline{\omega}) = K_3(\overline{\omega})$;

c) in region B, $\overline{K}_1(\overline{\omega}) = K_1(\overline{\omega})$, $\overline{K}_2(\overline{\omega}) = K_3(\overline{\omega})$ and $\overline{K}_3(\overline{\omega}) = K_2(\overline{\omega})$.

A little care is required on the dashed lines: the $\overline{K}_n(\overline{\omega})$ are there defined by continuity from both sides. The resulting $\overline{K}_n(\overline{\omega})$ are roots of (5.27) whose branch cuts run downwards in the complex $\overline{\omega}$-plane.

Matching

The inner-inner region solution is

$$k = k_0 + \epsilon^{1/2} \alpha \overline{K} + \ldots . \tag{5.31}$$

To avoid the complication of the modified branch cuts, we restrict attention to the half plane $\mathrm{Im}(\Delta) > 0$ so that $\overline{K}_n(\overline{\omega}) = K_n(\overline{\omega})$. As $\overline{\omega} \to \infty$ in this half plane, (5.29a)–(5.29c) and $K = W + 1/W$ yield

$$\epsilon^{1/2}\alpha\overline{K}_1 \sim \epsilon^{1/2}\alpha(2\Delta)^{1/3} = \epsilon^{1/3}\gamma, \tag{5.32a}$$

$$\epsilon^{1/2}\alpha\overline{K}_2 \sim \epsilon^{1/2}\alpha\mathrm{e}^{\mathrm{i}2\pi/3}(2\Delta)^{1/3} = \epsilon^{1/3}\mathrm{e}^{\mathrm{i}2\pi/3}\gamma, \tag{5.32b}$$

$$\epsilon^{1/2}\alpha\overline{K}_3 \sim \epsilon^{1/2}\alpha\mathrm{e}^{-\mathrm{i}2\pi/3}(2\Delta)^{1/3} = \epsilon^{1/3}\mathrm{e}^{-\mathrm{i}2\pi/3}\gamma \tag{5.32c}$$

where

$$\gamma = \alpha\left(-\frac{6}{\alpha^3 D^0_{kkk}}\left(D^0_\omega\hat{\omega} + \mu\cdot(\nabla_\chi D)^0\right)\right)^{1/3}. \tag{5.33}$$

Equations (5.32a)–(5.32c) with (5.33) describe the roots in the given half plane. They can be extended to all $\hat{\omega}$ by ensuring that $\gamma(\hat{\omega})$ has a branch cut which runs downwards from its branch point, $\hat{\omega} = -\mu\cdot(\nabla_\chi D)^0/D^0_\omega$. This is achieved by writing

$$\gamma = \alpha\mathrm{e}^{\mathrm{i}\pi/6}\left(-\frac{6D^0_\omega}{\alpha^3 D^0_{kkk}}\right)^{1/3}\left(-\mathrm{i}\left(\hat{\omega} + \frac{\mu\cdot(\nabla_\chi D)^0}{D^0_\omega}\right)\right)^{1/3}, \tag{5.34}$$

where the cube roots are principal values. Equation (5.34) agrees with (5.33) in the given half plane and has branch cut such that (5.32a)–(5.32c) describe the roots everywhere. Equations (5.32a)–(5.32c) match the inner region solution because

$$\hat{k}^{(1)} = \gamma,\ \hat{k}^{(1)} = \mathrm{e}^{\mathrm{i}2\pi/3}\gamma,\ \hat{k}^{(1)} = \mathrm{e}^{-\mathrm{i}2\pi/3}\gamma \tag{5.35}$$

are roots of (5.19). Matching gives the correspondence between the $\overline{K}_n(\overline{\omega})$ and roots of (5.19): (5.34) and (5.35) give the roots corresponding to $\overline{K}_1(\overline{\omega})$, $\overline{K}_2(\overline{\omega})$ and $\overline{K}_3(\overline{\omega})$ in that order.

The inner-region solution is

$$k = k_0 + \epsilon^{1/3}\hat{k}^{(1)} + \cdots, \tag{5.36}$$

where, as noted above, $\hat{k}^{(1)}$ has one of the values (5.35). As $\hat{\omega} \to \infty$, (5.34) and (5.35) give

$$\epsilon^{1/3}\hat{k}^{(1)} \sim \epsilon^{1/3}\alpha\mathrm{e}^{\mathrm{i}\pi/6}\left(-\frac{6D^0_\omega}{\alpha^3 D^0_{kkk}}\right)^{1/3}(-\mathrm{i}\hat{\omega})^{1/3} = \beta\left(-\mathrm{i}(\omega-\omega_0)\right)^{1/3}, \tag{5.37a}$$

$$\epsilon^{1/3}\hat{k}^{(1)} \sim \beta\mathrm{e}^{\mathrm{i}2\pi/3}\left(-\mathrm{i}(\omega-\omega_0)\right)^{1/3}, \tag{5.37b}$$

$$\epsilon^{1/3}\hat{k}^{(1)} \sim \beta\mathrm{e}^{-\mathrm{i}2\pi/3}\left(-\mathrm{i}(\omega-\omega_0)\right)^{1/3}, \tag{5.37c}$$

where (5.37a)–(5.37c) respectively correspond to $\overline{K}_1(\overline{\omega})$, $\overline{K}_2(\overline{\omega})$, $\overline{K}_3(\overline{\omega})$ and

$$\beta = \alpha\mathrm{e}^{\mathrm{i}\pi/6}\left(-\frac{6D^0_\omega}{\alpha^3 D^0_{kkk}}\right)^{1/3} \tag{5.38}$$

Matching of (5.37a)–(5.37c) to the outer region requires that three roots of (5.16) behave like

$$k^{(0)} \sim k_0 + \beta\left(-\mathrm{i}(\omega-\omega_0)\right)^{1/3} + \cdots, \tag{5.39a}$$

$$k^{(0)} \sim k_0 + \beta\mathrm{e}^{\mathrm{i}2\pi/3}\left(-\mathrm{i}(\omega-\omega_0)\right)^{1/3} + \cdots, \tag{5.39b}$$

$$k^{(0)} \sim k_0 + \beta\mathrm{e}^{-\mathrm{i}2\pi/3}\left(-\mathrm{i}(\omega-\omega_0)\right)^{1/3} + \cdots \tag{5.39c}$$

as $\omega \to \omega_0$.

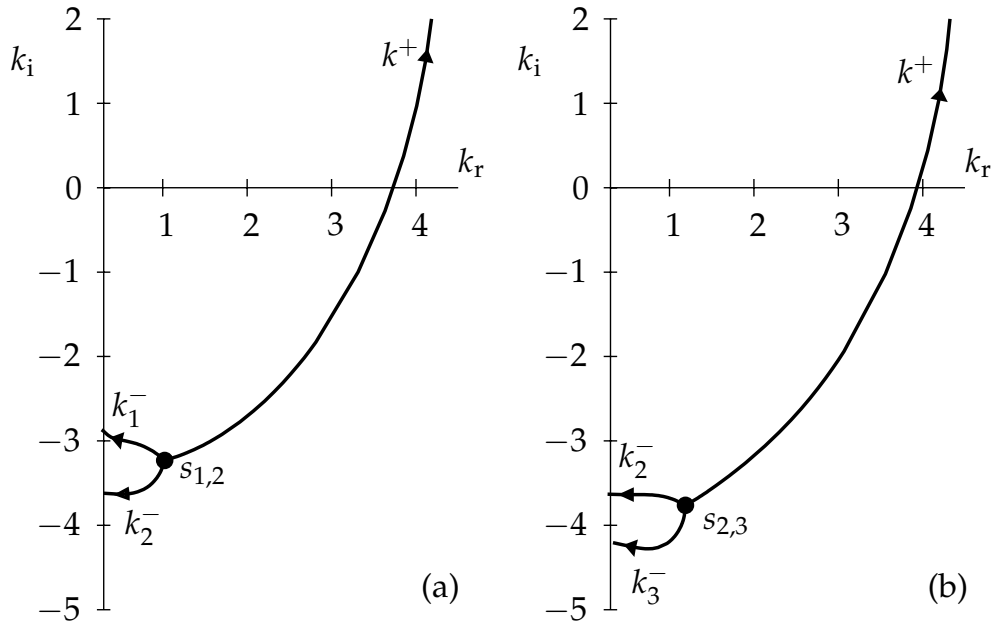

Figure 5.16 – Spatial branches (a) $k^+/k_1^-/k_2^-$ for $\omega_\mathrm{r} = 0.49075$ colliding at neutral third-order saddle-point $s_{1,2}$ (see figure 5.13a), $e = 0.2839$, $Re_\Omega = 403.21$, $Re_z = 50.115$; (b) $k^+/k_2^-/k_3^-$ for $\omega_\mathrm{r} = 0.50689$ colliding at neutral third-order saddle-point $s_{2,3}$ (see figure 5.13b), $e = 0.3032$, $Re_\Omega = 353.60$, $Re_z = 43.188$. Arrows indicate increasing values of ω_i.

Identification of spatial branches

The spatial branches colliding at a third-order saddle point can be identified by keeping $\omega_\mathrm{r} = \omega_{0,\mathrm{r}}$ at the double-saddle-point value and increasing ω_i from $\omega_{0,\mathrm{i}}$. Figure 5.16 show the example of $s_{1,2}$ and $s_{2,3}$ for which a k^+-branch collides with two k^--branches. k_2^- is shared by the two double saddle points.

Domains in parameter space

Denote by k_n $(n = 1, 2, 3)$ the three spatial branches. When $\chi \neq \chi_0$, the k_n collide by pairs of saddle points and three cases are possible

case 1) k_1/k_2 & k_1/k_3,

case 2) k_2/k_1 & k_2/k_3,

case 3) k_3/k_1 & k_3/k_2,

as illustrated in figure 5.17 (resp. figure 5.18), for three values of χ in the vicinity of $\chi_0(s_{1,2})$ (resp. $\chi_0(s_{2,3})$).

In the outer region, each k_n can be associated to a solution $k^{(0)}$ given by one of the formulas (5.39a)–(5.39c). These outer region solutions are themselves associated to inner-inner solutions $\overline{K}_1(\overline{\omega})$, $\overline{K}_2(\overline{\omega})$ and $\overline{K}_3(\overline{\omega})$, in that order. Therefore, the k_n can be matched with the $\overline{K}_n$ through (5.39a)–(5.39c). Moreover, we have proved that collisions between $\overline{K}_n$ in the inner-inner region were only possible between $\overline{K}_3$ and $\overline{K}_1$ or $\overline{K}_3$ and $\overline{K}_2$. Therefore

- if $\overline{K}_3 \equiv k_1$, then case 1 applies,

- if $\overline{K}_3 \equiv k_2$, then case 2 applies,
- if $\overline{K}_3 \equiv k_3$, then case 3 applies.

In figure 5.19, the data of figure 5.17 is reploted after some transformation. The k-branches are seen to approach k_0 with directions well predicted by theory. It is also observed that the branch common to both saddle points is always matching $\overline{K}_3$, as expected.

These three cases define domains in parameter space. The identification of their frontiers depends only on the determination of β, appearing in (5.39a)–(5.39c). The frontiers are given by the loci of the discontinuities of $\mu \mapsto \beta$. Upon choosing the square root of α^2 in (5.24) such that $\mathrm{Re}\,(\alpha^3 D^0_{kkk}/D^0_\omega) \leq 0$, discontinuities of β occur as

$$\mathrm{Re}\left(\alpha^3 D^0_{kkk}/D^0_\omega\right) = 0. \tag{5.40}$$

Let

$$a = \frac{2}{D^0_{kkk}},\ b = (\nabla_\chi D_k)^0 - (\nabla_\chi D)^0 \frac{D^0_{k\omega}}{D^0_\omega},\ \text{and}\ c = \frac{D^0_{kkk}}{D^0_\omega}, \tag{5.41}$$

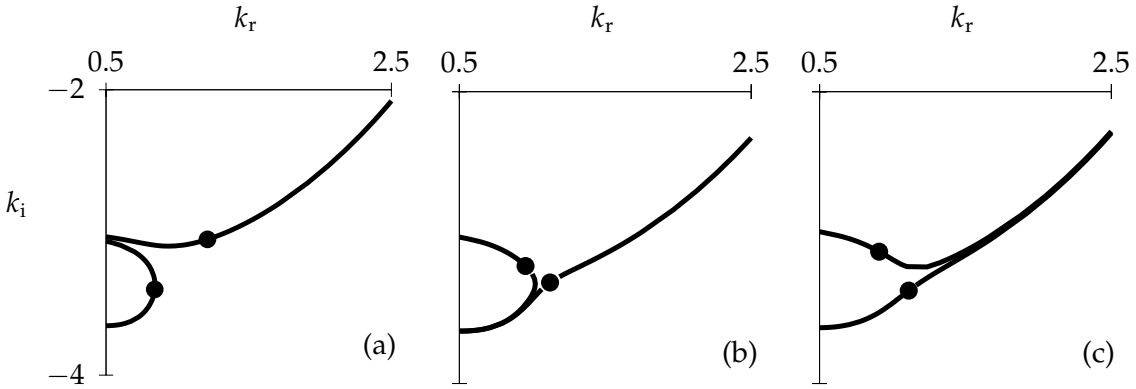

Figure 5.17 – The three patterns of collisions between k^+, k_1^- and k_2^- leading to saddle points s_1 and s_2, $Re_z = 50$. (a) $e = 0.27$, $Re_\Omega = 400$: k^+/k_1^- & k_1^-/k_2^-. (b) $e = 0.285$, $Re_\Omega = 410$: k^+/k_2^- & k_1^-/k_2^-. (c) $e = 0.29$, $Re_\Omega = 400$: k^+/k_1^- & k^+/k_2^-.

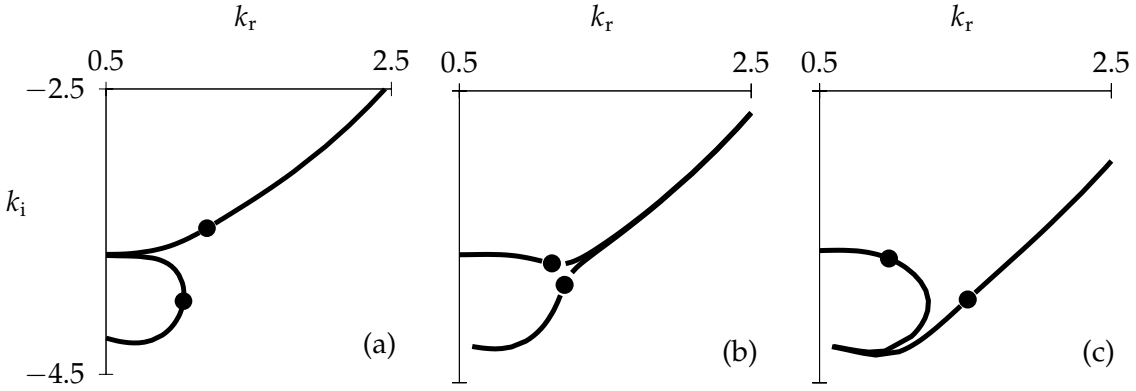

Figure 5.18 – The three patterns of collisions between k^+, k_2^- and k_3^- leading to saddle points s_2 and s_3, $Re_z = 43.188$. (a) $e = 0.29$, $Re_\Omega = 352$: k^+/k_2^- & k_2^-/k_3^-. (b) $e = 0.305$, $Re_\Omega = 348$: k^+/k_2^- & $k^- + /k_3^-$. (c) $e = 0.32$, $Re_\Omega = 352$: k^+/k_3^- & k_2^-/k_3^-.

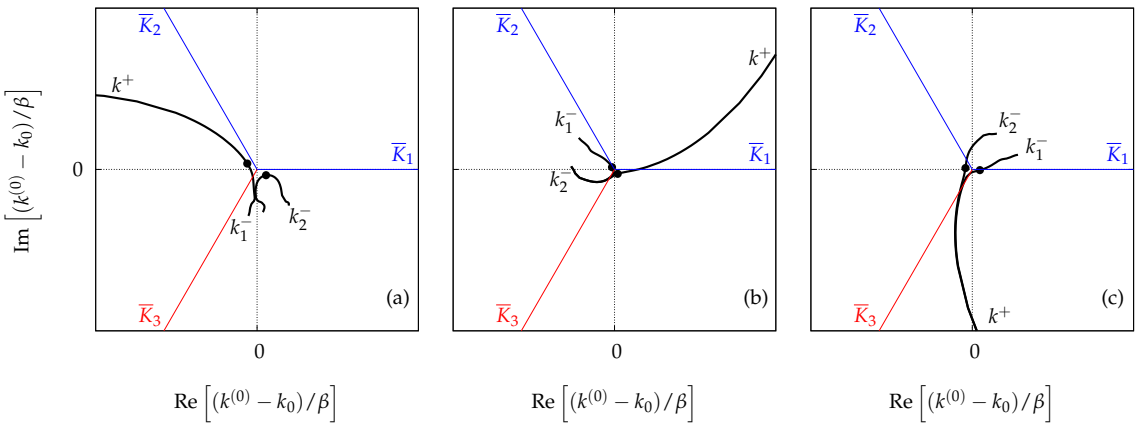

Figure 5.19 – Identification of branch $\overline{K}_3$: (a) $\beta = -0.58254 - 2.23862\mathrm{i}$, $\overline{K}_3 \equiv k_1^-$; (b) $\beta = 2.22998 + 0.614818\mathrm{i}$, $\overline{K}_3 \equiv k_2^-$; (c) $\beta = -1.64744 + 1.62381\mathrm{i}$, $\overline{K}_3 \equiv k^+$. Black lines correspond to data in figure 5.17.

then condition (5.40) reads

$$\arg([a(\mu \cdot b)]^{3/2} c) = \frac{\pi}{2} \mod \pi, \tag{5.42}$$

therefore, the angle $\Theta \equiv \arg(\mu \cdot b)$ can take on the values

$$\Theta = \frac{\pi}{3} - \frac{2}{3} \arg c - \arg a \mod \frac{2\pi}{3}. \tag{5.43}$$

Denote Θ_i $(i = 1, 2, 3)$ the three values in $[-\pi, \pi]$. These directions define hyperplanes of normal vector n_i

$$\mu \cdot n_i = 0, \text{ with } n_i = \mathrm{Im}\ b - \tan\Theta_i\ \mathrm{Re}\ b, \ i = 1, 2, 3. \tag{5.44}$$

In order to recover the equivalence with (5.43), additional constraints are added

$$\begin{cases} \mu \cdot \mathrm{Re}\ b \leq 0 & \text{if } -\pi/2 \leq \Theta_i < \pi/2, \ i = 1, 2, 3, \\ \mu \cdot \mathrm{Re}\ b < 0 & \text{otherwise.} \end{cases} \tag{5.45}$$

Equations (5.44)–(5.45) define the frontiers of the different domains. This criterion applied in the vicinity of $s_{1,2}$ and $s_{2,3}$ (see figures 5.20 & 5.21) give results consistent with figures 5.17 & 5.18. Cases (a), (b) and (c) fall into different domains of parameter space. The critical threshold associated with each saddle point is indicated on these plots. Combining on the same graph the critical curves together with the frontiers of the different domains is particularly useful. In domain (c) of figure 5.20, the two saddle points are pinch points, so the absolute instability threshold corresponds to the lower critical curve. However, only one saddle point is a genuine pinch point in domain (a), so an additional step is necessary to conclude. It is sufficient to check at one point if a neutral saddle point is spurious or not. If it is not, then the selected curve sets the frontier of absolute instability, otherwise, the other one does.

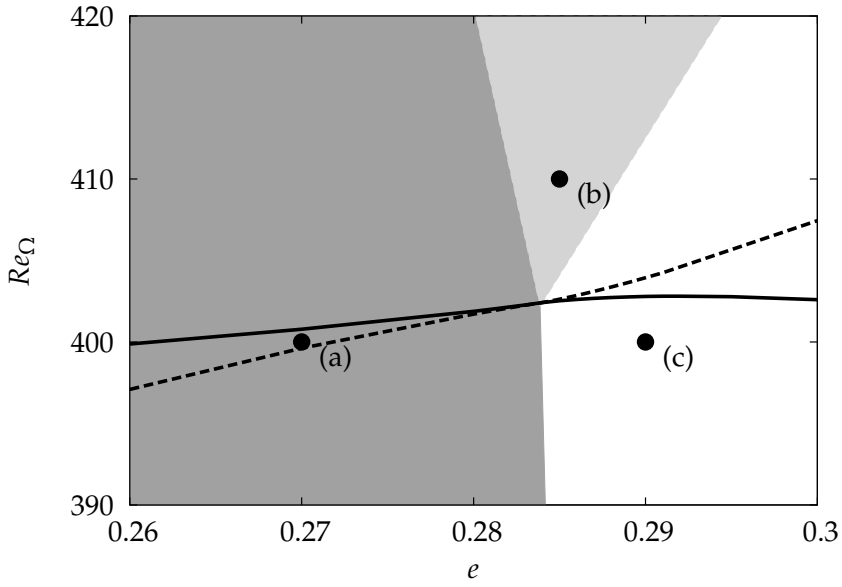

Figure 5.20 – Lines: critical curves $\omega_{0,\mathrm{i}} = 0$ for saddles s_1 and s_2, $Re_z = 50$. The solid line indicates the absolute instability threshold. The (e, Re_Ω)-plane is split into three regions, according to the three possible patterns (a), (b) and (c) of collision between the spatial branches, see figure 5.17. In (c), both saddle points are genuine pinch points, so the absolute instability threshold is given by the lower critical curve. In (a), only one saddle point is causal so the absolute instability threshold is given by the critical curve associated with the k^+/k_1^- saddle point. Upon crossing the border between (a) and (b), the saddle point governing the dynamics is changed into a k^+/k_2^-.

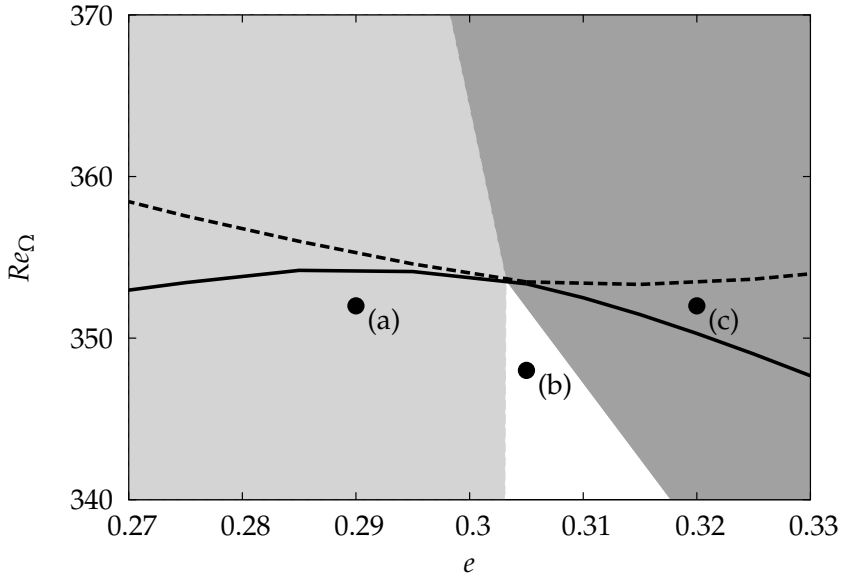

Figure 5.21 – Same caption as in figure 5.20, but now for s_2 and s_3, $Re_z = 43.188$. The third-order saddle point criterion is applied with respect to $s_{2,3}$ instead of $s_{1,2}$, in order to determine the three regions (a), (b) and (c).

Summary of the procedure

The different steps required to apply the criterion are summarized as follows:

1) The double saddle point is identified, using a Newton–Raphson iteration with the four real-valued constraints $\partial_k\omega = 0$, $\partial_{kk}\omega = 0$, satisfied by adjustment of k and two real control parameters.
2) The different derivatives appearing in (5.40) are computed. The dispersion relation is evaluated using its definition as determinant of the eigenvalue problem $D(k, \omega; \chi) = \det(\mathsf{A}_1 - \lambda\mathsf{I})$. Finite differences can be used to approximate the derivatives.
3) Frontiers are straightforwardly computed using (5.44)–(5.45).
4) The three spatial branches coalescing at the double saddle point are calculated, using Newton iteration to find k as a function of ω. Each branch is identified as a k^+ or a k^-.
5) In each of the three domains defined in 3) crossed by the two critical curves, the nature of the saddle points is assessed by following their associated k-branches. Only one calculation per critical curve and domain is necessary since the type of a saddle point is unchanged within a domain.
6) The absolute instability threshold is given by the lower critical curve associated to a pinch point, in each domain.

Discussion

Though there are many steps, calculations are not expensive. The aim of this criterion is, first and foremost, to provide a better understanding of the dispersion relation in the vicinity of third-order saddle points. It assigns a domain of validity to each saddle point, which cannot be obtained otherwise because of prohibitive computational effort. Indeed, the other approach would be to follow the spatial branches of each saddle point on a grid in parameter space, but this is impractical for large parameter spaces.

The weakness of this approach is evident because of the use of asymptotic techniques: it is only valid in the neighbourhood of the double saddle point. In figures 5.20 and 5.21, the criterion was successfully applied though at distances $\Delta e \sim 0.03$ and $\Delta Re_\Omega \sim 10$ from χ_0, which represent a few percent of the respective ranges of e and Re_Ω. In practice, when many parameters are varied and several saddle points potentially result from pinching, systematic computations of the spatial branches seem inevitable. Between 100 and 200 tests were performed to build confidence in the parametric analysis presented in this chapter.

5.7.2 Multiplicity of saddle points

To obtain the critical curves of each m, many saddle points were followed in parameter space, and many tests were performed to check whether the pinching criterion was satisfied or not. In figure 5.22, we show isocontours of the growth rate as a function of complex wanumber for $-2 \leq m \leq 2$ to illustrate the multiplicity of saddle points for

each m. All the saddle points denoted with a white dot were systematically tracked in parameter space, and tested with respect to the causality principle.

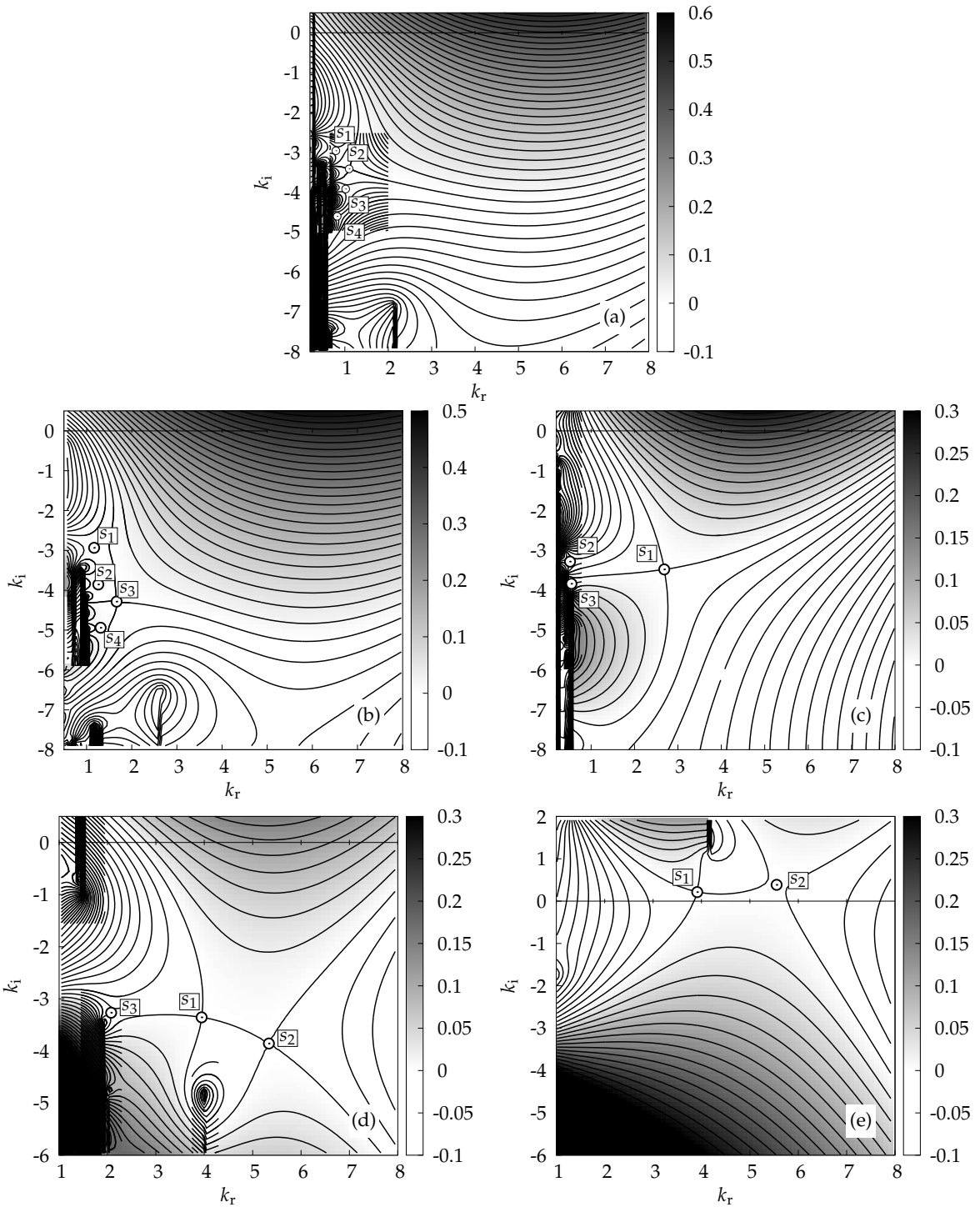

Figure 5.22 – Isocontours of $\omega_\mathrm{i} = \Omega_\mathrm{i}(k)$ (with step $\delta\omega_\mathrm{i} = 0.02$ except when refined) at criticality ($\omega_{0,\mathrm{i}} = 0$) for (a) $m = 0$, $e = 0.3075$, $Re_z = 60$, $Re_\Omega = 472.24$, (b) $m = 1$, $e = 0.3$, $Re_z = 30$, $Re_\Omega = 305.79$, (c) $m = -1$, $e = 0.3$, $Re_z = 30$, $Re_\Omega = 272.79$, (d) $m = 2$, $e = 0.2$, $Re_z = 6.29$, $Re_\Omega = 187.84$, (e) $m = -2$, $e = 0.2$, $Re_z = 12.43$, $Re_\Omega = 274.08$.

Figure 5.22(a) and 5.22(b) show a striking similarity between the dispersion relations of modes $m = 0$ and $m = 1$, explaining the close stability properties reported earlier in this chapter. The spatio-temporal dynamics of mode $m = -1$ is governed by only one pinch point, well separated from a large number of spurious saddle points in the range $0 < k_\mathrm{r} < 1$. For modes $m = \pm 2$, the maps show two pinch points sharing one spatial branch. The pinch point of larger temporal growth rate varies depending on the control parameters. Unlike for $m = 0, 1$, the pinch points have equal temporal growth rate for well separated values of k_r, so the associated mode wavelength varies discontinuously upon switching critical saddle point.

5.7.3 Complete critical surfaces

Continuation was applied with respect to both e and Re_z to define the critical surface separating regions of convective and absolute instability, for each $-2 \leq m \leq 2$. The results are shown in figure 5.23, and associated critical quantities $k_{0,\mathrm{r}}$, $k_{0,\mathrm{i}}$, $\omega_{0,\mathrm{r}}$ are plotted in figures 5.24, 5.25 and 5.26. The main results were already stated in §5.4 but curves were not shown for $m \neq 0$, and only with respect to e for $m = 0$.

Critical azimuthal Reynolds number $\boldsymbol{Re}_\Omega$

The dots and dashed lines in figure 5.23 indicate a change of critical saddle point for the same value of m. For all m, the critical Re_Ω decreases with e for moderate eccentricities before increasing when e approaches one. The effect ot Re_z is always stabilizing.

Critical absolute axial wavenumber $k_{0,\mathrm{r}}$

On figure 5.24, the discontinuity in absolute wavelength for $|m| = 2$ is easily visualized. We notice distinct behaviours on each side of the discontinuity for $m = 0, 1$: when $e \lesssim 0.3$, $k_{0,\mathrm{r}}$ decreases with Re_z whereas it increases for $e \gtrsim 0.3$. For large values of e, $k_{0,\mathrm{r}}$ increases for all m, because the available space in the 'small gap' ($\theta = \pi$) decreases.

Critical absolute spatial growth rate $-k_{0,\mathrm{i}}$

On figure 5.25, we notice that the spatial growth rate associated with absolute instability is of the same order for $m = 0, \pm 1$, larger for $m = 2$, and negative for $m = -2$ at low values of Re_z (the wavepacket propagates upstream in the convectively unstable régime).

Critical absolute frequency $\omega_{0,\mathrm{r}}$

The evolution of $\omega_{0,\mathrm{r}}$ resembles that of $k_{0,\mathrm{i}}$. For $m = -1, -2$, negative absolute frequency indicates upstream propagation of the wave under the stationary front of the wavepacket.

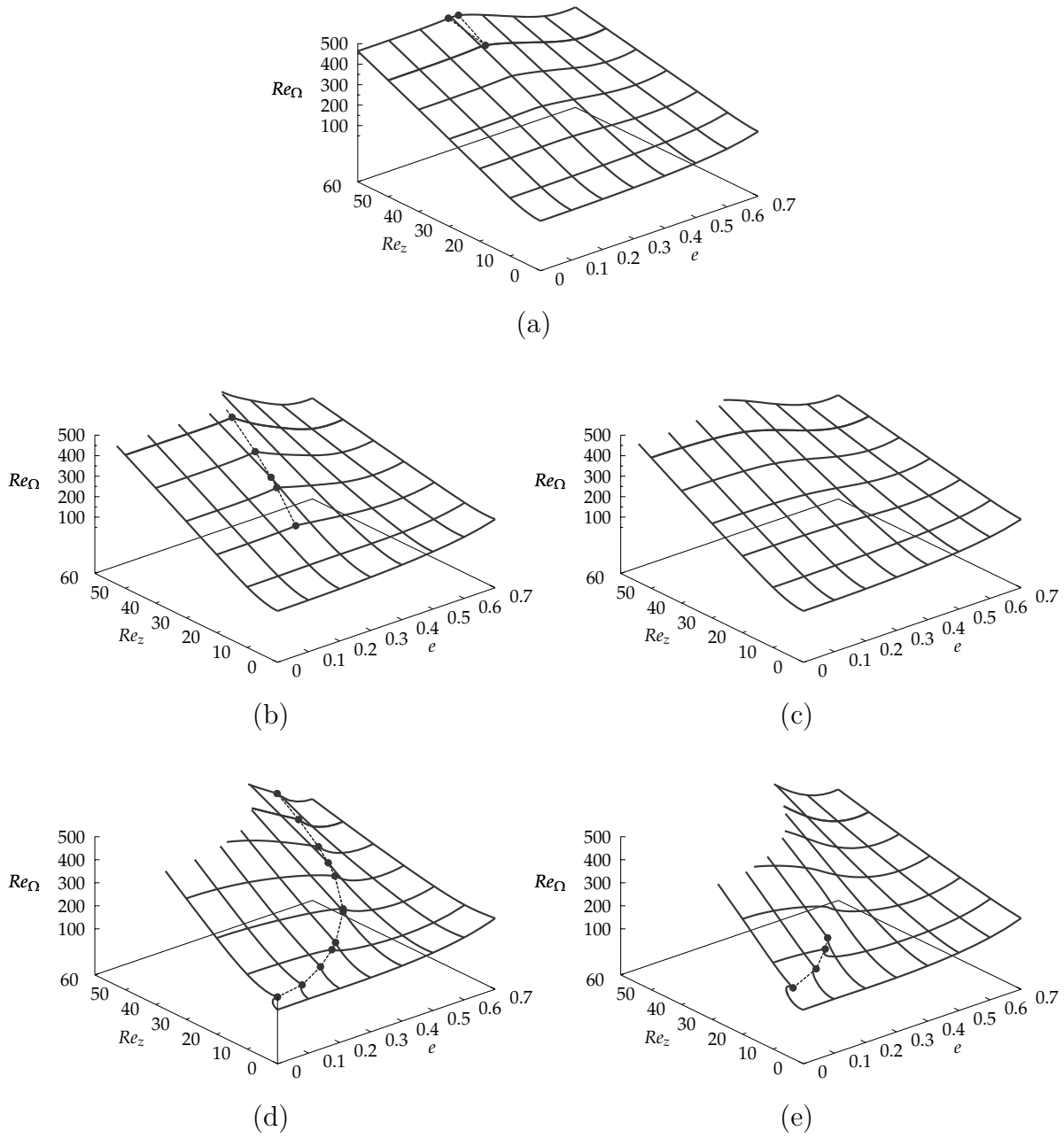

Figure 5.23 – Critical Re_Ω vs. e and Re_z for (a) $m = 0$, (b) $m = 1$, (c) $m = -1$, (d) $m = 2$, (e) $m = -2$. Dots and dashed lines indicate a change of critical saddle point.

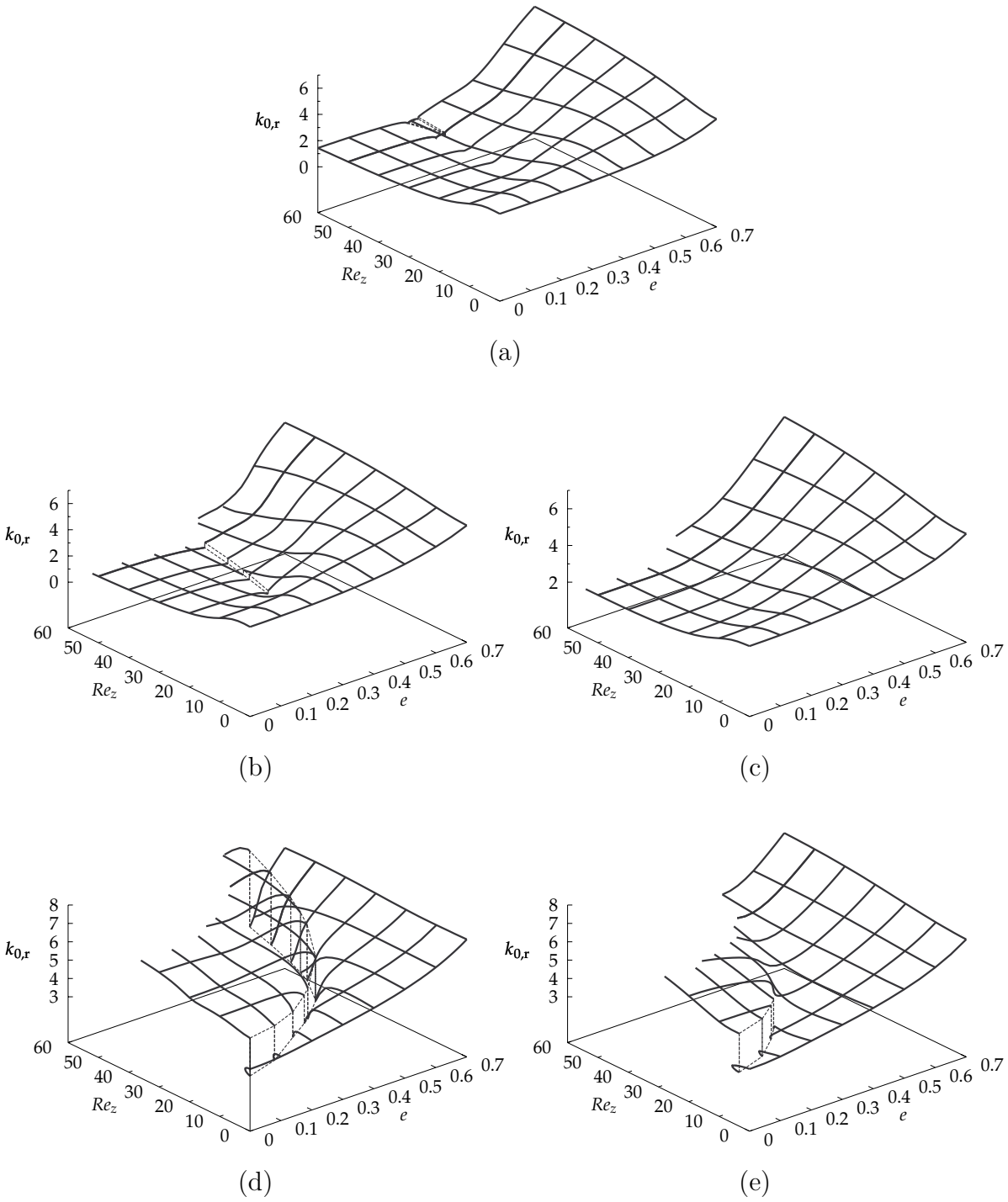

Figure 5.24 – Critical $k_{0,\mathrm{r}}$ vs. e and Re_z for (a) $m = 0$, (b) $m = 1$, (c) $m = -1$, (d) $m = 2$, (e) $m = -2$. Dots and dashed lines indicate a change of critical saddle point.

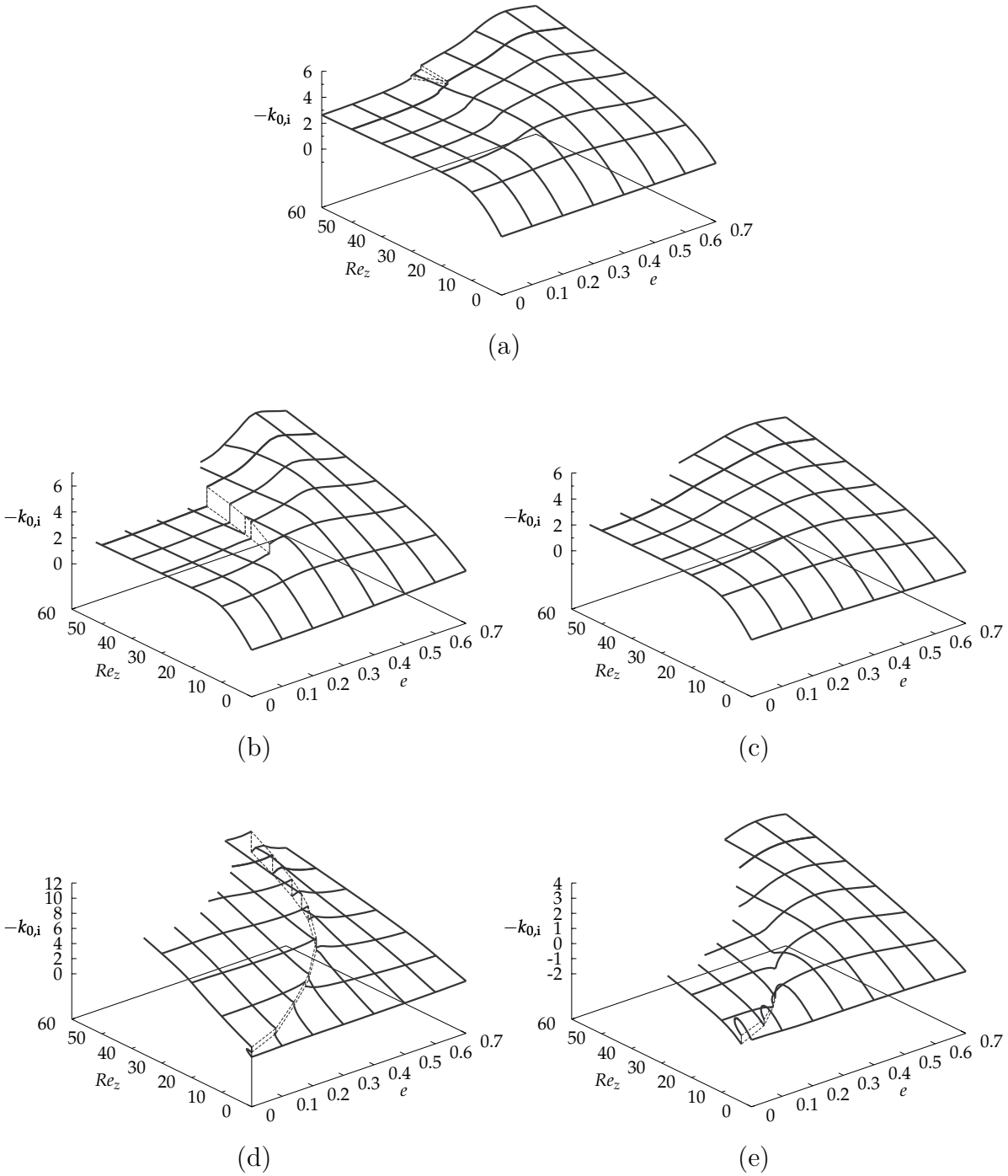

Figure 5.25 – Critical $k_{0,\mathrm{i}}$ vs. e and Re_z for (a) $m = 0$, (b) $m = 1$, (c) $m = -1$, (d) $m = 2$, (e) $m = -2$. Dots and dashed lines indicate a change of critical saddle point.

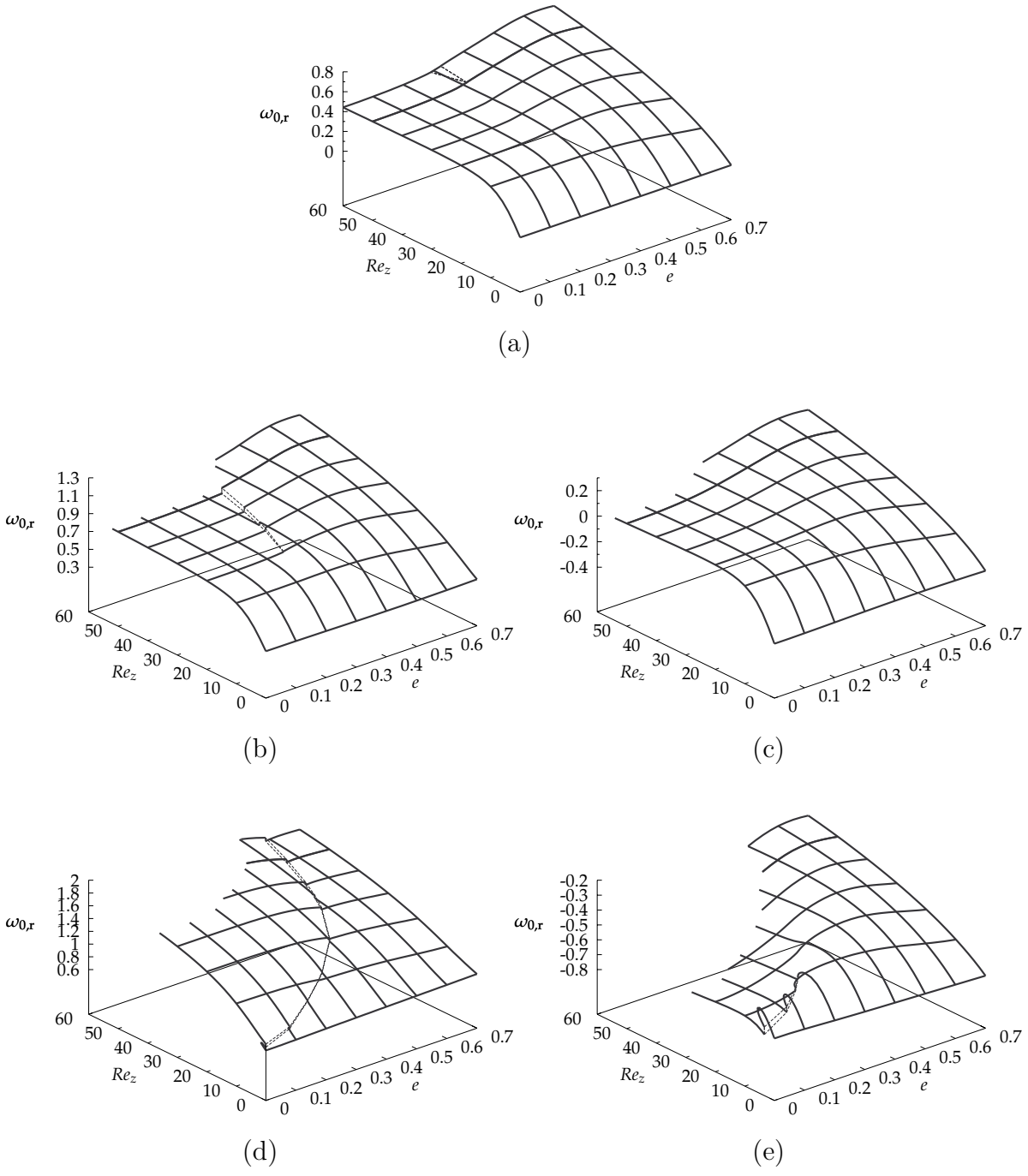

Figure 5.26 – Critical $\omega_{0,\mathrm{r}}$ vs. e and Re_z for (a) $m = 0$, (b) $m = 1$, (c) $m = -1$, (d) $m = 2$, (e) $m = -2$. Dots and dashed lines indicate a change of critical saddle point.

5.7.4 Helical modes at criticality

In this subsection, we describe the helical modes at criticality for $Re_z = 60$, for comparison with $m = 0$, discussed in §4.2.5. Specific values of e and Re_Ω corresponding to figures 5.27 and 5.28 are given in table 5.3.

	(a)		(b)		(c)	
m	e	Re_Ω	e	Re_Ω	e	Re_Ω
1	0.2	560.41	0.4	509.21	0.7	316.83
−1	0.2	537.81	0.4	460.11	0.7	331.85
2	0.505	488.41	0.6	396.83	0.7	339.52
−2	0.5	491.70	0.6	402.57	0.7	381.40

Table 5.3 – Parameter values for plots in figures 5.27 and 5.28.

Despite significant distortion due to eccentricity, the helical structures visually match their associated pseudo-azimuthal wavenumber given by m. For moderate eccentricity, modes $m = 1$ and $m = 2$ are localized in the diverging gap region, in the same fashion as $m = 0$ (see figure 5.11). The mode shape is particularly distorted in this region. For $e = 0.7$, all the modes have similar shapes, and are localized in the vicinity of the inner cylinder. Indeed, as e approaches one, the equivalent clearance of the Couette-like part of the flow becomes smaller and smaller, as indicated in §4.2.5. In the limit $e \to 1$, the flow would be locally similar to a plane Couette-like flow in the vicinity of the inner cylinder, with ϕ as the streamwise slowly-varying direction. In this approximation, m would become a continuous wavenumber, which would explain why the shape and stability properties of the critical modes are similar when e is close to one.

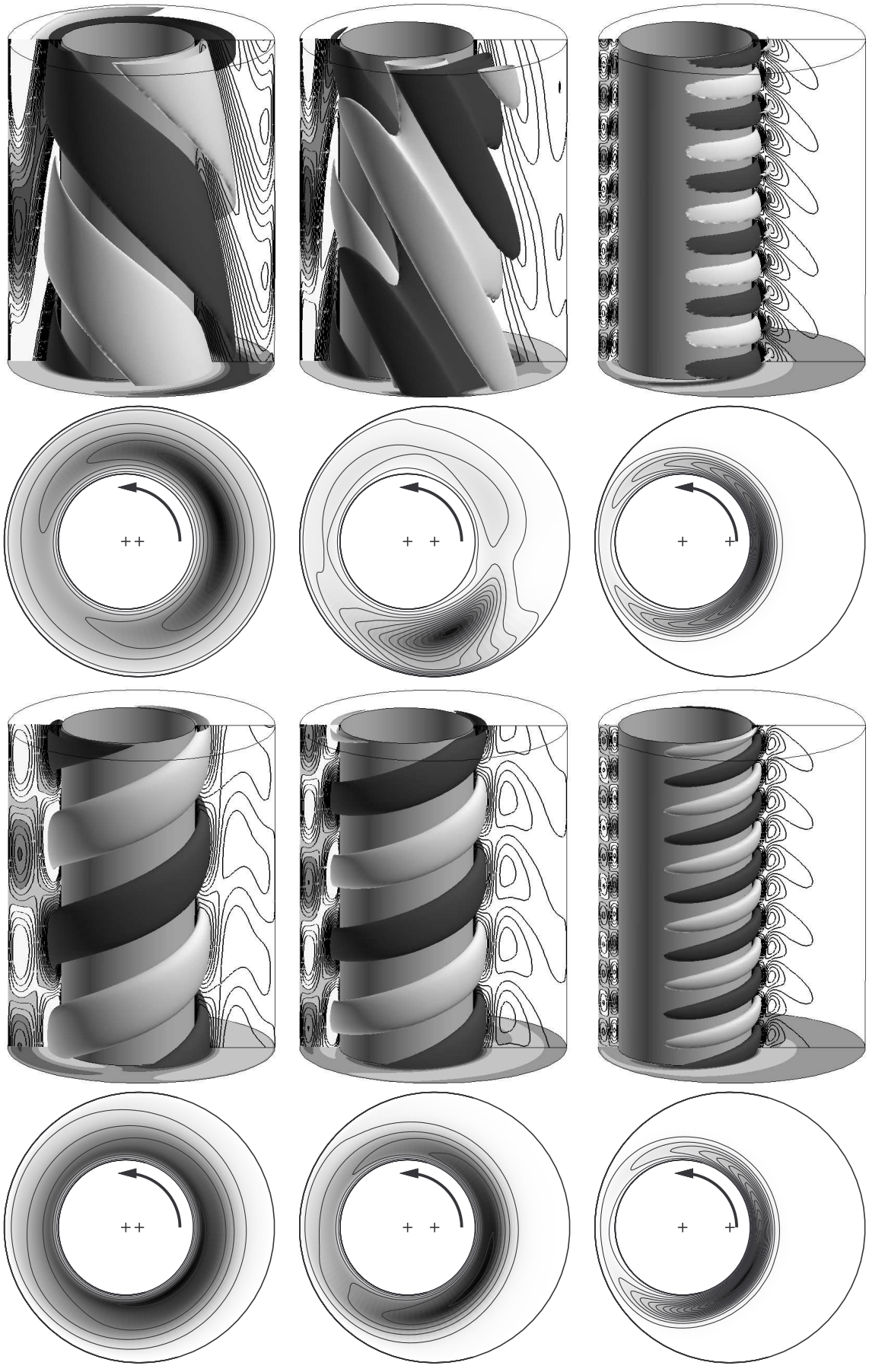

Figure 5.27 – Same caption as figure 5.11 but for $m = 1$ (top) and $m = -1$ (bottom) at $Re_z = 60$. Values of e and Re_Ω at criticality are given in table 5.3.

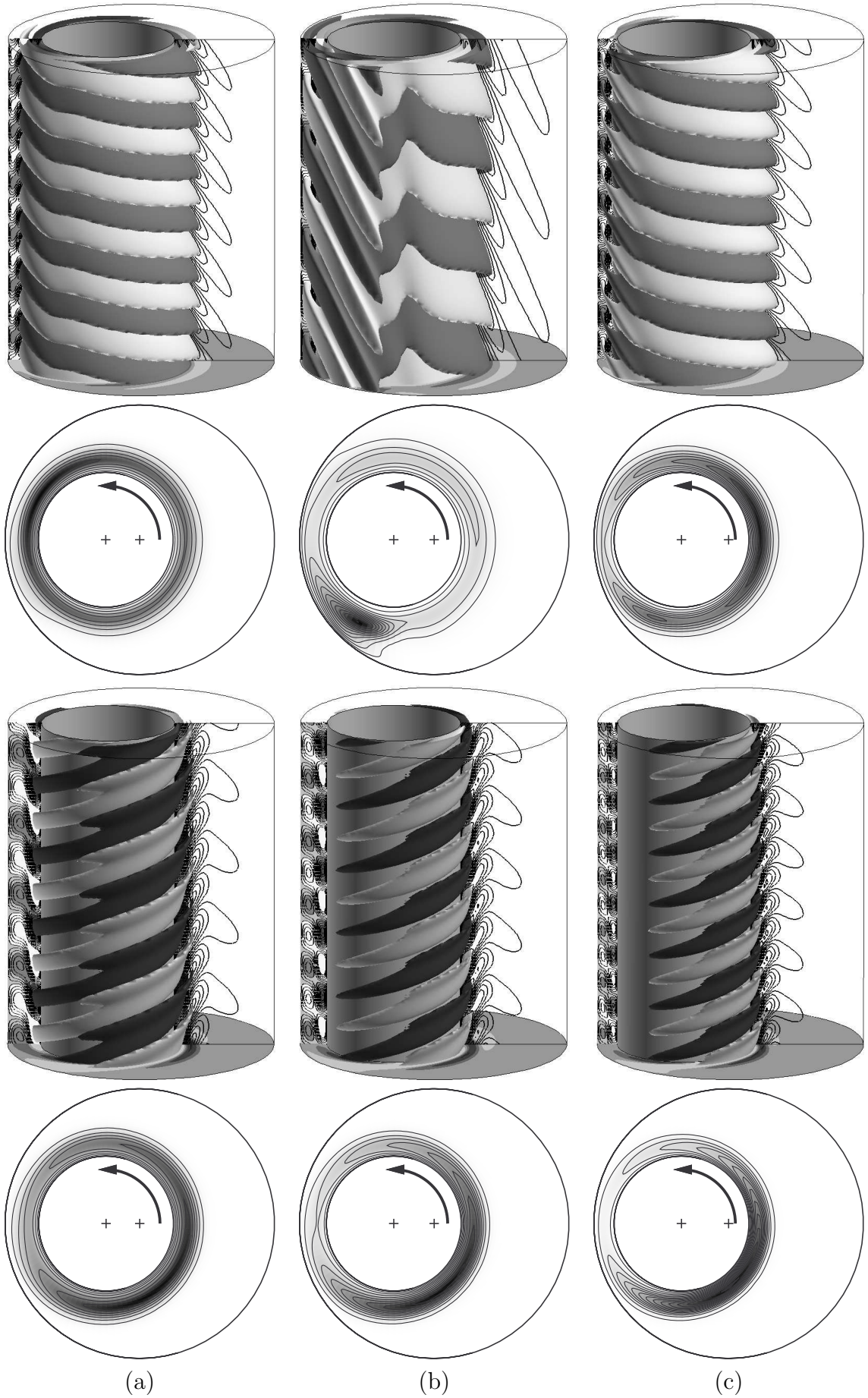

Figure 5.28 – Same caption as figure 5.11 but for $m = 2$ (top) and $m = -2$ (bottom) at $Re_z = 60$. Values of e and Re_Ω at criticality are given in table 5.3.

Chapter 6

Conclusions and future work

In this last chapter, we summarize the main results obtained in chapters 4 and 5, and suggest possible directions for future work.

6.1 Conclusions

In the present work, we have studied the combined effects of eccentricity and axial flow on the linear stability properties of the flow between two infinite cylinders, the outer one being fixed and the inner one rotating. This analysis complements previous studies which have considered the effects of eccentricity and axial flow separately. It is, to the author's knowledge, the first theoretical analysis taking the two effects into account simultaneously. Some experimental results dating from the seventies can be found in the literature, but they are restricted to the convective régime of the instability.

The eccentric Taylor–Couette–Poiseuille flow can be used to model the annular flow of mud between the drillstring and the wellbore in oil-well drilling operations. This flow has several engineering functions among which carrying the rock cuttings out of the well. The drillstring is locally eccentric with respect to the well because of the flexibility of the drillstring. Other applications of this flow have been identified, such as high-speed journal bearings.

A pseudospectral method has been implemented to solve the incompressible Navier–Stokes equations and compute the steady, axially invariant basic-flow solutions. The method is based on a conformal mapping of the eccentric annular domain allowing a Fourier–Chebyshev decomposition of the flow variables. The same decomposition has been used to discretize the normal modes, solutions of the linearized Navier–Stokes equations. A novel reduction method has been implemented to simplify greatly the eigenvalue problem associated with the discretized set of equations. There are four nondimensional control parameters: the eccentricity, e, the radius ratio, η, and the azimuthal and axial Reynolds numbers, Re_Ω and Re_z.

Though many results were already available regarding basic flow solutions, we recall some important properties. In particular, when eccentricity is low, the crossflow components resemble a deformed circular Couette flow, whereas for large enough e ($e \gtrsim 0.2 - 0.3$), a large recirculation zone develops in the wide gap. The separation is

caused by a strong adverse pressure gradient in the diverging gap. In the vicinity of the inner cylinder, the flow remains similar to a Couette flow, but with an 'equivalent' clearance scaling visually with the smallest gap width. The axial flow is driven by a pressure gradient so it is approximately parabolic in the pseudo-radial direction. However, because of distortion by the crossflow components, the maximum axial velocity does not occur at the widest gap location. The forces on the inner cylinder are such that there is no stable position, even when the cylinders are concentric, which is the only equilibrium position. As a result, complex motion of the inner cylinder is to be expected, with possible fluid-structure interaction.

6.1.1 Temporal stability properties

In the temporal stability analysis performed in chapter 4, we have shown that adding eccentricity to the Taylor–Couette–Poiseuille flow does not destabilise any new family of modes. Indeed, the modes with the largest temporal growth rates are always pseudo-toroidal or pseudo-helical vortices such as those found in the concentric case, but deformed by eccentricity. As in the concentric case, right-handed helical modes are always more stable than left-handed helical modes when axial flow is added. In the concentric case, the modes have an azimuthal angular order m because of the axisymmetry of the basic flow. When $e \neq 0$, we chose to label the modes with a pseudo-azimuthal wavenumber m obtained by continuation from the concentric case. For any given eccentricity, the critical value of m increases with Re_z. In other words, pseudo-toroidal vortices give way to left-handed helical modes of increasing pseudo-azimuthal wavenumber as advection increases.

The temporal instability threshold, in terms of critical Re_Ω, usually increases with axial advection, though a weak destabilising effect has been observed for large enough Re_z in the wide gap case $\eta = 0.5$.

For any given value of Re_z, increasing the eccentricity always reduces the maximal temporal growth rate, and this can be considered to be the main result of the temporal stability analysis. This stabilising effect of eccentricity has been interpreted as the consequence of the decrease in azimuthal volume flux in the basic flow, as the recirculation region becomes larger and larger with increasing e. The instability mechanism being centrifugal, it is therefore necessary to rotate the inner cylinder faster when the Couette-like part of the flow has a smaller radial extent. Axial advection tends to destabilise modes of higher pseudo-azimuthal wavenumber m. However, once Re_z is large enough, the temporal growth rate associated with a given m only varies with Re_Ω, confirming the centrifugal nature of the instability mechanism.

The axial wavenumber of the critical mode is always of the order of the clearance, and the phase speed is always of the order of (usually somewhat larger than) the mean axial velocity.

Results obtained in the large- and the small-gap cases are very similar. The main difference is that no destabilising effect of Re_z has been observed for the small gap case. Another qualitative difference is that the stability properties of helical modes with adjacent m are very similar for larger η, hence the switchover from one critical value of m to the next occurs more rapidly as Re_z increases. This effect can be interpreted

by considering the limit $\eta \to 1$, where curvature effects become negligible. In this limit, the circular Couette flow tends to a plane Couette flow, and m becomes a continuous wavenumber, explaining the similarity between the different helical modes when η is close to one.

Finally, comparisons with experimental results from the literature show good agreement with our theoretical predictions, despite small discrepancies which we attribute to the limited aspect ratio of the apparatus.

6.1.2 Absolute instabilities

The effect of eccentricity on absolute instabilities in the Taylor–Couette–Poiseuille flow has been investigated in chapter 5 for the wide gap case $\eta = 0.5$. Fives modes of instability have been considered, $m = -2, -1, 0, 1, 2$, thus including the most temporally unstable modes up to $Re_z = 50$. Throughout the range of Re_z and e considered in the present study, the mode with the largest absolute growth rate is always the pseudo-toroidal vortex flow corresponding to $m = 0$. Dominance of left-handed helical modes over right-handed ones does not always hold for the absolute growth rate.

Increasing Re_z tends to hinder absolute instability because axial flow sweeps perturbations away downstream.

The effect of eccentricity is more complex and *the most significant result of the absolute instability analysis is that eccentricity can be destabilising for large enough Re_z, this occuring in the range of moderate eccentricities* $0.3 \lesssim e \lesssim 0.6$. In this case, the critical mode has a complex structure, and the production of kinetic energy peaks at a well-defined region of the annulus, located in the diverging gap region. For e below ~ 0.3, eccentricity has a weak stabilising effect, while for e close to one, the stabilising effect is more pronounced.

The instability mechanism is purely centrifugal and the critical-mode axial wavelength and radial extent are controlled by the small gap region. When eccentricity is close to one, the effect of Re_z on the absolute instability threshold becomes weaker. To interpret this effect, we noted that the region where centrifugal effects dominate is localized in the vicinity of the inner cylinder whereas axial velocity peaks far from the inner cylinder, somewhere in the wide gap region. This spatial separation between the region of effective amplification of the perturbation and the region of effective axial advection may explain the weak sensitivity to Re_z when the cylinders are nearly touching.

Overall, many valid saddle points were found for the different instability modes, and the critical pinch point switches upon varying the flow parameters. The physical interpretation of the switchovers of saddle point occuring near $e \approx 0.3$ for $m = 0$ is unclear, because the saddle points are associated with modes having almost the same spatio-temporal properties. Indeed, when they swap, they almost collide into 'double saddle points' or third-order saddle points, at which the two saddle points become indistinguishable.

A useful rule of thumb can be deduced from this work: the rotational velocity needs to be approximately one order of magnitude greater than the axial velocity of the inner cylinder to trigger an absolute instability.

In the last section of chapter 5, we have theoretically studied the case of two colliding saddle points and derived a criterion to predict the nature of these saddle points, e.g. valid versus invalid, when control parameters are varied in the vicinity of the 'double saddle point'. The criterion was successfully applied to two double saddle points of the dispersion relation associated with $m = 0$. Despite limited practical interest because of its local nature, the criterion provides valuable information regarding this unusual situation.

6.2 Possible future work

We have a number of suggestions for future work regarding experimental, theoretical/numerical and applied aspects.

6.2.1 The need for more experimental data

The only experimental results regarding this flow were obtained more than forty years ago, and showed great sensitivity to the type of inlet of the apparatus and in the criterion used to identify the instability. Moreover, as noted earlier, the limited aspect ratio of the apparatus may have been responsible for deviations from our theoretical results. Finally, only the convective régime of the instability has been investigated experimentally, probably for the simple reason that the concept of absolute instability was unknown to the experimentalists when they made their observations. Indeed, the concept of absolute instabilities became widely known in the field of fluid mechanics a decade later. For these reasons, it seems crucial to carry out more experiments, preferably using a longer aspect-ratio apparatus. Experimental absolute instability thresholds remain to be established and the effect of inlet boundary condition needs to be clarified in the presence of eccentricity. The distance from the inlet necessary to reach order one amplitude could be compared with the theoretical scalings obtained by Couairon and Chomaz (1997a), successfully applied to axisymmetric Taylor–Couette–Poiseuille flow (Couairon and Chomaz, 1997b). It would also be interesting to reproduce the conditions that lead to the observation of the 'double-vortex system' and draw firmer conclusions building on our discussion in §4.4.5.

6.2.2 Further linear and nonlinear dynamics

Linear stability properties

- The modal stability properties at very high axial Reynolds number (say $Re_z \gtrsim 10^3$) remain to be investigated. It would be interesting to assess the potential importance of 'Sp-modes' found by Merzari et al. (2008) in eccentric annular Poiseuille flow and study the competition with centrifugal and Tollmien–Schlichting-like modes, in the spirit of the analysis of Cotrell and Pearlstein (2004) for the axisymmetric case. Such an endeavour is expected to lead to significant numerical difficulties though, because the three families of modes have quite different structures.

- The global linear stability properties in the case where the eccentricity is slowly varying along the axis could be considered (Huerre, 2000). Such an analysis would be relevant to oil-well drilling applications, where the drillstring deflection has, for instance, an axial length scale much larger than the well diameter. Interesting results may arise from the fact that the variation of the absolute growth rate with respect to eccentricity is non-monotonic.
- A structural sensitivity analysis (Giannetti and Luchini, 2003) could be used to gain more information about the feedback mechanism responsible for enhanced absolute instability in the moderate eccentricity case. This would potentially help explain the changes of critical saddle point for $e \sim 0.3$.
- The importance of non-modal effects has not been assessed here, because they are expected to be weak for the range $Re_z \lesssim 10^2$ of our analyses. However, a recent study Heaton (2008) has shown that they become important at larger advection rates in the axisymmetric configuration and it may be interesting to examine the effects of eccentricity.

Nonlinear dynamics

- A weakly nonlinear analysis in the vicinity of critical conditions would tell us if the transition is supercritical or subcritical. A particularly interesting case occurs when two modes become critical at the same time. 'Unfolding' the bifurcation (here double-Hopf) in such cases would be particularly challenging from a numerical viewpoint, and this type of approach has seldom been applied to flows of such complexity (see however Avila et al. (2006) and Meliga et al. (2009)).
- Fully nonlinear analyses could be carried out after significant modification of our code. Using three-dimensional DNS on a finite axial domain with periodic boundary conditions would yield the nonlinear wave solutions for unstable configurations. This would be particularly useful for comparisons with experimental results. Using a much longer axial domain (without periodic boundary conditions), any nonlinear state could in principle be simulated: steady, periodic, quasi-periodic or even turbulent.
- Another approach would be to implement Newton–Raphson iteration to solve for nonlinear wave patterns and their phase speed. Using this approach, one could follow potentially unstable solutions and build bifurcation diagrams by continuation. This method would also yield the nonlinear dispersion relation between the real frequency, real wavenumber and amplitude of the saturated waves. With the knowledge of the complete linear and nonlinear dispersion relations for a range of eccentricities, it would be possible to investigate the existence of nonlinear global modes in the case of slowly varying eccentricity, using the theory of Pier and Huerre (2001). In this situation, the local linear stability properties of the basic flow would vary along the axis, with regions of space being potentially stable, convectively unstable or absolutely unstable. For high values of the rotational Reynolds number, pockets of absolute instability would exist and nonlinear synchronized states leading to a sharp front are expected to emerge (Pier et al., 1998). The properties of such 'elephant modes' (Pier and Huerre, 2001) can be readily derived from the linear and nonlinear dispersion relations and then checked using direct numerical simulations. A different type of nonlinear synchronized structures called soft modes, or 'hat modes', theoretically predicted by Pier and Huerre (1996), might

also be found in this flow when axial advection is weak. Hat modes have been obtained for a one-dimensional model equation, but have yet to be observed in any real flows so far. It would thus be particularly exciting to confirm the physical relevance of hat modes by testing the theory on the present configuration.

6.2.3 Towards a higher-fidelity model for drilling applications

A different research path could be followed if one focuses on the oil-well drilling application. Indeed, even though the assumption of constant eccentricity through the well is unrealistic for this application, the assumption of a Newtonian fluid is probably an even bolder one, which may need to be relaxed first. Drilling muds are non-Newtonian fluids with complex rheological properties, which are expected to lead to different instability thresholds and mechanisms (Escudier et al., 2002, Chawda and Avgousti, 1996, Dris and Shaqfeh, 1998). However, adapting the code to take into account nonlinear rheological properties is expected to be a non-trivial task.

Another aspect would be taking into account the coupled dynamics of the inner cylinder and fluid. In practice, the centre of the inner cylinder is not held fixed, but moves according to the mechanical and hydrodynamic forces which act on it. A proper modelling of fluid-structure interaction and the handling of a time-dependent fluid domain would be required. Major difficulties would also arise from the fact that eccentricities close to one occur in practice. Simulating the coupled dynamics would be a very challenging problem, but one which might be rendered feasible by assuming a simplified motion, for example a circular orbit, as in Feng et al. (2007) and Feng and Fu (2007).

Appendix A

Pseudospectral method

A.1 Fourier–Galerkin decomposition

Let g be a 2π-periodic function over $\mathbb{R}$, then

$$g(\phi) = \sum_{k=-\infty}^{\infty} \hat{g}_k \mathrm{e}_k(\phi) \tag{A.1}$$

is its Fourier series representation. For numerical purposes, the series is truncated as

$$g(\phi) \approx g_K(\phi) = \sum_{|k|\leq K} \hat{g}_k e_k(\phi). \tag{A.2}$$

The advantage of a *spectral* approach such as this is that, for smooth g, it allows approximation with convergence faster than any negative power of K (Canuto et al., 1988). This may be contrasted with *local* approximations, such as finite differences, finite volumes or finite elements, which achieve only algebraic convergence with the discretization step.

Other than rapid convergence, Fourier decomposition is also very efficient for differentiation. Thus, the derivative of (A.2) of order p gives

$$\hat{g}_k^{(p)} = (\mathrm{i}k)^p \hat{g}_k, \ |k| \leq K, \tag{A.3}$$

whose calculation requires only $O(K)$ arithmetic operations.

If g is real-valued, then

$$\hat{g}_{-k} = \hat{g}_k^\star, \tag{A.4}$$

with '$\star$' denoting complex conjugation. The Hermitian symmetry allows us to write

$$g_K(\phi) = a_0 + \sum_{k=1}^{K} (a_k \cos k\phi + b_k \sin k\phi), \tag{A.5}$$

with $a_0 = \hat{g}_0$ and $a_k = 2\hat{g}_{k,\mathrm{r}}$, $b_k = -2\hat{g}_{k,\mathrm{i}}$ $(1 \leq k \leq K)$, where subscripts 'r' and 'i' denote real and imaginary parts. This allows more efficient numerical treatment of real fields, such as those of the basic flow.

Products of two functions of ϕ are treated using a pseudospectral approach (see e.g. Canuto et al. (1988), Peyret (2002)). Given the Fourier coefficients of the functions, zero-padded up to a total of N' using Orszag (1971)'s '3/2 rule' to avoid aliasing, FFT is used to compute the functions at the discrete points,

$$\phi_i = \frac{2\pi i}{N'}, \quad 0 \le i \le N' - 1. \tag{A.6}$$

The product is then taken in 'physical' space and inverse FFT employed to return to 'spectral' space. The resulting Fourier coefficients of the product are then truncated to $|k| \le K$. This approach is more efficient than taking convolutions in 'spectral' space.

A.2 Chebyshev collocation

Let h be a smooth function defined on $[-1, 1]$. It can be represented as a combination of Chebyshev polynomial as

$$h_M(\xi) = \sum_{j=0}^{M} \hat{h}_j T_j(\xi). \tag{A.7}$$

This provides an M^{th} degree polynomial approximation and, like the Fourier representation, has the advantage of spectral accuracy.

Let ξ_i be the set of Gauss–Lobatto collocation points on $-1 \le \xi \le 1$ given by

$$\xi_i = -\cos\frac{i\pi}{M}, \ 0 \le i \le M. \tag{A.8}$$

and $h_i = h(\xi_i)$ denote the values at these points. An M^{th} degree polynomial approximation which agrees with h at the collocation points is

$$h_M(\xi) = \sum_{j=0}^{M} h_j q_j(\xi), \tag{A.9}$$

where

$$q_j(\xi) = \prod_{\substack{i=0 \\ i \ne j}}^{M} \frac{\xi - \xi_i}{\xi_j - \xi_i}, \tag{A.10}$$

is the Lagrange interpolation polynomial of collocation point ξ_j.

Differentiating (A.9) gives

$$h'_M(\xi) = \sum_{j=0}^{M} h_j q'_j(\xi). \tag{A.11}$$

Evaluating this relation at the collocation points, a linear relation appears between the coefficients h_j and $h'_i \equiv h'(\xi_i)$

$$h'_i = \sum_{j=0}^{M} h_j q'_j(\xi_i). \tag{A.12}$$

Let $\mathsf{h} \equiv (h_0, h_1 \ldots, h_M)^T$ and $\mathsf{h}' \equiv (h'_0, h'_1, \ldots, h'_M)^T$ then (A.12) can be written as $\mathsf{h}' = \mathsf{D}\mathsf{h}$, with the differentiation matrix $\mathsf{D} \equiv (d_{ij}^{(1)}) = (q'_j(\xi_i))$ given by

$$\mathsf{D} = \begin{cases} d_{ij}^{(1)} = \dfrac{\bar{c}_i}{\bar{c}_j} \dfrac{(-1)^{i+j}}{(\xi_i - \xi_j)}, & 0 \leq i, j \leq M,\ i \neq j, \\ d_{ii}^{(1)} = -\dfrac{\xi_i}{2(1-\xi_i^2)}, & 0 < i < M, \\ d_{00}^{(1)} = -d_{MM}^{(1)} = \dfrac{2M^2+1}{6}, \end{cases} \tag{A.13}$$

where

$$\bar{c}_j = \begin{cases} 2 & \text{if } j = 0 \text{ or } j = M, \\ 1 & \text{if } 0 < j < M. \end{cases} \tag{A.14}$$

Higher-order derivatives $\mathsf{h}^{(p)} \equiv (h_0^{(p)}, h_1^{(p)}, \ldots, h_M^{(p)})^T$, with $h_j^{(p)} \equiv h_M^{(p)}(\xi_j)$ for any integer $p > 2$, are then obtained as

$$\mathsf{h}^{(p)} = \mathsf{D}\mathsf{h}^{(p-1)} = \mathsf{D}^2\mathsf{h}^{(p-2)} = \cdots = \mathsf{D}^p\mathsf{h}, \tag{A.15}$$

where $\mathsf{D}^p \equiv (d_{ij}^{(p)})$ is the p-order derivation matrix.

Roundoff errors

The Navier–Stokes equations are second order in space, so only D and D^2 are needed. In principle, if one considers the differentiation of a constant function at any order p, the following relation must hold

$$\sum_{j=0}^{M} d_{ij}^{(p)} = 0,\ i = 0, \ldots, M. \tag{A.16}$$

However, because of roundoff errors, this relation is not satisfied in practice. To avoid this source of inaccuracy, the method recommended by Bayliss et al. (1995) is followed. First, D is calculated from analytical formulas (A.13), but the diagonal terms are replaced by

$$d_{ii}^{(1)} = -\sum_{\substack{j=0 \\ j \neq i}}^{M} d_{ij}^{(1)} = 0,\ i = 0, \ldots, M, \tag{A.17}$$

using (A.16). The second order derivation matrix is then calculated as the product D^2, before replacing the diagonal entries with

$$d_{ii}^{(2)} = -\sum_{\substack{j=0 \\ j \neq i}}^{M} d_{ij}^{(2)} = 0,\ i = 0, \ldots, M. \tag{A.18}$$

The derivation matrices being full, large roundoff errors may occur during matrix vector products or resolution of linear systems, for large values of M. However, in the present study, $M + 1$ is typically 16, and no larger than 64, so the approach is fully valid.

A.3 Matrix form of linear operators for real fields

In-plane gradient (3.18a), divergence (3.18b) and scalar Laplacian (3.19) terms can be expressed using the truncated Fourier–Chebyshev decomposition (3.20). To do this, Fourier decomposition of scale factors μ_ξ and μ_ϕ are needed. Both metric coefficients are proportional to $\sqrt{J}$ so

$$\mu_\xi = \hat{\mu}_0 + \hat{\mu}_1(\mathrm{e}^{\mathrm{i}\phi} + \mathrm{e}^{-\mathrm{i}\phi}),\ \mu_\phi = \zeta\mu_\xi, \tag{A.19}$$

with

$$\hat{\mu}_0 = \frac{1+\gamma^2\rho^2}{1-\gamma^2},\ \hat{\mu}_1 = \frac{\gamma\rho}{1-\gamma^2}, \tag{A.20}$$

and

$$\zeta = \frac{\beta-1}{2\rho},\ \rho = 1 + \frac{1}{2}(\beta-1)(1+\xi). \tag{A.21}$$

Factors A and B and can also be Fourier decomposed, and (3.17) yields

$$\hat{A}_k = \zeta\hat{\mu}_k - \partial_\xi\hat{\mu}_k,\ \hat{B}_k = \zeta\mathrm{i}k\hat{\mu}_k. \tag{A.22}$$

The only non-zero terms are

$$\hat{A}_0 = \zeta\hat{\mu}_0 - \partial_\xi\hat{\mu}_0, \quad \hat{A}_{-1} = \hat{A}_1 = \zeta\hat{\mu}_1 - \partial_\xi\hat{\mu}_1, \quad \hat{B}_1 = -\hat{B}_{-1} = \mathrm{i}\zeta\hat{\mu}_1, \tag{A.23}$$

with

$$\partial_\xi\hat{\mu}_0 = \frac{\gamma^2\rho(\beta-1)}{1-\gamma^2}, \quad \partial_\xi\hat{\mu}_1 = \frac{\gamma(\beta-1)}{2(1-\gamma^2)}. \tag{A.24}$$

Assume for now that $K = \infty$ to express the Fourier components of (3.18a), (3.18b) and (3.19) for any integer k. Despite linearity of these terms with respect to the flow variables, product with the metric coefficients lead to convolution sums:

Gradient

Considering one Fourier harmonic k

$$\begin{aligned}\widehat{(D_\xi f)}_k = \widehat{(\mu_\xi\partial_\xi f)}_k &= \sum_{l=-\infty}^{\infty}\hat{\mu}_l\partial_\xi\hat{f}_{k-l} \\ &= \hat{\mu}_0\partial_\xi\hat{f}_k + \hat{\mu}_1\left[\partial_\xi\hat{f}_{k+1} + \partial_\xi\hat{f}_{k-1}\right],\end{aligned} \tag{A.25}$$

$$\begin{aligned}\widehat{(D_\phi f)}_k = \widehat{(\zeta\mu_\xi\partial_\phi f)}_k &= \mathrm{i}\zeta\sum_{l=-\infty}^{\infty}\hat{\mu}_l(k-l)\hat{f}_{k-l} \\ &= \mathrm{i}\zeta\left(\hat{\mu}_0 k\hat{f}_k + \hat{\mu}_1\left[(k+1)\hat{f}_{k+1} + (k-1)\hat{f}_{k-1}\right]\right),\end{aligned} \tag{A.26}$$

then using Chebyshev collocation for $0 \le i, j \le M$ (and Einstein summation convention)

$$\widehat{(D_\xi f)}_{ki} = \hat{\mu}_{0i}d^{(1)}_{ij}\hat{f}_{kj} + \hat{\mu}_{1i}d^{(1)}_{ij}\left[\hat{f}_{(k+1)j} + \hat{f}_{(k-1)j}\right], \tag{A.27}$$

$$\widehat{(D_\phi f)}_{ki} = \mathrm{i}\zeta\left(\hat{\mu}_{0i}k\hat{f}_{ki} + \hat{\mu}_{1i}\left[(k+1)\hat{f}_{(k+1)i} + (k-1)\hat{f}_{(k-1)i}\right]\right). \tag{A.28}$$

Divergence

Consider one Fourier harmonic k

$$\widehat{(\nabla_\perp \mathbf{u}_\perp)}_k = \widehat{(D_\xi u)}_k + \widehat{(D_\phi v)}_k + \widehat{(Au)}_k - \widehat{(Bv)}_k. \tag{A.29}$$

The first two terms in this equation are given by (A.25) and (A.26) for $f \equiv u, v$. The last two terms are

$$\begin{aligned}\widehat{(Af)}_k &= \sum_{l=-\infty}^{\infty} \hat{A}_l \hat{f}_{k-l} \\ &= \hat{A}_0 \hat{f}_k + \hat{A}_1(\hat{f}_{k-1} + \hat{f}_{k+1}),\end{aligned} \tag{A.30}$$

$$\begin{aligned}\widehat{(Bf)}_k &= \sum_{l=-\infty}^{\infty} \hat{B}_l \hat{f}_{k-l} \\ &= \hat{B}_1(\hat{f}_{k-1} - \hat{f}_{k+1}),\end{aligned} \tag{A.31}$$

then using Chebyshev collocation for $0 \le i \le M$

$$\widehat{(Af)}_{ki} = \hat{A}_{0i}\hat{f}_{ki} + \hat{A}_{1i}(\hat{f}_{(k-1)i} + \hat{f}_{(k+1)i}), \tag{A.32}$$

$$\widehat{(Bf)}_{ki} = \hat{B}_{1i}(\hat{f}_{(k-1)i} - \hat{f}_{(k+1)i}). \tag{A.33}$$

Scalar Laplacian

The scalar Laplacian is given by (3.19)

$$\begin{aligned}\nabla_\perp^2 &\equiv D_\xi^2 + D_\phi^2 + (AD_\xi - BD_\phi) \\ &= \mu_\xi^2(\partial_{\xi\xi}^2 + \zeta\partial_\xi + \zeta^2\partial_{\phi\phi}^2).\end{aligned} \tag{A.34}$$

The Fourier decomposition of μ_ξ^2 is

$$\mu_\xi^2 = \left[\hat{\mu}_0^2 + 2\hat{\mu}_1^2\right] + 2\hat{\mu}_0\hat{\mu}_1(\mathrm{e}^{\mathrm{i}\phi} + \mathrm{e}^{-\mathrm{i}\phi}) + \hat{\mu}_1^2(\mathrm{e}^{2\mathrm{i}\phi} + \mathrm{e}^{-2\mathrm{i}\phi}), \tag{A.35}$$

so for a scalar field f

$$\begin{aligned}\widehat{(\nabla_\perp^2 f)}_k &= \sum_{l=-\infty}^{\infty} \widehat{(\mu_\xi^2)}_l(\partial_{\xi\xi}^2 + \zeta\partial_\xi - \zeta^2(k-l)^2)\hat{f}_{k-l} \\ &= \left[\hat{\mu}_0^2 + 2\hat{\mu}_1^2\right](\partial_{\xi\xi}^2 + \zeta\partial_\xi - \zeta^2 k^2)\hat{f}_k \\ &+ 2\hat{\mu}_0\hat{\mu}_1\left[(\partial_{\xi\xi}^2 + \zeta\partial_\xi - \zeta^2(k-1)^2)\hat{f}_{k-1} + (\partial_{\xi\xi}^2 + \zeta\partial_\xi - \zeta^2(k+1)^2)\hat{f}_{k+1}\right] \\ &+ \hat{\mu}_1^2\left[(\partial_{\xi\xi}^2 + \zeta\partial_\xi - \zeta^2(k-2)^2)\hat{f}_{k-2} + (\partial_{\xi\xi}^2 + \zeta\partial_\xi - \zeta^2(k+2)^2)\hat{f}_{k+2}\right].\end{aligned} \tag{A.36}$$

Using Chebyshev collocation for $0 \le i, j \le M$

$$\begin{aligned}\widehat{(\nabla_\perp^2 f)}_{ki} = &\left[\hat{\mu}_{0i}^2 + 2\hat{\mu}_{1i}^2\right]\left[(d_{ij}^{(2)} + \zeta_i d_{ij}^{(1)})\hat{f}_{kj} - \zeta_i^2 k^2 \hat{f}_{ki}\right] \\ &+ 2\hat{\mu}_{0i}\hat{\mu}_{1i}\left[(d_{ij}^{(2)} + \zeta_i d_{ij}^{(1)})\hat{f}_{(k-1)j} - \zeta_i^2 (k-1)^2 \hat{f}_{(k-1)i}\right] \\ &+ 2\hat{\mu}_{0i}\hat{\mu}_{1i}\left[(d_{ij}^{(2)} + \zeta_i d_{ij}^{(1)})\hat{f}_{(k+1)j} - \zeta_i^2 (k+1)^2 \hat{f}_{(k+1)i}\right] \\ &+ \hat{\mu}_{1i}^2\left[(d_{ij}^{(2)} + \zeta_i d_{ij}^{(1)})\hat{f}_{(k-2)j} - \zeta_i^2 (k-2)^2 \hat{f}_{(k-2)i}\right] \\ &+ \hat{\mu}_{1i}^2\left[(d_{ij}^{(2)} + \zeta_i d_{ij}^{(1)})\hat{f}_{(k+2)j} - \zeta_i^2 (k+2)^2 \hat{f}_{(k+2)i}\right]. \end{aligned} \tag{A.37}$$

Let now ψ be any of the following linear operators $f \mapsto g \in \{D_\xi f, D_\phi f, Af, Bf, \nabla_\perp^2 f\}$. Relations (A.27), (A.28), (A.32), (A.33) and (A.37) between $\hat{g}_{ki}$ and $\hat{f}_{ki}$ are infinite sets of equations. Assume now that $|k| \leq K$, then these relations become linear systems with $(M+1)(2K+1)$ equations and unknowns, which can be represented each by a square matrix M. Such matrices are needed for basic flow computations, as explained later in §3.3.1, so from now on, f will be a real field. Because f and g are both real-valued, they have Hermitian symmetry and only the Fourier coefficients with $k \geq 0$ need be stored (see Appendix A.1). Moreover, the zeroth-order Fourier coefficient is real. Therefore, the coefficients $\hat{f}_{ki}$ and $\hat{g}_{ki}$ will be stored in two real-valued column-vectors f and g as follows

$$\mathsf{f} \equiv (\hat{\mathsf{f}}_{0,\mathrm{r}}, \hat{\mathsf{f}}_{1,\mathrm{r}}, \ldots, \hat{\mathsf{f}}_{K,\mathrm{r}}, \hat{\mathsf{f}}_{1,\mathrm{i}}, \ldots, \hat{\mathsf{f}}_{K,\mathrm{i}})^T, \quad \mathsf{g} \equiv (\hat{\mathsf{g}}_{0,\mathrm{r}}, \hat{\mathsf{g}}_{1,\mathrm{r}}, \ldots, \hat{\mathsf{g}}_{K,\mathrm{r}}, \hat{\mathsf{g}}_{1,\mathrm{i}}, \ldots, \hat{\mathsf{g}}_{K,\mathrm{i}})^T,$$

where each $\hat{\mathsf{f}}_{k,\mathrm{r/i}}$ and $\hat{\mathsf{g}}_{k,\mathrm{r/i}}$ is decomposed on the collocation points as

$$\hat{\mathsf{f}}_{k,\mathrm{r/i}} \equiv (\hat{f}_{k0,\mathrm{r/i}}, \hat{f}_{k1,\mathrm{r/i}}, \ldots, \hat{f}_{kM,\mathrm{r/i}}), \quad \hat{\mathsf{g}}_{k,\mathrm{r/i}} \equiv (\hat{g}_{k0,\mathrm{r/i}}, \hat{g}_{k1,\mathrm{r/i}}, \ldots, \hat{g}_{kM,\mathrm{r/i}}).$$

Given these conventions, relations (A.27), (A.28), (A.32), (A.33) and (A.37) can be written as $\mathsf{Mf} = \mathsf{g}$, with a four-block matrix M

$$\mathsf{M} = \begin{pmatrix} \mathsf{M}_{\mathrm{rr}} & \mathsf{M}_{\mathrm{ri}} \\ \mathsf{M}_{\mathrm{ir}} & \mathsf{M}_{\mathrm{ii}} \end{pmatrix}, \tag{A.38}$$

and block dimensions

$$\begin{aligned} &\mathsf{M}_{\mathrm{rr}} : (M+1)(K+1) \times (M+1)(K+1) \\ &\mathsf{M}_{\mathrm{ri}} : (M+1)(K+1) \times (M+1)K \\ &\mathsf{M}_{\mathrm{ir}} : (M+1)K \times (M+1)(K+1) \\ &\mathsf{M}_{\mathrm{ii}} : (M+1)K \times (M+1)K. \end{aligned}$$

Each of these blocks is composed of square sub-blocks of size $M+1$. Each line of each system of equations can be written as

$$\hat{g}_{ki,p} = \sum_q \sum_l \sum_j \mathsf{M}_{pq}[k,l;i,j]\hat{f}_{lj,q}, \tag{A.39}$$

where $p, q \in \{\mathrm{r}, \mathrm{i}\}$, $0 \leq i, j \leq M$ and

- if $p = q = \mathrm{r}$:

$$0 \leq k, l \leq K, \quad \mathsf{M}_{pq}[k,l;i,j] \equiv \mathsf{M}_{\mathrm{rr}}[i + k(M+1), j + l(M+1)],$$

- if $p = \mathrm{r}$ & $q = \mathrm{i}$

$$0 \le k \le K,\ 1 \le l \le K, \quad \mathsf{M}_{pq}[k,l;i,j] \equiv \mathsf{M}_{\mathrm{ri}}[i + k(M+1), j + (l-1)(M+1)],$$

- if $p = \mathrm{i}$ & $q = \mathrm{r}$

$$1 \le k \le K,\ 0 \le l \le K, \quad \mathsf{M}_{pq}[k,l;i,j] \equiv \mathsf{M}_{\mathrm{ir}}[i + (k-1)(M+1), j + l(M+1)],$$

- if $p = q = \mathrm{i}$

$$1 \le k, l \le K, \quad \mathsf{M}_{pq}[k,l;i,j] \equiv \mathsf{M}_{\mathrm{ii}}[i + (k-1)(M+1), j + (l-1)(M+1)].$$

Note that matrix entries labelling starts at $\mathsf{M}_{pq}[0,0]$, to match pointer convention in C^{++}.

Gradient

- Let $\underline{g \equiv D_\xi f}$, then $\mathsf{M}_{\mathrm{ri}} = 0$, $\mathsf{M}_{\mathrm{ir}} = 0$, whereas M_{rr} and M_{ii} are block-tridiagonal

$$\mathsf{M}_{\mathrm{rr}}[k,l;i,j] = \begin{cases} \hat{\mu}_{0i} d_{ij}^{(1)} & \text{if } l = k, \\ \hat{\mu}_{1i} d_{ij}^{(1)} & \text{if } l = k-1, k+1 \text{ and } (k,l) \neq (0,1), \\ 2\hat{\mu}_{1i} d_{ij}^{(1)} & \text{if } (k,l) = (0,1), \\ 0 & \text{otherwise,} \end{cases} \tag{A.40}$$

$$\mathsf{M}_{\mathrm{ii}}[k,l;i,j] = \begin{cases} \hat{\mu}_{0i} d_{ij}^{(1)} & \text{if } l = k, \\ \hat{\mu}_{1i} d_{ij}^{(1)} & \text{if } l = k-1, k+1, \\ 0 & \text{otherwise.} \end{cases} \tag{A.41}$$

- Let $\underline{g \equiv D_\phi f}$, then $\mathsf{M}_{\mathrm{rr}} = 0$, $\mathsf{M}_{\mathrm{ii}} = 0$, whereas M_{ri} and M_{ir} are block-tridiagonal

$$\mathsf{M}_{\mathrm{ri}}[k,l;i,j] = \begin{cases} -\zeta_i \hat{\mu}_{0i} l \delta_{ij} & \text{if } l = k, \\ -\zeta_i \hat{\mu}_{1i} l \delta_{ij} & \text{if } l = k-1, k+1 \text{ and } (k,l) \neq (0,1), \\ -2\zeta_i \hat{\mu}_{1i} \delta_{ij} & \text{if } (k,l) = (0,1), \\ 0 & \text{otherwise,} \end{cases} \tag{A.42}$$

$$\mathsf{M}_{\mathrm{ir}}[k,l;i,j] = \begin{cases} \zeta_i \hat{\mu}_{0i} l \delta_{ij} & \text{if } l = k, \\ \zeta_i \hat{\mu}_{1i} l \delta_{ij} & \text{if } l = k-1, k+1, \\ 0 & \text{otherwise.} \end{cases} \tag{A.43}$$

The special case $(k,l) = (0,1)$ corresponds to the fact that $\hat{f}_{-1} = \hat{f}_1^\star$.

Divergence

- Let $\underline{g \equiv Af}$, then $\mathsf{M}_{\mathrm{ri}} = 0$, $\mathsf{M}_{\mathrm{ir}} = 0$, whereas M_{rr} and M_{ii} are block-tridiagonal

$$\mathsf{M}_{\mathrm{rr}}[k,l;i,j] = \begin{cases} \hat{A}_{0i}\delta_{ij} & \text{if } l=k, \\ \hat{A}_{1i}\delta_{ij} & \text{if } l=k-1,k+1 \text{ and } (k,l)\neq(0,1), \\ 2\hat{A}_{1i}\delta_{ij} & \text{if } (k,l)=(0,1), \\ 0 & \text{otherwise,} \end{cases} \tag{A.44}$$

$$\mathsf{M}_{\mathrm{ii}}[k,l;i,j] = \begin{cases} \hat{A}_{0i}\delta_{ij} & \text{if } l=k, \\ \hat{A}_{1i}\delta_{ij} & \text{if } l=k-1,k+1, \\ 0 & \text{otherwise.} \end{cases} \tag{A.45}$$

- Let $\underline{g \equiv Bf}$, then $\mathsf{M}_{\mathrm{rr}}=0$, $\mathsf{M}_{\mathrm{ii}}=0$, whereas M_{ri} and M_{ir} are block-tridiagonal

$$\mathsf{M}_{\mathrm{ri}}[k,l;i,j] = \begin{cases} -\zeta_i\hat{\mu}_{1i}\delta_{ij} & l=k-1, \\ \zeta_i\hat{\mu}_{1i}\delta_{ij} & l=k+1 \text{ and } (k,l)\neq(0,1), \\ 2\zeta_i\hat{\mu}_{1i}\delta_{ij} & \text{if } (k,l)=(0,1), \\ 0 & \text{otherwise,} \end{cases} \tag{A.46}$$

$$\mathsf{M}_{\mathrm{ir}}[k,l;i,j] = \begin{cases} \zeta_i\hat{\mu}_{1i}\delta_{ij} & l=k-1, \\ -\zeta_i\hat{\mu}_{1i}\delta_{ij} & l=k+1, \\ 0 & \text{otherwise.} \end{cases} \tag{A.47}$$

The special case $(k,l)=(0,1)$ corresponds to the fact that $\hat{f}_{-1}=\hat{f}_1^\star$.

Scalar Laplacian

Let $\underline{g \equiv \nabla_\perp^2 f}$, then $\mathsf{M}_{\mathrm{ri}}=0$, $\mathsf{M}_{\mathrm{ir}}=0$, whereas M_{rr} and M_{ii} are block-pentadiagonal

$$\mathsf{M}_{\mathrm{rr}}[k,l;i,j] = \begin{cases} [\hat{\mu}_{0i}^2+2\hat{\mu}_{1i}^2](d_{ij}^{(2)}+\zeta_i d_{ij}^{(1)}-l^2\zeta_i^2\delta_{ij}) & \text{if } l=k \text{ and } (k,l)\neq(1,1), \\ 2\hat{\mu}_{0i}\hat{\mu}_{1i}(d_{ij}^{(2)}+\zeta_i d_{ij}^{(1)}-l^2\zeta_i^2\delta_{ij}) & \text{if } l=k-1,k+1 \text{ and } (k,l)\neq(0,1), \\ \hat{\mu}_{1i}^2(d_{ij}^{(2)}+\zeta_i d_{ij}^{(1)}-l^2\zeta_i^2\delta_{ij}) & \text{if } l=k-2,k+2 \text{ and } (k,l)\neq(0,2), \\ 4\hat{\mu}_{0i}\hat{\mu}_{1i}(d_{ij}^{(2)}+\zeta_i d_{ij}^{(1)}-\zeta_i^2\delta_{ij}) & \text{if } (k,l)=(0,1), \\ 2\hat{\mu}_{1i}^2(d_{ij}^{(2)}+\zeta_i d_{ij}^{(1)}-4\zeta_i^2\delta_{ij}) & \text{if } (k,l)=(0,2), \\ (\hat{\mu}_{0i}^2+3\hat{\mu}_{1i}^2)(d_{ij}^{(2)}+\zeta_i d_{ij}^{(1)}-\zeta_i^2\delta_{ij}) & \text{if } (k,l)=(1,1), \\ 0 & \text{otherwise,} \end{cases} \tag{A.48}$$

$$\mathsf{M}_{\mathrm{ii}}[k,l;i,j] = \begin{cases} [\hat{\mu}_{0i}^2+2\hat{\mu}_{1i}^2](d_{ij}^{(2)}+\zeta_i d_{ij}^{(1)}-l^2\zeta_i^2\delta_{ij}) & \text{if } l=k \text{ and } k\neq 1, \\ 2\hat{\mu}_{0i}\hat{\mu}_{1i}(d_{ij}^{(2)}+\zeta_i d_{ij}^{(1)}-l^2\zeta_i^2\delta_{ij}) & \text{if } l=k-1,k+1, \\ \hat{\mu}_{1i}^2(d_{ij}^{(2)}+\zeta_i d_{ij}^{(1)}-l^2\zeta_i^2\delta_{ij}) & \text{if } l=k-2,k+2, \\ (\hat{\mu}_{0i}^2+\hat{\mu}_{1i}^2)(d_{ij}^{(2)}+\zeta_i d_{ij}^{(1)}-\zeta_i^2\delta_{ij}) & \text{if } (k,l)=(1,1), \\ 0 & \text{otherwise.} \end{cases} \tag{A.49}$$

Special cases $(k,l)=(0,1),(0,2),(1,1)$ correspond to the fact that $\hat{f}_{-1}=\hat{f}_1^\star$ and $\hat{f}_{-2}=\hat{f}_2^\star$.

Remarks

- Mathematically, the scalar Laplacian is defined as the divergence of the gradient, as $\nabla_\perp^2 \equiv \nabla_\perp \cdot \nabla_\perp$. However, discretizing the gradient and divergence operators and multiplying the corresponding matrices does not yield the discretized version of $\nabla_\perp^2$, obtained directly from analytical formula (3.19). This can be readily illustrated on a small example. Let f be here a smooth 2π-periodic function, and consider linear operator ψ such that

$$g(\phi) \equiv \psi f(\phi) = (1 + 2\cos\phi) f'(\phi), \tag{A.50}$$

$$\begin{aligned} h(\phi) \equiv \psi^2 f(\phi) &= (1 + 2\cos\phi)[(1 + 2\cos\phi) f'(\phi)]' \\ &= -(2\sin\phi + 2\sin 2\phi) f'(\phi) + (3 + 4\cos\phi + 2\cos 2\phi) f'(\phi). \end{aligned} \tag{A.51}$$

The following relations hold for the Fourier coefficients of g and h with respect to those of f

$$\hat{g}_k = \mathrm{i}(k-1)\hat{f}_{k-1} + \mathrm{i}k\hat{f}_k + \mathrm{i}(k+1)\hat{f}_{k+1}, \tag{A.52}$$

$$\begin{aligned} \hat{h}_k = &-(k-2)(k-1)\hat{f}_{k-2} \\ &-(k-1)(2k-1)\hat{f}_{k-1} \\ &-3k^2\hat{f}_k \\ &-(k+1)(2k+1)\hat{f}_{k+1} \\ &-(k+2)(k+1)\hat{f}_{k+2}. \end{aligned} \tag{A.53}$$

If we write $\mathsf{f} \equiv (\hat{f}_{-1}, \hat{f}_0, \hat{f}_1)^T$, $\mathsf{g} \equiv (\hat{g}_{-1}, \hat{g}_0, \hat{g}_1)^T$ and $\mathsf{h} \equiv (\hat{h}_{-1}, \hat{h}_0, \hat{h}_1)^T$, we have $\mathsf{g} = \mathsf{A}\mathsf{f}$ and $\mathsf{h} = \mathsf{B}\mathsf{f}$ with

$$\mathsf{A} = \begin{pmatrix} -\mathrm{i} & 0 & 0 \\ -\mathrm{i} & 0 & \mathrm{i} \\ 0 & 0 & \mathrm{i} \end{pmatrix}, \quad \mathsf{B} = \begin{pmatrix} -3 & 0 & 0 \\ -1 & 0 & -1 \\ 0 & 0 & -3 \end{pmatrix}. \tag{A.54}$$

In this example,

$$\mathsf{A}^2 = \begin{pmatrix} -1 & 0 & 0 \\ -1 & 0 & -1 \\ 0 & 0 & -1 \end{pmatrix} \neq \mathsf{B} \tag{A.55}$$

even though $h = \psi g$. In the same fashion, the metric coefficient μ_ξ is responsible for the difference between discretized versions of $\nabla_\perp^2$ and $\nabla_\perp \cdot \nabla_\perp$. This has some important implications for the stability of the projection method explained in subsection §3.3.1.

- Matrix forms of linear operators $\psi : f \mapsto g \in \{D_\xi f, D_\phi f, Af, Bf, \nabla_\perp^2 f\}$ are also needed for f a complex scalar field, when dealing with normal modes. In this case, it is irrelevant to separate real and imaginary parts because of the absence of Hermitian symmetry. Matrices are easily built using formulas (A.27), (A.28), (A.32), (A.33) and (A.37).

Appendix B

Thomas algorithm

Poisson problems (3.33)–(3.34) and (3.37) and Helmholtz problem (3.35) written with the Fourier–Galerkin/Chebyshev-collocation method yield block-pentadiagonal matrices. Each block applies to a given Fourier harmonic evaluated at collocation points. Given the structure of the matrices, a variant of the Thomas (1949) algorithm efficiently solves linear systems

$$\mathsf{M}\mathsf{f} = \mathsf{g},$$

with

$$\mathsf{M} = \begin{pmatrix} \mathsf{B}_0 & \mathsf{C}_0 & \mathsf{CC}_0 & & & & 0 \\ \mathsf{A}_1 & \mathsf{B}_1 & \mathsf{C}_1 & \mathsf{CC}_1 & & & \\ \mathsf{AA}_2 & \mathsf{A}_2 & \mathsf{B}_2 & \mathsf{C}_2 & \mathsf{CC}_2 & & \\ & \ddots & \ddots & \ddots & \ddots & \ddots & \\ & & \mathsf{AA}_{N-2} & \mathsf{A}_{N-2} & \mathsf{B}_{N-2} & \mathsf{C}_{N-2} & \mathsf{CC}_{N-2} \\ & & & \mathsf{AA}_{N-1} & \mathsf{A}_{N-1} & \mathsf{B}_{N-1} & \mathsf{C}_{N-1} \\ 0 & & & & \mathsf{AA}_N & \mathsf{A}_N & \mathsf{B}_N \end{pmatrix}. \tag{B.1}$$

Each block of M is of size $(M+1)\times(M+1)$. The method is based on classical Gaussian elimination, or LU factorization

$$\mathsf{M} = \mathsf{L}\mathsf{U},$$

where L and U are lower and upper block-triangular matrices

$$\mathsf{L} = \begin{pmatrix} \mathsf{L}_0 & & & & 0 \\ \mathsf{G}_1 & \mathsf{L}_1 & & & \\ \mathsf{H}_2 & \mathsf{G}_2 & \mathsf{L}_2 & & \\ & \ddots & \ddots & \ddots & \\ 0 & & \mathsf{H}_N & \mathsf{G}_N & \mathsf{L}_N \end{pmatrix}, \quad \mathsf{U} = \begin{pmatrix} \mathsf{U}_0 & \mathsf{E}_0 & \mathsf{F}_0 & & 0 \\ & \ddots & \ddots & \ddots & \\ & & \mathsf{U}_{N-2} & \mathsf{E}_{N-2} & \mathsf{F}_{N-2} \\ & & & \mathsf{U}_{N-1} & \mathsf{E}_{N-1} \\ 0 & & & & \mathsf{U}_N \end{pmatrix}, \tag{B.2}$$

and L_n, U_n are of the form

$$\mathsf{L}_n = \begin{pmatrix} & & \\ & & \\ & 0 & \end{pmatrix}, \quad \mathsf{U}_n = \begin{pmatrix} 1 & & \\ & \ddots & \\ 0 & & 1 \end{pmatrix}. \tag{B.3}$$

In the following, L_n will denote the n^{th} block-row of linear system $\mathsf{M}\mathsf{f} = \mathsf{g}$.

Forward sweep: $\tilde{\mathsf{g}} \equiv \mathsf{L}^{-1}\mathsf{g}$

- $\underline{n=0}$:
  - LU decomposition: $\mathsf{B}_0 = \mathsf{L}_0\mathsf{U}_0$
  - $\tilde{L}_0 \leftarrow \mathsf{L}_0^{-1}L_0$

$$\text{l.h.s.: } \mathsf{U}_0 \equiv \widetilde{\mathsf{B}}_0 = \mathsf{L}_0^{-1}\mathsf{B}_0, \quad \mathsf{E}_0 \equiv \widetilde{\mathsf{C}}_0 = \mathsf{L}_0^{-1}\mathsf{C}_0, \quad \mathsf{F}_0 \equiv \widetilde{\mathsf{CC}}_0 = \mathsf{L}_0^{-1}\mathsf{CC}_0$$
$$\text{r.h.s.: } \tilde{\mathsf{g}}_0 = \mathsf{L}_0^{-1}\mathsf{g}_0$$

- $\underline{n=1}$:
  - $\mathsf{G}_1 \equiv \mathsf{A}_1\mathsf{U}_0^{-1}$. Eliminate A_1 with $L_1^* \leftarrow L_1 - \mathsf{G}_1\tilde{L}_0$

$$\text{l.h.s.: } \mathsf{B}_1^* = \mathsf{B}_1 - \mathsf{G}_1\widetilde{\mathsf{C}}_0, \quad \mathsf{C}_1^* = \mathsf{C}_1 - \mathsf{G}_1\widetilde{\mathsf{CC}}_0, \quad \mathsf{CC}_1^* = \mathsf{CC}_1$$
$$\text{r.h.s.: } \mathsf{g}_1^* = \mathsf{g}_1 - \mathsf{G}_1\tilde{\mathsf{g}}_0$$

  - LU decomposition: $\mathsf{B}_1^* = \mathsf{L}_1\mathsf{U}_1$
  - $\tilde{L}_1 \leftarrow \mathsf{L}_1^{-1}L_1^*$

$$\text{l.h.s.: } \mathsf{U}_1 \equiv \widetilde{\mathsf{B}}_1 = \mathsf{L}_1^{-1}\mathsf{B}_1^*, \quad \mathsf{E}_1 \equiv \widetilde{\mathsf{C}}_1 = \mathsf{L}_1^{-1}\mathsf{C}_1^*, \quad \mathsf{F}_1 \equiv \widetilde{\mathsf{CC}}_1 = \mathsf{L}_1^{-1}\mathsf{CC}_1^*$$
$$\text{r.h.s.: } \tilde{\mathsf{g}}_1 = \mathsf{L}_1^{-1}\mathsf{g}_1^*$$

- $\underline{2 \le n \le N-2}$:
  - $\mathsf{H}_n \equiv \mathsf{AA}_n\mathsf{U}_{n-2}^{-1}$. Eliminate AA_n with $L_n^* \leftarrow L_n - \mathsf{H}_n\tilde{L}_{n-2}$

$$\text{l.h.s.: } \mathsf{A}_n^* = \mathsf{A}_n - \mathsf{H}_n\widetilde{\mathsf{C}}_{n-2}, \quad \mathsf{B}_n^* = \mathsf{B}_n - \mathsf{H}_n\widetilde{\mathsf{CC}}_{n-2}, \quad \mathsf{C}_n^* = \mathsf{C}_n, \quad \mathsf{CC}_n^* = \mathsf{CC}_n$$
$$\text{r.h.s.: } \mathsf{g}_n^* = \mathsf{g}_n - \mathsf{H}_n\tilde{\mathsf{g}}_{n-2}$$

  - $\mathsf{G}_n \equiv \mathsf{A}_n^*\mathsf{U}_{n-1}^{-1}$. Eliminate A_n^* with $L_n^{**} \leftarrow L_n^* - \mathsf{G}_n\tilde{L}_{n-1}$

$$\text{l.h.s.: } \mathsf{B}_n^{**} = \mathsf{B}_n^* - \mathsf{G}_n\widetilde{\mathsf{C}}_{n-1}, \quad \mathsf{C}_n^{**} = \mathsf{C}_n^* - \mathsf{G}_n\widetilde{\mathsf{CC}}_{n-1}, \quad \mathsf{CC}_n^{**} = \mathsf{CC}_n^* = \mathsf{CC}_n$$
$$\text{r.h.s.: } \mathsf{g}_n^{**} = \mathsf{g}_n^* - \mathsf{G}_n\tilde{\mathsf{g}}_{n-1}$$

  - LU decomposition: $\mathsf{B}_n^{**} = \mathsf{L}_n\mathsf{U}_n$
  - $\tilde{L}_n \leftarrow \mathsf{L}_n^{-1}L_n^{**}$

$$\text{l.h.s.: } \mathsf{U}_n \equiv \widetilde{\mathsf{B}}_n = \mathsf{L}_n^{-1}\mathsf{B}_n^{**}, \quad \mathsf{E}_n \equiv \widetilde{\mathsf{C}}_n = \mathsf{L}_n^{-1}\mathsf{C}_n^{**}, \quad \mathsf{F}_1 \equiv \widetilde{\mathsf{CC}}_n = \mathsf{L}_n^{-1}\mathsf{CC}_n^{**}$$
$$\text{r.h.s.: } \tilde{\mathsf{g}}_n = \mathsf{L}_n^{-1}\mathsf{g}_n^{**}$$

- $\underline{n=N-1}$
  - $\mathsf{H}_{N-1} \equiv \mathsf{AA}_{N-1}\mathsf{U}_{N-3}^{-1}$. Eliminate AA_{N-1} with $L_{N-1}^* \leftarrow L_{N-1} - \mathsf{H}_{N-1}\tilde{L}_{N-3}$

$$\text{l.h.s.: } \mathsf{A}_{N-1}^* = \mathsf{A}_{N-1} - \mathsf{H}_{N-1}\widetilde{\mathsf{C}}_{N-3}, \quad \mathsf{B}_{N-1}^* = \mathsf{B}_{N-1} - \mathsf{H}_{N-1}\widetilde{\mathsf{CC}}_{N-3}, \quad \mathsf{C}_{N-1}^* = \mathsf{C}_{N-1}$$
$$\text{r.h.s.: } \mathsf{g}_{N-1}^* = \mathsf{g}_{N-1} - \mathsf{H}_{N-1}\tilde{\mathsf{g}}_{N-3}$$

  - $\mathsf{G}_{N-1} \equiv \mathsf{A}_{N-1}^*\mathsf{U}_{N-2}^{-1}$. Eliminate A_{N-1}^* with $L_{N-1}^{**} \leftarrow L_{N-1}^* - \mathsf{G}_{N-1}\tilde{L}_{N-2}$

$$\text{l.h.s.: } \mathsf{B}_{N-1}^{**} = \mathsf{B}_{N-1}^* - \mathsf{G}_{N-1}\widetilde{\mathsf{C}}_{N-2}, \quad \mathsf{C}_{N-1}^{**} = \mathsf{C}_{N-1}^* - \mathsf{G}_{N-1}\widetilde{\mathsf{CC}}_{N-2}$$
$$\text{r.h.s.: } \mathsf{g}_{N-1}^{**} = \mathsf{g}_{N-1}^* - \mathsf{G}_{N-1}\tilde{\mathsf{g}}_{N-2}$$

  - LU decomposition: $\mathsf{B}_{N-1}^{**} = \mathsf{L}_{N-1}\mathsf{U}_{N-1}$

– $\tilde{L}_{N-1} \leftarrow \mathsf{L}_{N-1}^{-1} L_{N-1}^{**}$

$$\text{l.h.s.: } \mathsf{U}_{N-1} \equiv \widetilde{\mathsf{B}}_{N-1} = \mathsf{L}_{N-1}^{-1}\mathsf{B}_{N-1}^{**}, \quad \mathsf{E}_{N-1} \equiv \widetilde{\mathsf{C}}_{N-1} = \mathsf{L}_{N-1}^{-1}\mathsf{C}_{N-1}^{**}$$
$$\text{r.h.s.: } \tilde{\mathsf{g}}_{N-1} = \mathsf{L}_{N-1}^{-1}\mathsf{g}_{N-1}^{**}$$

- $\underline{n = N}$
  – $\mathsf{H}_N \equiv \mathsf{AA}_N \mathsf{U}_{N-2}^{-1}$. Eliminate AA_N with $L_N^* \leftarrow L_N - \mathsf{H}_N \tilde{L}_{N-2}$

$$\text{l.h.s.: } \mathsf{A}_N^* = \mathsf{A}_N - \mathsf{H}_N\widetilde{\mathsf{C}}_{N-2}, \quad \mathsf{B}_N^* = \mathsf{B}_N - \mathsf{H}_N\widetilde{\mathsf{CC}}_{N-2}$$
$$\text{r.h.s.: } \mathsf{g}_N^* = \mathsf{g}_N - \mathsf{H}_N\tilde{\mathsf{g}}_{N-2}$$

  – $\mathsf{G}_N \equiv \mathsf{A}_N^* \mathsf{U}_{N-1}^{-1}$. Eliminate A_N^* with $L_N^{**} \leftarrow L_N^* - \mathsf{G}_N \tilde{L}_{N-1}$

$$\text{l.h.s.: } \mathsf{B}_N^{**} = \mathsf{B}_N^* - \mathsf{G}_N\widetilde{\mathsf{C}}_{N-1}$$
$$\text{r.h.s.: } \mathsf{g}_N^{**} = \mathsf{g}_N^* - \mathsf{G}_N\tilde{\mathsf{g}}_{N-1}$$

  – LU decomposition: $\mathsf{B}_N^{**} = \mathsf{L}_N\mathsf{U}_N$
  – $\tilde{L}_N \leftarrow \mathsf{L}_N^{-1} L_N^{**}$

$$\text{l.h.s.: } \mathsf{U}_N \equiv \widetilde{\mathsf{B}}_N = \mathsf{L}_N^{-1}\mathsf{B}_N^{**}$$
$$\text{r.h.s.: } \tilde{\mathsf{g}}_N = \mathsf{L}_N^{-1}\mathsf{g}_N^{**}$$

Backward sweep: $\mathsf{f} = \mathsf{U}^{-1}\tilde{\mathsf{g}}$

- $\underline{n = N}$

$$f_N = \mathsf{U}_N^{-1}\tilde{\mathsf{g}}_N$$

- $\underline{n = N-1}$

$$f_{N-1} = \mathsf{U}_{N-1}^{-1}[\tilde{\mathsf{g}}_{N-1} - \mathsf{E}_{N-1}f_N]$$

- $\underline{n = N-2, \ldots, 0}$

$$f_n = \mathsf{U}_n^{-1}[\tilde{\mathsf{g}}_n - \mathsf{E}_n f_{n+1} - \mathsf{F}_n f_{n+2}]$$

Roundoff errors In each decomposition of $\mathsf{B}_0, \mathsf{B}_1^*, \mathsf{B}_n^{**}$ in LU form $\mathsf{L}_n\mathsf{U}_n$, large numerical errors may arise from division by small coefficients. To enhance accuracy, rows are exchanged (*partial pivot change*) in order to pick the largest coefficient under the diagonal when performing the reduction, therefore, $\mathsf{P}_n\mathsf{B}_n^{**} = \mathsf{L}_n\mathsf{U}_n$ with P_n a permutation matrix. The entire block-line of the system should be multiplied by P_n, hence

$$\text{l.h.s.: } \mathsf{U}_n \equiv \widetilde{\mathsf{B}}_n = \mathsf{L}_n^{-1}\mathsf{P}_n\mathsf{B}_n^{**}, \quad \mathsf{E}_n \equiv \widetilde{\mathsf{C}}_n = \mathsf{L}_n^{-1}\mathsf{P}_n\mathsf{C}_n^{**}, \quad \mathsf{F}_1 \equiv \widetilde{\mathsf{CC}}_n = \mathsf{L}_n^{-1}\mathsf{P}_n\mathsf{CC}_n^{**}$$
$$\text{r.h.s.: } \tilde{\mathsf{g}}_n = \mathsf{L}_n^{-1}\mathsf{P}_n\mathsf{g}_n^{**}$$

replace the former equations at step n.

Storage Matrices L and U are stored in place of M, hence, no extra memory allocation is required.

Complexity Multiplication of a vector/matrix by inverse matrices L_n^{-1} or U_n^{-1} requires only $O(M)/O(M^2)$ operations (tridiagonal system solve). The cost of the forward and backward sweeps are both $O(NM^2)$, even with partial pivot change.

Appendix C

Numerical methods for eigenvalue problems

In §C.1, the numerical method to reduce the large generalized eigenvalue problem to a smaller standard eigenvalue problem is presented. In the following sections, we present iterative methods to compute the eigenvalues $\lambda_1, \lambda_2, \ldots, \lambda_n$ and corresponding eigenvectors $\mathsf{x}_1, \mathsf{x}_2, \ldots, \mathsf{x}_n$ of a non-symmetric complex matrix A in $\mathbb{C}^{n\times n}$, satisfying by definition the relation

$$\mathsf{A}\mathsf{x}_i = \lambda_i \mathsf{x}_i, \ \mathsf{x}_i \neq 0. \tag{C.1}$$

C.1 Numerical reduction of eigenvalue problem

The discretized version of $\tilde{\mathbf{q}}$ is a column-vector of complex numbers $\tilde{\mathsf{q}} \equiv (\tilde{\mathsf{u}}_\perp, \tilde{\mathsf{w}}, \tilde{\mathsf{p}}, \tilde{\pi})^T$, where we choose

$$\begin{aligned}
\tilde{\mathsf{u}}_\perp &\equiv (\tilde{\mathsf{u}}_1, \tilde{\mathsf{u}}_{M-1}, \tilde{\mathsf{u}}_2, \ldots, \tilde{\mathsf{u}}_{M-2}, \tilde{\mathsf{v}}_1, \ldots, \tilde{\mathsf{v}}_{M-1})^T \\
\tilde{\mathsf{w}} &\equiv (\tilde{\mathsf{w}}_1, \ldots, \tilde{\mathsf{w}}_{M-1})^T \\
\tilde{\mathsf{p}} &\equiv (\tilde{\mathsf{p}}_1, \ldots, \tilde{\mathsf{p}}_{M-1})^T \\
\tilde{\pi} &\equiv (\tilde{\mathsf{p}}_0, \tilde{\mathsf{p}}_M)^T.
\end{aligned}$$

This time, indices denote the pseudo-radial position ξ_j with $0 \leq j \leq M$, and each unknown $\tilde{\mathsf{f}}_j \in \{\tilde{\mathsf{u}}_j, \tilde{\mathsf{v}}_j, \tilde{\mathsf{w}}_j, \tilde{\mathsf{p}}_j\}$ is an N-dimensional row vector containing the $N = 2K+1$ Fourier components

$$\tilde{\mathsf{f}}_j \equiv (\hat{\tilde{f}}_{-Kj}, \hat{\tilde{f}}_{kj}, \ldots, \hat{\tilde{f}}_{Kj}).$$

The boundary points of $\tilde{\mathbf{u}}$ have been removed because of impermeability $\tilde{\mathsf{u}}_0 = \tilde{\mathsf{u}}_M = 0$ and no-slip condition $\tilde{\mathsf{v}}_0 = \tilde{\mathsf{v}}_M = \tilde{\mathsf{w}}_0 = \tilde{\mathsf{w}}_M = 0$. Note the unorthodox ordering of the vector $\tilde{\mathsf{u}}_\perp$. This simplifies the algebra later. With these conventions, the discretized eigenvalue problem can be written

$$(\mathsf{C} - \lambda \mathsf{I}_{2(M-1)})\tilde{\mathsf{u}}_\perp + \mathsf{E}\tilde{\mathsf{p}} + \mathsf{e}\tilde{\pi} = 0, \tag{C.2a}$$

$$\mathsf{F}\tilde{\mathsf{u}}_\perp + (\mathsf{G} - \lambda \mathsf{I}_{M-1})\tilde{\mathsf{w}} + \mathrm{i}k\mathsf{I}_{M-1}\tilde{\mathsf{p}} = 0, \tag{C.2b}$$

$$\mathsf{H}\tilde{\mathsf{u}}_\perp + \mathrm{i}k\mathsf{I}_{M-1}\tilde{\mathsf{w}} = 0, \tag{C.2c}$$

$$\mathsf{h}\tilde{\mathsf{u}}_\perp = 0, \tag{C.2d}$$

or collectively as

$$\begin{bmatrix} \mathsf{C}-\lambda\mathsf{I}_{2(M-1)} & 0 & \mathsf{E} & \mathsf{e} \\ \mathsf{F} & \mathsf{G}-\lambda\mathsf{I}_{M-1} & \mathrm{i}k\mathsf{I}_{M-1} & 0 \\ \mathsf{H} & \mathrm{i}k\mathsf{I}_{M-1} & 0 & 0 \\ \mathsf{h} & 0 & 0 & 0 \end{bmatrix} \begin{bmatrix} \tilde{\mathsf{u}}_\perp \\ \tilde{\mathsf{w}} \\ \tilde{\mathsf{p}} \\ \tilde{\pi} \end{bmatrix} = 0, \tag{C.2}$$

Here and henceforth, I_{M-1} denotes the $N(M-1)\times N(M-1)$ unit matrix. The matrices are of size:

$$\begin{aligned} \mathsf{C} &: 2(M-1)N \times 2(M-1)N \\ \mathsf{E} &: 2(M-1)N \times (M-1)N \\ \mathsf{e} &: 2(M-1)N \times 2N \\ \mathsf{F},\mathsf{H} &: (M-1)N \times 2(M-1)N \\ \mathsf{G} &: (M-1)N \times (M-1)N \\ \mathsf{h} &: 2N \times 2(M-1)N. \end{aligned}$$

Each matrix consists of $N \times N$ Fourier blocks. The first $(M-1)N$ rows of (C.2a) come from the radial component of the momentum equation at collocation points $\xi_1, \xi_{M-1}, \xi_2, \ldots, \xi_{M-2}$, while the last $(M-1)N$ rows represent the azimuthal component at $\xi_1, \ldots, \xi_{M-1}$. (C.2b) and (C.2c) arise respectively from the axial component of the momentum equation and the condition of incompressibility at $\xi_1, \ldots, \xi_{M-1}$. Finally, (C.2d) corresponds to the incompressibility constraint at ξ_0 and ξ_M, simply corresponding to the zero-derivative condition $\partial_\xi \tilde{u} = 0$. In this form, the generalized eigenvalue problem is of size $4(M-1)N+2N$, and if boundary points of $\tilde{\mathbf{u}}$ had been kept, it would have been of size $4(M+1)N$.

Equations (C.2a)–(C.2c) imply

$$(\mathsf{HC}-\lambda\mathsf{H})\tilde{\mathsf{u}}_\perp + \mathsf{HE}\tilde{\mathsf{p}} + \mathsf{He}\tilde{\pi} = 0, \tag{C.3}$$

$$\mathrm{i}k\mathsf{F}\tilde{\mathsf{u}}_\perp + (\mathrm{i}k\mathsf{G} - \mathrm{i}k\lambda\mathsf{I}_{M-1})\tilde{\mathsf{w}} - k^2\mathsf{I}_{M-1}\tilde{\mathsf{p}} = 0, \tag{C.4}$$

$$\lambda\mathsf{H}\tilde{\mathsf{u}}_\perp + \mathrm{i}k\lambda\mathsf{I}_{M-1}\tilde{\mathsf{w}} = 0. \tag{C.5}$$

The sum of these equations gives

$$(\mathsf{HE}-k^2\mathsf{I}_{M-1})\tilde{\mathsf{p}} = -(\mathsf{HC}+\mathrm{i}k\mathsf{F})\tilde{\mathsf{u}}_\perp - \mathrm{i}k\mathsf{G}\tilde{\mathsf{w}} - \mathsf{H}a\tilde{\pi}. \tag{C.6}$$

Thus,

$$\tilde{\mathsf{p}} = -(\mathsf{HE}-k^2\mathsf{I}_{M-1})^{-1}(\mathsf{HC}+\mathrm{i}k\mathsf{F})\tilde{\mathbf{u}}_\perp - \mathrm{i}k(\mathsf{HE}-k^2\mathsf{I}_{M-1})^{-1}\mathsf{G}\tilde{\mathsf{w}} - (\mathsf{HE}-k^2\mathsf{I}_{M-1})^{-1}\mathsf{He}\tilde{\pi}, \tag{C.7}$$

and so

$$\mathsf{E}\tilde{\mathsf{p}} + \mathsf{e}\tilde{\pi} = \mathsf{J}^{(1)}\tilde{\mathbf{u}}_\perp + \mathsf{J}^{(2)}\tilde{\mathsf{w}} + \mathsf{J}^{(3)}\tilde{\pi}, \tag{C.8}$$

where

$$\mathsf{J}^{(1)} = -\mathsf{E}(\mathsf{HE}-k^2\mathsf{I}_{M-1})^{-1}(\mathsf{HC}+\mathrm{i}k\mathsf{F}) \tag{C.9a}$$

$$\mathsf{J}^{(2)} = -\mathrm{i}k\mathsf{E}(\mathsf{HE}-k^2\mathsf{I}_{M-1})^{-1}\mathsf{G} \tag{C.9b}$$

$$\mathsf{J}^{(3)} = \mathsf{e} - \mathsf{E}(\mathsf{HE}-k^2\mathsf{I}_{M-1})^{-1}\mathsf{He}, \tag{C.9c}$$

with respective dimensions

$$\begin{aligned}\mathsf{J}^{(1)} &: 2(M-1)N \times 2(M-1)N\\ \mathsf{J}^{(2)} &: 2(M-1)N \times (M-1)N\\ \mathsf{J}^{(3)} &: 2(M-1)N \times 2N.\end{aligned}$$

Using this result, the eigenvalue problem becomes

$$\begin{bmatrix}\mathsf{C}+\mathsf{J}^{(1)}-\lambda\mathsf{I}_{2(M-1)} & \mathsf{J}^{(2)} & \mathsf{J}^{(3)}\\ \mathsf{H} & \mathrm{i}k\mathsf{I}_{M-1} & 0\\ \mathsf{h} & 0 & 0\end{bmatrix}\begin{bmatrix}\tilde{\mathsf{u}}_\perp\\ \tilde{\mathsf{w}}\\ \tilde{\pi}\end{bmatrix}=0, \tag{C.10}$$

i.e. the interior pressure variables have been eliminated.

Supposing $k \neq 0$ from here on, we employ (C.2c) in the form

$$\tilde{\mathsf{w}} = -\frac{1}{\mathrm{i}k}\mathsf{H}\tilde{\mathsf{u}}_\perp \tag{C.11}$$

to eliminate $\tilde{\mathsf{w}}$,

$$\begin{bmatrix}\mathsf{C}+\mathsf{J}^{(1)}-\mathrm{i}k\mathsf{J}^{(2)}\mathsf{H}-\lambda\mathsf{I}_{2(M-1)} & \mathsf{J}^{(3)}\\ \mathsf{h} & 0\end{bmatrix}\begin{bmatrix}\tilde{\mathsf{u}}_\perp\\ \tilde{\pi}\end{bmatrix}=0. \tag{C.12}$$

The matrix h has the structure

$$\mathsf{h}=\begin{bmatrix}d_{01}\mathsf{I}_1 & d_{0(M-1)}\mathsf{I}_1 & d_{02}\mathsf{I}_1 & \dots & d_{0(M-2)}\mathsf{I}_1 & 0 & \dots & 0\\ d_{M1}\mathsf{I}_1 & d_{M(M-1)}\mathsf{I}_1 & d_{M2}\mathsf{I}_1 & \dots & d_{M(M-2)}\mathsf{I}_1 & 0 & \dots & 0\end{bmatrix}, \tag{C.13}$$

with d_{0j} and d_{Mj}, $0 \leq j \leq M$ the first and last row elements of the Chebyshev differentiation matrix D defined in Appendix A.2. Hence (C.2d) gives

$$d_{01}\tilde{\mathsf{u}}_1 + d_{0(M-1)}\tilde{\mathsf{u}}_{M-1} = -\sum_{j=2}^{M-2} d_{0j}\tilde{\mathsf{u}}_j \tag{C.14}$$

$$d_{M1}\tilde{\mathsf{u}}_1 + d_{M(M-1)}\tilde{\mathsf{u}}_{M-1} = -\sum_{j=2}^{M-2} d_{Mj}\tilde{\mathsf{u}}_j. \tag{C.15}$$

The solution of these equations is

$$\tilde{\mathsf{u}}_1 = \sum_{j=2}^{M-2} e_j\tilde{\mathsf{u}}_j, \quad \tilde{\mathsf{u}}_{M-1} = \sum_{j=2}^{M-2} f_j\tilde{\mathsf{u}}_j, \tag{C.16}$$

where

$$e_j = \frac{d_{0(M-1)}d_{Mj} - d_{M(M-1)}d_{0j}}{d_{01}d_{M(M-1)} - d_{M1}d_{0(M-1)}}, \quad f_j = \frac{d_{M1}d_{0j} - d_{01}d_{Mj}}{d_{01}d_{M(M-1)} - d_{M1}d_{0(M-1)}}. \tag{C.17}$$

Thus,

$$\tilde{\mathsf{u}}_\perp = \mathsf{L}\tilde{\mathsf{q}}_1, \tag{C.18}$$

where $\tilde{\mathsf{q}}_1 = (\tilde{\mathsf{u}}_2, \dots, \tilde{\mathsf{u}}_{M-2}, \tilde{\mathsf{v}}_1, \dots, \tilde{\mathsf{v}}_{M-1})^T$,

$$\mathsf{L} = \begin{bmatrix}\mathsf{K}\\ \mathsf{I}_{2(M-1)}\end{bmatrix} \tag{C.19}$$

and

$$\mathsf{K} = \begin{bmatrix} e_2\mathsf{I}_1 & \dots & e_{M-2}\mathsf{I}_1 & 0 & \dots & 0 \\ f_2\mathsf{I}_1 & \dots & f_{M-2}\mathsf{I}_1 & 0 & \dots & 0 \end{bmatrix}. \tag{C.20}$$

The eigenvalue problem becomes

$$\left[\left(\mathsf{C} + \mathsf{J}^{(1)} - \mathrm{i}k\mathsf{J}^{(2)}\mathsf{H} - \lambda\mathsf{I}_{2(M-1)}\right)\mathsf{L} \quad \mathsf{J}^{(3)}\right]\begin{bmatrix}\tilde{\mathsf{q}}_1 \\ \tilde{\pi}\end{bmatrix} = 0. \tag{C.21}$$

As $\lambda \to \infty$,

$$\det\left[\left(\mathsf{C} + \mathsf{J}^{(1)} - \mathrm{i}k\mathsf{J}^{(2)}\mathsf{H} - \lambda\mathsf{I}_{2(M-1)}\right)\mathsf{L} \quad \mathsf{J}^{(3)}\right] \sim \lambda^{2(M-2)N}\det\mathsf{B}, \tag{C.22}$$

where

$$\mathsf{B} = \left[\mathsf{L} \quad \mathsf{J}^{(3)}\right]. \tag{C.23}$$

In what follows, we suppose B nonsingular, so $\det\mathsf{B} \neq 0$ and

$$\det\left[\left(\mathsf{C} + \mathsf{J}^{(1)} - \mathrm{i}k\mathsf{J}^{(2)}\mathsf{H} - \lambda\mathsf{I}_{2(M-1)}\right)\mathsf{L} \quad \mathsf{J}^{(3)}\right] \tag{C.24}$$

is a polynomial of degree $2(M-2)N$: this is then the number of (finite) eigenvalues. To make the assumption that B is nonsingular plausible, suppose that

$$\mathsf{B}\begin{bmatrix}\tilde{\mathsf{q}}_1 \\ \tilde{\pi}\end{bmatrix} = 0. \tag{C.25}$$

Next consider what happens when we modify the problem (C.3) by setting $\lambda = 1$ and $\mathsf{C} = \mathsf{F} = \mathsf{G} = 0$, while keeping $\mathsf{E}, \mathsf{H}, \mathsf{e}$ and h unchanged. This makes $\mathsf{J}^{(1)} = \mathsf{J}^{(2)} = 0$, but leaves $\mathsf{J}^{(3)}$ the same. Thus, (C.25) implies (C.21) and hence modified (C.3) holds with $\tilde{\mathsf{u}}_\perp$ given by (C.18), $\tilde{\mathsf{w}}$ by (C.11) and $\tilde{\mathsf{p}}$ by (C.7):

$$\begin{bmatrix} -\mathsf{I}_{2(M-1)} & 0 & \mathsf{E} & \mathsf{e} \\ 0 & -\mathsf{I}_{M-1} & \mathrm{i}k\mathsf{I}_{M-1} & 0 \\ \mathsf{H} & \mathrm{i}k\mathsf{I}_{M-1} & 0 & 0 \\ \mathsf{h} & 0 & 0 & 0 \end{bmatrix}\begin{bmatrix}\tilde{\mathsf{u}}_\perp \\ \tilde{\mathsf{w}} \\ \tilde{\mathsf{p}} \\ \tilde{\pi}\end{bmatrix} = 0. \tag{C.26}$$

This is a numerical approximation of

$$\tilde{\mathbf{u}} = \nabla\tilde{p} \tag{C.27a}$$

$$\nabla\cdot\tilde{\mathbf{u}} = 0 \tag{C.27b}$$

with $\tilde{\mathbf{u}} = 0$ on the boundary and $\mathrm{e}^{\mathrm{i}kz}$ dependence. It follows that the pressure satisfies

$$\nabla_\perp^2\tilde{p} - k^2\tilde{p} = 0 \tag{C.28}$$

and $\tilde{p} = \partial_\xi\tilde{p} = 0$ on the boundary. The only solution of this problem is $\tilde{p} = 0$ so $\tilde{\mathbf{u}} = 0$. If this property is shared by the numerical approximation (C.26), $\tilde{\mathsf{q}}_1 = \tilde{\pi} = 0$ and so B is indeed nonsingular.

From the definition of B,

$$\mathsf{B}^{-1}\mathsf{B} = \left[\mathsf{B}^{-1}\mathsf{L} \quad \mathsf{B}^{-1}\mathsf{J}^{(3)}\right] = \begin{bmatrix}\mathsf{I}_{2(M-2)} & 0 \\ 0 & \mathsf{I}_2\end{bmatrix} = 0, \tag{C.29}$$

hence

$$\mathsf{B}^{-1}\mathsf{L} = \begin{bmatrix} \mathsf{I}_{2(M-2)} \\ 0 \end{bmatrix}, \quad \mathsf{B}^{-1}\mathsf{J}^{(3)} = \begin{bmatrix} 0 \\ \mathsf{I}_2 \end{bmatrix}. \tag{C.30}$$

Multiplying (C.21) by B^{-1},

$$\left[\mathsf{A} - \lambda \begin{bmatrix} \mathsf{I}_{2(M-2)} \\ 0 \end{bmatrix} \begin{bmatrix} 0 \\ \mathsf{I}_2 \end{bmatrix}\right] \begin{bmatrix} \tilde{\mathsf{q}}_1 \\ \tilde{\pi} \end{bmatrix} = 0, \tag{C.31}$$

where

$$\mathsf{A} = \mathsf{DL} \tag{C.32}$$

and

$$\mathsf{D} = \mathsf{B}^{-1}\left(\mathsf{C} + \mathsf{J}^{(1)} - \frac{1}{\mathrm{i}k}\mathsf{J}^{(2)}\mathsf{H}\right). \tag{C.33}$$

Writing

$$\mathsf{A} = \begin{bmatrix} \mathsf{A}_1 \\ \mathsf{A}_2 \end{bmatrix}, \tag{C.34}$$

where A_1 is $2(M-2)N \times 2(M-2)N$ and A_2 is $2N \times 2(M-2)N$,

$$\mathsf{A}_1\tilde{\mathsf{q}}_1 = \lambda\tilde{\mathsf{q}}_1 \tag{C.35}$$

$$\tilde{\pi} = -\mathsf{A}_2\tilde{\mathsf{q}}_1 \tag{C.36}$$

(C.35) is a standard eigenvalue problem of size $2(M-2)N$. (C.36) determines $\tilde{\pi}$, (C.18) gives $\tilde{\mathsf{u}}_\perp$, (C.11) yields $\tilde{\mathsf{w}}$ and $\tilde{\mathsf{p}}$ follows from (C.7).

Using the definition of L and writing

$$\mathsf{B}^{-1}\mathsf{L} = \begin{bmatrix} \mathsf{D}_{11} & \mathsf{D}_{12} \\ \mathsf{D}_{12} & \mathsf{D}_{22} \end{bmatrix}, \tag{C.37}$$

where D_{11} is $2(M-2)N \times 2N$, D_{12} is $2(M-2)N \times 2(M-2)N$, D_{21} is $2N \times 2N$ and D_{22} is $2N \times 2(M-2)N$,

$$\mathsf{A}_1 = \mathsf{D}_{11}\mathsf{K} + \mathsf{D}_{12} \tag{C.38a}$$

$$\mathsf{A}_2 = \mathsf{D}_{21}\mathsf{K} + \mathsf{D}_{22}. \tag{C.38b}$$

The question remains, how to invert B? Suppose

$$\mathsf{B}\begin{bmatrix} \tilde{\mathsf{q}}_1 \\ \tilde{\pi} \end{bmatrix} = \begin{bmatrix} \nu \\ \kappa \end{bmatrix}, \tag{C.39}$$

where ν is a $2N$-dimensional column vector and κ a $2(M-2)N$-dimensional column vector. Given the definitions of L and B,

$$\mathsf{K}\tilde{\mathsf{q}}_1 + \mathsf{J}_1^{(3)}\tilde{\pi} = \nu \tag{C.40}$$

$$\tilde{\mathsf{q}}_1 + \mathsf{J}_2^{(3)}\tilde{\pi} = \kappa, \tag{C.41}$$

in which $\mathsf{J}^{(3)}$ has been written as

$$\mathsf{J}^{(3)} = \begin{bmatrix} \mathsf{J}_1^{(3)} \\ \mathsf{J}_2^{(3)} \end{bmatrix}, \tag{C.42}$$

where $\mathsf{J}_1^{(3)}$ is a $2N \times 2N$ matrix and $\mathsf{J}_2^{(3)}$ a $2(M-2)N \times 2N$ matrix. It follows that

$$\mathsf{P}\tilde{\pi} = \nu - \mathsf{K}\kappa, \tag{C.43}$$

where

$$\mathsf{P} = \mathsf{J}_1^{(3)} - \mathsf{K}\mathsf{J}_2^{(3)}. \tag{C.44}$$

Thus,

$$\tilde{\pi} = \mathsf{P}^{-1}(\nu - \mathsf{K}\kappa), \tag{C.45}$$

$$\tilde{\mathsf{q}}_1 = \kappa - \mathsf{J}_2^{(3)}\mathsf{P}^{-1}(\nu - \mathsf{K}\kappa). \tag{C.46}$$

We conclude that

$$\mathsf{B} = \begin{bmatrix} -\mathsf{J}_2^{(3)}\mathsf{P}^{-1} & \mathsf{I}_{2(M-2)} + \mathsf{J}_2^{(3)}\mathsf{P}^{-1}\mathsf{K} \\ \mathsf{P}^{-1} & -\mathsf{P}^{-1}\mathsf{K} \end{bmatrix}. \tag{C.47}$$

Summary of the solution procedure

1) Calculate

$$\mathsf{J}^{(1)} = -\mathsf{E}(\mathsf{H}\mathsf{E} - k^2\mathsf{I}_{M-1})^{-1}(\mathsf{H}\mathsf{C} + \mathrm{i}k\mathsf{F}) \tag{C.9a}$$

$$\mathsf{J}^{(2)} = -\mathrm{i}k\mathsf{E}(\mathsf{H}\mathsf{E} - k^2\mathsf{I}_{M-1})^{-1}\mathsf{G} \tag{C.9b}$$

$$\mathsf{J}^{(3)} = \mathsf{e} - \mathsf{E}(\mathsf{H}\mathsf{E} - k^2\mathsf{I}_{M-1})^{-1}\mathsf{H}\mathsf{e} \tag{C.9c}$$

2) Determine

$$e_j = \frac{d_{0(M-1)}d_{Mj} - d_{M(M-1)}d_{0j}}{d_{01}d_{M(M-1)} - d_{M1}d_{0(M-1)}}, \quad f_j = \frac{d_{M1}d_{0j} - d_{01}d_{Mj}}{d_{01}d_{M(M-1)} - d_{M1}d_{0(M-1)}}. \tag{C.17}$$

from which the matrix K follows as

$$\mathsf{K} = \begin{bmatrix} e_2\mathsf{I}_1 & \dots & e_{M-2}\mathsf{I}_1 & 0 & \dots & 0 \\ f_2\mathsf{I}_1 & \dots & f_{M-2}\mathsf{I}_1 & 0 & \dots & 0 \end{bmatrix}. \tag{C.20}$$

3) Writing

$$\mathsf{J}^{(3)} = \begin{bmatrix} \mathsf{J}_1^{(3)} \\ \mathsf{J}_2^{(3)} \end{bmatrix}, \tag{C.42}$$

calculate

$$\mathsf{P}^{-1} = (\mathsf{J}_1^{(3)} - \mathsf{K}J_2^{(3)})^{-1} \tag{C.44}$$

and hence

$$\mathsf{B} = \begin{bmatrix} -\mathsf{J}_2^{(3)}\mathsf{P}^{-1} & \mathsf{I}_{2(M-2)} + \mathsf{J}_2^{(3)}\mathsf{P}^{-1}\mathsf{K} \\ \mathsf{P}^{-1} & -\mathsf{P}^{-1}\mathsf{K} \end{bmatrix}. \tag{C.48}$$

4) Determine $\mathsf{D}_{11}, \mathsf{D}_{12}, \mathsf{D}_{21}$ and D_{22} from

$$\begin{bmatrix} \mathsf{D}_{11} & \mathsf{D}_{12} \\ \mathsf{D}_{12} & \mathsf{D}_{22} \end{bmatrix} = \mathsf{B}^{-1}\left(\mathsf{C} + \mathsf{J}^{(1)} - \frac{1}{\mathrm{i}k}\mathsf{J}^{(2)}\mathsf{H}\right) \tag{C.49}$$

and hence A_1 and A_2 from

$$\mathsf{A}_1 = \mathsf{D}_{11}\mathsf{K} + \mathsf{D}_{12} \tag{C.38a}$$

$$\mathsf{A}_2 = \mathsf{D}_{21}\mathsf{K} + \mathsf{D}_{22}. \tag{C.38b}$$

5) Compute the eigenvalues, λ, (and, if required, the eigenvectors, $\tilde{\mathsf{q}}_1$) of A_1.

6) If required, complete the eigenvectors using (C.36), (C.18), (C.11) and (C.7).

C.2 Power and inverse power iteration

Power iteration

The power method is introduced first, as it is a very simple iterative algorithm at the root of any eigenvector computation routine. Assume A has n eigenvalues labelled in the following order

$$|\lambda_1| > |\lambda_2| > \cdots > |\lambda_n|,$$

and assume that the associated eigenvectors $\{\mathsf{x}_1, \mathsf{x}_2, \ldots, \mathsf{x}_n\}$ are linearly independent.

Decompose any random vector $\mathsf{q}^{(0)}$ on the basis of eigenvectors

$$\mathsf{q}^{(0)} = c_1\mathsf{x}_1 + c_2\mathsf{x}_2 + \cdots + c_n\mathsf{x}_n. \tag{C.39}$$

Define $\mathsf{q}^{(1)}$ as

$$\mathsf{q}^{(1)} = \mathsf{A}\mathsf{q}^{(0)} = \lambda_1 c_1\mathsf{x}_1 + \lambda_2 c_2\mathsf{x}_2 + \cdots + \lambda_n c_n\mathsf{x}_n, \tag{C.40}$$

and more generally, for $j \geq 1$

$$\mathsf{q}^{(j)} = \mathsf{A}\mathsf{q}^{(j-1)} = A^j\mathsf{q}^{(0)} = \lambda_1^j c_1\mathsf{x}_1 + \lambda_2^j c_2\mathsf{x}_2 + \cdots + \lambda_n^j c_n\mathsf{x}_n. \tag{C.41}$$

Since $\lambda_1 \neq 0$, we have

$$\mathsf{q}^{(j)} = \lambda_1^j[c_1\mathsf{x}_1 + (\lambda_2/\lambda_1)^j c_2\mathsf{x}_2 + \cdots + (\lambda_n/\lambda_1)^j c_n\mathsf{x}_n] \xrightarrow[j\to\infty]{} \lambda_1^j c_1\mathsf{x}_1, \tag{C.42}$$

so after a few iterations, $\mathsf{q}^{(j)}$ tends towards a multiple of eigenvector x_1, associated with the leading eigenvalue λ_1. Power iteration 'damps' contributions from any eigenvector associated with a subdominant eigenvalue.

Inverse power iteration

If an approximate eigenvalue $\sigma \approx \lambda_i$ is known beforehand, the corresponding eigenvector x_i can be found using inverse power method. Starting with any initial vector $\mathsf{q}^{(0)}$, we define $\mathsf{q}^{(k+1)}$ as the solution of the linear system:

$$(\mathsf{A} - \sigma\mathsf{I})\mathsf{q}^{(k+1)} = \mathsf{q}^{(k)}. \tag{C.43}$$

It is simply the power method applied to the 'shifted-inverted' matrix $(\mathsf{A} - \sigma\mathsf{I})^{-1}$, the eigenvalues of which are $1/(\lambda_j - \sigma)$ while the eigenvectors are the same as those of A. The power method will amplify the eigenvector x_i associated with the eigenvalue of larger modulus, namely $1/(\lambda_i - \sigma)$, since σ is an approximation of λ_i. This method is used to compute eigenvectors once the eigenvalues have been obtained (using for example the QR method to be described in the next section). The shift-invert spectral transformation presented here is also used later in the Arnoldi method.

C.3 QR method

The QR method is used to compute the full spectrum of eigenvalues of a matrix. In practice, we used an optimized version of the algorithm, freely available in the software

package LAPACK (routine 'zgeev'). The intent here is only to give the main ideas of the method, and by no means to give all the lenghty implementation details. For more details and proofs, we refer to Golub and Van Loan (1989), Quarteroni et al. (2006), Watkins (2008).

Schur decomposition

Let A be a $n \times n$ square matrix with complex entries, then there exists a *unitary* matrix[1] Q such that

$$\mathsf{Q}^{-1}\mathsf{A}\mathsf{Q} = \mathsf{Q}^{H}\mathsf{A}\mathsf{Q} = \begin{pmatrix} \lambda_1 & t_{12} & \dots & t_{1n} \\ & \lambda_2 & \ddots & t_{2n} \\ & & \ddots & \vdots \\ 0 & & & \lambda_n \end{pmatrix} = \mathsf{T}. \tag{C.44}$$

Q and A being *similar*, they have the same eigenvalues. Moreover, T being triangular, its eigenvalues are the diagonal entries: $\lambda_1, \lambda_2, \dots, \lambda_n$. The principle of the QR algorithm is to obtain a Schur decomposition of A by iterative means, and then read the eigenvalues on the diagonal of T.

QR decomposition

Any square matrix A in $\mathbb{C}^{n\times n}$ may be decomposed as

$$\mathsf{A} = \mathsf{Q}\mathsf{R}, \tag{C.45}$$

with Q a unitary matrix and R an upper triangular matrix. The QR decomposition is not unique.

'Basic' QR method

Starting with $\mathsf{A}_0 = \mathsf{A}$, the basic QR iteration step consists in performing a QR decomposition of $\mathsf{A}_k = \mathsf{Q}_k\mathsf{R}_k$, and then multiply matrices Q_k and R_k in backwards order to obtain A_{k+1}:

$$\mathsf{A}_k = \mathsf{Q}_k\mathsf{R}_k, \quad \mathsf{A}_{k+1} = \mathsf{R}_k\mathsf{Q}_k. \tag{C.46}$$

By doing so, we compute a series of similar matrices $\mathsf{A}_{k+1} = \mathsf{Q}_k^H\mathsf{A}_k\mathsf{Q}_k$, eventually converging to a triangular matrix T. After k iterations, one observes that $\mathsf{A}_k = \mathsf{Q}^H\mathsf{A}_0\mathsf{Q}$ with $\mathsf{Q} = \mathsf{Q}_0\mathsf{Q}_1 \dots \mathsf{Q}_{k-1}$, which gives the Schur decomposition when A_k is triangular up to machine precision.

1. complex matrix such that $\mathsf{Q}\mathsf{Q}^H = \mathsf{Q}^H\mathsf{Q} = \mathsf{I}$, Q^H denoting the conjugate transpose of Q.

Hessenberg-QR method

Hessenberg matrices $\mathsf{H} = (h_{ij})$ satisfy $h_{ij} = 0$ for $i > j + 1$:

$$\mathsf{H} = \begin{pmatrix} \bullet & \bullet & \cdots & \bullet \\ \bullet & \bullet & & \bullet \\ & \ddots & \ddots & \vdots \\ 0 & & \bullet & \bullet \end{pmatrix}. \tag{C.47}$$

Linear combinations and products of Hessenberg matrices conserve the Hessenberg structure. Because of their sparsity, these matrices are cheap to work with. In particular, QR iterations are performed much more efficiently if in a first step, A_0 is converted to a Hessenberg matrix $\mathsf{A}_1 = \mathsf{Q}_0^H \mathsf{A}_0 \mathsf{Q}_0$. The reduction can always be done using similarity transformations. In the next QR iterations, Q_k and A_k will then always be Hessenberg matrices, leading to $O(n^2)$ flops per iteration instead of $O(n^3)$.

Deflation

If at some stage k, one sub-diagonal element of $\mathsf{A}_k = (a_{ij}^{(k)})$ is 'zero' (below fixed tolerance), say $a_{(i+1)i}^{(k)} \approx 0$, then one can write

$$\mathsf{A}_k = \begin{pmatrix} \mathsf{A}_{11} & \mathsf{A}_{12} \\ 0 & \mathsf{A}_{22} \end{pmatrix}, \tag{C.48}$$

with block dimensions $\mathsf{A}_{11} : i \times i$, $\mathsf{A}_{22} : (n-i) \times (n-i)$, $\mathsf{A}_{12} : i \times (n-i)$, and the problem decouples into two smaller problems involving A_{11} and A_{22}. If we keep the labelling of the eigenvalue in the following order

$$|\lambda_1| > |\lambda_2| > \cdots > |\lambda_n|,$$

then all subdiagonal elements tend to zero as $|a_{(i+1)i}^{(k)}| = O(|\lambda_{i+1}/\lambda_i|^k)$ during Hessenberg-QR iterations.

Shifted-QR algorithm

The rate of convergence of the subdiagonal elements can be greatly enhanced by introducing a shift σ

$$\mathsf{A}_k = \mathsf{Q}_k \mathsf{R}_k - \sigma \mathsf{I}, \quad \mathsf{A}_{k+1} = \mathsf{R}_k \mathsf{Q}_k + \sigma \mathsf{I}, \tag{C.49}$$

then $|a_{(i+1)i}^{(k)}| = O(|(\lambda_{i+1} - \sigma)/(\lambda_i - \sigma)|^k)$. Note that one step of the shifted-QR algorithm still yields $\mathsf{A}_{k+1} = \mathsf{Q}_k^H \mathsf{A}_k \mathsf{Q}_k$. In practice, σ should be chosen close to an eigenvalue, to obtain fast convergence. The classical approach is to compute, at each iteration the eigenvalue of the lower-right-hand 2×2 submatrix of A closer to $a_{nn}^{(k)}$ (Wilkinson shift Wilkinson (1965)). The shift can be updated at each iteration, leading to an even greater convergence rate. In practice, multiple shifts $\sigma_1, \sigma_2, \ldots, \sigma_m$ are simultaneously applied (eigenvalues of the $m \times m$ trailing submatrix of A), using an implicit formulation ('buldge-chasing') described in detail in Watkins (2008).

C.4 Arnoldi method

The QR method that was just presented returns the full spectrum of a dense matrix. However, in stability analyses, only a few eigenvalues dominate the linear dynamics, and one would like to compute only those 'most unstable' ones. If the eigenvalue problem is cast in terms of $\lambda = \mathrm{i}\omega$, then we are typically interested in the eigenvalues with smaller algebraic real part λ_r corresponding to the largest temporal growth rate ω_i. In some cases, it is useful to be able to follow a specific eigenvalue in the spectrum, as control parameters are varied, and full spectrum computations are then useless. The principle of the Arnoldi factorization is to project the matrix A onto a small subspace containing the desired 'eigen-information'. The resulting projected matrix has Hessenberg structure, then implicit shifted QR iteration can be applied to eliminate its subdiagonal elements. The diagonal elements of this small triangular matrix yield the desired subset of the spectrum of A.

Krylov subspace

By applying power iteration, an initial vector $\mathsf{q}^{(0)}$ is amplified preferentially in the direction of x_1, the eigenvector associated with λ_1. However, significant amplification may also occur in the directions associated with the next largest eigenvalues λ_2, λ_3, etc., and one may be interested in keeping the information related to a small number of leading eigenvalues. To achieve this, *Krylov subspace* methods keep the information from the first $m-1$ power iterations, and consider the associated subspace:

$$\mathcal{K}_m(\mathsf{A}, \mathsf{q}^{(0)}) = \mathrm{span}\left\{\mathsf{q}^{(0)}, \mathsf{A}\mathsf{q}^{(0)}, \mathsf{A}^2\mathsf{q}^{(0)}, \ldots, \mathsf{A}^{m-1}\mathsf{q}^{(0)}\right\}. \tag{C.50}$$

Arnoldi factorization

The principle of Arnoldi factorization is to project the potentially large matrix A onto the small Krylov subspace $\mathcal{K}_m(\mathsf{A}, \mathsf{q}^{(0)})$, which, by construction, contains information about the m most unstable eigenpairs [2]. An orthonormal basis of $\mathcal{K}_m(\mathsf{A}, \mathsf{q}^{(0)})$ is created, using some numerically stable version of the Gram–Schmidt orthogonalization process, with the usual inner product on $\mathbb{C}^n$ denoted with $(.,.)$. Starting with an initial random (but normalized) vector $\mathsf{q}^{(0)}$, the next vectors $\mathsf{q}^{(j+1)}$ for $j = 0, \ldots, m-1$ are defined by:

$$h_{ij} = (\mathsf{A}\mathsf{q}^{(j)}, \mathsf{q}^{(i)}), \quad i = 0, \ldots, j, \tag{C.51}$$

$$\mathsf{w}^{(j)} = \mathsf{A}\mathsf{q}^{(j)} - \sum_{i=0}^{j} h_{ij}\mathsf{q}^{(i)}, \tag{C.52}$$

$$h_{j+1,j} = \|\mathsf{w}^{(j)}\|_2, \tag{C.53}$$

$$\mathsf{q}^{(j+1)} = \mathsf{w}^{(j)}/h_{(j+1)j}, \tag{C.54}$$

and if at some point $h_{j+1,j} = 0$, the iteration stops.

For any integer j, the vectors $(\mathsf{q}^{(0)}, \mathsf{q}^{(1)}, \ldots, \mathsf{q}^{(j)})$ form an orthonormal basis of $\mathcal{K}_{j+1}(\mathsf{A}, \mathsf{q}^{(0)})$. The coefficients h_{ij} are obtained by successive orthogonal projections of

2. eigenpair = eigenvalue + eigenvector.

$\mathsf{Aq}^{(j)}$ on previous $\mathsf{q}^{(i)}, i = 0, \ldots, j$. After projection of $\mathsf{Aq}^{(j)}$ onto $\mathcal{K}_{j+1}(\mathsf{A}, \mathsf{q}^{(0)})$, there remains a contribution $\mathsf{w}^{(j)} \notin \mathcal{K}_{j+1}(\mathsf{A}, \mathsf{q}^{(0)})$ which defines $\mathsf{q}^{(j+1)}$ after normalization. This process leads to the decomposition of $\mathsf{Aq}^{(j)}$:

$$\mathsf{Aq}^{(j)} = \sum_{i=0}^{j} h_{ij}\mathsf{q}^{(i)} + h_{(j+1)j}\mathsf{q}^{(j+1)}. \tag{C.55}$$

If we denote by V_m the $n \times m$ matrix formed by the vectors $(\mathsf{q}^{(0)}, \mathsf{q}^{(1)}, \ldots, \mathsf{q}^{(m-1)})$, orthogonal basis of $\mathcal{K}_m(\mathsf{A}, \mathsf{q}^{(0)})$, and H_m the small $m \times m$ matrix of general term (h_{ij}), then one can rewrite equation (C.55) in matrix form

$$\mathsf{AV}_m = \mathsf{V}_m\mathsf{H}_m + \mathsf{re}_m^T, \text{ with } \mathsf{r} = h_{(m+1)m}\mathsf{v}^{(m+1)} \text{ and } \mathsf{e}_m^T = (\underbrace{0, \ldots, 0}_{m-1}, 1). \tag{C.56}$$

Given the fact that $\mathsf{Aq}^{(j)}$ is not rigorously in $\mathcal{K}_{j+1}(\mathsf{A}, \mathsf{q}^{(0)})$, $h_{(j+1)j} \neq 0$ in general, and H_m is a Hessenberg matrix. Multiplying (C.56) by V_m^H, one obtains:

$$\mathsf{V}_m^H\mathsf{AV}_m = \mathsf{H}_m, \tag{C.57}$$

so H_m is the orthogonal projection of A onto $\mathcal{K}_m(\mathsf{A}, \mathsf{q}^{(0)})$, and re_m^T in (C.56) is a residual matrix:

$$\mathsf{re}_m^T = \tag{C.58}$$

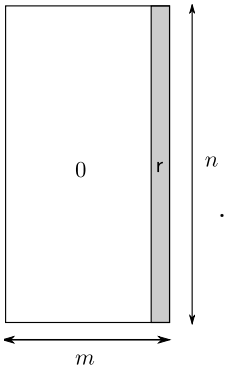

This residual is a consequence of the choice of $\mathsf{q}^{(0)}$, for which $\mathcal{K}_m(\mathsf{A}, \mathsf{q}^{(0)})$ is not an invariant subspace of A [3]. Eigenvalues θ (resp. eigenvectors y) of H_m are called Ritz values and (resp. Ritz vectors) of A. For any Ritz-pair (θ, y)

$$\|\mathsf{AV}_m\mathsf{y} - \theta\mathsf{V}_m\mathsf{y}\| = |y_m|\|\mathsf{r}\|. \tag{C.59}$$

Therefore, if the residual $\|\mathsf{r}\|$ is small, then θ (resp. $\mathsf{V}_m\mathsf{y}$) is an approximate eigenvalue (resp. eigenvector) of A. If $\mathsf{q}^{(0)}$ is in a m-dimensional invariant subspace of A, then $\|r\| = 0$ after a m-step Arnoldi factorization.

Restarting Arnoldi method

The idea behind restarting Arnoldi method is to drive the residual r to zero by forcing the initial vector $\mathsf{q}^{(0)}$ into a k-dimensional invariant subspace of A. The new initial vector $\mathsf{q}^{(0)+}$ is defined as

$$\mathsf{q}^{(0)+} \leftarrow p(\mathsf{A})\mathsf{q}^{(0)}, \tag{C.60}$$

3. subspace $\mathcal{S}$ invariant by A: for any $\mathsf{v} \in \mathcal{S}$, $\mathsf{Av} \in \mathcal{S}$.

where p is a polynomial. If $\mathsf{q}^{(0)}$ is decomposed onto the basis of eigenvectors $\{\mathsf{x}_i\}$ of A as $\mathsf{q}^{(0)} = \sum_{i=1}^{n} \gamma_i \mathsf{x}_i$, then the new starting vector is

$$\mathsf{q}^{(0)+} \equiv p(A)\mathsf{q}^{(0)} = \sum_{i=1}^{n} p(\lambda_i)\gamma_i \mathsf{x}_i. \tag{C.61}$$

If the polynomial p is chosen such that $p(\lambda_i)$ is zero for some eigenvalues, the corresponding eigenvectors x_i will be filtered out from $\mathsf{q}^{(0)}$. Therefore, *polynomial filtering* can be applied to damp undesired eigenvectors before restarting the Arnoldi factorization with the new initial vector x_i. The spectrum of H_m, which approximates a subset of the spectrum of A, can be split between k wanted eigenvalues $\mu_1, \ldots, \mu_k$ and $p = m - k$ unwanted eigenvalues $\sigma_1, \ldots, \sigma_p$. An order p polynomial defined with the p shifts

$$p(X) = (X - \sigma_1)(X - \sigma_2)\ldots(X - \sigma_p), \tag{C.62}$$

will remove the projections of q_0 onto the unwanted Ritz vectors. This simple strategy forces $\mathsf{q}^{(0)}$ into a k-dimensional subspace of H_m, spanned by the k wanted Ritz vectors. In the explicit implementation of the method, the m-step Arnoldi iteration is iteratively restarted after filtering of the unwated Ritz-vector components of $\mathsf{q}^{(0)}$, until convergence.

Implicitly restarted Arnoldi method

In practice, a more efficient and more numerically stable implementation of polynomial filtering is used, known as *implicit restarting*. Starting with a m-step Arnoldi factorization, as in (C.56)

$$\mathsf{A}\mathsf{V}_m = \mathsf{V}_m\mathsf{H}_m + \mathsf{r}\mathsf{e}_m^T, \tag{C.63}$$

apply the first factor $(X - \sigma_1)$ of $p(X)$ to all basis vectors $\mathsf{q}^{(j)}$

$$(\mathsf{A} - \sigma_1\mathsf{I})\mathsf{V}_m = \mathsf{V}_m(\mathsf{H}_m - \sigma_1\mathsf{I}) + \mathsf{r}\mathsf{e}_m^T. \tag{C.64}$$

Let $\mathsf{H}_m - \sigma_1\mathsf{I} = \mathsf{Q}_1\mathsf{R}_1$, then

$$(\mathsf{A} - \sigma_1\mathsf{I})\mathsf{V}_m = \mathsf{V}_m\mathsf{Q}_1\mathsf{R}_1 + \mathsf{r}\mathsf{e}_m^T, \tag{C.65}$$

$$\mathsf{A}(\mathsf{V}_m\mathsf{Q}_1) = (\mathsf{V}_m\mathsf{Q}_1)(\mathsf{R}_1\mathsf{Q}_1 + \sigma_1\mathsf{I}) + \mathsf{r}\mathsf{e}_m^T\mathsf{Q}_1, \tag{C.66}$$

so a new factorization is obtained

$$\mathsf{A}\mathsf{V}_m^+ = \mathsf{V}_m^+\mathsf{H}_m^+ + \mathsf{b}_m^+, \tag{C.67}$$

with

$$\mathsf{V}_m^+ \equiv \mathsf{V}_m\mathsf{Q}_1 \tag{C.68}$$

$$\mathsf{H}_m^+ \equiv \mathsf{R}_1\mathsf{Q}_1 + \sigma_1\mathsf{I} = \mathsf{Q}_1^H H_m\mathsf{Q}_1 \tag{C.69}$$

$$\mathsf{b}_m^+ \equiv \mathsf{r}\mathsf{e}_m^T\mathsf{Q}_1. \tag{C.70}$$

We notice that

- H_m^+ is a Hessenberg matrix,
- V_m^+ is unitary, since both V_m and Q_1 are unitary,

- multiplying (C.65) by $\mathsf{e}_1 = (1, \underbrace{0, \ldots, 0}_{n-1})^T$

$$(\mathsf{A} - \sigma_1 \mathsf{I}) \underbrace{\mathsf{V}_m \mathsf{e}_1}_{\mathsf{v}^{(1)}} = \underbrace{\mathsf{V}_m \mathsf{Q}_1 \mathsf{R}_1 \mathsf{e}_1}_{r_{11}\mathsf{v}_1^{(1)+}} + \underbrace{\mathsf{r} \mathsf{e}_m^T \mathsf{e}_1}_{0}, \tag{C.71}$$

  with r_{ij} the entries of the upper triangular matrix R_1. Therefore, $\mathsf{q}_1^{(0)+}$ is a multiple of $(\mathsf{A} - \sigma_1 \mathsf{I})\mathsf{q}^{(0)}$, as wanted.

This procedure is equivalent to applying a shifted QR iteration to H_m, with shift σ_1. Such step can be repeated with all p shifts σ_j with $j = 1, \ldots, p$, and a factorization of the form (C.67) is obtained with $\mathsf{Q} = \mathsf{Q}_1 \mathsf{Q}_1 \ldots \mathsf{Q}_p$ instead of Q_1. Hence, by applying p implicitly shifted QR iterations to H_m, polynomial filtering with p of order p is applied to $\mathsf{q}^{(0)}$.

The residual b_m^+ in factorization (C.67) is now of the form

$$\mathsf{b}_m^+ = \tag{C.72}$$

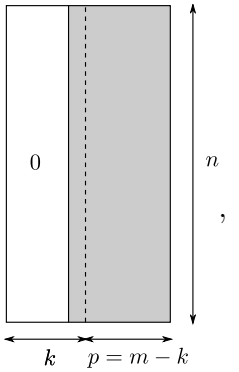

so a k-step Arnoldi factorization can be recovered by simply eliminating the last $p = m-k$ columns of (C.67). The next step in the procedure consists in performing p steps of the Arnoldi iteration to recover a m-dimensional factorization of the initial form (C.56). Then implicit restarting is applied again iteratively until convergence of the eigenvalues of H_m to the k wanted eigenvalues of A. Implicitly restarted Arnoldi method can be seen as a truncated version of the implicitly shifted QR iteration (Lehoucq et al., 1997).

This method is implemented in the free software package ARPACK [4], used in this work. More details can be found in Lehoucq et al. (1997), Saad (2011).

Shift-invert spectral transformation

Since Arnoldi method is based on power iteration, the principle of inverse power iteration can also be used if we want to follow a specific eigenvalue λ_i in the spectrum (see §C.2). The idea is to apply the Arnoldi method to the 'shifted-inverted' matrix $(\mathsf{A} - \sigma \mathsf{I})^{-1}$, with shift σ close to λ_i. The method will converge a few eigenvalues in the vicinity of the shift, and the eigenvectors will be the same as those of the initial problem. Note that in order to construct the Krylov basis, one needs to solve a sequence of linear systems with matrix $(\mathsf{A} - \sigma \mathsf{I})$ (cf. equation (C.43)). An efficient implementation factorizes the matrix in LU form in an initial step, and then performs a sequence of forward and backward solves to compute the basis.

4. http://www.caam.rice.edu/software/ARPACK/

Appendix D

Continuation methods

D.1 Newton–Raphson iteration

Newton–Raphson iteration is an efficient method to find a root $\mathbf{x}_0$ of a nonlinear continuously differentiable function $\mathbf{f} : \mathbb{R}^m \to \mathbb{R}^m$

$$\mathbf{f}(\mathbf{x}_0) = 0. \tag{D.1}$$

Assume at step n we know an approximate root $\mathbf{x}^n = \mathbf{x}_0 - \delta\mathbf{x}$, and linearize (D.1) about $\mathbf{x}^n$, then

$$\mathbf{f}(\mathbf{x}^n) + \mathbf{Df}(\mathbf{x}^n)\delta\mathbf{x}^n \approx 0, \tag{D.2}$$

where $\mathbf{Df}$ is the Jacobian matrix $(Df)_{ij} = \partial f_i/\partial x_j$. A new approximation $\mathbf{x}^{n+1} = \mathbf{x}^n + \delta\mathbf{x}^n$ at step $n+1$ is found by solving (D.2) for $\delta\mathbf{x}^n$:

$$\delta\mathbf{x}^n = -(\mathbf{Df})^{-1}(\mathbf{x}^n)\mathbf{f}(\mathbf{x}^n). \tag{D.3}$$

The iteration stops when $\|\mathbf{f}(\mathbf{x}^n)\| \leq \epsilon$, with ϵ a specified tolerance, typically 10^{-6} in our computations.

D.2 Natural continuation

Now assume $\mathbf{f}$ depends continuously on a real parameter χ, and denote $\mathbf{x}_0$ a solution of

$$\mathbf{f}(\mathbf{x}, \chi) = 0, \tag{D.4}$$

for a given value of χ. If the Jacobian of $\mathbf{f}$ with respect to $\mathbf{x}$ is non-singular for the chosen value of χ, then one can write

$$\mathbf{f}(\mathbf{x}_0(\chi), \chi) = 0, \tag{D.5}$$

using implicit function theorem. In other terms, the solution $\mathbf{x}_0$ can be parametrized by χ. Therefore, by taking small steps $\delta\chi$, the solution $\mathbf{x}_0$ can be followed continuously when χ varies (see figure D.1a). At each step, the exact value of $\mathbf{x}_0$ is converged using Newton iteration. The iteration is started with an estimated root extrapolated from the previous values of $\mathbf{x}_0$ computed at $\chi - \delta\chi$, $\chi - 2\delta\chi$, etc.

D.3 Pseudo-arclength continuation

When the graph representing the relation between $\mathbf{x}_0$ and χ displays a fold, as illustrated on figure D.1(b) (where $m = 1$ for clarity), then implicit function theorem is not applicable and it is no longer possible to parametrize the curve by χ. In this case, the solution is parametrized by an arclength variable s, on which both $\mathbf{x}$ and χ depend on the solution curve. Denote by $(\mathbf{x}_0, \chi_0)$ a solution of

$$\mathbf{f}(\mathbf{x}(s), \chi(s)) = 0, \tag{D.6}$$

for a given value of s. Small steps δs can be taken to follow this root along the associated continuous solution manifold. Newton iteration is applied at each step to converge both $\mathbf{x}_0$ and χ_0. The function $\mathbf{f}$ is differentiated with respect to both $\mathbf{x}$ and χ in the Newton iteration, so an additional constraint is needed to close the system of equations. This constraint is known as the *normalization equation* of the tangent vector $(\dot{\mathbf{x}}_0, \dot{\chi}_0) \equiv (\partial_s \mathbf{x}_0, \partial_s \chi_0)$:

$$\|\dot{\mathbf{x}}_0\|^2 + \dot{\chi}_0^2 = 1. \tag{D.7}$$

With this equation, the definition of the arclength coordinate s is unique. In practice, an approximated version of (D.7) is used (cf. Keller (1977))

$$\begin{aligned} N(\mathbf{x}, \chi) &\equiv (\mathbf{x} - \mathbf{x}_0)^T \dot{\mathbf{x}}_0 + (\chi - \chi_0)\dot{\chi}_0 - \delta s \\ &= 0, \end{aligned} \tag{D.8}$$

which corresponds to (D.7) when $\delta s \to 0$. This is the equation of a hyperplane perpendicular to the tangent vector and positioned at a distance δs from the previous point. Derivatives $\dot{\chi}_0$ and $\dot{\mathbf{x}}_0$ are simply approximated with first-order backward differences with respect to s. Newton–Raphson iteration is hence applied to solve an 'augmented' nonlinear system of size $m + 1$

$$\begin{pmatrix} \mathbf{f}(\mathbf{x}, \chi) \\ N(\mathbf{x}, \chi) \end{pmatrix} = 0. \tag{D.9}$$

Initial values for the Newton scheme are usually obtained by linear extrapolation from the previous values (see figureD.1b).

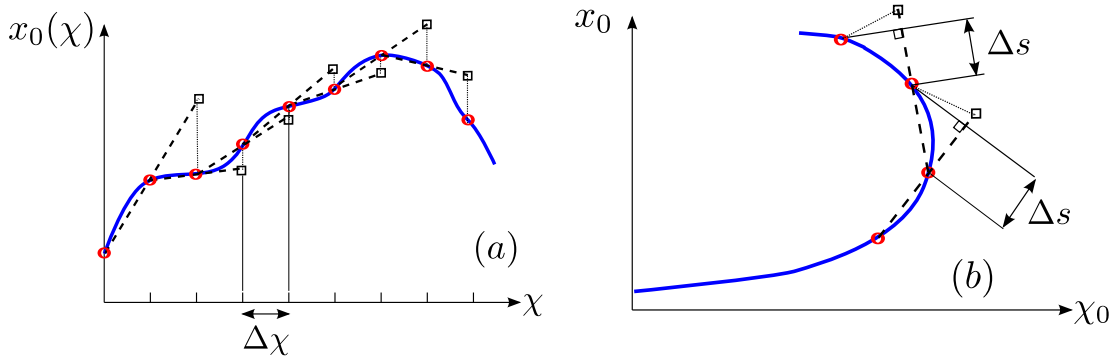

Figure D.1 – Continuation with respect to (a) 'natural' parameter χ, (b) pseudo-arclength variable s. □: estimated value from linear extrapolation, ○: converged value.

Appendix E

Eccentric Taylor–Couette flow in the Stokes régime

In this appendix, we report the formulas derived by Wannier (1950) for the eccentric Taylor–Couette flow in the Stokes limit, expressed with our system of variables and control parameters.

First, define non-dimensional distances

$$s = \frac{1}{2e\delta}\sqrt{(1-e^2)[(2+\delta)^2 - e^2\delta^2]}, \tag{E.1}$$

$$d_1 = \frac{2+\delta}{2e\delta} - \frac{e}{2}, \tag{E.2}$$

$$d_2 = \frac{2+\delta}{2e\delta} + \frac{e}{2}, \tag{E.3}$$

and some intermediate variables

$$K_1 = \frac{d_1 + s}{d_1 - s}, \tag{E.4}$$

$$K_2 = \frac{d_2 + s}{d_2 - s}, \tag{E.5}$$

$$\mathrm{den} = \frac{(1+\delta)^2 + 1}{\delta}\ln\frac{K_1}{K_2} - 4se\delta, \tag{E.6}$$

$$\{.\} = \frac{1}{(1+\delta)^2+1}\left[\frac{2(d_2^2 - d_1^2)\delta^2}{\mathrm{den}} + \frac{(1+\delta)^2}{se\delta}\right]. \tag{E.7}$$

used in the following definitions:

$$A = -\frac{1}{2}(d_1 d_2 - s^2)\{.\}, \tag{E.8}$$

$$B = (d_1 + s)(d_2 + s)\{.\}, \tag{E.9}$$

$$C = (d_1 - s)(d_2 - s)\{.\}, \tag{E.10}$$

$$D = \frac{1}{\mathrm{den}}\left[d_1 \ln K_2 - d_2 \ln K_1 - 2s\frac{(1+\delta)^2 - 1}{(1+\delta)^2 + 1}\right] - \frac{(1+\delta)^2}{e\delta[(1+\delta)^2+1]}, \tag{E.11}$$

$$\tag{E.12}$$

$$E = \frac{1}{2\text{den}} \ln \frac{K_1}{K_2}, \tag{E.13}$$

$$F = \frac{e}{\text{den}}. \tag{E.14}$$

F_y and T are then given by the following formulas:

$$F_y = -\frac{8\pi}{Re_\Omega} F, \tag{E.15}$$

$$T = \frac{8\pi}{Re_\Omega} \left(A + F d_1\right). \tag{E.16}$$

The stream function along $y = 0$ (symmetry plane) is given as a function of $x' = x + d_1$ by

$$\psi(x', e) = 2(A + Fx') \ln \left| \frac{s + x'}{s - x'} \right| + B \frac{x'}{s + x'} + C \frac{x'}{s - x'} + Dx' + E(x'^2 + s^2). \tag{E.17}$$

The azimuthal volume flux Q_ϕ can be calculated by evaluating the stream function on the inner and outer cylinders, located respectively at

$$x'_i = d_1 + 1/\delta, \tag{E.18}$$

$$x'_o = d_2 + 1 + 1/\delta. \tag{E.19}$$

Bibliography

S. Altmeyer, C. Hoffmann, and M. Lücke. Islands of instability for growth of spiral vortices in the Taylor–Couette system with and without axial through flow. *Phys. Rev. E*, 84:046308, 2011.

C. D. Andereck, S. S. Liu, and H. L. Swinney. Flow regimes in a circular Couette system with independently rotating cylinders. *J. Fluid Mech.*, 164:155–183, 1986.

W. E. Arnoldi. The principle of minimized iterations in the solution of the matrix eigenvalue problem. *Q. Appl. Maths*, 9:17–29, 1951.

M. Avila, A. Meseguer, and F. Marques. Double Hopf bifurcation in corotating spiral Poiseuille flow. *Phys. Fluids*, 18:064101, 2006.

K. L. Babcock, G. Ahlers, and D. S. Cannell. Noise-sustained structure in Taylor–Couette flow with through flow. *Phys. Rev. Lett.*, 67:3388–3391, 1991.

K. L. Babcock, D. S. Cannell, and G. Ahlers. Stability and noise in Taylor–Couette flow with through-flow. *Physica D*, 61:40–46, 1992.

K. L. Babcock, G. Ahlers, and D. S. Cannell. Noise amplification in open Taylor–Couette flow. *Phys. Rev. E*, 50:3670–3692, 1994.

A. Bayliss, A. Class, and B. J. Matkowsky. Roundoff error in computing derivatives using the Chebyshev differentiation matrix. *J. Comput. Phys.*, 116:380–383, 1995.

A. Bers. Space-time evolution of plasma instabilities–absolute and convective. In *Handbook of Plasma Physics* (ed. M. Rosenbluth & R. Sagdeev), pages 451–517. North-Holland, 1983.

R. J. Briggs. *Electron-stream Interactions with Plasmas*, pages 1–46. MIT Press, 1964.

J. E. Burkhalter and E. L. Koschmieder. Steady supercritical Taylor vortices after sudden starts. *Phys. Fluids*, 17:1929–1935, 1974.

C. Canuto, M. Y. Hussaini, A. Quarteroni, and T. A. Zang. *Spectral methods in fluid dynamics*. Springer, 1988.

P. Castle and F. R. Mobbs. Hydrodynamic stability of the flow between eccentric rotating cylinders: Visual observations and torque measurements (paper 6). In *Institution of Mechanical Engineers, Conference Proceedings*, volume 182, pages 41–52, 1967.

S. Chandrasekhar. The hydrodynamic stability of viscid flow between coaxial cylinders. *P. Natl Acad. Sci. USA*, 46:141–143, 1960.

S. Chandrasekhar. *Hydrodynamic and hydromagnetic stability*. Dover, 1981.

A. Chawda and M. Avgousti. Stability of visoelastic flow between eccentric rotating cylinders. *J. Non-Newtonian Fluid Mech.*, 63:97–120, 1996.

J.-M. Chomaz. Global instabilities in spatially developing flows: non-normality and nonlinearity. *Annu. Rev. Fluid Mech.*, 37:357–392, 2005.

J. A. Cole. Experiments on the flow in rotating annular clearances (paper 15). In *Proceedings of the Conference on Lubrication and Wear*, pages 16–19. Institution of Mechanical Engineers, 1957.

J. A. Cole. Taylor vortices with eccentric rotating cylinders. *Nature*, 216:1200–1202, 1967.

J. A. Cole. Taylor vortices with eccentric rotating cylinders. *Nature*, 221:253–254, 1969.

J. E. R. Coney. *Taylor vortex flow with special reference to rotary heat exchangers*. PhD thesis, Leeds University, 1971.

J. E. R. Coney and J. Atkinson. The effect of Taylor vortex flow on the radial forces in an annulus having variable eccentricity and axial flow. *Trans. ASME: J. Fluids Engng*, 100:210–214, 1978.

J. E. R. Coney and F. R. Mobbs. Hydrodynamic stability of the flow between eccentric rotating cylinders with axial flow: visual observations (paper 2). *Proc. Inst. Mech. Engrs*, 184 Pt 3L:10–17, 1969–70.

D. L. Cotrell and A. J. Pearlstein. The connection between centrifugal instability and Tollmien–Schlichting-like instability for spiral Poiseuille flow. *J. Fluid Mech.*, 509: 331–351, 2004.

D. L. Cotrell, L. R. Sarma, and A. J. Pearlstein. Computational assessment of subcritical and delayed onset in spiral Poiseuille flow experiments. *J. Fluid Mech.*, 509:353–378, 2004.

A. Couairon and J.-M. Chomaz. Absolute and convective instabilities, front velocities and global modes in nonlinear systems. *Physica D*, 108:236–276, 1997a.

A. Couairon and J. M. Chomaz. Pattern selection in the presence of a cross flow. *Phys. Rev. Lett.*, 79:2666–2669, 1997b.

M. Couette. Sur un nouvel appareil pour l'étude du frottement des fluides. *C. R. Acad. Sci. (Paris)*, 107:388–390, 1888a.

M. Couette. La viscosité des liquides. *Bull. Sci. Phys.*, 4:40–62,123–133,262–278, 1888b.

R.-X. Dai, Q. Dong, and A. Z. Szeri. Flow between eccentric rotating cylinders: bifurcation and stability. *Intl J. Engng Sci.*, 30:1323–1340, 1992.

J. A. Davies. Conditions for absolute instability in the cyclotron resonance maser. *Phys. Fluids B*, 1:663–669, 1989.

R. C. DiPrima. The stability of viscous flow between rotating concentric cylinders with a pressure gradient acting round the cylinders. *J. Fluid Mech.*, 6:462–468, 1959.

R. C. DiPrima. The stability of a viscous fluid between rotating cylinders with an axial flow. *J. Fluid Mech.*, 9:621–631, 1960.

R. C. DiPrima. A note on the stability of flow in loaded journal bearings. *Trans. Am. Soc. Lubric. Engrs*, 6:249–253, 1963.

R. C. DiPrima and J. T. Stuart. Flow between eccentric rotating cylinders. *J. Lubric. Tech.*, 94:266–274, 1972a.

R. C. DiPrima and J. T. Stuart. Non-local effects in the stability of flow between eccentric rotating cylinders. *J. Fluid Mech.*, 54:393–415, 1972b.

R. C. DiPrima and J. T. Stuart. The nonlinear calculation of Taylor vortex flow between eccentric rotating cylinders. *J. Fluid Mech.*, 67:85–111, 1975.

R. C. DiPrima and H. L. Swinney. Instabilities and transition in flow between concentric rotating cylinders. In *Hydrodynamic instabilities and the transition to turbulence* (eds. H. L. Swinney and J. P. Gollub), pages 139–180. Springer, 1985.

R. C. DiPrima, P. M. Eagles, and B. S. Ng. The effect of radius ratio on the stability of Couette flow and Taylor vortex flow. *Phys. Fluids*, 27:2403–2411, 1984.

I. M. Dris and E. S. G. Shaqfeh. Experimental and theoretical observations of elastic instabilities in eccentric cylinder flows: local versus global instability. *J. Non-Newtonian Fluid Mech.*, 80:1–58, 1998.

P. M. Eagles, J. T. Stuart, and R. C. DiPrima. The effects of eccentricity on torque and load in Taylor-vortex flow. *J. Fluid Mech.*, 87:209–231, 1978.

M. J. El-Dujaily and F. R. Mobbs. The effect of end walls on subcritical flow between concentric and eccentric rotating cylinders. *Intl J. Heat Fluid Flow*, 11:72–78, 1990.

M. P. Escudier and I. W. Gouldson. Effects of centrebody rotation on laminar flow through an eccentric annulus. In *Developments in laser techniques and applications to fluid mechanics. Proc. Eighth Int. Symp., Lisbon, 1996* (eds. R. J. Adrian, D. F. G. Durao, F. Durst, M. V. Heitor, M. Maeda and J. H. Whitelaw), pages 299–310. Springer, 1997.

M. P. Escudier, I. W. Gouldson, P. J. Oliveira, and F. T. Pinho. Effects of inner cylinder rotation on laminar flow of a newtonian fluid through an eccentric annulus. *Intl J. Heat Fluid Flow*, 21:92–103, 2000.

M. P. Escudier, P. J. Oliveira, and F. T. Pinho. Fully developed laminar flow of purely viscous non-newtonian liquids through annuli, including the effects of eccentricity and inner-cylinder rotation. *Intl J. Heat Fluid Flow*, 23:52–73, 2002.

S. Feng and S. Fu. Influence of orbital motion of inner cylinder on eccentric Taylor vortex flow of newtonian and power-law fluids. *Chin. Phys. Lett.*, 24:759–762, 2007.

S. Feng, Q. Li, and S. Fu. On the orbital motion of a rotating inner cylinder in annular flow. *Intl J. Numer. Meth. Fluids*, 54:155–173, 2007.

J. Frêne and M. Godet. Transition from laminar to Taylor vortex flow in journal bearings. *Tribology*, 4:216–217, 1971.

M. Gaster. A note on the relation between temporally-increasing and spatially-increasing disturbances in hydrodynamic stability. *J. Fluid Mech.*, 14:222–224, 1962.

F. Giannetti and P. Luchini. Receptivity of the circular cylinder's first instability. In *Proc. 5th Eur. Fluid Mech. Conf., Toulouse*, 2003.

K. Goda. A multistep technique with implicit difference schemes for calculating two- or three-dimensional cavity flows. *J. Comput. Phys.*, 30:76–95, 1979.

G. H. Golub and C. F. Van Loan. *Matrix computations* (3rd edition). Johns Hopkins University Press, 1989.

B. Guo and G. Liu. *Applied Drilling Circulation Systems — Hydraulics, calculations, models*. Elsevier, 2011.

J. J. Healey. On the relation between the viscous and inviscid absolute instabilities of the rotating-disk boundary layer. *J. Fluid Mech.*, 511:179–199, 2004.

C. J. Heaton. Optimal linear growth in spiral Poiseuille flow. *J. Fluid Mech.*, 607: 141–166, 2008.

P. Huerre. Open shear flow instabilities. In *Perspectives in Fluid Dynamics* (eds. G. K. Batchelor, H. K. Moffat & M. G. Worster), pages 159–229. Cambridge University Press, 2000.

P. Huerre and P. A. Monkewitz. Absolute and convective instabilities in free shear layers. *J. Fluid Mech.*, 159:151–68, 1985.

P. Huerre and P. A. Monkewitz. Local and global instabilities in spatially developing flows. *Annu. Rev. Fluid. Mech.*, 22:473–537, 1990.

N. J. Huggins. Tests on a 24-in diameter journal bearing: transition from laminar to turbulent flow. In *Symposium on Journal Bearings for Reciprocating and Turbo Machinery, Proc. Inst. Mech. Engrs*, volume 181 (Pt 3B), page 81, 1966–67.

J. Y. Hwang and K. S. Yang. Numerical study of Taylor–Couette flow with an axial flow. *Comput. Fluids*, 33:97–118, 2004.

J. D. Jansen. Non-linear rotor dynamics as applied to oilwell drillstring vibrations. *J. Sound Vib.*, 147:115–135, 1991.

M. P. Juniper. The effect of confinement on the stability of two-dimensional shear flows. *J. Fluid Mech.*, 565:171–195, 2006.

M. M. Kamal. Separation in the flow between eccentric rotating cylinders. *J. Basic Engng*, 88:717–724, 1966.

T. Karasudani. Non-axis-symmetric Taylor vortex flow in eccentric rotating cylinders. *J. Phys. Soc. Japan*, 56:855–858, 1987.

T. von Kármán. Some aspects of the turbulence problem. In *Proc. 4th Int. Congr. Appl. Mech. (Cambridge, England)*, pages 54–91, 1934.

H. B. Keller. Numerical solution of bifurcation and nonlinear eigenvalue problems. In *Applications of Bifurcation Theory* (ed. P. Rabinowitz), pages 359–384. Academic, 1977.

E. L. Koschmieder. Taylor vortices between eccentric cylinders. *Phys. Fluids*, 19:1–4, 1976.

C. Leclercq, B. Pier, and J. F. Scott. Temporal stability of eccentric Taylor–Couette–Poiseuille flow. *J. Fluid Mech.*, 733:68–99, 2013.

R. B. Lehoucq, D. C. Sorensen, and C. Yang. ARPACK users' guide: Solution of large-scale eigenvalue problems with implicitly restarted Arnoldi methods, 1997.

T. T. Lim and S. S. Lim. Modified expression for critical Reynolds number in eccentric Taylor Couette flow. *AIAA J.*, 46:277–280, 2008.

M. Lücke and A. Recktenwald. Amplification of molecular fluctuations into macroscopic vortices by convective instabilities. *Europhys. Lett.*, 22:559, 1993.

P. A. Mackrodt. Stability of Hagen–Poiseuille flow with superimposed rigid rotation. *J. Fluid. Mech.*, 73:153–164, 1976.

A. Mallock. Determination of the viscosity of water. *Proc. R. Soc. Lond.*, 45:126–132, 1888.

F. Marques and J. M. Lopez. Spatial and temporal resonances in a periodically forced hydrodynamic system. *Physica D*, 136:340–352, 2000.

D. Martinand, E. Serre, and R. M. Lueptow. Absolute and convective instability of cylindrical Couette flow with axial and radial flows. *Phys. Fluids*, 21:104102, 2009.

P. Meliga, J.-M. Chomaz, and D. Sipp. Global mode interaction and pattern selection in the wake of a disk: a weakly nonlinear expansion. *J. Fluid Mech.*, 633:159–189, 2009.

E. Merzari, S. Wang, H. Ninokata, and V. Theofilis. Biglobal linear stability analysis for the flow in eccentric annular channels and a related geometry. *Phys. Fluids*, 20: 114104, 2008.

A. Meseguer and F. Marques. On the competition between centrifugal and shear instability in spiral Couette flow. *J. Fluid Mech.*, 402:33–56, 2000.

A. Meseguer and F. Marques. On the competition between centrifugal and shear instability in spiral Poiseuille flow. *J. Fluid Mech.*, 455:129–148, 2002.

F. R. Mobbs and M. S. Ozogan. Study of sub-critical Taylor vortex flow between eccentric rotating cylinders by torque measurements and visual observations. *Intl J. Heat Fluid Flow*, 5:251–253, 1984.

F. R. Mobbs and M. A. M. A. Younes. The Taylor vortex regime in the flow between eccentric rotating cylinders. *Trans. ASME: J. Lubric. Tech.*, pages 127–134, 1974.

H. Nagib. *On instabilities and secondary motions in swirling flows through annuli*. PhD thesis, Illinois Institute of Technology, 1972.

B. S. Ng and E. R. Turner. On the linear stability of spiral flow between rotating cylinders. *Proc. R. Soc. Lond.* A *Mat.*, 382:83–102, 1982.

M. Oikawa, T. Karasudani, and M. Funakoshi. Stability of flow between eccentric rotating cylinders. *J. Phys. Soc. Japan*, 58:2355, 1989a.

M. Oikawa, T. Karasudani, and M. Funakoshi. Stability of flow between eccentric rotating cylinders with a wide gap. *J. Phys. Soc. Japan*, 58:2209, 1989b.

G. Ooms and B. E. Kampman-Reinhartz. Influence of drill pipe rotation and eccentricity on pressure drop over borehole during drilling. *Eur. J. Mech. B–Fluids*, 15:695–711, 1996.

S. A. Orszag. On the elimination of aliasing in finite-difference schemes by filtering high-wavenumber components. *J. Atmos. Sci.*, 28:1074–1074, 1971.

J. R. A. Pearson. Rheological principles and measurements applied to the problems of drilling and completing oil wells. In *Proc. X^{th} Int. Cong. Rheology*, volume 1, pages 73–78, 1988.

R. Peyret. *Spectral methods for incompressible viscous flow*. Springer, 2002.

B. Pier and P. Huerre. Fully nonlinear global modes in spatially developing media. *Physica D*, 97:206–222, 1996.

B. Pier and P. Huerre. Nonlinear synchronization in open flows. *J. Fluids Struct.*, 15: 471–480, 2001.

B. Pier, P. Huerre, J.-M. Chomaz, and A. Couairon. Steep nonlinear global modes in spatially developing media. *Phys. Fluids*, 10:2433–2435, 1998.

B. Pier, P. Huerre, and J.-M. Chomaz. Bifurcation to fully nonlinear synchronized structures in slowly varying media. *Physica D*, 148:49–96, 2001.

A. Pinter, M. Lücke, and C. Hoffmann. Spiral and Taylor vortex fronts and pulses in axial through flow. *Phys. Rev. E*, 67:026318, 2003.

E. V. Podryabinkin and V. Y. Rudyak. Moment and forces exerted on the inner cylinder in eccentric annular flow. *J. Engng Thermophys.*, 20:320–328, 2011.

A. Quarteroni, R. Sacco, and F. Saleri. *Méthodes numériques pour le calcul scientifique : programmes en MATLAB*. Springer, 2006.

I. Raspo, S. Hugues, E. Serre, A. Randriamampianina, and P. Bontoux. A spectral projection method for the simulation of complex three-dimensional rotating flows. *Comput. Fluids*, 31:745–767, 2002.

L. Rayleigh. On the dynamics of revolving fluids. *Proc. R. Soc. Lond.* A *Mat.*, 93: 148–154, 1917.

A. Recktenwald, M. Lücke, and H. W. Müller. Taylor vortex formation in axial through-flow: linear and weakly nonlinear analysis. *Phys. Rev. E*, 48:4444–4454, 1993.

W. H. Reid. Review of 'The hydrodynamic stability of viscid flow between coaxial cylinders' by S. Chandrasekhar (Proc. Natl Acad. Sci. USA **46**, 141–143, 1960). *Math. Rev.*, 22:565, 1961.

G. S. Ritchie. On the stability of viscous flow between eccentric rotating cylinders. *J. Fluid Mech.*, 32:131–144, 1968.

Y. Saad. *Numerical methods for large eigenvalue problems* (2nd edition). SIAM, 2011.

P. J. Schmid and D. S. Henningson. *Stability and transition in shear flows.* Springer, 2001.

J. Sep. Journal bearing with an intensive axial oil flow–experimental investigation. *Scientific Problems of Machines Operation and Maintenance*, 43:21–29, 2008.

H. A. Snyder. Experiments on the stability of spiral flow at low axial Reynolds numbers. *Proc. R. Soc. Lond.* A *Mat.*, 265:198–214, 1962.

H. A. Snyder. Experiments on the stability of two types of spiral flow. *Ann. Phys.–New York*, 31:292–313, 1965.

J. B. Swift, K. L. Babcock, and P. C. Hohenberg. Effects of thermal noise in Taylor–Couette flow with corotation and axial through-flow. *Physica A*, 204:625–649, 1994.

R. Tagg. A guide to literature related to the Taylor–Couette problem. In *Ordered and turbulent patterns in Taylor–Couette flow*, pages 303–354. Springer, 1992.

D. I. Takeuchi and D. F. Jankowski. Numerical and experimental investigation of the stability of spiral Poiseuille flow. *J. Fluid Mech.*, 102:101–26, 1981.

G. I. Taylor. Stability of a viscous liquid contained between two rotating cylinders. *Phil. Trans. R. Soc. Lond.*, 223:289–343, 1923.

L. H. Thomas. Elliptic problems in linear difference equations over a network. Technical report, Watson Sci. Comput. Lab., Columbia University, New York, 1949.

A. Tsameret and V. Steinberg. Noise-modulated propagating pattern in a convectively unstable system. *Phys. Rev. Lett.*, 67:3392–3395, 1991a.

A. Tsameret and V. Steinberg. Convective *vs.* absolute instability in Couette–Taylor flow with an axial flow. *Europhys. Lett.*, 14:331–336, 1991b.

A. Tsameret and V. Steinberg. Absolute and convective instabilities and noise-sustained structures in the Couette–Taylor system with an axial flow. *Phys. Rev. E*, 49:1291–1308, 1994.

P. L. Versteegen and D. F. Jankowski. Experiments on the stability of viscous flow between eccentric rotating cylinders. *Phys. Fluids*, 12:1138–1143, 1969.

J. A. Vohr. An experimental study of Taylor vortices and turbulence in flow between eccentric rotating cylinders. *Trans. ASME: J. Lubric. Tech.*, 90:285–296, 1968.

G. H. Wannier. A contribution to the hydrodynamics of lubrication. *Q. Appl. Maths*, 8:1–32, 1950.

D. S. Watkins. The QR algorithm revisited. *SIAM rev.*, 50:133–145, 2008.

G. B. Whitham. *Laminar boundary layers* (ed. L. Rosenhead), chapter III: The Navier–Stokes equations of motion. Clarendon Press, Oxford, 1963.

J. H. Wilkinson. *The algebraic eigenvalue problem*. Clarendon Press, Oxford, 1965.

W. W. Wood. The asymptotic expansions at large Reynolds numbers for steady motion between noncoaxial rotating cylinders. *J. Fluid Mech.*, 3:159–175, 1957.

Q. Xiao, T. T. Lim, and Y. T. Chew. Experimental investigation on the effect of eccentricity on Taylor–Couette flow. In *Transport Phenomena in Thermal Science and Process Engineering*, pages 685–689, Kyoto, Japan, 1997.

M. A. M. A. Younes. *The hydrodynamic stability of spiral flow between eccentric rotating cylinders*. PhD thesis, Leeds University, 1972.

M. A. M. A. Younes, F. R. Mobbs, and J. E. R. Coney. Hydrodynamic stability of the flow between eccentric rotating cylinders with axial flow: torque measurements (paper C76/72). In *Tribology convention, Institution of Mechanical Engineers*, pages 14–19, 1972.

Résumé

Cette thèse porte sur les effets combinés de l'excentricité et du débit axial sur les propriétés de stabilité linéaire de l'écoulement de Couette circulaire avec cylindre extérieur fixe. Cet écoulement intervient, entre autres, lors du forage de puits de pétrole. Une méthode pseudo-spectrale est mise en œuvre pour calculer l'écoulement de base, stationnaire et invariant suivant la direction axiale, ainsi que les modes normaux d'instabilité. L'écoulement est régi par quatre paramètres adimensionnels : rapport de rayons η et excentricité e pour la géométrie, nombres de Reynolds azimuthal et axial, Re_Ω et Re_z, pour la dynamique.

La première partie de l'étude est consacrée aux propriétés de stabilité temporelle. Il apparaît que l'excentricité repousse le seuil d'instabilité convective vers de plus fortes valeurs de Re_Ω. L'effet de l'advection axiale sur le seuil est principalement stabilisant également. L'excentricité a pour conséquence de déformer la structure des modes par rapport au cas concentrique. Le mode au plus fort taux de croissance temporelle est ainsi constitué de tourbillons de Taylor « pseudo-toroïdaux » lorsque le débit axial est nul, et de structures « pseudo-hélicoïdales » d'ordre azimuthal croissant lorsque Re_z augmente. Les résultats sont qualitativement similaires lorsque l'on change le rapport de rayons. Les prédictions théoriques sont en bon accord avec les quelques résultats expérimentaux disponibles.

Dans une seconde partie, l'instabilité absolue est étudiée par application d'un critère de point selle à la relation de dispersion. Le débit axial a pour effet d'inhiber fortement l'instabilité absolue, d'origine centrifuge, et la valeur de Re_Ω au seuil est typiquement supérieure à celle de Re_z d'un ordre de grandeur. L'effet de l'excentricité est plus complexe : légère stabilisation aux faibles valeurs de e, puis déstabilisation marquée aux excentricités modérées lorsque Re_z est suffisament grand, et enfin stabilisation lorsque e croît davantage. Contrairement au cas de l'instabilité convective, le mode dominant l'instabilité absolue correspond à l'écoulement tourbillonnaire « pseudo-toroïdal » pour toute la gamme de paramètres considérée.

Mots-clés: écoulement de Taylor–Couette–Poiseuille, excentricité, instabilités convective et absolue.

Abstract

This work is concerned with the combined effects of eccentricity and pressure-driven axial flow on the linear stability properties of circular Couette flow with a fixed outer cylinder. An example of this flow can be found in oil-well drilling operations. A pseudospectral method is implemented to compute the basic flow, steady and homogeneous in the axial direction, as well as the normal modes of instability. There are four non-dimensional parameters: the radius ratio η and the eccentricity e for the geometry, the azimuthal and axial Reynolds numbers, Re_Ω and Re_z, for the dynamics.

The first part of the study is devoted to the temporal stability properties. It is found that eccentricity pushes the convective instability threshold towards higher values of Re_Ω. The effect of axial advection on the threshold also tends to be stabilising. Eccentricity deforms the modes structure compared to the concentric case. As a result, the mode with the largest temporal growth rate takes the form of 'pseudo-toroidal' Taylor vortices in the absence of axial flow, and 'pseudo-helical' structures with increasing azimuthal order as Re_z becomes larger. Results are qualitatively similar for different radius ratios. Agreement with the few available experimental data is good.

In a second part, absolute instability is studied by applying the pinch-point criterion to the dispersion relation. Axial flow is found to strongly inhibit absolute instability, the mechanism of which being centrifugal, and the value of Re_Ω at the threshold is typically one order of magnitude larger than that of Re_z. The effect of eccentricity is more complex: weak stabilisation for low values of e, marked destabilisation for moderate eccentricities and high enough Re_z, and finally stabilisation as e is further increased. Unlike temporal instability, the dominant absolutely unstable mode is the 'pseudo-toroidal' Taylor vortex flow over the whole range of parameter space considered.

Keywords: Taylor–Couette–Poiseuille flow, eccentricity, convective and absolute instability.